Molecular characterisation of childhood craniopharyngioma and identification and testing of novel drug targets

John Richard Apps

Thesis submitted to University College London (UCL) for the degree of Doctor of Philosophy

2017

UCL Cancer Institute and Developmental Biology and Cancer Programme,

GOSH-UCL Institute of Child Health, University College London

Declaration

I, John Richard Apps, confirm that the work presented in this thesis is my own. Where information has been derived from other sources, I confirm that this has been indicated in the thesis.

Abstract

Background:

Adamantinomatous Craniopharyngiomas (ACPs) are clinically challenging sellar region tumours, known to be characterised by mutations in *CTNNB1*. ACPs are often histologically complex, with different morphological cell types and surrounded by a florid glial reaction. Murine models have been generated through activating β-catenin and support a critical role for nucleo-cytoplasmic accumulating β-catenin cell clusters ('clusters') in driving tumorigenesis.

Aims:

- To phenotype in detail the 3D growth patterns of human and murine ACP.
- To characterise the genomic and transcriptomic landscape of human and murine ACP, including of clusters.
- To characterise therapeutically targetable molecular pathways and perform pre-clinical therapeutic trials.

Methods:

Human ACP samples underwent micro-focus-CT scanning, whole genome sequencing, targeted next generation sequencing and RNA sequencing, both with, and without, laser capture microdissection. The growth dynamics of murine ACP was characterised by serial MRI and a cohort of murine ACPs, at various stages, underwent RNA and exome sequencing. A pre-clinical murine trial using a Sonic Hedgehog (SHH) pathway inhibitor was performed.

Results:

CTNNB1 mutations in human ACP were confirmed as clonal within tumour epithelia. Gene expression signatures corresponding to tumour epithelia, reactive glia and immune infiltrate were derived and novel ACP genes were identified (e.g. *BCL11B*). A relationship between human and murine ACPs with the developing tooth was also established, in particular the similarity of clusters to the enamel knot. Further

molecular dissection identified a complex interplay between tumour cell compartments demonstrating a role for paracrine signalling. Inhibition of the SHH pathway in the pre-clinical murine trial resulted in a decrease in median survival from 33 weeks to 11.9 weeks (p=0.048). A signature of inflammasome activation in ACP was also identified in solid and cystic components of ACP.

Conclusions:

ACPs have clonal mutations in *CTNNB1* and exhibit complex signalling interplay between different cell compartments. Expression analysis reveals a new molecular paradigm for understanding ACP tumorigenesis as an aberrant copycat of natural tooth development, with inflammation driven by activation of inflammasomes. Caution is recommended in the use of SHH pathway inhibitors in patients with ACP.

Acknowledgements

I am extremely grateful to the large number of people who have made this thesis possible. Many of the experiments have been collaborative in nature and without their help and support much of what is documented here would have been impossible.

First, I would like to thank my supervisors who have given me constant support throughout the project. Professor JP Martinez-Barbera has been an inspiration to work for and taught me many valuable lessons about all aspects of science. Dr Tom Jacques has also been invaluable in providing support, both with the management and assessment of samples, but also in bridging the basic science to the clinical setting. Finally, Dr Darren Hargrave has provided an insightful therapeutic perspective to all of the experiments.

In addition to my supervisors, my thanks also go to their teams, past and present, which have provided invaluable support. In particular, from JP Martinez-Barbera's group, Mario Gonzalez-Meljem, for taking the time to teach me many of the laboratory methods, Scott Haston, for his assistance in immunofluorescent stainings, Leonidas Panousopoulos for his PCR expertise and efficiency, Gabriela Carreno for her technical expertise and support in the murine ACP trial and Christina Stache for her deep insight into craniopharyngioma biology. From Tom Jacques' group; Alex Virasami for his help in management and sectioning of human samples, ably supported by Aimee Avery, and Tom Stone for introducing me to the basics of R and RNA sequencing analysis.

In addition to my supervisors and their teams, I have been extremely fortunate to work with a number of collaborators. I would particularly like to thank Dr Hywel Williams for his supervision of the human RNA sequencing analysis and the help from Nital Jani in initial data processing, Dr Ciaran Hutchinson for his help in performing micro-CT analysis, Dr Jessica Boult and Dr Simon Robinson for MRI imaging of murine ACP, Professor Lou Chesler and his team (particularly Dr Laura Danielson) for their running of the Vismodegib trial in murine ACP, Dr Tim Forshew and Alice Gutteridge for their work on Targeted NGS sequencing, Dr David Adams

and Manamur Rashid for their exome sequencing of murine ACP, Dr Sam Behjati for his help in analysing the whole genome sequencing data of human ACP, Dr Ying Hong, for her help in running the MSD multiplex ELISA and Dr Kyoko Tossell for training me in laser capture microdissection.

This thesis covers many different fields of research and I am very grateful for the advice of Professor Martyn Cobourne, Dr Selvam Thavaraj and Dr Cynthia Andoniadou with respect to the biology of the tooth, Professor Jesus Gil with respect to senescence and Professor Paul Brogan with regard to inflammasome mediated inflammation. I am also extremely grateful for the opportunity to attend the extremely well taught Cancer Research UK Bioinformatics Summer Schools (2015, 2016) and Winter School (2016), run by Dr Mark Dunning, without which I would not have been able to perform many of the bioinformatics analyses that underpin the work of this thesis.

The samples used in this thesis were available thanks to the support and help of many clinicians across the UK and Europe. In particular I would like to thank, Mr Krisitian Aquilina, Kim Phipps, Professor Richard Grundy, Dr Lisa Storer, Dr Abhijit Joshi, Dr David Hilton, Professor Francesco Roncaroli, Professor Marta Korbonitis, Professor Hermann Muller, Dr Chris-Anne McKenzie, Miss Benedetta Pettorini, as well as staff at the Children's Cancer and Leukaemia Group tissue bank (Gita Mistry, Alison Page), Brain UK (Clare Mitchell) and Human and Developmental Biology Resource (Dianne Gerelli).

This work has only been possible through generous funding from several sources. Foremost, Cancer Research UK, through my Clinical Research Training Fellowship. In addition, funds from the Great Ormond Street NIHR Biomedical Research Centre, the Children's Cancer and Leukaemia Group and Children with Cancer UK, as well as local financial support from many of the collaborators mentioned above. I am extremely grateful for the opportunities that this funding has allowed me to pursue.

Finally I would like to thank my wife, Julia, and children, Sophie and Felicity, for supporting me through this time and putting up with absences from home, distractions and hearing about my experimental and analytical frustrations.

Table of contents

List of Figures

List of Tables

Supplementary Material

Supplementary Table 1: Full targeted sequencing results

Supplementary Table 2: Human DE results

Supplementary Table 3: Human WGCNA results

Supplementary Table 4: Murine DE results

Supplementary Table 5: Murine WGCNA results

Supplementary Table 6: Murine Exome sequencing results

Supplementary Table 7: Human WGS results

Supplementary Videos 1-3: Virtual dissection of human adamantinomatous craniopharnygioma specimens by micro-CT imaging. Nodules and islands of tumour are visible within reactive glial tissue. Epithelial whorls/clusters are present. Areas of wet keratin have higher grey level values (appear whiter).

Abbreviations

ACP	Adamantinomatous craniopharyngioma
BMP	Bone morphogenic proteins
BMPR	Bone morphogenic protein receptor
BRASS	BReakpoint AnalySiS
C	Cluster
CaVEMan	Cancer Variants Through Expectation Maximization
CCLG	Children's Cancer and Leukaemia Group
cfDNA	Cell free DNA
Chr	Chromosome
CNV	Copy number variant
CP	Craniopharyngioma
DAB	Diaminobenzidine
DAPI	Diamindino-2-Phenylindole
ddPCR	Digital droplet PCR
DE	Differential expression
dpc	Days post coitum
EDTA	Ethylenediaminetetraacetic acid
EGFR	Epidermal growth factor receptor
EGTA	Ethylene glycol-bis(2-aminoethylether)-N,N,N',N'-tetraacetic acid
ELISA	Enzyme linked immunosorbant assay
FFPE	Formalin fixed paraffin embedded
FGF	Fibroblast growth factor
FGFR	Fibroblast growth factor receptor
GDF	Growth and differentiation factors
GO	Gene ontology
GOSH	Great Ormond Street Hospital
GSEA	Gene set enrichment analysis
H+E	Haematoxylin and eosin
HDBR	Human Developmental Biology Resource
HED	Hyperhidrotic ectodermal dysplasia
ICH	Institute of Child Health
ICHTB	Imperial College Hospital NHS Tissue Bank
ICR	Institute of Cancer Research
IEE	Inner enamel epithelium
IFN	Interferon
Indel	Insertion or deletion
Micro-CT	Microfocus computed tomography
NGMGCT	Non germinomatous malignant germ cell tumour
NGS	Next generation sequencing
PBS	Phosphate buffered saline
PCP	Papillary craniopharyngioma
PD	Pharmacodynamics

PE	Palisading epithelium
PK	Pharmacokinetics
RIN	RNA integrity number
SHH	Sonic hedgehog
SNP	Single nucleotide polymorphism
SNV	single nucleotide variant
SR	Stellate reticulum
SSCP	Single-strand conformation polymorphism analysis
TGF	Transforming growth factor
TGFBR	Transforming growth factor β receptor
TGFβ	Transforming growth factor β
WGCNA	Weighted gene co-expression network analysis
WGS	Whole genome sequencing
WT	Wild-type
YFP	Yellow fluorescent protein

Chapter 1 Introduction

1.1 Introduction

The diagnostic and therapeutic landscape of cancer is currently undergoing profound changes as a result of understanding the molecular processes underlying and driving tumourigenesis, so called 'precision' or 'personalised' oncology.

Analysis of patient samples, particularly through the use of modern molecular technologies is resulting in tumour types and subtypes being redefined based on molecular characteristics e.g. in paediatric brain tumours such as medulloblastoma (Taylor, Northcott et al. 2012, Schwalbe, Hayden et al. 2013). Using this knowledge of underlying tumour biology, targeted therapies have been developed e.g. Sonic Hedgehog and other pathway inhibitors (Gould, Low et al. 2014, Zhao and Adjei 2014). A key aspect to this process has been the use of representative mouse models, which facilitate both detailed *in vivo* investigation of molecular pathways and their interactions, but also increasingly more rationalised drug development and testing (Day, Merlino et al. 2015, Le Magnen, Dutta et al. 2016).

Tumours are the leading cause of death in children in the UK and it is recognised that many tumours of childhood relate to aberrations in normal development (Scotting, Walker et al. 2005, Cancer Research UK 2017). In this thesis I explore the molecular biology of craniopharyngioma, a rare, but clinically important paediatric tumour. Through molecular profiling and use of mouse models, I explore its relationship to developmental processes and characterise and test potential novel therapeutic opportunities.

1.2 Craniopharyngioma: Clinical challenges and opportunities for precision medicine

Craniopharyngiomas (CPs) are benign epithelial tumours of the sellar region. Two subtypes have been defined; adamantinomatous craniopharyngioma (ACP) is the commonest tumour of the sellar region in childhood and has a biphasic distribution of age of incidence at 5-15 years and 45-50 years (Louis, Ohgaki et al. 2016). There are approximately 17 new cases of childhood craniopharyngioma registered in the

UK each year (Childhood cancer registration in England, 2015-2016, Public Health England). In contrast, papillary craniopharyngioma (PCP) is predominantly a disease of adults, peaking incidence at 40-55 years (Louis, Ohgaki et al. 2016). This thesis predominantly focuses on ACP.

CPs are clinically challenging due to their often supra-sellar origin and tendency to grow, invade and destroy eloquent surrounding structures, notably the pituitary, hypothalamus and visual pathways (Kasai, Hirano et al. 1997, Kawamata, Kubo et al. 2005, Apps, Hutchinson et al. 2016, Louis, Ohgaki et al. 2016, Muller, Merchant et al. 2017). ACPs are variably cystic and solid and exhibit marked clinical heterogeneity. Some tumours remain indolent despite partial resection, whilst others relapse frequently, despite apparent complete resections and radiotherapy (Muller 2010, Tan, Patel et al. 2017).

The current mainstay of treatment is surgery and radiotherapy, both of which themselves can result in further damage to the local structures (Muller, Merchant et al. 2017). For recurrent cystic fluid accumulation, intra-cystic administration of cytotoxic agents and radio-nucleotides has previously been used, but have now been discontinued due to toxicities (Bartels, Laperriere et al. 2012). Intra-cystic administration of IFNα is currently performed in some centres, based on similarities in epithelial origin between head and neck squamous cell carcinoma and ACP (Cavalheiro, Dastoli et al. 2005, Bartels, Laperriere et al. 2012). Whilst effects on cystic fluid accumulation have been reported, definitive evidence of efficacy is currently lacking and there are some concerns regarding toxicity. Sharma *et al*. 2015, report a case of an 8 year old girl who suffered transient expressive aphasia, relating to a leakage of IFNα (Sharma, Bonfield et al. 2015). The authors also highlight previous adverse events, including progressive vegetative state, relating to intrathecal administration for other indications (Sharma, Bonfield et al. 2015). Consequently, the management of recurrent cystic accumulation remains clinically challenging.

Despite overall 5 and 10 year survival rates for childhood ACP of greater than 90%, there is a long term high risk of relapse (~ 50% at 20 years) and increased mortality

(Sterkenburg, Hoffmann et al. 2015, Muller, Merchant et al. 2017). At 20 years, survival rates between 62-95% are reported, with worse survival in those with hypothalamic damage (Crowley, Hamnvik et al. 2010, Visser, Hukin et al. 2010, Sterkenburg, Hoffmann et al. 2015).

The majority of patients develop sequelae resulting in poor quality of life and long term psychosocial functioning (Table 1-1) (Steinbok 2015, Sterkenburg, Hoffmann et al. 2015, Muller, Merchant et al. 2017). Whilst reduction of some of the sequelae may be achieved by emerging surgical risk-stratification strategies (e.g. the use of radiological and clinical criteria to assess hypothalamic involvement and safety of aggressive surgery), there is an urgent need for more rationally determined therapeutics, both as an adjunct for surgery and radiotherapy, but also for rescue treatment in those who progress despite surgery and radiotherapy or have recurrent cystic fluid accumulation (Puget, Garnett et al. 2007, Mallucci, Pizer et al. 2012, Apps and Martinez-Barbera 2016).

Considerable efforts have been invested in understanding the biology of craniopharyngioma to speed up the development of such novel therapeutic strategies (Apps and Martinez-Barbera 2016). For PCP, which harbour activating p.V600E mutations in the *BRAF* gene, BRAF and MEK inhibitors have been found to have some benefit in the limited cohorts of patients published to date (Aylwin, Bodi et al. 2015, Brastianos, Shankar et al. 2016). In contrast, no such novel, rationally targeted therapies have yet been successful for ACP.

Table 1-1: Summary of long term sequelae of craniopharyngioma (Steinbok 2015, Sterkenburg, Hoffmann et al. 2015, Muller, Merchant et al. 2017)

Long term effect	Details
Endocrinopathy (up to 95%)	Isolated diabetes insipidus to pan hypopituitarism
Visual impairment (50-80%)	Including complete blindness
Hypothalamic obesity	Associated with:Type 2 diabetes mellitus, hypertension, increased cardiovascular risk, non alcoholic fatty steatohepatitis
Congitive impairment	Including emotional lability, memory deficits, attention deficits
Other	Headaches, cerebrovascular abnormalities, seizures diarrhoea, dyspnoea

1.3 Histopathology of craniopharyngioma

ACPs are histologically complex tumours with variable cystic, calcified and solid components and frequent invasion of adjacent tissues, with tumour infiltrating finger-like structures surrounded by a florid glial and inflammatory reactive tissue (Louis, Ohgaki et al. 2016). Within tumour epithelia, a peripheral layer of palisading epithelium (PE) encloses more loosely packed stellate cells, called stellate reticulum (SR) and epithelial whorls (Figure 1-1). A pathognomonic feature is the presence of eosinophilic anuclear ghost cells, also known as wet keratin (Figure 1-1).

The name 'adamantinomatous' craniopharyngioma derives from the histological resemblance with adamantinomas of the jaw (now known as ameloblastoma), highlighting similarities between ACP and odontogenesis and odontogenic tumours. Indeed ghost cells are only otherwise observed in calcifying odontogenic cysts and a type of hair follicle tumour called pilomatricoma (Rumayor, Carlos et al. 2015). Whilst similarities to odontogenesis have long been recognised histologically, the molecular relationships have been relatively unexplored, other than limited immune-histochemical characterisations of co-expression of enamel proteins, proteinases and some keratins (Gorlin and Chaudhry 1959, Kalnins 1971, Bernstein and Buchino 1983, Paulus, Stockel et al. 1997).

In contrast to ACP, PCPs are predominantly cystic and characterised by more well circumscribed pseudostratified epithelium forming pseudo-papillae often around fibro-vascular cores (Figure 1-1) (Louis, Ohgaki et al. 2016). Unlike ACP, no similarities to odontogenesis have been observed (Paulus, Stockel et al. 1997).

The relationship of craniopharyngioma biology to tooth development emerges from many of the analyses in this thesis and will be covered in detail in Chapters 5, 6 and the discussion. An overview of tooth development is introduced in section 1.9.

Figure 1-1: Histopathology of ACP and PCP. a) Representative histology of ACP samples showing and areas of tumour (T), reactive glial tissue (G), wet keratin/ghost cells (WK), epithelial whorls (EW), palisading epithelium (PE) and stellate reticulum (SR). Immunohistochemistry using antibodies against β-catenin on case JA029 showing clusters of cells with nuclear-cytoplasmic accumulation. b) Representative histology of PCP showing epithelia (E) and fibro-vascular core (FV). Scale bars = 400µm (low power), 100µm (high power)

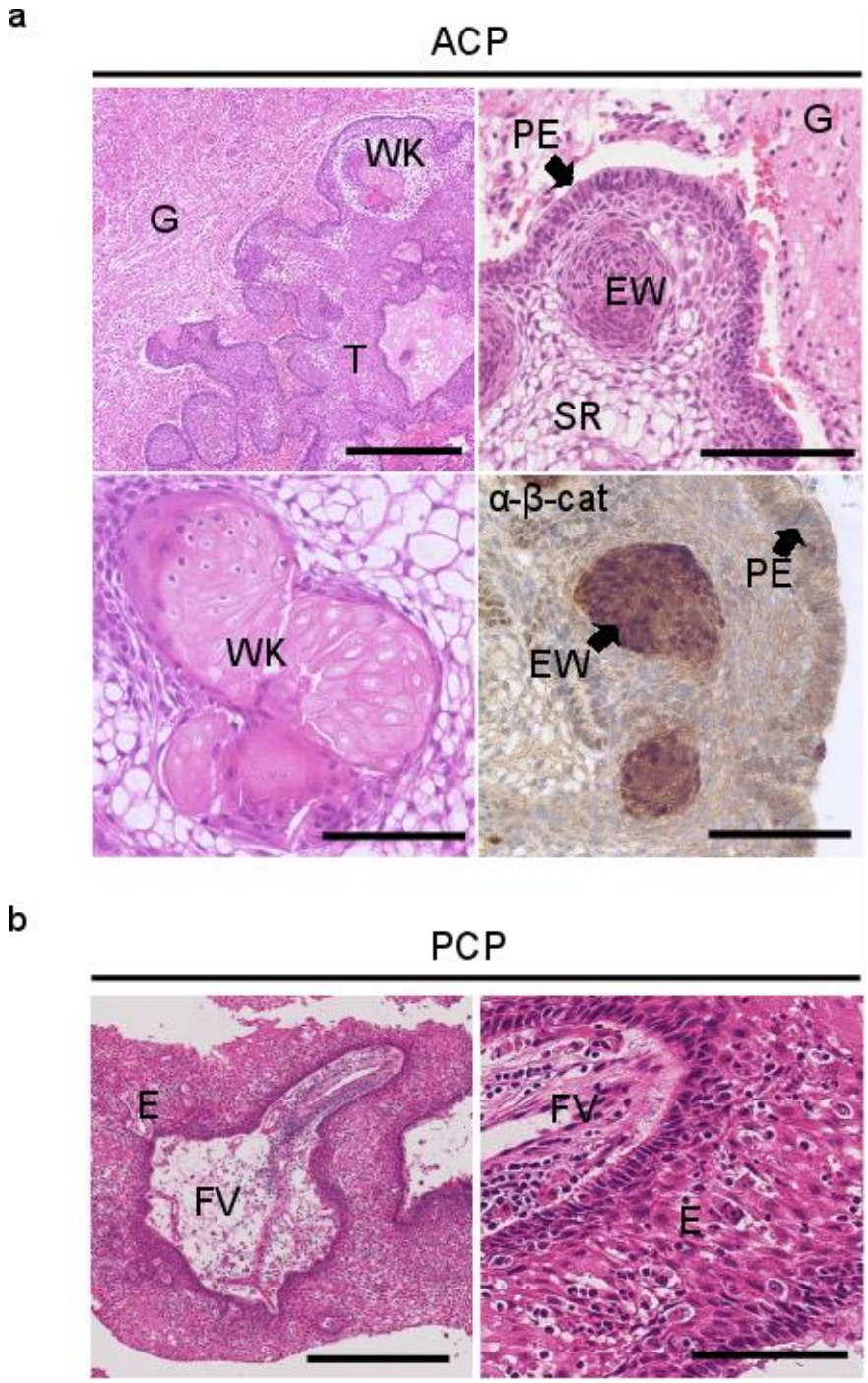

1.4 Theories of cell of origin

Historically there have been two main theories regarding the origin of ACP. Firstly that they derive from remnants of Rathke's pouch, the oral ectoderm primodium of the anterior pituitary gland (anterior and intermediate lobes) and pars intermedia (Larkin and Ansorge 2013). Alternatively it is thought they derive from ectopic embryonic enamel rests within the pituitary (Goldberg and Eshbaugh 1960). The processes of pituitary development and tooth development are discussed in more detail in section 1.9, with particularly reference to pathways of interest in ACP formation.

ACP is increasingly recognised as a developmental disorder (Martinez-Barbera 2015). Consistent with this, retrospective analysis has shown decreased heights of children with childhood ACP from 10-12 months of age, compared to healthy controls, several years prior to presentation suggesting early pituitary/hormonal disruption and rare cases of fetal craniopharyngioma are reported (Sosa-Olavarria, Diaz-Guerrero et al. 2001, Muller, Emser et al. 2004, Jurkiewicz, Bekiesinska-Figatowska et al. 2010).

1.5 Genetic changes in ACP

Activating mutations of the WNT pathway gene *CTNNB1* (encoding β-catenin) have been identified by several groups in ACP over the last 10 years and are increasingly recognised to occur in the majority, if not all ACPs (Sekine, Sato et al. 2003, Kato, Nakatani et al. 2004, Buslei, Nolde et al. 2005). Indeed, immunostaining and/or sequencing of *CTNNB1* in surgical samples are now used in practice in some centres to support diagnosis.

The *CTNNB1* mutations identified in ACP are identical to those observed in other tumour types and are predicted to lead to enhanced half-life of β-catenin, resulting in its nucleo-cytoplasmic accumulation (Martinez-Barbera and Buslei 2015). The pattern of β-catenin expression in ACP is unusual, as nucleo-cytoplasmic accumulation is limited to a proportion of the tumour cells, often only those cells within the epithelial whorls/nests (Figure 1-1) (Kato, Nakatani et al. 2004, Buslei,

Nolde et al. 2005). These will hereafter be referred to as clusters. The consequence of nuclear accumulation of β-catenin is transcription of specific targets, including *Axin2* and *LEF1*. Consistent with β-catenin immunohistochemistry, expression of these targets in ACP is limited to clusters (Holsken, Kreutzer et al. 2009). The reasons for this heterogeneity in β-catenin protein localisation and signalling are not fully understood. The WNT pathway is described in more detail in section 1.10.1 and in Chapter 3, where I explore whether the *CTNNB1* mutations identified in ACP are present in all tumour epithelial cells, or limited to these clusters.

Immuno-histochemical studies have sought to further characterise ACP clusters and confirmed expression of stem cell makers, e.g. CD40, and CD133, secreted factors, e.g. SHH, BMP4, activation of cell surface receptors, e.g. EGFR, as well as absence of proliferation and reduced expression of E-cadherin (Holsken, Gebhardt et al. 2011, Andoniadou, Gaston-Massuet et al. 2012, Holsken, Stache et al. 2014, Preda, Larkin et al. 2015). Many of these will be discussed in further detail in later sections.

Whether mutations in other genes contribute to tumour formation or tumour behaviour (e.g. infiltrative capacity) is also unknown. The first exome sequences of ACP were published in 2012 by Brastianios *et al.,* who by sequencing 12 ACP samples and matched germline DNA, found *CTNNB1* mutations to be the only recurrent mutations between individual cases (Brastianos, Taylor-Weiner et al. 2014). Mutations in other cancer-related genes (including transcriptional regulators, epigenetic regulators, DNA repair and cell adhesion genes) were also identified in individual cases, but were not recurrent between patients in this small series. (Brastianos, Taylor-Weiner et al. 2014). Consistent with other paediatric tumours, they found the overall mutation frequency to be relatively low in human ACP (Brastianos, Taylor-Weiner et al. 2014). With respect to genomic copy number alterations, previous studies using G banding or comparative genomic hybridisation have given variable, often controversial results. Whilst the majority showed normal karyotype, cases with copy number variants were described in some cohorts (Rienstein, Adams et al. 2003, Yoshimoto, de Toledo et al. 2004, Holsken, Sill et al. 2016). A better molecular characterisation of more ACP tumours is therefore required to determine and refine the mutational landscape of these tumours. In

Chapter 7 I explore this through whole genome sequencing of a cohort of five childhood ACPs.

In 2014, *BRAF* pV600E mutations were identified in PCP highlighting a different molecular driver to ACP (Brastianos, Taylor-Weiner et al. 2014). Subsequently several further studies have reproduced these findings, however there have been case reports of overlap cases harbouring both *CTNNB1* and *BRAF* mutations (Larkin, Preda et al. 2014). Many of these studies have used relatively insensitive molecular techniques. In Chapter 4 I comprehensively characterise a cohort of 23 ACP and five PCP using a sensitive targeted next generation sequencing panel, Sanger sequencing and mutation specific antibodies, looking to address whether differences in the literature may reflect inadequate sensitivities of more commonly used assays.

1.6 Gene expression and methylation analyses of ACP

The first genome-wide transcriptome cohort study using expression arrays of 15 ACPs was published during 2015 (Gump, Donson et al. 2015). In addition to highlighting several pathways previously identified by others (e.g. SHH and EGFR), using the Ingenuity IPA Knowledge based programme, this analysis identified expression of a number of other potential therapeutic target genes (including *MMP12*, *IL2B*, *LCK* and *EphA2*) (Holsken, Gebhardt et al. 2011, Andoniadou, Gaston-Massuet et al. 2012, Gump, Donson et al. 2015). Gene Ontology analysis of genes differentially expressed in ACP, revealed genes implicated in odontogenesis, epidermis genes (e.g. keratins) and cell adhesion genes (Gump, Donson et al. 2015).

A further 18 ACP samples underwent expression array analysis and were compared with 10 PCP samples by Holsken e*t al*. in 2016 (Holsken, Sill et al. 2016). This study also highlighted the activation of the WNT and SHH pathway in ACP. In this paper, the methylation profiles of 25 ACP and 18 PCPs were also assessed, revealing distinct patterns between tumour types. Specifically, ACP was found to show hypo methylation of the WNT pathway gene *AXIN2* and the SHH pathway genes *GLI2* and *PTCH1* when compared with PCP (Holsken, Sill et al. 2016).

Whilst these studies have given insight to the transcriptional landscape of ACP, correlation between these dysregulated gene pathways and tumour architecture has been restricted to limited immuno-histochemical studies. In Chapter 5 I further explore the transcriptional landscape of ACP through RNA sequencing of ACP, with and without laser capture microdissection of individual histological components.

1.7 Experimental models of ACP

Several experimental models of ACP have been developed to provide a platform on which to perform controlled experiments, exploring the role and therapeutic potential of various molecular pathways.

Primary cell cultures have been used by a number of groups, however these are challenging and confirmation of tumour containing cells, as evidence by persistence of *CTNNB1* mutations, has not been reported (Holsken, Gebhardt et al. 2011, Chen, Zheng et al. 2016, Holsken and Buslei 2017, Nie, Huang et al. 2017)(G Carreno, personal communication). Similarly, primary xenografts have been performed, both subcutaneously and orthotopically, and whilst engraftment has been successful, a low engraftment efficiency and slow growth has limited the experimental usage (Bullard and Bigner 1979, Xu, You et al. 2006, Stache, Holsken et al. 2015).

Two genetically engineered models (GEMMs) of ACP have been developed by the host laboratory (Gaston-Massuet, Andoniadou et al. 2011, Andoniadou, Matsushima et al. 2013). In both models, cells express an oncogenic form of β-catenin, which is functionally comparable to that identified in human ACP tumours. Phosphorylation of serine residues of β-catenin, encoded by exon 3 of the *CTNNB1* gene, is critical for targeting the protein for proteasomal degradation (Larkin and Ansorge 2013). In the mouse models, expression of oncogenic β-catenin is achieved through Cre-recombinase-mediated excision of exon 3, whilst human tumours harbour over-activating mutations in exon 3 (Hassanein, Glanz et al. 2003, Sekine, Sato et al. 2003, Kato, Nakatani et al. 2004, Buslei, Holsken et al. 2007, Gaston-Massuet, Andoniadou et al. 2011, Andoniadou, Matsushima et al. 2013). The final outcome is the same in mouse and human ACP, namely the expression of a

degradation-resistant form of mutant β -catenin leading to the over-activation of the WNT/β-catenin pathway (Harada, Tamai et al. 1999).

1.7.1 Embryonic model of ACP

The anterior pituitary derives from an invagination of the oral ectoderm known as Rathke's pouch (further details section 1.9.1). Lineage tracing has shown that *Hesx1* expressing cells within Rathke's pouch give rise to all the hormone producing cells within the anterior pituitary (Gaston-Massuet, Andoniadou et al. 2011). Using a *Hesx1-Cre* mouse, exon 3 was deleted from the *Ctnnb1* locus by Cre-mediated recombination in cells of the developing pituitary (*Hesx1*$^{Cre/+}$;*Ctnnb1*$^{lox(ex3)/+}$). The pituitaries of these mice were initially enlarged and dysfunctional. A high proportion of mice died at birth due to enlarged pituitaries causing airway obstruction, however those that survived were smaller (growth hormone deficient) and went on to develop large cystic-solid pituitary tumours leading to death at around 6 months (Gaston-Massuet, Andoniadou et al. 2011). This ability to induce craniopharyngioma like tumours in Rathke's pouch derivatives has given precedence to the Rathke's pouch theory of ACP origin (Martinez-Barbera and Buslei 2015).

Analogous to human ACP tumours, these mice showed isolated clusters of nucleo-cytoplasmic accumulating β-catenin cells in the developing pituitary, despite activation of the cre-recombinase in all cells within Rathke's pouch (Figure 1-2) (Gaston-Massuet, Andoniadou et al. 2011). Increased expression of markers of WNT pathway activation, e.g. *Lef1*, *Axin2* and Cyclin D1 were also limited to these clusters. The murine clusters did not express markers of hormone-producing cell differentiation and a proportion expressed the pituitary stem cell marker SOX2 (Gaston-Massuet, Andoniadou et al. 2011). Activation of the WNT pathway in *Pit1*+ve committed progenitors or differentiated hormone-producing cells of the pituitary did not lead to cluster or tumour formation, highlighting a need for the tumour-initiating mutation to occur in an undifferentiated cell type (Gaston-Massuet, Andoniadou et al. 2011).

Using a mouse line reporting WNT pathway activation, Andoniadou *et al*. successfully isolated the cluster cells by flow-activated cell sorting in the embryonic

model and performed expression analysis comparing cluster versus non-cluster pituitary tissue (Andoniadou, Gaston-Massuet et al. 2012). This identified the high expression of many secreted factors by the cluster cells, including Sonic Hedgehog (SHH) and members of the Fibroblast growth factor (FGF), Transforming growth factor β (TGFβ) and Bone morphogenic protein (BMP) families of growth factors as well as many inflammatory mediators such as cytokines and chemokines (Andoniadou, Gaston-Massuet et al. 2012). These findings were subsequently confirmed by *in situ* hybridisation in human tumours suggesting a strong homology both histologically and molecularly between mice and human clusters (Andoniadou, Gaston-Massuet et al. 2012). An overview of these pathways is presented below in section 1.10.

In addition to the molecular similarities, the embryologic ACP GEMM model shows other similarities to human ACP. Late stage murine tumours are frequently cystic, often haemorrhagic, with histological areas of micro-cystic change similar to that seen in the stellate reticulum of the human tumours (Figure 1-2) (Gaston-Massuet, Andoniadou et al. 2011). Importantly, there are also differences. The tumours do not calcify and ghost cells or wet keratin has not been observed. Similarly, the finger-like invasions, that pose a challenge to treating clinicians, are not seen in the mouse model. The reasons underlying these differences are not fully understood. Calcification may require longer terms than a few months, and although highly similar overall, there are specific anatomical differences between the hypothalamo-pituitary axis in mice and humans, which may explain the lack of brain invasion in murine ACP (Martinez-Barbera 2015).

1.7.2 Inducible model of ACP reveals a non-cell autonomous mechanism of tumourigenesis

Building on the embryonic GEMM, oncogenic β-catenin was specifically expressed in SOX2 positive adult pituitary stem cells using a tamoxifen inducible, mutated form of Cre recombinase (*Sox2-CreERT2* mouse line). The SOX2 cell population was confirmed to have both self-renewal and differentiation capacity into all lineages of the anterior pituitary, thus demonstrating that stem cells are contained within the

Sox2-expressing cell compartment (Andoniadou, Matsushima et al. 2013). Similar to the embryonic model, activation of the WNT pathway in these SOX2 positive cells, from 6 weeks of age, led to the development of undifferentiated tumours (synaptophysin and hormone negative) within the normal pituitary tissue, including the presence of nucleo-cytoplasmic accumulating β-catenin cell clusters (Andoniadou, Matsushima et al. 2013).

Surprisingly, lineage tracing, using yellow fluorescent protein (YFP), revealed that the tumours themselves were not derived from these cluster cells and did not carry the activating β-catenin mutation, as confirmed by laser capture microdissection and PCR (Andoniadou, Matsushima et al. 2013). This suggests an apparent non-cell autonomous mechanism of tumourigenesis (Figure 1-2), possibly through the paracrine activities of secreted proteins such as SHH, FGFs, BMPs, TGFB, cytokines among others (Figure 1-2). This phenomenon is increasingly described in several other cancer model systems and extends the traditional understanding of cancer initiation as a cell autonomous process (Nicholes, Guillet et al. 2002, Lujambio, Akkari et al. 2013, Kode, Manavalan et al. 2014).

Subsequent lineage tracing of the embryonic model using both YFP, or TdTomato, under the Rosa26 locus, has also confirmed that *Hesx1*$^{Cre/+}$*;Ctnnb1*$^{lox(ex3)/+}$ tumours are non *Hesx1* expressing cell derived and that tumour cells were non recombined (Figure 1-2). This therefore confirmed that *Hesx1*$^{Cre/+}$*;Ctnnb1*$^{lox(ex3)/+}$ tumours also undergo non cell autonomous tumourigenesis. Further investigation also confirmed an initial expansion of endomucin positive cells in embryonic pituitaries and a subsequent influx and expansion of non-*Hesx1* expressing derived cells.

The growth dynamics and molecular pathways underlying the development and growth of murine ACP are incompletely characterised. In Chapter 3, serial MRI and post mortem high resolution micro-computed CT imaging of the embryonic model are described. In Chapter 6, I perform gene expression profiling at various stages of tumour development and in Chapter 7, exome sequencing of late stage murine tumours, to determine whether they have acquired somatic mutations.

Figure 1-2: Genetically engineered murine models of ACP a) Embryonic model: Immunohistochemistry showing β-catenin accumulating clusters at E18.5. Macroscopic and histological images of late stage tumours. b) Proposed model of non-cell autonomous tumour formation of inducible murine model of ACP. Tamoxifen induced activation of the WNT pathway at 6 weeks of age results in β-catenin accumulating cell clusters. Tumours subsequently develop, however lineage tracing shows these are not derived from the β-catenin accumulating cell clusters. c) Lineage tracing of the embryonic model of ACP with YFP showing that at early stages the majority of pituitary cells are Hesx1 lineage derived, however as tumours develop this tissue is non Hesx1 derived (20 and 30 weeks) (M. Gonzalez-meljem).

a

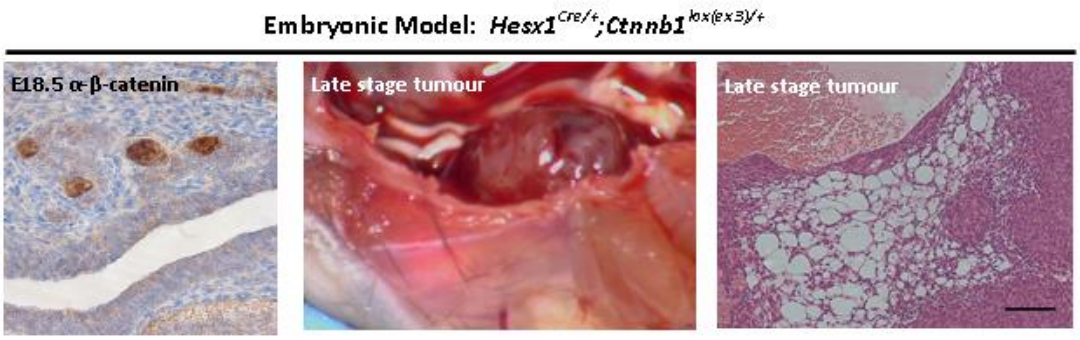

b

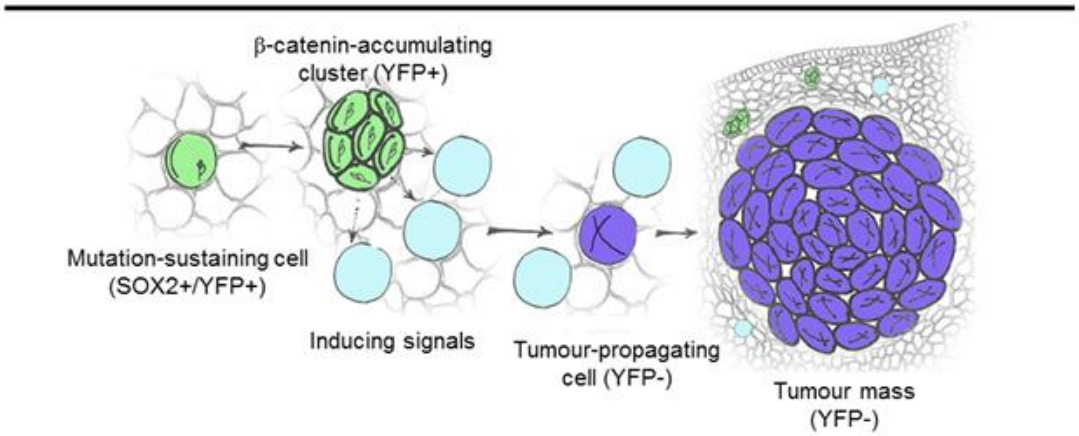

c

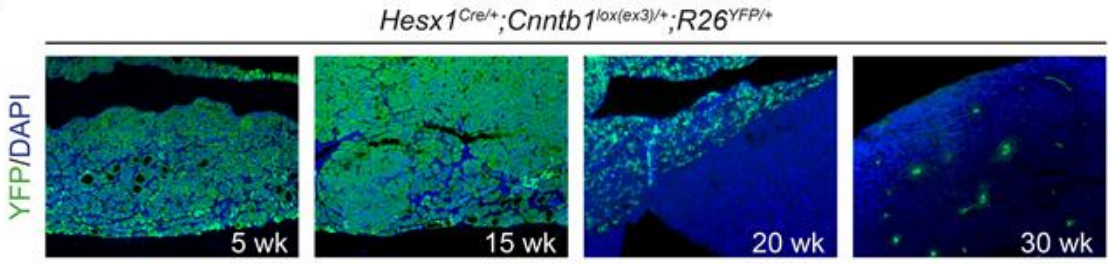

1.8 Role of senescence in tumourigenesis

Work by others in the host laboratory, particularly Dr Mario Gonzalez-Meljem, has highlighted the potential role of cellular senescence in murine and human ACP. Cellular senescence is defined as a cellular state of stable and long-term loss of proliferative capacity, but with retention of normal metabolic activity and viability. It is characterized by specific morphological, metabolic and phenotypic cellular changes and whilst traditionally considered a tumour suppressive mechanism has increasingly been shown to have pro-tumourigenic effects, particularly through paracrine activities (Coppe, Desprez et al. 2010).

Murine and human clusters have been shown to express markers of senescence, specifically a lack of proliferative markers (Ki67, pHH3) and expression of markers of (i) cell cycle arrest (CDKN1A/p21); (ii) DNA damage and activation of a DNA damage response (DDR) (phosphorylated H2AX, p53, DNA-PKcs, PARP1 and phospho-ATM) (iii) increased lysosomal content (GLB1, senescence-associated β-galactosidase (SA-βgal), LAMP1, LAMP2) iv) activation of the Nf-kB pathway, a common senescence driver (Gonzalez-Meljem, Haston et al. 2017).

Clusters have also been shown to secrete a large number of soluble factors, often referred to as the secretory associated senescent phenotype, known as SASP. In addition to the expression of developmental factors (e.g. SHH, BMPs, WNTs, FGFs) by clusters, murine ACP pituitaries were shown to express higher levels of cytokines such as IL1A, IL6(Gonzalez-Meljem, Haston et al. 2017). Of note, when expression of these SASP factors was reduced, either when activation of β-catenin was induced in older animals in the inducible model, or when activation of the WNT pathway was achieved though deletion of *APC* (as opposed to excision of exon 3 of *CTNNB)*, then late stage tumours did not form. This suggests a critical role for senescence and these factors in the non-cell autonomous tumourigenesis observed in the mouse models (Gonzalez-Meljem, Haston et al. 2017).

In Chapters 5 and 6, I explore at the transcriptional level evidence of activation of senescence and SASP signatures in human and murine clusters. In addition I assess cross species similarities between human and murine clusters.

1.9 Pituitary and tooth development

Many of the pathways identified as expressed in murine and human ACP are also involved in the normal development of the pituitary gland and also teeth. In both these processes reciprocal signalling between different tissue components and closely regulated expression of key transcriptional factors is critical for normal development. Through studying patients with mutations and genetically modified mice, the roles of individual pathway members and transcription factors are slowly being elucidated. Key pathways include the Hedgehog, Wnt, FGF, TGFβ and BMP signalling pathways. In many cases, these pathways form regulatory loops with expression reciprocally alternating across tissue boundaries. In the next sections, I briefly describe pituitary and tooth development and an overview of the key pathways.

1.9.1 Pituitary development

The pituitary gland is of dual origin. The anterior pituitary (adenohypophysis), comprising the anterior and intermediate lobes derives from oral ectoderm, whist the posterior pituitary (neurohypophysis) is derived from the ventral diencephalon (Figure 1-3).

In the mouse thickening of the oral ectoderm is observed at 8.5 days post coitum (dpc) and by 10.5dpc dismays a distinctive lumen known as Rathke's pouch which by 12.5 dpc has completely separated from the oral ectoderm (Kelberman, Rizzoti et al. 2009). Cells derived from this pouch differentiate to form the hormone producing cells of the anterior pituitary (Kelberman, Rizzoti et al. 2009).

The posterior lobe forms from an outpouching of the ventral diencephalon and is connected by the pituitary stalk/infundibulum. Axons originating in the hypothalamus secrete the systemic hormones oxytocin and vasopressin (DDAVP) and release hormones, which stimulate (e.g. TRH, GnRH), or inhibit (e.g. somatostatin) hormone secretion by the anterior pituitary. A schematic of pituitary development is presented in Figure 1-3.

Figure 1-3: Schematic representation showing dual origin of pituitary in development. An outpouching or oral ectoderm forms Rathke's pouch forming the anterior pituitary, whilst an extension of the ventral diencephalon forms the posterior pituitary.

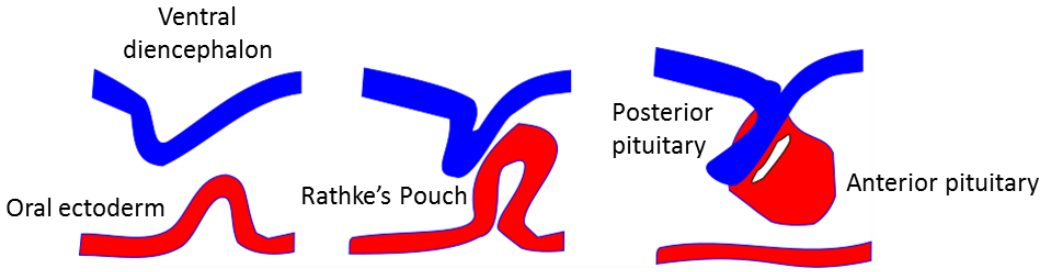

1.9.2 Tooth development

Similar to pituitary development, odontogenesis requires the interaction between cells from two distinct embryological origins. Oral ectoderm gives rise to ameloblasts, that make enamel and neural crest derived mesenchyme gives rise to odontoblasts which secrete dentin (Thesleff 2003, Tucker and Sharpe 2004, Jussila and Thesleff 2012).

There are several morphological stages in odontogenesis (Thesleff 2003, Tucker and Sharpe 2004, Jussila and Thesleff 2012, Balic and Thesleff 2015). Briefly;

1) Placodes form from the dental lamina, a horseshoe shaped strip of stratified oral epithelium along the mandible and maxilla. These express a number of transcription factors including Pitx2, Foxi3, Dlx2, Lef1, p63.
2) Bud stage: Signals, such as Shh, Wnt10, Bmp2, Fgf20, are restricted to form the early signalling centre. This stimulates growth of the placode to invaginate the nearby dental mesenchyme to form the tooth bud.
3) Cap stage: Cells at the tip of the bud enter cell cycle arrest, expressing p21 to form a histologically distinct transient structure, the primary enamel knot. This signalling centre expresses many signals, including Fgfs 3, 4, 9, 20, Shh, Wnt 3, 6, 10a, 10b, Bmp2, 4, 7. These stimulate the growth of nearby epithelium to give rise to the cervical loop. The cervical loops encompass the surrounding mesenchyme to form the dental papilla which will eventually become dental pulp and odontoblasts.
4) Bell stage: Further epithelial growth and folding determines the shape and size of the tooth crown. In molar teeth a secondary enamel knot forms. Secreting similar factors to primary enamel knots, which determine the characteristics of the tooth cusp. At the cap/bell stages the epithelium, the enamel organ, consists of two basal cell layers, the inner enamel epithelium, which gives rise to ameloblasts and the outer enamel epithelium. The epithelium is surrounded by loosely arranged stellate reticulum cells and stratum intermedium. The inner enamel epithelium encloses the dental papilla which gives rise to odontoblasts and pulp cells.

At late bell stage, signals from the enamel knots induce odontoblast differentiation. In turn, these signal initiate differentiation of the inner enamel epithelium into ameloblasts, beginning at the cervical loops. Odontoblasts secrete dentin, initiated by secretion of non-collagenous proteins, the most abundant of which is Dentin sialophosphoprotein (DSPP) ((Balic and Thesleff 2015)).

Ameloblast differentiation has several stages i) The initial stage, ii) secretory stage, where proteins are released into the surrounding are to form enamel matrix, iii) maturation, where enamel proteins (enamelin, amelogenin, ameloblastin, tuftelins) are secreted, and mineralisation with hydroxyappetite occurs. Proteases (MMP20, KLK4) digest the enamel proteins and ameloblasts undergo apoptosis such that enamel cannot be regenerated.

When ameloblast differentiation reaches the crown boundary, the inner enamel epithelium, rather than differentiating into ameloblasts, forms Hertwig's epthielum root sheath with the outer enamel epithelium, which along with dental follicle cells forms the root, cementum and periodontal ligament (Jussila and Thesleff 2012).

Figure 1-4: Schematic representation of tooth formation. a) Schematic of different stages of tooth development.b) Reciprocal signalling between epithleilal and mesencyhmal components. Secreted factors, transcription factors and other markers expressed at given stages. Adapted from Thesleff, 2003.

a

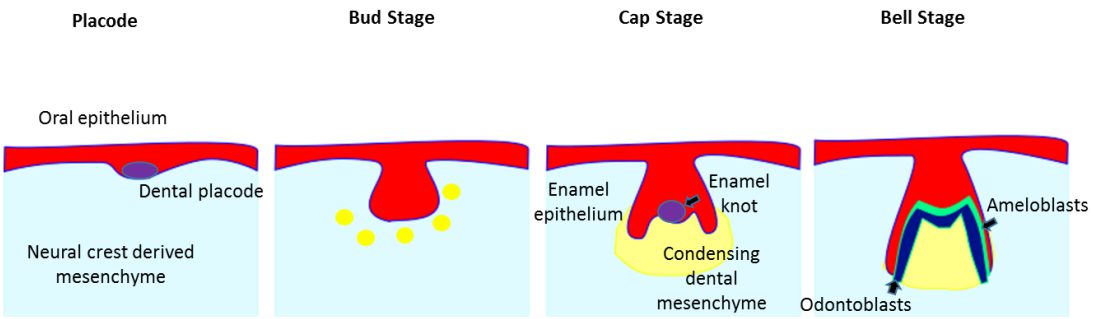

b

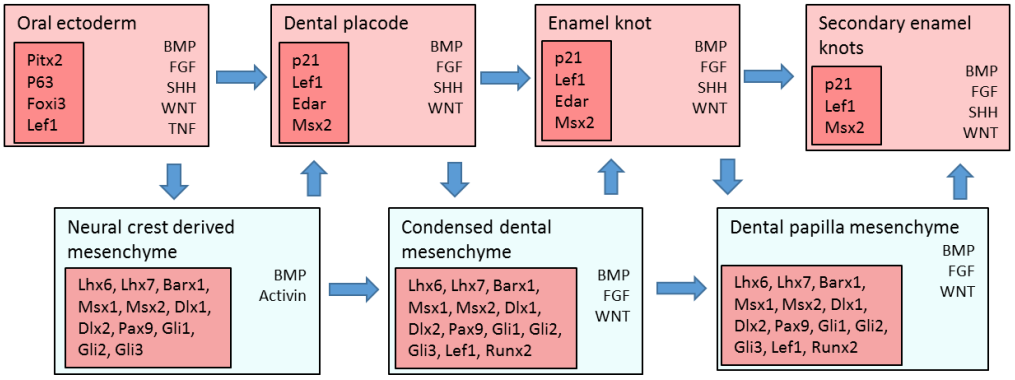

1.10 Important pathways in ACP

Several of the pathways implicated in pituitary and tooth development have been shown to be deregulated in ACP. Here I briefly summarise several of these and their roles in tumours and development. These pathways are characterised in detail by RNA sequencing and immunofluorescence in both human and murine ACP in Chapters 5 and 6.

1.10.1 WNT pathway

Wnt proteins, of which 19 have been described in humans, are secreted glycoproteins with crucial roles in development and stem cell maintenance. In development they act as morphogens, where effects of cell fate determination are determined by their concentration gradients (Husken and Carl 2013).

Wnt proteins signal through binding of Frizzled (FZD) receptors. This results in inhibition of a protein complex, including adamantinomatous polyposis coli (APC), glycogen synthase kinase 3 (GSK3β) and axins 1 and 2. In the absence of Wnt signalling, this complex phosphorylates β-catenin, resulting in its poly-ubiquitination and proteosomal destruction. On Wnt ligand binding this destruction is inhibited, resulting in nuclear translocation of β-catenin, displacing TLE repressing factors and facilitating TCF/LEF mediated transcription (Figure 1-5) (Larkin, 2013). Wnt proteins can also signal through additional β-catenin independent (non-canonical) pathways.

Activation of the Wnt pathway, particularly through mutation of the *CTNNB1* and *APC* genes, is a common feature of many tumours and cancers. Whilst germline mutation in *CTNNB1* does not appear to be viable, germline mutation in APC results in familial adenomatous polyposis (FAP), characterised by thousands of colonic polyps and increased risk of cancer, particularly colorectal carcinoma.

The Wnt pathway is important in tooth development. Indeed, supernumerary teeth are often observed in patients with FAP, whilst patients with *AXIN2* mutations have oligodontia (Lammi, Arte et al. 2004). Similarly, activation of the pathway in mouse models, by either β-catenin activation or APC inactivation, results in supernumerary

teeth (Jarvinen, Salazar-Ciudad et al. 2006, Wang, O'Connell et al. 2009). Of particular note, and analogy to ACP, *Ctnnb1* activation in the epithelia of developing teeth results in continual tooth formation with multiple enamel knots. Enamel knots are themselves known to accumulate nucleocytoplasmic β-catenin and express Wnts (e.g. Wnts 3, 6, 10a) and the downstream target Lef1 (Obara and Lesot 2004, Balic and Thesleff 2015). Wnt pathway activation also appears to play a role in odontoblast differentiation, with activation of the pathway resulting in premature differentiation and dentin deposition, and decreased signalling reducing dentin deposition (Balic and Thesleff 2015).

Figure 1-5: Schematic representation of the canonical WNT signalling. In the absence of Wnt ligands, β-catenin is targeted for proteosomal destruction through phosphorylation of amino acids encoded in exon 3 by the Axin/GSK3β/APC complex. On ligand binding this is sequestered to the cell membrane, facilitating translocation of β-catenin to the nucleus and activation of transcription.

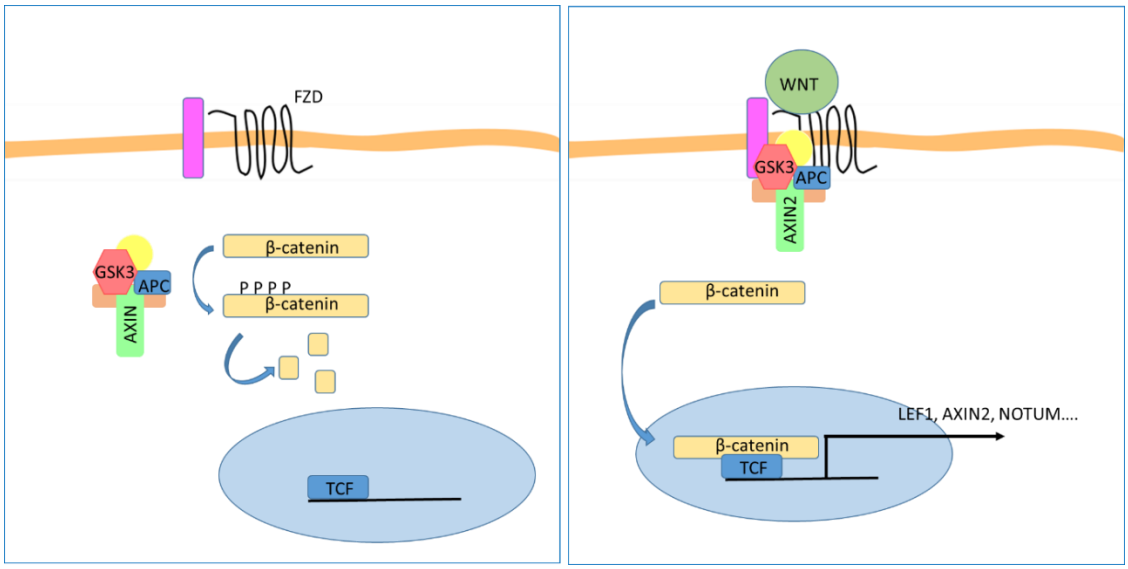

1.10.2 Sonic hedgehog pathway

SHH is an important morphogen with critical developmental roles, particularly in central nervous system and craniofacial development. On binding to its receptor, Patched (*PTCH1)*, inhibition of the transmembrane protein Smoothened (*SMO*) is relieved, allowing trafficking to primary cilia and stabilisation and activation of Gli2 proteins and inhibition of Gli3. This results in transcriptional activation and expression of SHH pathway target genes, including *Ptch1, Gli1* and *Gli3* and genes that regulate cell cycle entry (Figure 1-6) (Ruch and Kim 2013).

Mutations in the SHH pathway, particularly *PTCH1*, resulting in activation of the pathway, are observed in many tumour types, including the paediatric brain tumour medulloblastoma (Taylor, Northcott et al. 2012). Indeed, germline mutations result in Gorlin's syndrome, characterised by recurrent basal cell carcinomas and other tumours, including occasional reports of craniopharyngioma (Musani, Gorry et al. 2006). In addition, paracrine activation of the SHH pathway, through increased secretion of SHH, is seen in a wider range of tumours, including pancreatic ductal adenocarcinoma and colorectal carcinoma (Scales and de Sauvage 2009).

The SHH pathway is also important in pituitary and tooth development. In the pituitary, SHH is required for proliferation and normal specification of Rathke's pouch progenitors (Carreno, Apps et al. 2017). In the tooth, SHH is one of the fist markers to be expressed in the dental epithelium and apparently regulates proliferation of dental epithelial cells to form the tooth bud (Cobourne and Sharpe 2005). Subsequently it is expressed highly by the enamel knot, regulated by BMP4 and Wnt signalling, with downstream Gli1 and Ptch1 expressed in the epithelia and mesenchyme (Balic and Thesleff 2015). SHH signalling is required for normal tooth formation and conditional deletion of *Shh* or *Smo* in dental epithelium results in disrupted polarity and organisation of the ameloblast layer and abnormal tooth shape and growth (Dassule, Lewis et al. 2000, Cobourne and Sharpe 2005).

Due to its role in tumourigenesis, a number of SHH pathway inhibitors have been developed, particularly through inhibition of the Smoothened receptor (Smoothened inhibitors) (Scales and de Sauvage 2009, Ruch and Kim 2013). These

have been successful in patients with basal cell carcinoma and the first of these agents, Vismodegib (GDC-0449), is licenced for use in this condition (Sekulic, Migden et al. 2012). Other inhibitors, such as LDE-225, are also in trails and use in this and other tumour types.

Whilst broadly successful in tumours harbouring *PTCH1* mutations, inhibition of the SHH pathway has not been successful in tumours with paracrine activation of the pathway (Amakye, Jagani et al. 2013, Ruch and Kim 2013). Indeed, in pancreatic ductal adenocarcinoma a recent trial had to be stopped early due to increased progression (Lou 2014). Subsequent pre-clinical data has demonstrated how loss of SHH pathway activation of tumour stroma can result in promotion of malignant tumour characteristics through alterations in the tumour microenvironment (Ozdemir, Pentcheva-Hoang et al. 2014, Rhim, Oberstein et al. 2014). This has highlighted the importance of appropriate pre-clinical study of such agents prior to their use in man.

Within ACP, *SHH* has been shown to be overexpressed (Gomes, Jamra et al. 2015, Gump, Donson et al. 2015, Coy, Du et al. 2016, Holsken, Sill et al. 2016). *In situ* hybridisation has shown *SHH* expression by clusters and *PTCH1* in clusters and palisading epithelium (Andoniadou, Gaston-Massuet et al. 2012).

Figure 1-6: Schematic representation of the Sonic Hedgehog pathway. In the absence of SHH, PTCH1 binds to and inhibits Smothened (Smo). On ligand binding this repression is released, enabling activation of Smo, and translocation of Gli proteins (GLI1/3) to the nucleus where they activate transcription.

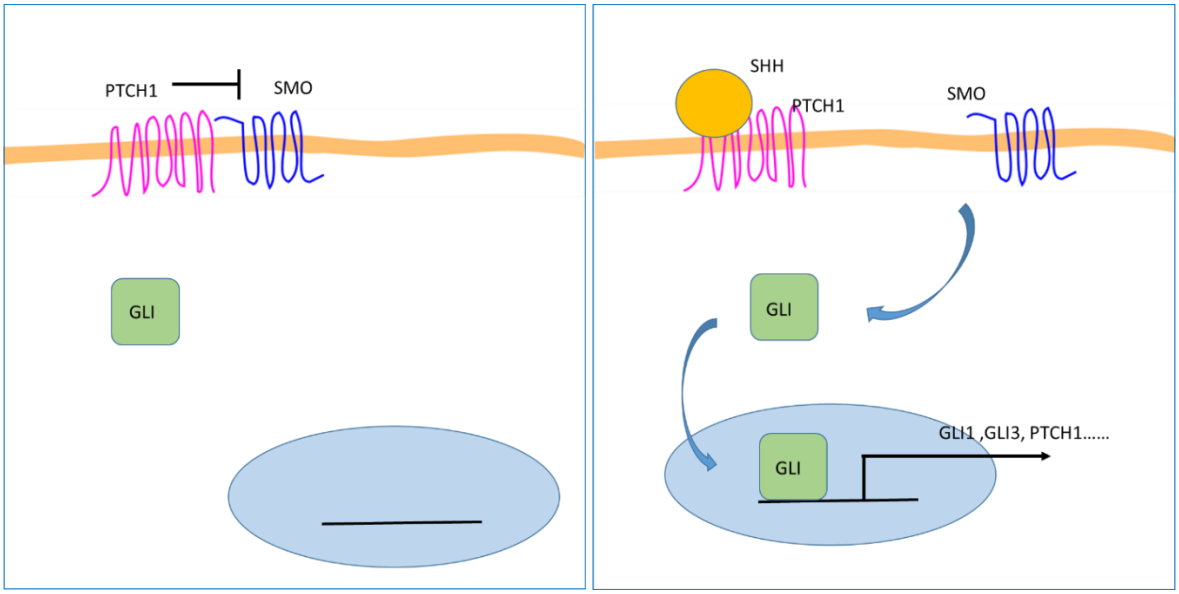

1.10.3 Fibroblast growth factor signalling

Fibroblast growth factors (FGFs) were initially identified from brain and pituitary tissue as mitogens for fibroblasts (Gospodarowicz 1975, Gospodarowicz, Bialecki et al. 1978). Subsequently they have been shown to play important roles in development and tumourigenesis (Itoh and Ornitz 2011, Ahmad, Iwata et al. 2012). Twenty-two FGF proteins (Fgf1-23) have been reported in mouse and man with Fgf15 a mouse ortholog of human FGF19 (Ahmad, Iwata et al. 2012). There are four FGF receptor genes (*FGFR1-4*), which through alternative splicing encode seven separate major FGFR proteins (FGFRs 1b, 1c, 2b, 2c, 3b, 3c and 4) with differing ligand-binding specificity. Variability in dimerization of ligands, receptors and heparin sulphate binding partners facilitates diverse activity of this receptor pathway system.

FGF proteins have been broadly grouped into three types, based on their function and activity:

- *Canonical/Paracrine FGF proteins: FGF1/2/5, FGF3/4/6, FGF7/10/22, FGF8/17/18, FGF9/16/20)* bind and activate cell surface tyrosine kinase FGFRs with heparin/heparan sulphate as a cofactor. FGF binding to FGFRs induces functional dimerization, receptor trans-phosphorylation and activation of four major downstream signalling pathways: RAS-RAF-MAPK, PI3K-AKT, STAT and PLCγ (Itoh and Ornitz 2011). FGF1, FGF2 and FGF3 have also been reported to directly translocate to the nucleus and act in an intracrine manner (Itoh and Ornitz 2011).
- Hormone like/Endocrine FGF proteins: FGF15(19)/21/23 bind heparin/heparan sulphate with very low affinity and are able to signal through FGFRs over considerable distance (Itoh and Ornitz 2011). FGF19 has high affinity for the FGFR4 receptor.
- Intracellular FG proteinss: FGF11/12/13/14 are non-secreted intracellular molecules which act in an FGFR-independent manner and their only known role is in regulating the electrical excitability of neurons and possibly other cell types (Itoh and Ornitz 2011).

Mutations in all four FGFR genes have been seen in tumours, including paediatric brain tumours, through mutation, amplification and translocation (Ahmad, Iwata et al. 2012, Jones, Hutter et al. 2013). In addition, overexpression has been observed in many others. Similarly amplification and/or overexpression of FGFs is also seen in mouse models suggesting that FGF overexpression can play a role in induction of tumourigenesis. For example, over expression of *FGF19* in skeletal muscle resulted in development of hepatocellular carcinoma and mesenchymal overexpression of *Fgf10* was sufficient to induce epithelial transformation leading to prostatic adenocarcinomas (Nicholes, Guillet et al. 2002, Memarzadeh, Xin et al. 2007) .

Reciprocal FGF signalling is important throughout normal odontogenesis. Mutations of pathway members have been identified in patients, resulting in abnormal teeth, including *FGF3* (microdontia) and in *FGFR2*, where patients have tooth abnormalities as part of more complex craniofacial abnormality syndromes (Itoh and Ornitz 2011, Li, Prochazka et al. 2014).

Fgf8 and *9* are expressed by the initial dental lamina and have been shown to be essential for tooth induction (Balic and Thesleff 2015). *Fgfs 4, 9 20* are highly expressed in the enamel knot, whereas *Fgf10* is expressed in dental mesenchyme, Fgf3 is expressed both in the enamel knot and mesenchyme and *Fgf*1 variably by epithelial and mesenchymal elements (Helsinki 1996-2007, Balic and Thesleff 2015). Functional analyses in mice suggest there appears to be some redundancy amongst family members, for instance conditional *Fgf4-/-* and, *Fgf3-/-* mice lack phenotype whereas compound knockouts of *Fgf3-/-Fgf10-/-* display reduced enamel formation (Li, Prochazka et al. 2014, Balic and Thesleff 2015). Similarly, *Fgf9-/-Fgf20-/* mice had reduced enamel knot size, whereas *Fgf20-/-* mice appeared to have normal enamel knots, though smaller molar teeth (Haara, Harjunmaa et al. 2012).

In both human and murine ACP, expression of *FGF3* has been shown within clusters by in situ hybridisation and additional FGFs (including *Fgf4*, *Fgf20*, *Fgf9*) in murine ACP clusters by expression microarray analysis (Andoniadou, Gaston-Massuet et al. 2012).

1.10.4 Epithelial growth factor receptor

The epidermal growth factor receptor (EGFR) has been shown to be phosphorylated in ACP, specifically in clusters (Holsken, Gebhardt et al. 2011). EGFR is a member of a receptor tyrosine kinase family compiled of EGFR, ERBB2 (Her2/neu), ERBB3 and ERBB4 (Normanno, De Luca et al. 2006). On ligand binding, these receptors form dimers that, on activation, initiate a range of signalling pathways including the MAPK and PI3K pathways (Normanno, De Luca et al. 2006). There are multiple ligands; epidermal growth factor (EGF), transforming growth factor-alpha (TGFA), heparin-binding EGF-like growth factor (HBEGF), betacellulin (BTC), amphiregulin (AREG), epiregulin (EREG) and epigen (EPGN). Of these, EGF has been shown to be up-regulated in murine ACP clusters, suggestive of autocrine signalling (Andoniadou, Gaston-Massuet et al. 2012).

EGFR has been implicated in the pathogenesis of several tumours (e.g. lung cancer), particularly through amplification or activating mutations or deletions (Normanno, De Luca et al. 2006). This has made it an attractive target for therapy and several generations of monoclonal antibodies and small molecular inhibitors have been developed. Gefitinib, a first generation inhibitor, has been shown to inhibit ACP tumour cell migration and increase sensitivity to radiotherapy *in vitro* (Holsken, Gebhardt et al. 2011).

EGFR has also been to be shown to be expressed in the developing tooth and a role in tooth eruption suggested (Shroff, Kashner et al. 1996). It is variably expressed by epithelial and mesenchymal compartments during development, but has not been observed in the enamel knot (Cobo, Hernandez et al. 1992, Davideau, Sahlberg et al. 1995).

1.10.5 Mitogen activated protein kinase (MAPK) pathway

The MAPK pathway is a major downstream signalling pathway of both FGFR and EGFR signalling. Briefly, on receptor binding, the Ras GTPase enzyme swaps GDP for GTP. This enables activation of RAF which in turn activates a phosphorylatation cascade. This activates mitogen activated protein kinase kinases (MAPKK) (MEK1

and 2), which in turn activates mitogen activated protein kinases (MAPK) (ERK1 and 2) by phosphorylation (pERK1/2). These activate a range of downstream kinases leading to alteration of cell behaviour (e.g. proliferation, differentiation) (Zhao and Adjei 2014). This pathway also includes negative feedback loops and interacts with multiple other cellular signalling pathways (e.g. PI3K) (Zhao and Adjei 2014) (Figure 1-7).

Activation of the MAPK pathway, through activating p.V600E mutation in the *BRAF* gene, and confirmed by phosphorylation of pERK1/2, is observed in PCP (Brastianos, Taylor-Weiner et al. 2014, Haston, Pozzi et al. 2017). Targeting of this pathway, by either BRAF or MEK1/2 inhibitors alone, or in combination, has been observed to result in profound tumour responses in the limited cohorts of PCP studied to date (Aylwin, Bodi et al. 2015, Brastianos, Shankar et al. 2016). Whilst *BRAF* mutations appear to be rare in ACP, downstream activation of the pathway within ACP has not been formally assessed.

Figure 1-7: Schematic representation of the MAPK pathway Growth factor binding results in exchange of GDT for GTP on RAS, this binds to RAF triggering a cascade of phosphorylation which subsequenly leads to increased transcription, driving proliferation and other cellular processes.

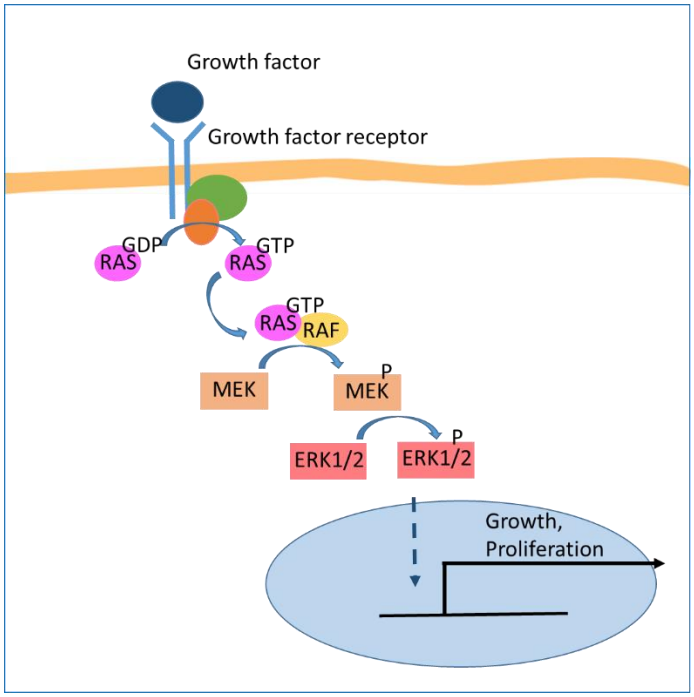

1.10.6 Transforming growth factor β superfamily

The transforming growth factor β (TGFβ) superfamily includes a range of ligands with diverse functions. These include: TGFβs, bone morphogenic proteins (BMPs), activin and inhibin, growth and differentiation factors (GDFs), anti-mullerian hormone and nodal (Massague 2008, Massague 2012).

These ligands signal through binding of a type 2 receptor (e.g. TGBRII or BMPR2) resulting in formation of a heterodimer with, and phosphorylation of, a type 1 receptor (e.g. TGFBR1, BMPR1A). This leads to phosphorylation of receptor regulated SMAD (R-SMAD) proteins (e.g. SMAD3 and SMAD2 for TGFB receptor signalling, SMADs 1, 5, 8 for BMP signalling), which when complexed with SMAD4 proteins activate transcription. The receptors may also activate other signalling pathways (e.g. MAPK). Signalling is further modulated by a range of inhibitors (e.g. noggin, follistatin, lefty) and regulatory SMADs (6 and 7).

TGFβs (TGFB1, TGFB2, TGFB3) are signalling cytokines that play a diverse range of functions in development, the immune response and carcinogenesis. Most commonly considered an immunosuppressive cytokine, TGFβ can have pro- and anti-tumourigenic effects through direct effects on cancer cells and through modulation of the local tumour stroma microenvironment (Massague 2008).

BMPs play important roles in the morphogenesis of many organs (Wang, Green et al. 2014). Within ACP, expression of *BMP4, 2* and *7* in both murine and human clusters has previously been shown by *in situ* hybridisation (Andoniadou, Gaston-Massuet et al. 2012).

Within the tooth, BMP4 plays important roles in epithelial and mesenchymal differentiation and is variably expressed by cells derived from both types at different stages of development. *Bmp4* is initially expressed by epithelia and induces expression of transcription factors in neighbouring mesenchyme, where it also antagonises the effects of Fgf8 (Tucker and Sharpe 2004). Subsequently in the bud stage, it is expressed by the dental mesenchyme an plays and important role in

induction of the enamel knot, from which it is then expressed along with *Bmp2* and *Bmp7* (Thesleff 2003, Balic and Thesleff 2015).

BMP/TGFβ members are also important in odontoblast differentiation. Conditional deletion of *Tgfβr2*, *Bmp4* or *Bmp2* at early stages result in defects in delayed osteoblast differentiation and dentin abnormalities (Jussila and Thesleff 2012, Balic and Thesleff 2015). Similarly, odontoblast derived BMPs are required for ameloblast differentiation where conditional deletion of *Bmp4* or *Bmp2* significantly reduces enamel thickness (Balic and Thesleff 2015). Loss of SMAD4 signalling or overexpression of *SMAD4* at early stages result in non-polarised odontoblasts, a more osteoblast like differentiation and deposition of bone like structure and *SMAD3-/-* mice result have abnormal enamel (Yokozeki, Afanador et al. 2003, Li, Huang et al. 2011, Balic and Thesleff 2015).

Other related members of the TGFβ superfamily are the Activins. Activins are formed by dimers of the inhibin β subunit (Inhba, Inhbb, Inhbc, Inhbe). Inhibin has opposing functions and is formed of a dimer of the alpha subunit (encoded by Inha) and a β subunit. Receptors include the ACVR1/ALK3 and ACVR2A, which may also be activated by BMP ligands. Recurrent mutations in *ACVR1* have been identified in the paediatric brain tumour diffuse intrinsic pontine glioma (DIPG) (Taylor et al 2014).

1.11 Other processes implicated in ACP tumourigenesis

1.11.1 Inflammation and cystic fluid in ACP

For many patients, it is the cystic component rather than the solid tumour that poses a significant clinical challenge. Cyst fluid has a so-called "motor oil" appearance and is cholesterol rich with variable necrotic and inflammatory debris (Zada, Lin et al. 2010). Several studies have investigated the molecular biology underlying cyst formation as existing intra-cystic therapies have been largely empirical in their mechanism of action (Pettorini, Inzitari et al. 2010, Bartels, Laperriere et al. 2012, Apps and Martinez-Barbera 2016).

It has long been recognised that leak of cystic fluid can lead to local inflammation, and this has been modelled by injection of cystic fluid into the brain of rats, which induces an inflammatory response and increase in GFAP expression (Shida, Nakasato et al. 1998, Tena-Suck, Hernandez-Campos et al. 2014, Tena-Suck, Morales-Del Angel et al. 2015). Expression of a number of inflammatory mediators such as IL6, IL1A, TNF and α-defensins 1-3 have been identified in cystic fluid, generating interest in the use of immune-modulators for the treatment of cysts (Mori, Takeshima et al. 2004, Pettorini, Inzitari et al. 2010, Martelli, Iavarone et al. 2014). In addition to the cholesterol within cysts, cholesterol deposits are observed within tumour parenchyma, and lipid laden 'foamy' macrophages are a common feature.

Through the study of senescence, upregulation of inflammatory cytokines *IL1A* and *IL6* has been noted in the pituitaries of $Hesx1^{Cre/+};Ctnnb1^{lox(ex3)/+}$ animals (Gonzalez-Meljem, Haston et al. 2017).

In Chapter 5, I further explore the inflammatory signature of ACP through transcriptional profiling, proteomic analysis of cystic fluid and integration with proteomic datasets from analysis of ACP cystic fluid by collaborators (Todd Hankinson and Benedetta Pettorini).

1.11.2 Angiogenesis

Several studies have investigated the microvascular densities in ACP and the expression of a range of pro-angiogenic (e.g. vascular endothelial growth factor, VEGF) and anti-angiogenic (e.g. endostatin) mediators, with conflicting results in regard to association with recurrence risk (Vaquero, Zurita et al. 1999, Vidal, Kovacs et al. 2002, Dallago, Oliveira et al. 2005, Agozzino, Ferraraccio et al. 2006, Xu, Zhang et al. 2006, Sun, Akgun et al. 2010). One functional study using a corneal angiogenesis assay revealed that recurrent ACP samples had a significantly higher angiogenic potential than non-recurrent ACP, but less than glioblastoma multiforme or arteriovenous malformations (Sun, Akgun et al. 2010). Imatanib-loaded microspheres reduced neovascularisation in this model but the use of this or other anti-angiogenic approaches in patients has not been reported in the literature (Karal-Yilmaz, Ozkan et al. 2013).

Within murine ACP there is non-cell autonomous expansion of endomucin positive cells in late embryonic/early postnatal pituitaries. These cells are thought to be endothelial derived, however disappear at later stages and their functional significance is unclear. Little is known about the vasculature of late stage tumours, though haemorrhage into cysts is noted.

1.11.3 Tumour recurrence

Primary treatment of ACP aims to minimise the risk of recurrence, with maximum preservation of the hypothalamic-pituitary axis and quality of life. Understanding why some patients relapse, whilst others do not, could help in tailoring the approach to management of patients. Similarly, current treatments for relapse are often unsatisfactory, leading to further surgery, increased morbidity and reduced quality of life. It is in these patients, with persistent recurrences, where novel therapies could perhaps be most rapidly translated.

Many studies have compared the expression of specific molecules in samples of recurrent ACP, with or without comparison to non-recurrent ACP. One study performed expression microarray analysis in two pairs of matched primary and

relapse samples and identified 20 genes, including CXCR4 and CXCL12, up-regulated in relapses (Gong, Zhang et al. 2014). The authors then went on to assess these two markers in a larger retrospective cohort of 45 patients and found those with higher levels to have a higher risk of relapse. In another study, Lefranc *et al.* found that recurrent ACP expresses higher levels of RARγ, cathepsin K and lower levels of Galectin-3, RARβ and cathepsin D than in non-recurrent ACP (Lefranc, Chevalier et al. 2003). A review in 2013 found variable associations of recurrence with proliferation markers and TP53 expression (Prieto, Pascual et al. 2013).

These individual studies on recurrence have generally used univariate analyses on relatively low sample numbers of archival specimens, limiting the generalizability of their findings and likely contributing to their lack of reproducibility or consistency when repeated.

Malignant transformation of ACP is extremely uncommon. In the limited molecular studies to date, increased expression of proliferation markers and TP53 have been observed in malignantly transformed specimens as well as in some rapidly recurring tumours (Ishida, Hotta et al. 2010, Prieto, Pascual et al. 2013). Whilst TP53 expression appears to be rare in non-transformed ACP, its related family member TP63, an important transcription factor in tooth and other epithelial differentiation, has been shown to be widely expressed (Momota, Ichimiya et al. 2003, Cao, Lin et al. 2010, Esheba and Hassan 2015).

1.12 Aims and objectives

Through understanding the molecular biology of ACP, particularly in its histological context, it will be possible to improve patient care through identifying novel therapeutic approaches and markers of disease behaviour.

The aims of this thesis are:

1) To phenotype in detail the 3D growth patterns of human and murine ACP
2) To characterise the genetic and transcriptional landscape of human and murine ACP, both globally and within individual histological components.
3) To identify therapeutically targetable molecular pathways, novel therapeutics and test efficacy in pre-clinical models of ACP.

1.13 Summary

ACP is a clinically challenging tumour of the sellar region characterised by activating mutations in *CTNNB1*. Through the study of human samples by genome wide and targeted methods and the development and interrogation of genetically engineered mouse models of ACP, we have greatly increased our understanding of the molecular basis of ACP. However, these advances have not fully been integrated with the complex histological tumour architecture of ACP and are yet to translate into patient benefit.

Chapter 2 Materials and Methods

2.1 Samples

2.1.1 Human samples

Human ACP samples and control tissues were accessed from multiple sources including, Great Ormond Street Hospital (GOSH), Department of Histopathology, Children's Childhood Cancer and Leukaemia Group (CCLG), Brain UK (a national virtual biobank cataloguing tissues in UK neuropathology centres) and individual national and international collaborators and biobanks (Table 2-1).

As control tissues for RNA sequencing, human fetal pituitary tissue was collected and accessed through the Human Developmental Biology Resource (HDBR) at ICH and pituitary adenoma tissue from collaborators and through brain UK.

Where possible, samples of formalin fixed paraffin embedded (FFPE) and fresh frozen tumour were sought, along with germline DNA (or tissues from which it could be extracted), and any other relevant material (e.g. CSF, cystic fluid, plasma). Where feasible, plasma was separated from whole blood within one hour of blood collection to facilitate isolation of cell free DNA (cfDNA).

Ethical approval for the use of human tissues was gained either through approval by individual biobanks (CCLG, Brain UK, Imperial College Hospital NHS Tissue Bank, Edinburgh) or by Research Ethics Committee approval 14/LO/2265. All material is stored and used in compliance with the Human Tissue Act.

Phenotype information was accessed either from GOSH, collaborators or through the appropriate tissue banks, through local collaborators, as permitted by specific ethical approval.

Table 2-1: Sources of Tissue

Source of Tissue	Type of Tissue	Ethical Approval	Contact
Great Ormond Street Hospital NHS Trust	ACP: FFPE, Frozen, Cyst fluid, germline DNA, plasma	CCLG Brain UK 14/LO/2265	Alex Virasami
Children Cancer and Leukaemia Group Tissue Bank	ACP: FFPE, Frozen, germline DNA	CCLG tissue bank approval	Gita Mistry
National Hospital for Nervous Diseases	Adult ACP and PCP: FFPE	Brain UK	Professor Sebastian Brandner
Plymouth Hospitals NHS Trust	Adult ACP and PCP:FFPE	Brain UK	Dr David Hilton
Royal Victoria Infirmary, Newcastle	Adult ACP and normal adult pituitary: Frozen and FFPE	14/LO/2265	Dr Abhijit Joshi
Queens Medical Centre, Nottingham	Adult ACP: FFPE (childhood ACP via CCLG)	Brain UK	Dr Lisa Storer
Imperial College Hospital NHS Tissue Bank (ICHTB)	Adult ACP: Frozen and FFPE	ICHTB approval	Professor Franscesco Roncaroli
Queen Mary's University of London	Non functioning pituitary adenoma: Frozen	14/LO/2265	Professor Marta Korbonitis
Germany	Adult ACP: Frozen	14/LO/2265	Professor Hermann Muller
Edinburgh Brain and Tissue Bank	Normal adult pituitary: FFPE and Frozen	Edinburgh Brain and Tissue Bank approval	Dr Chis-Anne McKenzie
Human Developmental Biology Resource (HDBR)	Fetal normal pituitary: FFPE and Frozen	HDBR approval	Dr Dianne Gerelli

2.1.2 Human sample processing

FFPE samples were processed by GOSH Department of Histopathology standard protocols. Sections were cut and stained with haematoxylin and eosin as per standard departmental operating procedures.

Where sufficient material was available, frozen specimens were divided into four pieces; cryosections were taken from one piece and stained with haematoxylin and eosin, RNA extracted from another, DNA from a third and a fourth piece stored at -80 degrees Celsius for future proteomics work. For large specimens further piece(s) were stored, whereas if small, priority was given to obtaining histology and RNA.

All sections were reviewed both by myself and Dr Tom Jacques (consultant paediatric neuropathologist). This was to confirm diagnosis, and if the sample was to be included in analyses, to estimate tumour content (% nuclear area), the type of reactive tissue (e.g. glial), and any other features of note (e.g. morphological clusters, areas of inflammation).

2.2 Laser capture microdissection (LCM)

Cases were selected as suitable where matched FFPE and frozen tissue was available and in which analysis of FFPE sections found good correlation between clusters identified morphologically (haematoxylin and eosin staining) and those identified by immunohistochemistry showing nuclear β-catenin accumulation.

7-20µm frozen sections were mounted on Zeiss 1.0 PEN membrane slides (Item No 415190-9041-00) and stained with haematoxylin and eosin.

Laser capture micro-dissection was performed using the Zeiss PALM MicroBeam system. Clusters (C), Palisading epithelia (PE, non-cluster (NC)), stellate reticulum (SR) and glial reactive tissue (G) were identified morphologically and separately collected on adhesive caps (Zeiss, Adhesive caps opaque 415190-9201-001) and stored at -80 degrees Celsius.

2.3 Murine samples

All animal procedures were performed under compliance of the Animals (Scientific Procedures) Act 1986 and current Home Office legislation. Mice were bred and housed under conditions complying with the Home Office code of practice for the housing and care of animals bred, supplied or used for scientific purposes.

2.3.1 Mouse strains

The *Hesx1*$^{Cre/+}$ line had previously been generated in the host laboratory (Andoniadou, Signore et al. 2007). Briefly, the coding region of *Hesx1* gene was replaced with a Cre recombinase cassette. Hesx1 is a transcription factor essential for normal pituitary and hypothalamus development (Dattani, Martinez-Barbera et al. 1998). It is expressed in the anterior hypothalamus, ventral diencephalon, oral ectoderm and Rathke's pouch by 9.5dpc. Lineage tracing has identified that all terminally differentiated pituitary cell types are derived from Hesx1 expressing cells (Gaston-Massuet, Andoniadou et al. 2008). Homozygotes are embryologically lethal and therefore heterozygous mice have been maintained on a C57/Bl6 background for over 50 generations.

The *Ctnnb1*$^{lox(ex3)/lox(ex3)}$ line had previously been obtained in the laboratory from Professor Taketo (Harada, Tamai et al. 1999). *LoxP* sites flank exon 3, together with a neo-cassette, such that Cre-mediated recombination results in an in frame deletion connecting exons 2 and 4. This results in loss of the β-catenin degradation domain resulting in functional activation, analogous to the point mutations observed in human cancers. A colony of homozygotes was maintained.

Embryonic ACP model, *Hesx1*$^{Cre/+}$*;Ctnnb1*$^{lox(ex3)/+}$*,* mice, were generated by mating *Hesx1*$^{Cre/+}$ and *Ctnnb1*$^{lox(ex3)/lox(ex3)}$ mice.

2.3.2 Genotyping of mice

Genomic DNA was extracted from ear biopsies using DNAreleasy (Anachem) at 1:5 dilution in a final volume of 25µl for 30 minutes at 65^{o}C. Ear biopsy was usually

performed at 1-2 weeks of age. Negative controls without tissue biopsy and positive controls of samples of known genotypes were included.

Genotyping was performed using established polymerase chain reaction (PCR) primers and protocols (Table 2-2, Table 2-3). Gel electrophoresis using a 2% agarose gel was performed and PCR products visualised by ultraviolet light. During the first year the majority of the PCR reactions were performed by myself and more lately by research assistant Leonidas Panousopoulos.

Table 2-2: PCR primers for genotyping

Mouse line	Primer sequences	Annealing temperature	Conditions	Products
$Hesx1^{Cre/+}$	OL39:TCAGCAAAGCTACAAGGTGAACTG OL89:GGAGACAATTCTTTTGTGAAACCCTG OL91: CCAGAGTGTCTGGCTTCTGTC CreT: CAGAAGCATTTTCCAGGTATGCTC	58° for 30 seconds 35 cycles	JD buffer	WT: 500 Mutant: 300
$Ctnnb1^{lox(ex3)/l+}$	bcatFwd: AGAATCACGGTGACCTGGGTTAAA bcatRev:CATTCATAAAGGACTTGGGAGGTGT	62° for 20 seconds 40 cycles	Taq Poly buffer	WT:600 Mutant: 550

Table 2-3: Protocol for PCR reactions

	PCR with Taq Polymerase buffer (hot start) (µl)			PCR with JD Buffer (µl)	
	DNA mix	Enzyme mix		DNA mix	Enzyme mix
DNA stock	1.0	-	DNA stock	1.0	-
H20	7.08	6.4	H20	1.7	1.55
Taq Pol buffer x 10	1.2	0.8	JD buffer x 3	2.5	0.83
MgCl2 25 mM	0.72	0.48	-	-	-
Primer 1 (25 µM)	1.0	-	Primer 1 (10 µM)	0.5	-
Primer 2 (25 µM)	1.0	-	Primer 2 (10 µM)	0.5	-
dNTP 25 mM	-	0.16	dNTP 25 mM	0.3	-
Taq Pol 5 u/ µl	-	0.16	Taq Pol	-	0.12
Total volume	11	8	Total volume	5.5	2.5
Protcol:	94°C for 4 min 85°C for 30s Add enzyme mix 40 cylces of: 96°C for 20s 62°C for 20s 72°C for 30s 72°C for 10mins			94°C for 2 min 85°C for 30s Add enzyme mix 35 cycles of 94°C for 30s 58°C for 30s 72°C for 45s 72°C for 10mins	

2.3.3 Collection of murine samples

Whole mouse heads were collected at post-natal day 1 (P1). Beyond P7 pituitaries were individually dissected. Tissues were either fixed in 4% paraformaldehyde or 10% formalin for 12-48 hours or frozen immediately on dry ice and stored at -80 degrees celscius.

Fixed samples were washed 3 times in 1x phosphate buffered saline (1x PBS) and then progressively dehydrated to 70% ethanol (25%, 50%, 70%). They were stored at 4°C prior to further dehydration to 100% ethanol (80, 90, 95, 100%), washing twice in Histoclear (National Diagnostics) and embedding in paraffin wax. Durations of steps varied depending on the size of sections but ranged from 30 mins to 1.5 hours. A small proportion of late stage tumours were processed, embedded and sectioned by GOSH Department of Histopathology using their standard protocols.

Histological sections were cut between 3 and 7µm on a microtome, mounted on slides and baked at 37°C overnight.

Existing laboratory stocks of sections of heads of *Hesx1*$^{Cre/+}$;*Ctnnb1*$^{lox(ex3)/+}$ mice collected at 18.5dpc were also used, where 0.5dpc was defined as the first day on which a vaginal plug was observed.

Addition samples relating to the pre-clinical trial of Vismodegib are discussed in section 2.16.

2.3.3.1 Survival Analysis

Survival analysis was performed using the survival (v2.38) package in R.

2.4 Histological staining

2.4.1 Haematoxylin and eosin staining

Haematoxylin and Eosin (H+E) stainings were performed as per standard laboratory procedures. For paraffin embedded sections this was predominantly performed on the Leica Autostainer XL H&E staining machine.

When performed manually, sections were dipped serially in Histoclear or Xylene until paraffin was removed, followed by 100% and 70% ethanol, Sections were placed in Harris Haematoxylin for 5 minutes, briefly immersed in 10% acid alcohol and then placed under running water for 5 minutes. They were placed in Eosin for a further 5 minutes, excess stain washed off with running tap water and then dehydrated in 70% and 100% ethanol, prior to two washes in Histoclear or Xylene and mounting.

For frozen sections, following brief fixation in formalin and omission of the Histoclear/xylene and initial rehydration the times were adjusted to 30 seconds, in Harris Haematoxylin, 1-2 minutes wash with running water and 5 seconds in Eosin.

For laser capture microdissection, Diethyl pyrocarbonate (DEPC) treated milliQ filtered water was used to perform the washing steps.

2.4.2 Immunofluorescence

Immunostaining was performed by established laboratory protocols (Andoniadou, Matsushima et al. 2013). Briefly, slides were dewaxed in Histoclear and slowly rehydrated from 100% Ethanol to water. Antigen retrieval was performed with either citrate buffer pH6 or tris-EDTA pH9 (Table 2-4). Slides were heated (110°C) at pressure for 2 minutes in a BioCare Medical decloaking chamber NXGEN. Sections were rinsed and permeabilised in PBT (0.1% Triton X-100 in 1x phosphate buffered saline (PBS)). Slides were incubated for 1 hr at room temperature with 10% Heat inactivated sheep serum (HISS) in blocking buffer (Table 2-4). Antibody staining was performed using concentrations as described in Table 2-5. Primary and secondary antibodies were diluted in 1% HISS in 1x PBS. Slides were incubated with primary

antibodies overnight at 4°, rinsed and incubated with secondary antibodies for 1 hour at room temperature. Where indicated, amplification was performed using biotin-conjugated secondary antibodies (Dako) and detected by incubation with streptavidin conjugated to a fluorochrome (usually Alex-Fluor 555) for 1 hour at room temperature. Auto-fluorescence blocking was performed by incubation in 0.1% Sudan black (Sigma) in 70% ethanol for 5 minutes at room temperature. After washing in 0.02% Triton-X in 1x PBS, sections were counterstained with 4',-Diamindino-2-Phenylindole (DAPI) for 5 minutes (1:10,000 Sigma) and mounted on coverslips with VectaMount (H-1000, Vecta Laboratories).

Table 2-4: Buffers used for immunohistochemistry

0.01M Citrate buffer, pH6	1.92g anhydrous citric acid in 1L H20. Adjust to pH6
Tris-EDTA buffer, pH9	Dissolve 14.4 g Tris and 1.44 EDTA to 0.55 L. Adjust to pH 9 with 1 M HCL. Add 0.3 ml Tween 20. Make up to 600 ml with H2O.This is a 10x solution.
Blocking buffer	0.1% Triton X-100, 0.15% glycine, 2mg/ml BSA in x 1x PBS.

Table 2-5: Antibodies used for immunofluorescence

Name (clone/catalog no)	Species	Supplier	Antigen Retrieval	Concentration	Secondary Antibody/ Amplifciation
CTNNNB1 Clone 6F9	Mouse	Sigma	Citrate pH6 or Tris-EDTA pH9	1:300	
CTNNB1 RB-9035-P1	Rabbit	Thermofisher	Tris-EDTA pH9	1:300	
CTNNB1 S37F mutation specific antibody (26168)	Mouse	Neweast Biosciences	Tris-EDTA pH9	1:25	Anti-Mouse biotinylated
CTNNB1 S33F mutation specific antibody (26304)	Mouse	Neweast Biosciences	Tris-EDTA pH9	1:50	Anti-Mouse biotinylated
CTNNB1 T41 mutation specific antibody (26306)	Mouse	Neweast Biosciences	Tris-EDTA pH9	1:25	Anti-Mouse biotinylated
BCL11B/CTIP2 Clone 25B6 (ab18464)	Rat	Abcam	Citrate pH6	1:250	
TP63 Clone 4A4 (ab735)	Mouse	Abcam	Tris-EDTA pH9	1:250	Anti-Mouse biotinylated
P21 Clone M19 (sc-471)	Rabbit	Santa Cruz	Tris-EDTA pH9	1:400	
Ki67 (ab42170)	Rabbit	Abcam	Tris-EDTA pH9	1:100	Anti-Rabbit biotinylated
pERK1/2 #9101	Rabbit	Cell signalling	Citrate pH6	1:250	Anti-Rabbit biotinylated
EDAR Clone E-19 (sc-15289)	Goat	Santa Cruz	Tris-EDTA pH9	1:100	
EDA (C-16) (sc-18927)	Goat	Santa Cruz	Tris-EDTA pH9	1:200	
pSMAD1,5,8/9 #9511	Rabbit	Cell signalling	Tris-EDTA pH9	1:200	Anti-Rabbit biotinylated
pSMAD3 (ab52903)	Rabbit	Abcam	TrisEDTA pH9	1:100	Anti-Rabbit Biotinylated

2.4.3 3,3′-Diaminobenzidine (DAB) immunohistochemistry

Slides were processed as per the protocol for immunofluorescence. Following incubation with secondary biotinylated antibodies sections were incubated with an avidin-biotinylated peroxidase complex (Vector). Chromogenic detection was then conducted with addition of 3,3’-diaminobenziidine (DAB, vector) for 2-5 minutes and then counterstained with Mayer’s haematoxylin (Sigma).

The majority of stainings were performed on Leica BondMax® automated immunohistochemistry machine as per Table 2-6.

BRAF V600E immunohistochemistry staining was performed by the IqPath service at the UCL Institute of Neurology using the Leica Bondmax instrument with the Bond Polymer Refine Detection Kit (Leica DS9800). Pre-treatment with Leica AR9640 for 15 minutes was performed and the BRAF V600E (Spring Bioscience E19290) antibody used at 1:50.

Anti-MSX-2 staining was performed by Annett Holsken using the Benchmark ULTRA IHC/ISH Staining Module; Ventana Roche; Illkirch, France) and the streptavidin-biotin-staining system Ventana, DAB following the manufacturer's recommendations. Murine generated monoclonal anti-MSX2/Hox8 antibody (clone 2E12, Abcam) was used at 1:200.

Table 2-6: Details of immunohistochemistry performed on Leica BondMax®

Antibody	Species	Supplier	Detection kit	Concentration
β CATENIN (clone Bcat-1,code M3539)	Mouse	DAKO	Bond-Max Protocol F	1:100
CD68 (PGM1) (clone 514H12, cat PA0273)	Mouse	LEICA	Bond-Max Protocol F	1:100
CD4 (clone 4B12, cat PA0368)	Mouse	LEICA	Bond-Max Protocol F	Pre-diluted
CD3 (clone LN10, cat PA0553)	Mouse	LEICA	Bond-Max Protocol F	Pre-diluted
CD8 (clone 4B11, cat PA0183)	Mouse	LEICA	Bond-Max Protocol F	Pre-diluted
GFAP (cat 20334)	Rabbit	DAKO	Bond-Max Protocol F	1:2000
pERK1/2 (197G2)	Rabbit	Cell signalling	Bond-Max Protocol F	1:50
CCL2 B96881	Rabbit	Sigma	Bond-Max Protocol F	1:100
IL6R (C-20) SC661	Mouse	Santa Cruz	Bond-Max Protocol F	1:300

2.5 Microscopy

Immunofluorescent images were taken on a Leica DM500 and images were captured using a CoolSNAPPro camera connected to MicroManager Image J software. Confocal images were taken using a Zeiss LSM 710 inverted confocal microscope.

Individual Brightfield images were taken on a Zeiss Avioplan 2 microscope and captured using a Ziess AxioCam HR camera connected to Axiovision 4 software. A proportion of slides were also imaged completely using either the Hamamatsu Nanozoomer C9600-01 with NDP.view 2.4.32 software or the Leica SCN400F scanner (http://www.leicabiosystems.com/digital-pathology/aperio-digital-pathology-slide-scanners/). Subsections of images were captured using PicPick (https://picpick.en.softonic.com/)

Images were processed using Image J and panels made using Microsoft Publisher or Inskape.

2.6 Imaging

2.6.1 Micro-focus computerised tomography (micro-CT) imaging

Micro CT was performed by Dr Ciaran Hutchinson using the Nikon XTH 225 ST micro CT scanner (http://www.nikonmetrology.com/en_EU/Products/X-ray-and-CT-Inspection/Computed-Tomography/XT-H-225-ST-Industrial-CT-Scanning). Stored frozen tissue was fixed in 10% formalin for a minimum 48 hours and then placed in 2.5% Lugol's iodine (25g I2 + 50g KI made up to 1000mls) for at least 72 hours. Data was initially processed in Volume Graphics®. Stacks of images were then analysed in Imaris®. Surfaces were manually annotated through consensus agreement between myself and Dr Ciaran Hutchinson to generate 3D visualisations of tumour and cluster.

2.6.2 Imaging of mouse model

Embryonic model mice were serially imaged by MRI by Dr Jessica Boult. Briefly, ^{1}H MRI was performed on a 7T horizontal bore micro-imaging system (Bruker, Ettlingen, Germany) using a 30 mm birdcage coil and 1 mm thick slices acquired over a 25 mm × 25 mm field of view (FOV). Anaesthesia was induced using 3% isoflurane in 100% oxygen (1 L/min) and maintained with 1% isoflurane (for longitudinal screening/monitoring). Micro CT images of decapitated mouse heads were acquired as per section 2.6.1.

2.7 Nucleic acid extraction

2.7.1 DNA extraction

2.7.1.1 Human and murine frozen tumour and germline DNA samples

DNA was extracted from frozen tumour or mouse tails using the Qiagen DNeasy Blood and Tissue kit®. Samples were homogenised using the Omni Tissue Homogenizer with Qiagen Tissue Ruptor tips and left over night with proteinase K. DNA was extracted from blood either by the regional genetics service or using the DNeasy Blood and Tissue kit®. DNA was quantified by nanodrop and Qubit® assay and on a 1% agarose gel.

2.7.1.2 Laser capture micro-dissected (LCM) samples

For LCM samples, DNA was extracted using the Qiagen QIAmp DNA Microkit. DNA was quantified by digital droplet PCR (ddPCR), a very sensitive quantitative PCR method where samples are split into thousands of individual droplets and amplified individually (ddPCR performed by Alice Gutteridge) (Hindson, Ness et al. 2011).

2.7.1.3 FFPE embedded samples

DNA from FFPE tissue sections was extracted by GOSH Acquired Genomics department. The Maxwell FFPE plus LEV DNA purification kit AS1135 (Promega) was used. Briefly, 5x10µm rolled sections were incubated overnight at 70°C in incubation buffer. Lysis buffer was added the following morning and the entire mix added to the Maxwell cartridge. DNA was extracted by the Maxwell 16 robot (Promega). Concentration and quality of extracted DNA was assessed using the Nanodrop.

2.7.2 RNA extraction

RNA was extracted from frozen tumour samples using the Qiagen miRNeasy® mini kit. As per DNA extraction, tissues were homogenised using the Omni Tissue Homogenizer with Qiagen Tissue Ruptor tips. RNA was assessed using a nanodrop to estimate quantity and purity (260/280 and 260/230 ratio) and Agilent bioanalyser to assess RNA quality (RNA integrity number (RIN) score).

RNA from LCM samples was extracted using the Qiagen RNeasy® micro kit and assessed on the bioanalyser.

2.8 Sanger sequencing of *CTNNB1*

Sanger sequencing of *CTNNB1* exon 3 mutation hotspots was performed either by GOSH Acquired Genomics department, or by myself at ICH.

At GOSH Acquired Genomics, primers as per Table 2-7 were used to generate a 415bp product using Amplitaq Gold (Applied Biosystems) with final concentration of 1.5mM Mg^{++} and a touchdown programme (TD45, see below). Amplicons were sequenced using BigDye Terminator kit (Applied Biosystems) and an Applied Biosystem 3500 analyser.

At ICH, primers previously designed by Lucie Wolfe (Table 2-7), MSc student, were used with the standard Taq polymerase buffer conditions as per Table 2-3.

Table 2-7: *CTNNB1* PCR Primers

	Primers	Amplicon size	Amplicon size	Protocol
GOSH Acquired genomics	β-Catenin F	CATTTCCAATCTACTAATGCT	415bp	As per Table 2-8
	β-Catenin R	CTGCATTCTGACTTTCAGTAA		
Institute of Child Health (ICH)	n1HTbCA F	GGGAATTCGGCTGTCTTTGACATTTGACTT	316bp	Taq polymerase as per Table 2-8: GOSH *CTNNB1* PCR conditionsTable 2-3
	n1HTbCA R	AGTCTAGACAGGACTTGGGAGGTATCCA		

Table 2-8: GOSH *CTNNB1* PCR conditions

Touch Down Cycle - TD45		
95°C		7mins
93°C	x10 (<1°C per cycle)	45secs
65 °C → 56 °C		45secs
72°C		1min 30secs
93°C	x35	45secs
56°C		45secs
72°C		1min 30secs
72°C		10mins
4 °C		Forever

2.9 Targeted DNA sequencing

Performed by Dr Tim Forshew's group at UCL Advanced Diagnostics

A next generation targeted amplicon sequencing panel was designed by Dr Tim Forshew to include all known craniopharyngioma mutations of exon 3 of *CTNNB1* and other common paediatric brain tumour hotspots. Targeted amplicon sequencing uses two PCR steps. Firstly, a traditional PCR amplifies a region of interest; this is followed by barcode attachment and a second round of PCR. Initially used in the context of cell free DNA, this facilitates detection of low allele frequency variants (Forshew, Murtaza et al. 2012).

Primers were designed to specifically target exon 3 *CTNNB1*, *BRAF V600, H3.1, H3.3, IDH1 and IDH.*2 mutation hotspots and sequencing was preformed using a protocol adapted from Weaver *et al*., 2014 (Table 2-9)(Weaver, Ross-Innes et al. 2014). After the two separate rounds of PCR, resulting amplicons consisted of the genomic region flanked by adapter sequences, a 5' sample-specific barcode, and lastly by Illumina adapter sequences for complementarity to the flow cell. The samples were pooled, purified and then sequenced on an Illumina MiSeq. Reads were aligned to the human genome using bwa mem (v0.7.13-r1126) and variants were detected by VarScan mpileup2snp (v2.3) with a minimum variant allele frequency of 0.05%. Gene regions were failed if fewer than 100 reads were seen using bamreadcount. Variants were considered valid if present in duplicate sequencing reactions with at least 50 reads in the variant allele.

2.10 *BRAF* digital droplet PCR

Performed by Dr Tim Forshew's Group at UCL Advanced Diagnostics

DNA was diluted 5-fold with nuclease-free water (Ambion). Each digital PCR reaction was made up to 20 µL with 2 µL diluted DNA, 10 µL ddPCR™ Supermix for Probes (No dUTP; Bio-Rad), forward & reverse primers, dual-labelled probes for wild-type and mutant templates, and nuclease-free water. Sequences for the BRAF-V600E assay oligonucleotides are from Hindson *et al*. (Hindson, Ness et al. 2011)

and were used at the concentrations stated. Reactions were partitioned into ~23,000 droplets with Droplet Generation Oil for Probes (Bio-Rad) using the QX200 Droplet Generator (Bio-Rad). All samples were tested in duplicate, with no-template controls included in all columns. Standard cycling conditions as recommended by the manufacturer were used with a T_a of 60°C.

Results were analysed with QuantaSoft ™ software, v1.7. A mean of 19,080 droplets were successfully read in each well, including controls. Two droplets positive for wild-type template were seen in the negative controls, indicating a negligible degree of contamination.

Table 2-9: Primers used for targeted amplicon sequencing

Gene	Primer name	Primer sequence	Amplicon length (bp)
HIST1H3A	H3.1_F1	GGTAACGGTGAGGCTTTTTCAC	102
	H3.1_R3	GGAAATCCACCGGCGGT	102
IDH1	IDH1 R132_F	CTTGTGAGTGGATGGGTAAAACCTA	81
	IDH1R132CG_R	CACATTATTGCCAACATGACTTACTTGAT	81
CTNNB1	CTNNB1_F2	GCTGTTAGTCACTGGCAGCA	100
	CTNNB1_R2	CCTCAGGATTGCCTTTACCACT	100
BRAF	BRAF_V600E_F	CTACTGTTTTCCTTTACTTACTACACCTCAGA	118
	BRAF_AS3	ACTGATGGGACCCACTCCAT	118
H3F3A	H3F3A-K27M_F	AGCACCCAGGAAGCAACTG	126
	H3F3A-K27M_R3	ACAAGAGAGACTTTGTCCCATT	126
IDH2	IDH2-R172S_3F	GATCCCCTCTCCACCCTGG	94
	IDH2-R172S_3R	AAACATCCCACGCCTAGTCC	94

2.11 RNA Sequencing

2.11.1 Human ACP

Human ACP cases were selected for RNA sequencing where the diagnosis of craniopharyngioma was confirmed on frozen section and where good quality RNA (RIN>6, as advised by UCL Genomics) was available. As the cell of origin of craniopharyngioma is unknown, control samples of human fetal pituitary were used. In addition, samples of non-functioning pituitary adenomas (NFPA) were selected as controls as these closely group with human adult pituitary in previous mRNA expression array studies (Gump, Donson et al. 2015).

For un-dissected human ACP, sequencing libraries were prepared using the TruSeq Stranded mRNA Library Prep kit (Illumina) and sequenced to a depth of approximately 50 million paired end reads of 80bp (performed by UCL genomics).

For LCM samples, RNA was amplified using the Clontech SMARTer® low input RNA kit and sequencing libraries generated using the Nextera XT library prep and sequenced to a depth of approximately 15 million 76bp single end reads (performed by UCL genomics).

2.11.2 Murine ACP

For murine ACP samples sequencing was performed by the Oxford Wellcome Trust Centre for Human Genetics. Sequencing libraries were prepared using the TrusSeq Stranded mRNA library prep kit (illumina). For samples collected at P1, RNA was amplified using the Clontech SMARTer® low input RNA and sequencing libraries generated using the NEBNext® DNA Library Prep Master Mix Set (New England Biolabs). For all samples, sequencing was performed to a depth of approximately 30 million 76bp paired end reads.

2.12 RNA sequencing data analysis

2.12.1 Alignment

For human analyses, FASTQ files were assessed using FASTQC and aligned using STAR aligner against UCSC human reference genome hg19. (*Performed by Nital Jani)*. Exon 3 *CTNNB1* were assessed using the integrative genome viewer (IGV) (Broad Institute) and the variant allele frequency calculated as a proportion of all reads of a given base.

FASTQ and BAM files have been uploaded to Array Express: Human frozen ACP RNA seq cohort: E-MTAB-5267, Human LCM cohort: E-MTAB-5266

For murine analyses, FASTQ files were aligned against the GRCm38.ERCC reference genome (performed by The Wellcome Trust Centre for Human Genetics).

Downstream analyses were performed by myself using Bioconductor in RStudio.

2.12.2 Normalisation

Following alignment, a read count per gene was generated for each sample using RSubread. Normalisations were then performed. The normalisation used most widely in this project was the variance stabilising transformations implemented by DESeq2. This fits a negative binomial distribution to the data in order to normalise across samples. This adjusts for the heteroskedastisity of the per gene read count, with greater variance observed for those genes with fewest counts. The transformation does not normalise for gene length, such that at an equal level of expression, longer gene will have a higher normalised count. The variance stabilised transformation gives only positive values facilitating easier downstream analyses than the similar rlog transformation.

2.12.3 Data visualisation and clustering

To visualise the datasets several approaches were used, all using standard alogrithms in Bioconductor.

2.12.3.1 Principal Component Analysis (PCA)/Multi-Dimensional Scaling (MDS):

Principal component analysis (PCA) is a method that reduces the complexity of data to a set of eigenvectors that explain its variance. These are ordered such that the first principal component (PC1) explains the most variability. Multi-dimensional scaling performs this analysis in a similar manner based on Euclidean distances between samples.

2.12.3.2 Sample distances:

Sample distance measures attempt to quantify the similarities between two sets of data plotted in multidimensional space. Distances measures, such as Euclidean distance, assess the actual numerical distance between datasets, whereas correlation distances compare the patterns.

2.12.3.3 Clustering:

There are multiple ways of clustering data; the process of grouping objects into classes. These can broadly be divided into partitioning algorithms (e.g. k-means) where objects are placed into a set number (k) of classes and hierarchical clustering algorithms whereby objects are grouped by either splitting them by difference (Top down/Divisive) or grouping them from individual objects (Agglomerative). Consequently, hierarchical clustering algorithms generate trees of hierarchy linking the inferred relationships between samples. Hierarchical clustering was performed using the hclust function in the stats package in R.

There are different methods of linking objects based around what constitutes the 'shortest distance' between samples based on their inter sample distances. In single linkage the shortest distance between objects leads to grouping in clusters. In complete linkage, the shortest of the most distant links (cluster members) and in average linkage the shortest distance between centres of clusters. In contrast, Ward's minimal variance method of agglomerative clustering groups samples by the minimal increase in the sum of the squared differences between samples. This gives results often similar to those obtained through average clustering. For the analyses performed in this thesis results were similar regardless of the exact algorithm used.

2.12.3.4 Consensus clustering:

A limitation of hierarchical clustering is that the interpretation is biased by preconceptions of meaningful group and is sensitive to anomalies and idiosyncrasies within the data (Monti, Tamayo et al. 2003). Therefore to investigate how many groups there are within a dataset Consensus Clustering was performed with R package Consensus Cluster Plus (Wilkerson and Hayes 2010). This form of k means clustering uses an iterative process by repeatedly subsampling the dataset, partitioning into k number of groups and then forming a consensus of which group each sample is in. The results for each value of k can then be assessed for their stability. Consensus distribution plots quantify the "concentration" of the consensus distribution, with the aim of identifying the number of clusters (k) that maximises the concentration. This is determined by identifying the K that induces the largest increase in area under the corresponding CDF plot. Further increasing of K beyond this adds little to the stability of the clustering. Whilst theoretically giving a hypothesis-independent assessment of clustering, consensus clustering has been observed to identify clusters in truly random computer generated datasets and therefore it is important that the results are interpreted in their biological context (Senbabaoglu, Michailidis et al. 2014).

2.12.4 Differential expression

Differential expression (DE) analysis identifies differences in expression levels of genes between two groups of samples. It was performed using DESeq2 (Love, Huber et al. 2014). DESeq2 applies normalisation factors in its analysis based on a negative binomial model. As with the variance stabilising transformation, this adjusts for the heteroskedastisity of the per gene read count, with greater variance observed for those genes with fewest counts. DEseq2 also applies independent filtering, through which only those gene where there are sufficient reads for differential expression to be detected are included in the final statistical analysis.

The results of DESeq2 analysis include a mean expression value, log2 Fold Change (log2FC), Standard error of log2 Fold Change (SE), Wald statistic (log2FC/SE) and a p-

value. P-values are adjusted for multiple testing using the Benjamini-Hochberg method to give an adjusted p-value (padj).

2.12.5 Downstream analysis

2.12.5.1 Gene ontology analysis

Due to the heteroskedastic nature of RNA seq data, gene ontology enrichment analysis of differential expressed gene lists must take into account length of a gene. Therefore gene ontology analyses of DE results from DESeq were performed using the GOSeq package in R (Young, Wakefield et al. 2010). To visualise this, results were plotted using quickGO (https://www.ebi.ac.uk/QuickGO/), which plots GO terms by their hierarchy.

2.12.5.2 Gene set enrichment analysis

Gene set enrichment analysis (GSEA) assesses where a set (list) of genes falls within a ranked list of genes. It assesses whether the given set of genes is 'enriched' at the top or bottom of the ranked list more than expected by chance alone (Subramanian, Tamayo et al. 2005). A Kolmogorov–Smirnov like enrichment statistic is calculated, whereby the analysis 'walks' down the list, from the most up-regulated to most down-regulated, calculating a running total. If a given gene is in the gene set then the total increases, if absent it decreases. The normalised enrichment score (NES) adjusts this for differences in gene set size and other relationships between the gene set and gene list. The false discovery rate (FDR) is the estimated probability that a gene set with a given NES represents a false positive finding, i.e. FDR=0.1 represents 10% chance it is a false positive result. Broadly, an NES >1 and FDR<0.25 would be considered to represent enrichment of gene set (Subramanian, Tamayo et al. 2005).

GSEA was initially developed for analysis of gene expression microarray data. For RNA sequencing results the pre-ranked tool was used. This assesses the results of differential expression analyses. The results of DESeq2 analyses were ranked by the Wald statistic (log2FoldChange/standard error of log2FoldChange). This integrates both fold change and the degree of variability, making it more suitable than fold change (can have large fold change but be non-significant) or p-value (the most

significant genes may have small fold change) alone. Using the weighted analysis attributes more significance to genes at the top and bottom of the list when calculating the GSEA statistics.

Gene sets were either downloaded from the Molecular Signatures Database (MSigDB, Broad Institute), accessed from collaborators (e.g. senescence gene sets), or created *de novo* based on experimental or published data (Table 2-10). GSEA was performed using graphical user interface GSEA version2.2.4 downloaded from the Broad Institute (http://software.broadinstitute.org/gsea/index.jsp).

Table 2-10: Gene sets used in analyses

Name	Description	Link/Reference
Hallmark v5.2 gene sets	50 curated gene sets representing well defined biological states or processes with coherent expression. Based on amalgamating overlaps of multiple founding gene sets.	http://software.broadinstitute.org/gsea/msigdb
Tooth gene sets	Genes confirmed to be expressed in various compartments of the developing teeth in human, mice, vole and other species. Inner enamel epithelium, ameloblast, dental mesenchyme and odontoblast gene sets extracted. Combined and mutually exclusive gene sets also derived.	http://bite-it.helsinki.fi/ (Helsinki, 1996-2007)
Senescence gene sets	Oncogene induced senesncence: Genes upregulated with fold change >1.5 in human IMR90 ER:RAS fibroblasts where Ras has been activated by tamoxifen, compared to those without Ras activation. SASP proteins upregualted in cultured media in Ras activated IMR90 ER:RAS fibroblasts as assesed by mass spectroscopy	(Acosta, Banito et al. 2013)
WGCNA modules	The genes included in each of the 12 WGCNA modules identified in 5.6.	Derived from results of section 5.6 (Supplementary table 3).
Human clusters and tumours	The top 100 or 500 genes up-regulated in human clusters or tumours as assessed by differential expression analysis	Derived from results of sections 5.5 and 5.11 (Supplementary table 3).
Expression patterns of brain cell types.	RNA sequencing derived expression signatures of major CNS cell types, specifically neurons, astrocytes, oligodendrocytes of differing maturation stages, pericytes, microglia and endothelial cells.	(Zhang, Chen et al. 2014)
Mesenchymal stem cells	Mesenchymal lineage signature of 489 genes based on a deep comparative analysis of multiple transcriptomic expression data series of mesenchymal stem cells at different sites and stages compared with other cell types.	(Roson-Burgo, Sanchez-Guijo et al. 2016)
Germ cell tumours	399 gene probe sets enriched in germinomas and 292 in non germinomatous malignant germ cell tumours based on expression microarray comparison	(Wang, Wu et al. 2010)
IL1β response	200 genes upregulated on treatment of macrophages with IL1β as assessed by expression microarray (http://software.broadinstitute.org/gsea/msigdb/geneset_page.jsp?geneSetName=GSE8515_CTRL_VS_IL1_4H_STIM_MAC_DN) 98 genes upregulated (fold change>3) in PHM1-31 myometial cells after IL1β stimulation 48 genes upregulated after 2 hours of IL1β stimulation on SW1353 chondrosarcoma cells	(Vincenti and Brinckerhoff 2001, Chevillard, Derjuga et al. 2007, Jura, Wegrzyn et al. 2008)
Atherosclerosis	29 genes upregulated in atherosclerotic plaques (aorta, carotid or femoral) compared with non atherosclerotic placques (Fold change > 15, FDR<0.05)	(Sulkava, Raitoharju et al. 2017)

Weighted gene co-expression network analysis (WGCNA)

WGCNA is a systems biology approach used to identify co-regulated gene networks across data sets in a hypothesis-independent manner (Zhang and Horvath 2005, Horvath, Zhang et al. 2006, Langfelder and Horvath 2008). First described in the context of brain tumours, this approach has been used to identify novel candidate pathogenic genes (Zhang and Horvath 2005, Horvath, Zhang et al. 2006, Langfelder and Horvath 2008).

Genes whose patterns of expression across samples are similar are grouped together in modules based on their Pearson correlation coefficient. WGCNA uses soft thresholding to weight/emphasize high correlations at the expense of low correlations, generating an adjacency measure for each gene. Groups of closely interconnected (co-expressed) genes, as assessed using a network analysis function (topographical overlap measure) are then defined as modules and assigned a colour. Full details are available in Langfelder and Horvath, 2008, and discussed in brief below (Langfelder and Horvath 2008). Analysis performed was based on the code included within tutorials from the creator laboratories website (https://labs.genetics.ucla.edu/horvath/htdocs/CoexpressionNetwork/Rpackages/WGCNA/Tutorials/).

Initially, WGCNA was performed using variance stabilised transformed counts of all, or just the top 5000, most variably expressed genes as assessed by their median absolute deviation. As results were very similar, for computational ease, we decided to perform all the subsequent analyses with the top 5000 most dysregulated genes. This could be performed on a standard laptop computer.

2.12.5.3 Detection of modules

Pearson correlation values are calculated between the expression values for each gene. An adjacency value is then calculated by raising these correlations to the power of the soft threshold (in this thesis, selected as 12). This serves to emphasise strongly correlating genes, whilst minimising the input of those which poorly correlate. Genes are clustered based on their topology overlap measure, a network analysis approach that filters to exclude spurious or isolated connections during

network construction. Modules are detected by cutting the clustering tree using dynamic branch cutting methods for detecting clusters in a dendrogram depending on their shape. The relationship between these modules is then explored and where modules show similar expression patterns they can be merged. This can be done by varying the thresholds and plotting of resultant modules to identify the most stable configuration. In this thesis, a threshold of 0.2 was selected for analysis of human samples. The dynamic threshold was used for murine samples.

2.12.5.4 Correlation of Modules with phenotypic information

For each module an Eigen gene (a numerical value) was calculated to represent the pattern of the gene expression of the whole module. This was correlated with available sample phenotype information of the tumours (e.g. diagnosis, histological features, *CTNNB1* mutation allele frequency, age, RNA integrity number (RIN)).

2.12.5.5 Module Ontology enrichment

Ontology analysis of modules was performed using the GOStats package (Falcon and Gentleman 2007). This facilitates assessment of enrichment of genes of a module within the context of specifying the 5000 genes included in the WGCNA analysis. Ontology enrichment was also performed using the AnnotDBi package, as per the WGCNA tutorials, and gave similar results. Results were also generated using g:Profiler, a quick online tool for assessing ontology enrichment amongst a set of genes (http://biit.cs.ut.ee/gprofiler/)(Reimand, Arak et al. 2016).

To assess gene enrichment of gene sets within individual modules, genes were ranked by their module membership score of a specific module, a measure of the extent to which a given genes' expression pattern matches that of the module. Gene enrichment scores and barcode plots were generated using the geneSetTest and barcodeplot functions in Limma (Ritchie, Phipson et al. 2015). This was chosen in preference to the GSEA graphic user interface as it gives a more direct assessment of the position of genes within a list.

2.12.5.6 Assessment of module preservation:

To assess whether patterns of gene expression are conserved in independent datasets module preservation analysis was used. This was performed as described

in Langfelder *et al,* 2011 and using code from the module preservation tutorial (Langfelder, Luo et al. 2011). This analysis assesses module preservation in several ways, which is then summarised as a Zsummary statistic. A Zsummary statistc of > 10 indicates strong preservation, and a result between 2 and 10 represents weak to moderate preservation.

2.13 Analysis of published datasets

For analysis of the data presented in Gump et al, normalised expression data was downloaded from the the National Centre for Biotechnology Information Gene Expression Omnibus (GEO) database (accession numbers GSE68015, GSE26966) (Gump, Donson et al. 2015).

Comparison of expression of genes between ACP and PCP samples was made using the dataset published in Holsken *et al.* (Holsken, Sill et al. 2016). Differential expression analysis was performed by Dr David Jones (DKFZ, Heidelberg) and GSEA by inputting normalised per gene expression array intensity values into GSEAv2.2.4.

2.14 Proteomics

2.14.1 Protein extraction

Protein lysates were extracted from pieces of fresh frozen ACP. Briefly, 6-28mg samples were placed in 250µl of lysis buffer (150mM NaCl, 20mM Tris pH 7.5, 1mM EDTA, 1mM EGTA, 1% Triton, with Protease inhibitor (Roche), 1mM Sodium Orthovanadate and 25mM Sodium fluoride). Samples were sonicated on ice and left for 30 minutes at 4°C, followed by centrifugation at 20,000G for 10 minutes and collection of supernatant. Protein concentrations were quantified by Bradford assay.

2.14.2 Multiplex enzyme linked immunosorbent assay (ELISA)

Performed by Dr Ying Hong

50µl of solid tumour protein lysates or 50µl of ACP cystic fluid were added to Meso Scale Discovery (MSD) multiplex kit (Meso Scale Diagnostics) to measure TNF-α, Interferon-γ, IL-1β, IL-6. IL-8, IL-10 and IL-18, levels. For tumour lysate samples, results were normalised against total amount of protein added.

2.14.3 Other datasets

Cytometric bead analysis of cytokines in ACP and pilocytic astrocytoma cystic fluid performed by Andrew Donson and Todd Hankinson were interrogated (Donson, Apps et al. 2017). Similarly, mass spectroscopy data of human ACP cystic fluid acquired by Benedetta Pettorini was also evaluated (personal communication).

2.15 Whole genome sequencing and exome sequencing

In whole genome sequencing (WGS), the whole genome is broken into millions of fragments. These are then sequenced using next generation sequencing and the resultant sequencing reads aligned against the host reference genome. By comparing the sequences from tumours, with that from their germline, it is possible to identify somatically acquired point mutations. In addition to detecting single nucleotide variants and small insertions and deletions (indels), analysis of the reads is also able to inform about larger scale chromosomal copy number changes and rearrangement.

In contrast, through using capture probes, exome sequencing limits sequencing to only of 1% of the genome that is expressed at the RNA level. This greatly reduces cost and the amount of data produced, however, copy number and chromosomal rearrangement information is also reduced.

2.15.1 Exome sequencing of murine ACP

Sequencing and initial bioinformatics analysis performed by Dr David Adams group at the Wellcome Sanger Centre

Fully developed pituitary tumours and matched tail samples of 15 *Hesx1*$^{Cre/+}$*;Ctnnb1*$^{lox(ex3)/+}$ mice were collected at humane end-points. DNA was extracted using the DNeasy bloods and tissue kit (Qiagen).

Exonic DNA was captured using the Agilent whole exome capture kit (SureSelect Mouse All Exon). Captured material was indexed and sequenced on the Illumina platform at the Wellcome Trust Sanger Institute at 30x depth. Raw pair end sequencing reads were aligned with BWA-mem to the GRCm38 mouse reference genome (Li 2013). Duplicated reads were marked using biobambam (Tischler and Leonard 2014). Somatic variants were detected using CaVEMan, an expectation maximization–based somatic substitution-detection algorithm (Jones, Raine et al. 2016). Detected somatic variants were then filtered using an array of quality filters and common mouse genome variants were excluded (Keane, Goodstadt et al. 2011,

Jones, Raine et al. 2016). SIFT and PROVEAN were used to predict the functional importance of mutations (Kumar, Henikoff et al. 2009, Choi and Chan 2015).

A sub-selection of 14 genes, where mutant variant allele frequencies were greater than 20% and at least 3 mutant reads were detected, were validated by Sanger sequencing. Primers were designed in flanking regions (Table 2-11). PCR was performed as per Table 2-3 with Taq Polymerase conditions. Sequencing of the PCR fragments was performed by Source BioScience (UK).

Table 2-11: Primers used in validation of *Hesx1$^{Cre/+}$;Ctnnb1$^{lox(ex3)/+}$* tumour exome sequencing results

Case	Gene	Primer 1	Primer 2
MD5190	Apcs	TGTGACCTTTGAAACCCTCC	CAGTGTCAAGGGCAGAGACA
MD5194	Sohlh2	CCTGGAGGGATGTGTGAAGT	TGAGCTGCAGTGTTAGGCAC
MD5184	Kcnd3	AAACAACCAGGAGTCCATGC	GTGTCCAGGCAAAAGAAAGC
MD5196	Col9a2	GGAACAGTGGGCTCACAACT	TCTGGTCTAACCCAATCCCA
MD5186	Ncdn	CCAGAAACTTGCTCCCAGAG	TTTCCAAAGAGCCGAAGATG
MD5195	Kmt2c	TTTGAACAGGAATATGGTGTCAG	GACAATCGGGAGAAGATAGCA
MD5197	Pak1	CGCTTGCTTCAAACATCAAA	ATCACACTGGCGCTTTCTTT
MD5186	Slco2b1	AGGAGATCCCAAAAGGCTGT	GGGGCAATCGAGTGACTTAC
MD5194	Trappc11	ACAATTTCCTTGTTTTGCCG	GCCTGTTAAAGGGTGTCCAA
MD5193	Sipa1l2	GTTTTCAGTGCAGGGGTTGT	CTCTGTTCCTTTCTCGGCTG
MD5186	Efcab6	GCAGCCTGTCAGGAGAAATC	GGGGAGGCTAAAGTACCAGG
MD5189	Nell2	TTTGTTTCTACCCACCTGGC	GATATTGACGAATGCGGGAC
MD5196	Spsb3	CTCGGCTTCAAAACAGAAGG	GGTTGCAGTTCATGCTCAGA
MD5189	Olfr137	GGTACCCAGAGCAAGGACAA	ATGGCCTCATCTGGAAGTTG

2.15.2 Whole genome sequencing of human ACP

Samples were selected for WGS where the diagnosis of craniopharyngioma was confirmed on frozen section and where good quality tumour DNA and matched germline DNA was available. Samples were sent to the Beijing Genomics Institute (BGI) for whole genome sequencing at 75x coverage for tumour samples and 30x coverage for germline samples as per the 100K Genome Project protocol

2.15.2.1 Data analysis

No pipeline for analysis of cancer genome sequencing data was available at the Institute of Child Health at the time of this project and so the whole genome

sequencing data was analysed through the Sanger centre Cancer Genome Project (CGP) pipeline through collaboration with Dr Sam Behjati. Results were interrogated and interpreted by myself at UCL.

Analysis was as described in Nik-Zainel *et al*. ((Nik-Zainal, Davies et al. 2016)) Briefly, reads were aligned against the human reference genome GRCh37.

Structural variants were investigated using the BRASS (BReakpoint AnalySiS) (https://github.com/cancerit/BRASS) algorithm. This identifies rearrangements through identifying discordantly mapping paired end reads and reads which span breakpoints to produce a consensus sequence of each rearrangement.

Somatic substitutions were identified by the CaVEMan (Cancer Variants Through Expectation Maximization (http://cancerit.github.io/CaVEMan/) algorithm (Jones, Raine et al. 2016).

The presence of small insertions and deletions (Indels) was assessed by Pindel (http://cancerit.github.io/cgpPindel/), where they were required to be present in at least 5 reads and excluded if they occurred in regions of 10 or more repeats.

Results were filtered against a database of variants identified by sequencing 100 normal healthy controls at the Wellcome Sanger centre as well as known SNPs from established databases. Results were also assessed against a Sanger Centre curated list of 616 established cancer driver genes.

2.15.2.2 Validation:

Primers were designed to detect structural rearrangements identified by WGS. For large deletions, primers were designed spanning the 5' (and in some cases the 3') breakpoint, and following the break. Similarly, primers were designed to detect a translocation. For smaller deletions primers were designed on either side. Gel extractions were performed on identified mutant bands. Briefly, bands of appropriate size were identified on 2% agarose gels using UV light illumination and the DNA extracted using the QIAquick Gel extraction kit.

Single nucleotide variants at EcoRI restriction enzyme sites were identified. Restriction enzyme digest was performed with 500ng of genomic DNA, 6 units EcoRI (Promega, 12units/µl), 1.5µl Buffer H (Promega), made up to 15µL with RNase free water and incubated for 90 minutes at 37°C. This was followed by PCR amplification, purification and sequencing as per sections 2.3 and 2.8. All primers can be found in Table 2-12. Reactions were performed by Leonidas Pansouopolous with close guidance and review by myself.

Table 2-12: Primers used in validation of WGS results. For each genomic locus: Genomic change annotation as per results in Table 7-9 or Supplementary Table 7. Case number for validation, primer combinations and expected product band size.

Translocation: Chr.3 171753134(36)--CC--99550849(51) Chr.15 (score 99)			
3TF	GCCAGGCATGTTCAGTTCAT		
3TR	TCTGAACAGCACCAGGGAAA		
15TF	ATACCCCGGATGCACTTGTA		
15TR	AAATGGACCAATCAGCAGGA		
	Case 30779		bp
	WT Chr 3	3TF+3TR	203
	WT Chr 15	15TF+15TR	587
	Translocation	3TF+15TR	371
Large deletions:			
Chr.3 178998499(502)--TCA--179001459(62) Chr.3 (score 99)			
Primer	Annealing sequence	Overhang sequence	
3F	TGGGACAGGTGCAGGAATAA		
3WT	GATTCCTGAGTCACCTGCTTTGT		
3MT	ACCTTGCTGTTTTGGTTACTGT		
	Case: 30776		
	WT	3F+3WT	650
	Mut	3F+3MT	510
Chr.2 212351172] TT [212415756 Chr.2			
	Annealing sequence	Overhang sequence	
2F	TGTATCTGCTAACTGTGGATTCA		
2WT	ACCTACACCCATCACCTGTT		
2MT	TTGTGTATGTCAGCGGCATG		
	Case 30779		
	WT	2F+2WT	435
	Mutant	2F+2MT	502
Chr.17 41227451(52)--T--41342301(02) Chr.17			
17F	CCCTATTGCCTGCCTTTTCA		
17WT	TCTCACCCATCTTCAATCCAGG		
17MT	AACCTGAGCATGCCATCTGA		
	Case 30777		
	WT	17F+17WT	246
	Mutant	17F+17MT	386
Chr.4 40437859] C [40469659 Chr.4			
4F	CAATAAGCTCTACCCTCCGACT		
4WT	CACCATTCTCCTATCTCAGCCT		
4MT	GGCTGGTCTTGAACTCTTGATC		
	Case 30779		
	WT	4F+4WT	408
	Mut	4F+4MT	613
Repeated with additional primers			
4F	CAATAAGCTCTACCCTCCGACT		
4WT	CACCATTCTCCTATCTCAGCCT		
4F2	GAGACTTACTGTTCTGCCCCTA		
4MT2	ACTCATCTTGACCTCCCAAAGT		
	5' WT	4F+4WT	408
	3' WT	4F2+4MT2	647
	Mut	4F1+4MT2	580
Chr.2 44318598(604)--AGGAAC--44321180(86) Chr.2 (score 97)			
2delF1	TGGAGAAGGAAGAGGTGGTAAG		
2delR1	GGTACTAAGCTCTTGGGACTGA		

2delF2	GCTCCCAATTACGATTCCACAA		
2delR2	CACTCTGCATCTGACAACTGAG		
	Case 30777		
	5' WT	2delF1+2delR1	385
	3'WT	2delF2+2delR2	514
	Mut	2delF1+2delR2	688
Chr.7 32822895(97)--AG--32824956(58) Chr.7)			
7F1	GAAACTTCCACAGAGCCTTAGG		
7R1	TGGCTCCCTCATGAATGGCTTA		
7F2	CGAAGTGACCATACTGAGCAAG		
7R2	GCAGCTCCTCATTCTCTCCTAA		
	Case 30777		
	5' WT	7F1+7R1	635
	3'WT	7F2+7R2	481
	Mut	7F1+7R2	581
Chr.13 105462847(50)--AAG--105476831(34) Chr.13			
13F1	TTCTCACTGTTATGGCGAACC		
13R1	GATGTGGGTTCTGACTCTACCT		
13F2	TCAACCCTCTTAATCCAGGTGG		
13R2	TCCCACTAAGAAGAGTAGCTGG		
	Case 30776		
	5' WT	13F1+13R1	212
	3'WT	13F2+13R2	433
	Mut	13F1+13R2	441
Small deletions			
Chr 1: 7889947 217bp deletion			
1delF	CTAGCAGTGTGTTACAGGCAAC		
1delR	ATGGTGATTGTGGTAGCGCTTA		
	Case 30777		
		WT	575
		Mut	358
Chr 17: del 39340681 337bp			
17delF	CATATCATGGGATGGTGACTGG		
17delR	CCTCTGACACCATGGTTAACTC		
	Case 30776		
		WT	501
		Del	164
Chr 19, 1418734		Del 342bp	
19delF	GTCGATTGGGAAGGATTAAGCC		
19delR	TCAAGTGGAGCAGTAAAGTGGC		
	Case 30779		
		WT	646
		Del	304
Chr 1, 244927378 Del 204bp			
Del1F	CCATTGTTTTCTTGCAGCGG		
Del1R	ACAGGAGAATCGCTTGAACC		
	Case 30779		
		WT	386bp
		Del	204bp
SNPs:			
Chr18: 74464442 T->C			
S18F	CAACAACGATTTTCTGCAGGTC		

S18R	CTCACCCTTGGCATTGTCTTAG		
	Case 30779		
	Product:	249 bp	
Chr 5, 65437974 G->A			
S5F	CTACATGCTCAGTCTGGAATGC		
S5R	AAAGCAGACATTAAAAAGGTTTG		
	Case 30776		
	Product:	378bp	
Chr 11, 90532787 C->T			
S11F	JohnApps_8_1	TGGACGCTTGTAATCCCACT	
S11R	JohnApps_8_2	TGAAGTGCAGTGGTGTGATC	
	Case 30779		
	Product	236bp	

2.16 Trial of GDC-449 Inhibition of SHH pathway in embryonic model of ACP

A collaboration was established with Prof Louis Chesler's group at the Institute of Cancer Research, Sutton, UK to perform pre-clinical trials in ACP, in association with pre-clinical imaging by Dr Jessica Boult. The trial was necessarily designed and performed with input from several team members at ICH and ICR. I was actively involved in developing the collaboration, designing the trial, genotyping and transferring mice from ICH, collecting samples and in data analysis.

2.16.1 Pharmacokinetic and pharmacodynamics experiments

To select the optimum dose and dose regimen the published details of pharmacokinetics (PK) and pharmacodynamics (PD) were reviewed (Wong, Chen et al. 2009, Wong, Alicke et al. 2011, Gould, Low et al. 2014). To ensure that the results were applicable to the embryonic mode,l 1-7 oral doses were administered to the mice and pituitaries, whole blood (blood spot) and plasma were collected (cardiac puncture). PK was determined by mass spectrometry (*performed by Ruth Ruddle*). Expression of target gene Gli-1 was determined using RT-PCR and *in situ* hybridisation (*performed by Gabriela Carreno*). Samples were also collected for histological examination and immunohistochemistry.

2.16.2 Randomised trial

Mice were bred and genotyped at ICH. At three weeks of age they were transferred in cohorts to ICR, where they acclimatised for 1 week before initiation of drug treatment. Mice were block randomised between drug and vehicle at a ratio of 1:1 and treated for 56 doses (maximum limit allowed by project licence). Mice were serially imaged fortnightly until radiological signs of progression were observed after which they were imaged weekly. Following completion of drug they were monitored and culled once they reached a humane endpoint, usually when they showed signs of being unsteady, gross hydrocephalus or there were other clinical concerns. Survival analysis was performed using the survival (v2.38) package in R.

Chapter 3 Imaging of human and murine ACP

3.1 Introduction

In this chapter samples of human and murine ACP were subjected to advanced imaging techniques. The aims of this were:

- To further understand the spatial relationships of human ACP tissue invasion.
- To understand the temporal dynamics of murine ACP tumourigenesis and assess the utility of *in vivo* serial imaging for pre-clinical therapeutic testing.

3.2 High resolution imaging of human ACP

The management of many cases of ACP is challenging due to the inability to completely resect the tumour without significant damage to surrounding structures. This is often due to infiltration into the surrounding tissues and the resultant lack of a well demarcated surgical tissue plane. Several publications have highlighted the structures and often diversity of features at this tumour/normal tissue boundary. Kawamata *et al*, reviewed the histological interface of 15 ACPs describing the three patterns of interface: in type 1, a capsule like boundary composed on tumour and inflammatory cells, in type 2 a relatively clear cleavage between tumour and surrounding gliosis and in type 3, perhaps the most challenging, inter-digitation of tumour epithelia with surrounding gliosis (Kawamata, Kubo et al. 2005). Such 'finger-like' extensions of tumour into areas of profound local reaction, including dense fibrosis, cholesterol clefts, giant cells, lymphocytes and haemosiderin laden macrophages have been observed by others, including Burghaus *et al*, who through immunohistochemistry described a specific niche of cells at the tumour/reactive tissue interphase characterised by expression of Nestin and MAP2c (Kasai, Hirano et al. 1997, Burghaus, Holsken et al. 2010).

The ACP clusters described in the Introduction have been suggested to play an important role in tumour invasion based on the observation that in human ACP and also a murine xenograft model, that clusters are frequently observed at the leading edge of tumour invasion (Stache, Holsken et al. 2015).

To date these studies have used standard histological approaches to examine the tumour/normal tissue boundary and have therefore been limited to 2 dimensional planes.

3.2.1 Micro-CT: An emerging method for visualising biological tissues

Led by Professor Neil Sebire, Dr Owen Arthurs and PhD student/Pathology trainee Dr Ciaran Hutchinson, the histopathology and radiology departments at GOSH have developed an expertise in micro-focus computed tomography (micro-CT) of human tissues. Micro-CT was initially designed for the non-destructive testing of industrial components, but is increasing emerging as useful in providing high resolution imaging of biological specimens, facilitating detailed 3D non-destructive visualisation at resolutions comparable with low magnification light microscopy (Metscher 2009, Hutchinson, Barrett et al. 2016, Hutchinson, Ashworth et al. 2017).

Micro-CT relies on the differential X-ray absorption between tissue compartments to delineate structures. Contrast is achieved through treating tissues with contrast agents, most commonly potassium tri-iodide, though prolonged scans of non-contrasted embedded FFPE tissues has also been successful (Scott, Vasilescu et al. 2015). Prior to this study, only one study had investigated the use of micro-CT in studying cancer invasion. In this study, Tang *et al,* performed intraoperative micro-CT of breast cancer specimens to visualise areas of calcification, but did image to histological levels of detail (Tang, Buckley et al. 2013).

The variable density of the histological structures within ACP (e.g. clusters – dense, stellate reticulum – less dense), makes micro-CT a potentially exciting method to investigate the 3D patterns of invasion. Three frozen samples of ACP were selected where there was adequate tissue. Samples were thawed and fixed in formalin and placed in potassium tri-iodide for at least 72 hours before imaging (Table 3-1).

Following imaging, samples were embedded in paraffin and processed by standard protocols, including staining with Haematoxylin and Eosin and immunohistochemistry for glial fibrillary acidic protein (GFAP) and β-catenin to assess whether potassium iodide affected immunohistochemistry.

3.2.2 Micro-CT reveals complex tissue architecture with clusters at the leading edge of tumours

3D image volumes were successfully acquired for all three samples with isotropic voxel sizes of 4–6µm (equivalent to a resolution of 5–7µm when taking account of the focal spot size of 3µm (Rueckel, Stockmar et al. 2014). The images were successfully correlated with their low power histological counterparts demonstrating the ability to identify individual structures by micro-CT (Figure 3-1). The 3D image volumes could be virtually dissected in any image plane giving much greater spatial information of the samples than that possible by individual histological slices (Supplementary Videos).

In sample JA003 the spatial relationship of the tumour compartments and reactive tissue was further explored in 3D. Differential grey values allowed tumour boundaries and clusters to be segmented from reactive glial tissue within manually determined regions. Segmentation tools merged the largest connected areas bounded by the maximum intensity of voxels within a user-defined range, creating a three dimensional model of the tumour within the reactive tissue (Figure 3-2). This highlighted the complex relationships of tumour and reactive tissue with nodules and islands interspersed across a region of the sample.

An area of apparent 'finger-like' protrusions was further analysed and found to be part of a relatively larger complex area of tumour tissue (Figure 3-2). Clusters were visualised predominantly at protrusions of tumour in both areas assessed, consistent with their suggested role in promoting invasion (Figure 3-2).

As demonstrated in Figure 3-2c, immunohistochemistry was successful, demonstrating that treatment with potassium tri-iodide does not impair immunohistochemistry.

Figure 3-1 Micro-CT imaging of adamantinomatous craniopharyngioma. a) Micro-CT and matched histological tissue section of ACP case JA0003 showing areas of tumour interspersed by reactive glial tissue. Scale bar indicates 1mm. b) 20x images of specific tumour compartments from boxed regions of a. The left panel shows epithelial whorls ('clusters') within an area of tumour and the right panel shows wet keratin which has a higher grey value on CT imaging. Scale bars=100µm. c & d) Matched micro-CT and histological images of cases JA025 and JA051. Scale bars=1mm. EW = Epithelial Whorls, SR = Stellate Reticulum, PE = Palisading Epithelium, G = Reactive Glial Tissue, WK = Wet **Keratin** (Adapted from Apps et al, 2016)

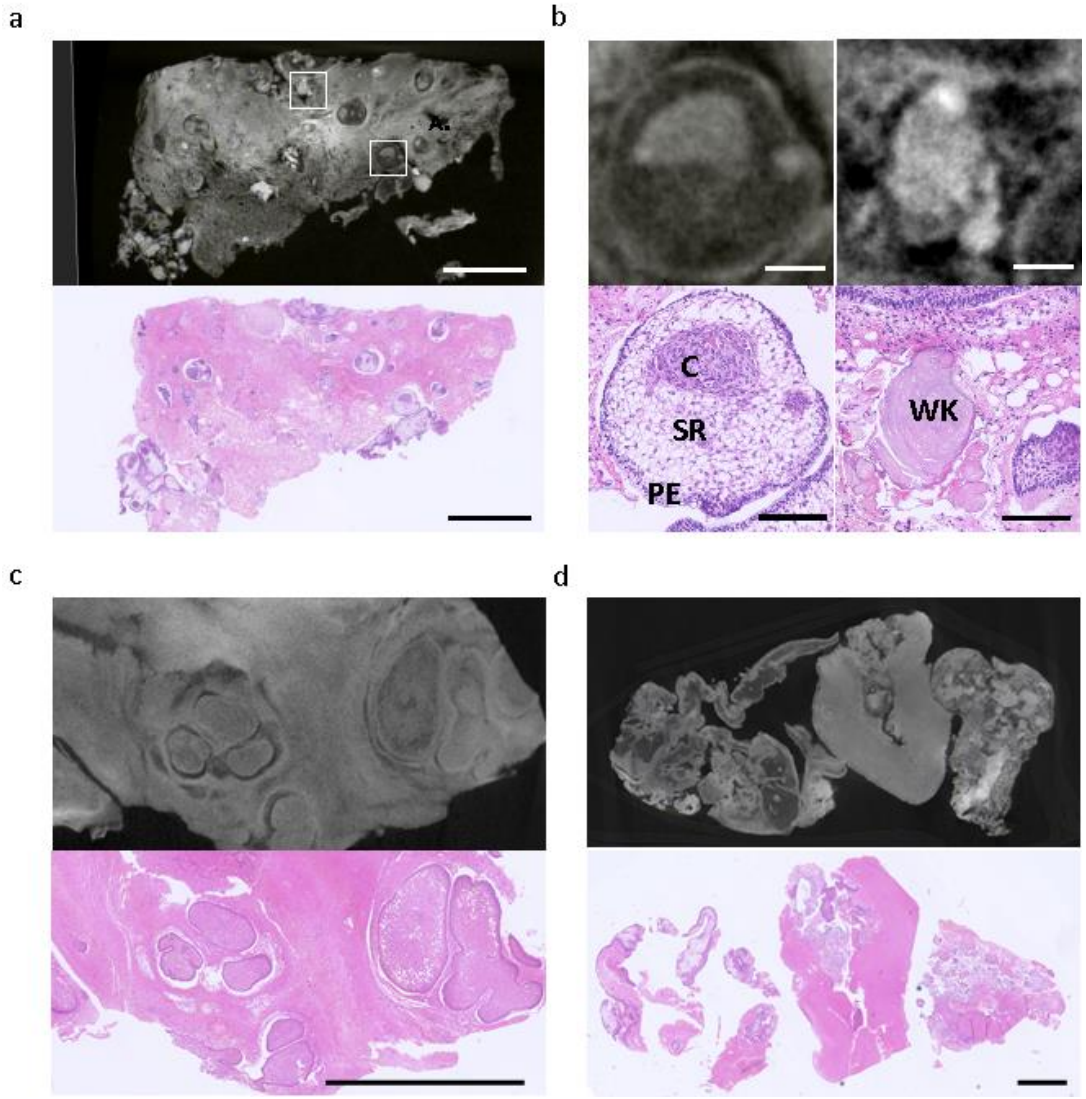

Figure 3-2: Three dimensional annotation of micro-CT of human ACP. a) Three dimensional annotation of an area of case JA003. Green indicates the border of tumour demonstrating nodules and islands with some interconnections. Connections of less than 5µm are not well visualised at this resolution, possibly explaining discontinuities. Purple indicates epithelial whorls/clusters. b) An area of finger-like protrusions. The upper panel shows the micro-CT image; the lower panel shows 3D annotation revealing a complex 3D structure in this region. c) Immuno-histochemical staining of the post micro-CT samples demonstrating appropriate antigenic reactivity following iodination. Upper panel β-catenin showing a cluster with nucleo-cytoplasmic accumulation (JA003), lower panel glial fibrillary acidic protein (GFAP) (JA051). Scale bars=100µm (Adapted from Apps et al, 2016)

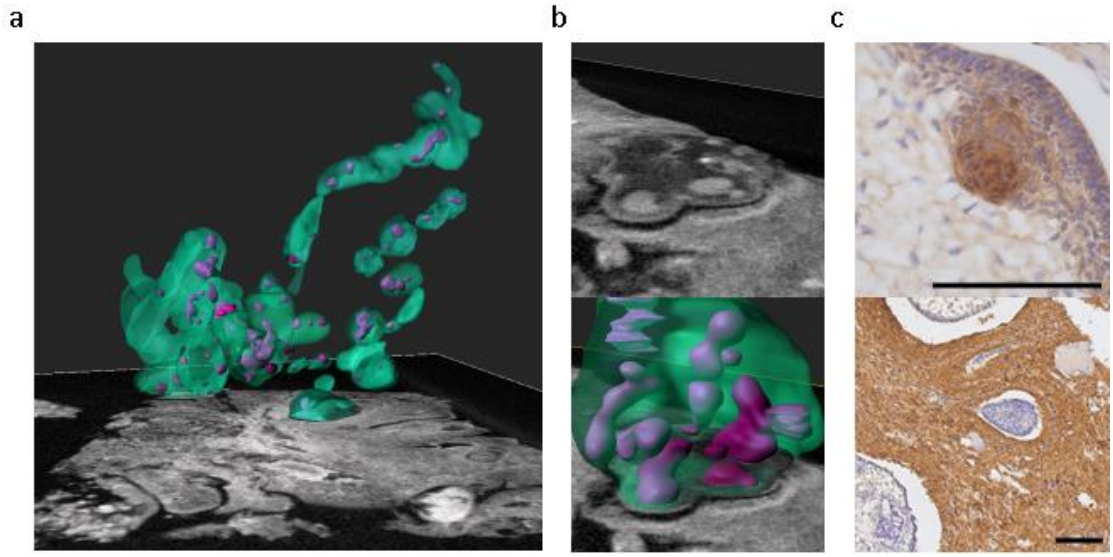

Table 3-1: Description of cases undergoing micro-CT imaging

Case:	Age of Patient:	Type:	Comment:
JA003	10 years	Primary resection	Radiological hypothalamic damage prior to surgery. At follow up pan-hypopituitarism requiring hormonal replacement
JA025	8 years	Primary resection	Clinical details not available.
JA051	43years	Primary resection	Imaging at diagnosis shows calcified lesion impinging on 3rd ventricle. At follow up pan-hypopituitarism and obesity.

3.3 Imaging the embryonic mouse model of ACP reveals similarities to human ACP

To further understand the growth dynamics of murine ACP tumours, serial imaging of embryonic ACP mice was performed using MRI. In addition, post mortem micro-CT was performed, enabling higher resolution images at different stages and correlation with histological features.

Understanding the temporal dynamics of tumour growth is important for the design of appropriate pre-clinical therapeutic treatment strategies. This is both for identifying appropriate stages for treatment, but also in assessing the potential of using imaging quantification of therapy response as a measure of therapeutic efficacy.

To perform the MRI studies, collaboration was established with Dr Jessica Boult and Dr Simon Robinson at the Institute of Cancer Research, Sutton, Surrey. Micro-CT images were acquired by Dr Ciaran Hutchinson. All mice were bred and coordinated by myself and interpretation of analyses of images done in collaboration with Drs Boult and Hutchinson.

MRI and micro-CT imaging performed at 8 weeks of age revealed enlargement and disruption of the pituitary of *Hesx1*$^{Cre/+}$*;Ctnnb1*$^{lox(ex3)/+}$ mice, when compared with wildtype control mice. This is consistent with the previously observed pituitary hyperplasia prenatally (Gaston-Massuet, Andoniadou et al. 2011). Serial imaging every two weeks revealed no significant additional changes for a period of several weeks, followed by a period of solid tissue expansion, the development of cysts (hyper-intense relative to the midbrain) and subsequent haemorrhage (relatively hypo-intense) (Figure 3-3).

Of particular note, in a proportion of tumours, cysts remained hyper-intense on FLAIR images. In this image acquisition technique signals from CSF and other motile fluid compartments would usually be suppressed. These cysts were also relatively hyper-intense on T_1-weighted images. These features are frequently seen in cysts in

patients with ACP, and is thought to relate to their 'engine oil' consistency (Curran and O'Connor 2005)

In other cases cystic fluid attenuated to the same degree as ventricular CSF on FLAIR and was isointense to the midbrain on T_1-weighted images (Figure 2A, centre panel, open head arrow). In some cases both of these cystic phenotypes were identified within individual lesions (Figure 3-3).

Ex vivo micro-CT images of intact tumour-bearing *Hesx1*$^{Cre/+}$*;Ctnnb1*$^{lox(ex3)/+}$ mouse heads, which had been imaged *in vivo* by MRI prior to necropsy, provided higher resolution 3D visualization of the tumours *in situ*. This confirmed the complex architecture observed on MRI and provided additional detailed evaluation of micro-cystic components within the solid tumour (Figure 3-4). H&E stained sections confirmed the histological features observed by MRI and micro-CT; for example densely cellular areas of solid tumour, cysts containing proteinaceous fluid and/or red blood cells, and demonstrated that the walls of large cysts consisted of a simple epithelial layer (Figure 3-4).

No invasion of the brain parenchyma by the tumour was evident by any technique.

3.3.1 Imaging reveals non-linear growth pattern

Reviewing the patterns of tumour development in these mice revealed considerable heterogeneity in tumour dynamics. Of 18 *Hesx1*$^{Cre/+}$*;Ctnnb1*$^{lox(ex3)/+}$ mice followed by serial MRI, tumour progression was identified in thirteen prior to 1 year of age. Progression occurred at a median age of 17.7 weeks (range 8.3-35.3 weeks) with median overall survival in the cohort at 22.6 weeks (range 10.1 – 41.0 weeks) (Figure 3-4). It was noted that tumours that presented later appeared to progress more slowly. Accordingly, the age at which progression was identified correlated significantly with progression time (Pearson r=0.85, p=0.0002) (Figure 3-4).

Figure 3-3: Imaging of embryonic model of ACP. a) Axial *in vivo* T_2-weighted MRI (upper panel) and *ex vivo* micro-CT (µCT) (lower panel) images of the pituitary region of 8 week old control and *Hesx1*$^{Cre/+}$;*Ctnnb1*$^{lox(ex3)/+}$ mutant mice (each image acquired from a different mouse). Note the expansion and increased heterogeneity of the *Hesx1*$^{Cre/+}$;*Ctnnb1*$^{lox(ex3)/+}$ pituitaries (solid arrows) relative to the controls (dashed arrows). Arrowheads indicate the posterior lobe of pituitary also detectable in µ-CT images and * denotes the sphenoid bone in control mice. (MRI resolution 98×98×1000 µm; micro-CT resolution approximately 9 µm) b). T_2-weighted MRI images of a *Hesx1*$^{Cre/+}$;*Ctnnb1*$^{lox(ex3)/+}$ mouse demonstrating the evolution of a tumour. In this mouse the first remarkable change was detected at 17.7 weeks, which was followed by rapid tumour progression including growth of the solid component, cyst formation and haemorrhage. c) T2-weighted (T_2-w), fluid attenuated inversion recovery (FLAIR) and T_1-weighted (T_1-w) MRI images from three *Hesx1*$^{Cre/+}$;*Ctnnb1*$^{lox(ex3)/+}$ mice demonstrating different cyst imaging presentation. Arrows denote cystic fluid that did not attenuate on FLAIR and was hyperintense on T_1-weighted MRI; arrowheads denote cystic fluid that attenuated on FLAIR and was isointense on T_1-weighted MRI. The example on the right shows both cyst phenotypes in the same tumour. (Adapted from Boult, Apps et al, 2017)

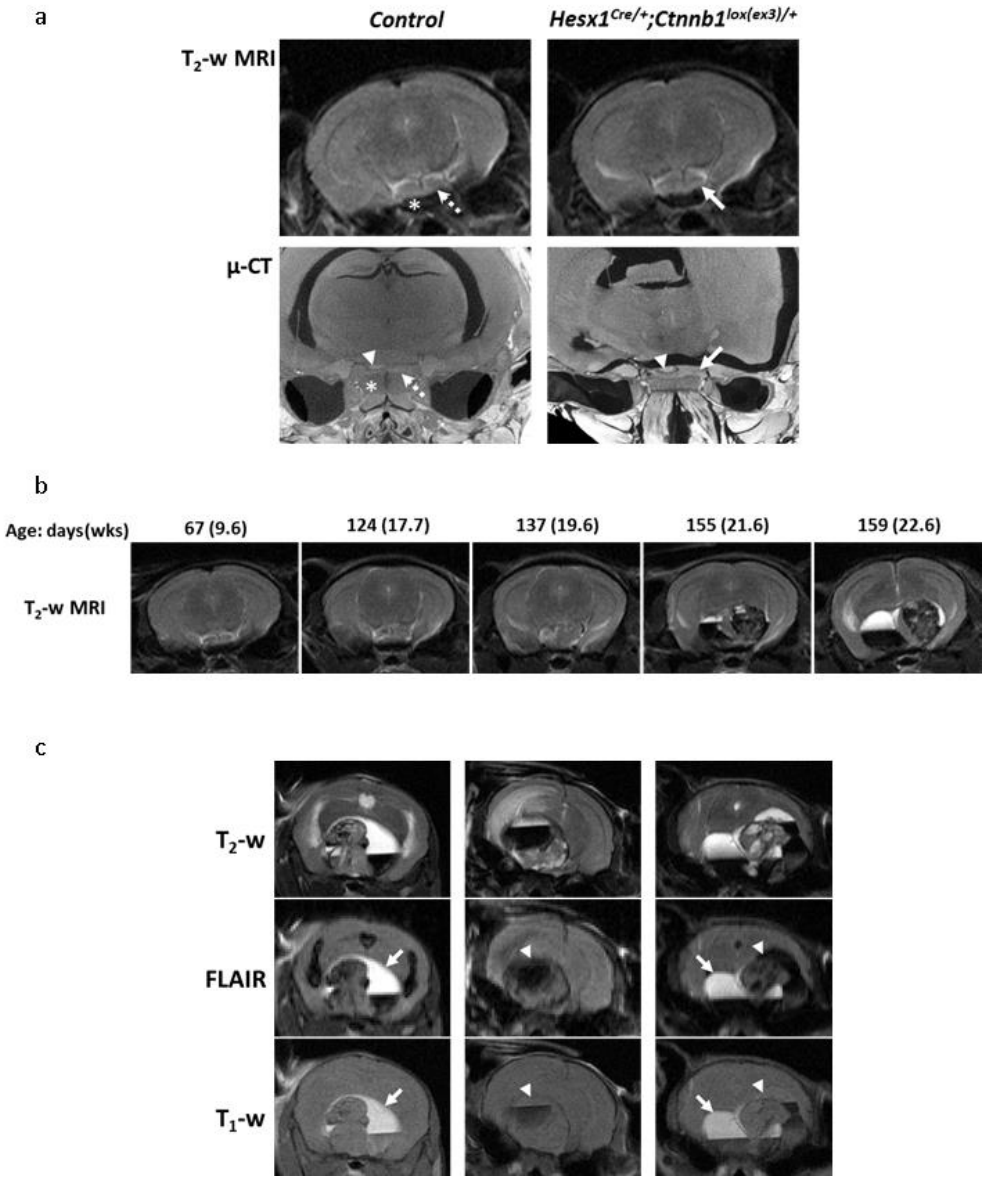

Figure 3-4 Murine ACP Survival and correlation of MRI, micro-CT and histology. a) *In vivo* T_2-weighted MRI, *ex vivo* micro-CT and H&E stained sections from two tumour-bearing *Hesx1*$^{Cre/+}$;*Ctnnb1*$^{lox(ex3)/+}$ mouse heads. Arrow denotes densely cellular solid tumour. Small cysts contained proteinaceous fluid (+) and/or red blood cells (*). Arrowhead indicates the simple epithelial layer that made up the wall of a large cyst. (MRI slice thickness 1000 µm, µ-CT slice thickness ≈ 9 µm, tissue sections 5 µm). c) Progression-free and overall survival curves to 1 year of age representing data from seventeen *Hesx1*$^{Cre/+}$;*Ctnnb1*$^{lox(ex3)/+}$ mice alongside the correlation between time to tumour identification and time between identification of tumour and death for twelve animals. (adapted from Boult, Apps et al, 2017**)**

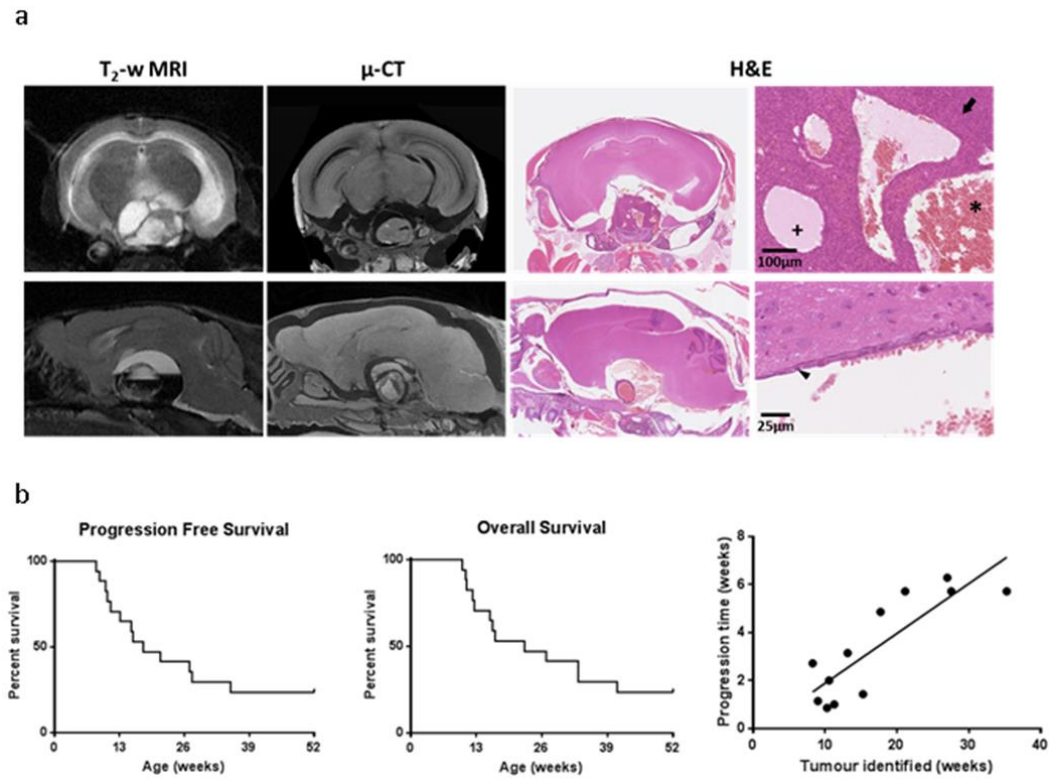

3.4 Survival study of mice reveals longer survival with sex differences

Following the variable survival durations observed in the mice undergoing imaging, survival data was collected on a larger cohort of *Hesx1*$^{Cre/+}$;*Ctnnb1*$^{lox(ex3)/+}$ mice which had been followed at ICH. Included in the analysis were 93 mice who were culled at a humane end point, or which were still alive as of 16/1/17 (study end date). The Kaplan-Meier curves are presented in Figure 3-5. Overall median survival was 24.9 weeks (inter-quartile range 17.9-29.4 weeks).

The survival time was significantly shorter in males (n=45, median survival 16.1 weeks) than females (n=48, median 31.7), (Hazard ratio 1.95 (95% confidence interval 1.24-3.05), p=0.0039) (Figure 3-5).

These survival graphs highlight a shift from the previously published survival data of median survival of 11 weeks. Reasons for this could include i) a relatively small cohort of 16 mice in the original study. ii) Genetic drift: the *Hesx1*$^{Cre/+}$ and *Ctnnb1*$^{lox(ex3)/+}$ mice were initially crossed with C57Bl/6J mice. In the original study published in 2011, these mice analysed were possibly in the first 3-4 generations (Gaston-Massuet, Andoniadou et al. 2011). For the present study, the mice have been back-crossed to C57BL/6J animals for more generations, which could have influenced the median survival. iii) Changes in housing of animals. Until 2014, mice were housed in standard cages, these were changed to individually ventilated cages. This alters the immune environment for the mice, a factor that could influence tumour progression.

Sex differences in incidence and outcome of cancers are not infrequent (Cook, McGlynn et al. 2011). For these tumours, female sex appears to increase the time to tumour formation and death. Reasons for this could include: i) hormonal differences e.g. oestrogens are relatively immunosuppressive, which given potential roles of inflammatory mediators in ACP tumour initiation could impact on the time course of tumour progression, ii) gene expression differences related to the presence/absence of the Y chromosome, iii) differences in anti-oxidative capacity. (Cook, McGlynn et al. 2011)

Figure 3-5: Kaplan-Meier survival curves of 93 *Hesx1$^{Cre/+}$;Ctnnb1$^{lox(ex3)/+}$* mice followed at ICH. a) All mice, b) Separated by sex. 95% confidence intervals are included.

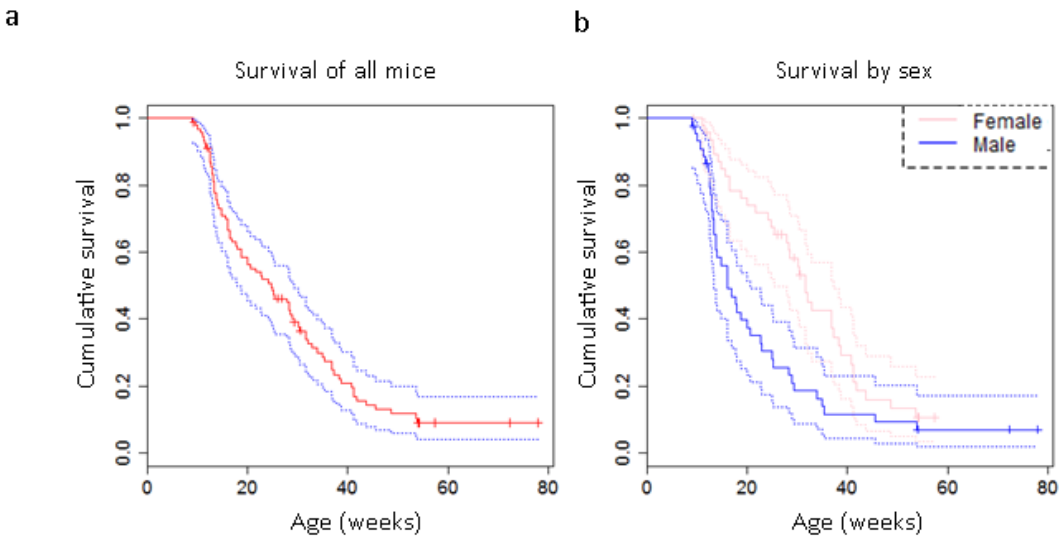

3.5 Summary

In this chapter I used micro-CT to demonstrate the complex 3D structure of human ACP and the location of clusters at the leading edge of tissue invasion. This provides the first detailed 3D visualisation of human tumour invasion and provides proof-of-principle for the use of this technology in assessing tumour/normal tissue boundaries. Whilst the relative densities of ACP tissue compared to reactive gliosis facilitated delineation of tissue compartments, how well this can be achieved in other tumour types remains to be assessed.

Imaging of the embryonic mouse model highlights a complex non-linear growth pattern, with early enlargement of the pituitary, a rapid expansion (hereafter referred to as post expansion stage) at around 17 weeks followed by tumour progression and cystic accumulation, ultimately leading to symptoms and a requirement to cull animals at around 20 weeks (hereafter referred to as late stage tumours). The results also highlight the heterogeneity of murine ACP model, both in imaging features and progression dynamics. Such heterogeneity provides additional challenges to using the model in pre-clinical testing of therapies, for instance making quantification of imaging response difficult, but may also reflect the heterogeneity seen in patients.

To further understand the molecular mechanisms of tumour initiation and progression, samples collected from mice in the ICH cohort were subsequently used in transcriptome (n=8) and exome (n=15) sequencing experiments, along with additional samples collected at intermediate stages. These will be described in detail in Chapters 6 and 7.

Chapter 4 Targeted NGS of human ACP

4.1 Introduction

Whilst *CTNNB1* mutations have been described in ACP for over a decade and *BRAF V600E* mutations have now increasingly been observed in PCP, there remain controversies. Following the publication of case reports of craniopharyngioma harbouring both *CTNNB1* and *BRAF* mutations, the mutual exclusivity of these mutations has been questioned (Larkin, Preda et al. 2014). Similarly, whilst the majority of ACPs have been found to harbour *CTNNB1* mutations, there remains a cohort where they have not been described. How much this relates to the lack of sensitivity of the various assays used remains unclear, particularly in the complex histological setting of ACP. A summary of published results to date are summarised in Table 4-1.

The pattern of immuno-histochemical staining of β-catenin in human ACP and the non-cell autonomous model of murine ACP pathogenesis suggested by Andoniadou *et al*,. has questioned whether mutations are present in all tumour cells (Andoniadou, Matsushima et al. 2013). Whilst Holsken *et al.,* 2009, attempted to answer this through performing LCM and Sanger sequencing, the results of this are controversial, particularly the finding of different *CTNNB1* mutations within different compartments of the same tumour (Holsken, Kreutzer et al. 2009).

To further investigate the pattern of mutations in ACP, working with Dr Tim Forshew, we developed a highly sensitive targeted sequencing panel of genes commonly mutated in paediatric brain tumours. This included the mutation hotspots in *CTNNB1* exon3 and the V600 locus of *BRAF*, as well as several genes mutation hotspots in high grade glioma, specifically *IDH1*, *IDH2*, *H3F3A* and *H3.1*.

The benefit of targeted next generational sequencing (NGS) over older approaches, such as Sanger sequencing, is its ability characterise variant allele frequencies, enabling an estimation of the proportion of cells within a sample that harbour a given mutation. In addition, through a second amplification step, targeted amplicon sequencing is very sensitive, enabling it to identify mutations at variant allele

frequencies well below that reliably detected by Sanger sequencing (limited to ~20%) (Forshew, Murtaza et al. 2012).

In this chapter, targeted NGS is performed on a cohort of archival FFPE samples of ACP and PCP. LCM and targeted NGS was also performed on three cases of ACP to confirm in which compartments the CTNNB1 mutations are present. Finally, to independently validate these results, β-catenin mutation specific immuno-staining was performed.

Table 4-1: Summary of published literature of *CTNNB1* and *BRAF* mutations in craniopharyngioma.

Paper	Methodology	Results	Comment
Sekine *et al.,* 2002 (Sekine, Shibata et al. 2002)	Sanger sequencing	*CTNNB1* exon3 point mutations in 10/10 cases of ACP, 0/6 PCP	*CTNNB1* mutations also present in "mesenchymal" cells but not glial tissue
Kato *et al,* 2004 (Kato, Nakatani et al. 2004)	Sanger sequencing	*CTNNB1* mutation in 9/14 ACP	*CTNNB1* mutations also identified in pilomatricomas and calcified odontogenic cysts, tumours associated with wet keratin.
Oikonomou et al, 2005 (Oikonomou, Barreto et al. 2005)	Sanger sequencing	*CTNNB1* mutation in17/43 ACP, 0/8 PCP & 0/22 pituitary adenoma	Lowest published estimate of *CTNNB1* mutation
Buslei *et al,* 2005 (Buslei, Nolde et al. 2005)	Single strand confirimation polymorphism (SSCP) analysis and sanger sequencing	*CTNNB1* mutation detected 28/4 ACP, 0/6 PCP	Deletion including exon 3 of *CTNNB1* also described in manuscript (unpublished data) No APC mutations
Holsken *et al,* 2009 (Holsken, Kreutzer et al. 2009)	SSCP and Sanger sequencing with laser capture microdissection	CTNNB1 mutation detected in 8/8 cells. Mutations identified in cells accumukating and not accumulating nuclear β-catenin. In 2 cases > 1 mutation and in 3 cases differences in mutations between nuclear accumulating and non accumulating cells.	Surprising finding of differnet mutations in different compartments. Concerns re contamination. No mutations in exon 4, or 8-13 of *CTNNB1* in 32 ACP.
Brastianos *et al,* 2014 (Brastianos, Taylor-Weiner et al. 2014)	Exome sequencig and Sanger sequencing	*CTNNB1* mutation in 11/12 ACP and 0/3 PCP on exome sequencing 51/53 ACP by Sanger sequencing	First desciption of *BRAF* mutation in PCP.
Larkin *et al,.* 2014 (Larkin, Preda et al. 2014)	Sanger sequencing	*BRAF V600E* mutation in 2/16 ACP with confirmed CTNNB1 mutations	Only description of coexistence of *CTNNB1* and *BRAF* mutations in CP
Goschzik *et al.* 2017 (Goschzik, Gessi et al. 2017)	Sanger sequecning, next generation panel sequencing, pyrosequencing. LCM in 25 cases of low epithelial content	*CTNNB1* mutations identified 89/117 ACP cases by sanger sequencing. Only idenitifed in 12/25 subjected to LCM. NGS sequencing of 26 ACP confirmed *CTNNB1* mutaton in all but 4 cases, in 2 where no mutation detected by sanger sequencing.No *BRAF* mutations identified in ACP.	Surpisingly low frequency of *CTNNB1* mutations, particularly in context of LCM. No *DDX3X* mutations identified
Malgulwar *et al,* 2017 (Malgulwar, Nambirajan et al. 2017)	Sanger sequencing and immunohistochemistry	*CTNNB1* mutations in 27/43 ACP, *BRAF V600E* mutation in 4/7 PCP.	Mutation and immunohistochemical results did not overlap

4.2 Targeted sequencing of archival FFPE craniopharyngioma confirms mutual exclusivity of *CTNNB1* and *BRAF* mutations

To detect whether the variable previous reported prevalence of *CTNNB1* mutations related to limited sensitivities of assays, and whether all ACPs carry *CTNNB1* mutations if sequenced sufficiently deeply, we identified a cohort of archival FFPE samples of 23 ACP and 5 PCP for which ample tissue was available. Diagnosis was confirmed histologically and samples ranged in their tumour content from 10-90% (Table 4-2). DNA was extracted and underwent targeted amplicon next generation sequencing. Sanger sequencing of *CTNNB1* was also performed on ACP cases and *BRAF V600E* digital PCR on PCP cases.

4.2.1 ACP harbour *CTNNB1* mutations

Of the 23 samples, adequate quality and quantity of DNA was extracted from 22. *CTNNB1* mutations were identified by targeted NGS in 21/22 (95%) samples (Table 4-2)

Full results, including filtering are presented in (Supplementary Table 1). The variant allele frequencies were predominantly consistent with the histologically assessed tumour content of samples (correlation r=0.70, p=0.004) (Table 4-1).

Sanger sequencing was successful in 19/22 samples and detected mutations in 12 (63%) In case 105, where no mutation was confirmed, a S33F mutation was identified in only one of two duplicates, in two separate sequencing runs and therefore did not pass the threshold for detection. No mutation was identified by Sanger sequencing in this case. Review of histology confirmed reasonable (60%) tumour content of this sample. Repeat analysis of this case is currently underway with repeated DNA extraction and sequencing by a separate targeted next generation panel of 78 paediatric brain tumour genes (through Dr Mike Hubank, Institute of Cancer Research, Sutton)

In three cases PCR amplification for Sanger sequencing was unsuccessful, this may relate to the larger amplicon size used in Sanger sequencing relative to the targeted

NGS and the degraded nature of FFPE derived DNA. In all other cases, where detected, there was concordance in mutation between targeted NGS and Sanger sequencing results.

In case 95 an E9K change was also identified by Sanger sequencing. This was outside the amplicon used for targeted NGS and is not thought to be pathogenic.

All other mutations were in known ACP mutated loci, particularly S33, S37 and T41, loci where mutation is expected to disrupt the degradation of the β-catenin protein and consistent with the mutations distribution in other tumour types (Table 4-1) (Forbes, Beare et al. 2016).

No hotspot mutations of *BRAF, H3F3A, H3.1, IDH1,* or *IDH2*, were identified in ACP, despite adequate coverage in all but 5 cases for *H3F3A,* for 1 case for *BRAF V600E*.

Table 4-2: Targeted sequencing results of ACP. Sanger sequencing failed in 3 cases both at ICH and GOSH**.**

Case No	Diagnosis	Tumour content (% nuclear area)	DNA conc (copies/ul)	*CTNNB1* Mutation	Average Mutation allele frequency	Detected on Sanger Sequencing
21	ACP	20	1100	T41I	17%	Yes
22	ACP	70	2315	T41I	28%	Yes
24	ACP	70	390	S37F	15%	No
25	ACP	60	1155	S45F	35%	Failed
27	ACP	10	525	S33F	3%	No
28	ACP	50	680	S37A	16%	No
32	ACP	70	770	T41I	21%	No
40	ACP	80	8854	T41I	35%	Yes
64	ACP	80	395	S33C	39%	Yes
65	ACP	80	2273	T41I	29%	Yes
85	ACP	70	143	T41I	15%	Yes
88	ACP	45	2087	S33C	19%	Yes
89	ACP	80	439	T41I	26%	Yes
90	ACP	90	1573	D32N	31%	Yes
94	ACP	50	195	S33C	30%	Yes
95	ACP	40	237	T41A	25%	Yes plus E9K
98	ACP	40	520	S37A	17%	Yes
100	ACP	90	470	I35S	43%	Failed
105	ACP	60	260	No mutation	NA	No
106	ACP	25	1256	S37F	3%	No
107	ACP	20	1460	S33F	18%	No
108	ACP	70	4505	S37C	47%	Failed

Figure 4-1: CTNNB1 mutations in ACP. a) Correlation of *CTNNB1* mutation allele frequency with histologically assessed tumour content b) Distribution of *CTNNB1* mutations in ACP cohort. Each substitution indicated by a box with the letter of resultant amino acid.

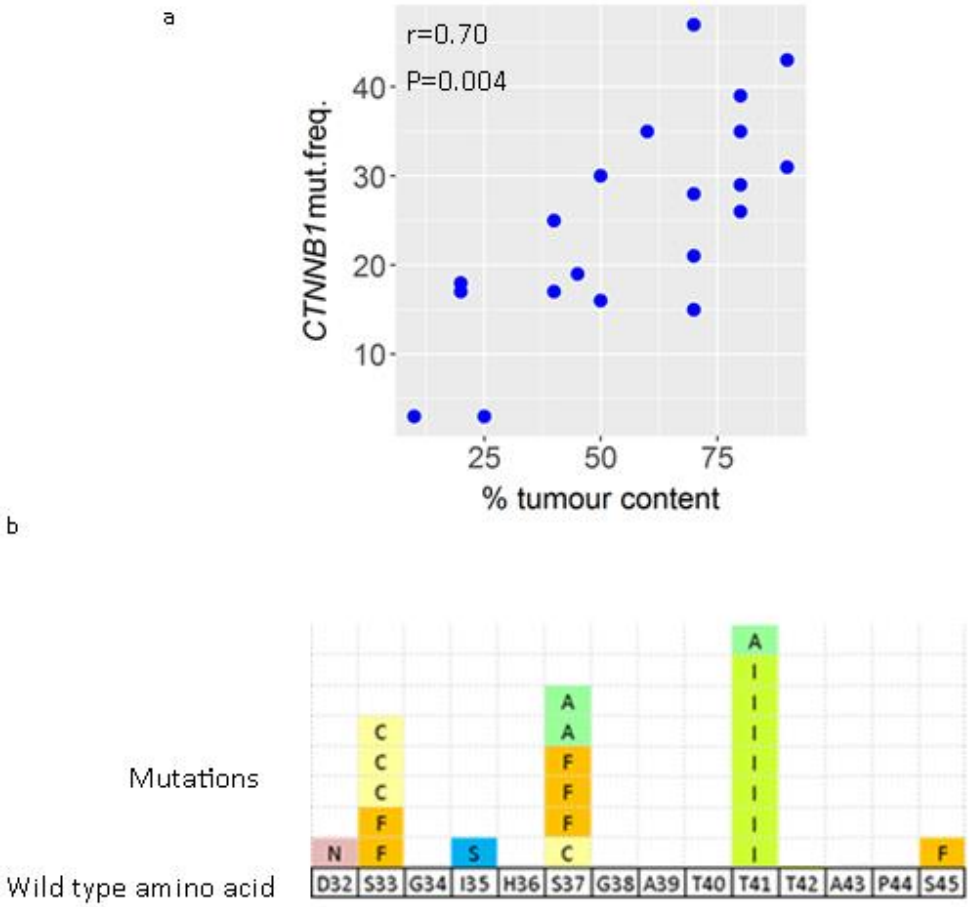

4.2.2 PCP harbour *BRAF V600E* mutations

Targeted sequencing of five PCP samples confirmed the presence of *BRAF V600E* mutations, but no mutations in *CTNNB1*, *H3F3A*, *H3.1*, *IDH1* or *IDH2*. *BRAF* mutations were also confirmed by digital droplet PCR. Variant allele frequencies were consistent with the histologically assessed tumour proportions. V600E specific immunohistochemistry was also performed and was consistent with these results (Table 4-3).

Table 4-3: Sequencing results for PCP.

Case No	Diagnosis	Tumour content (% nuclear area)	DNA conc (copies/ul)	Targeted Sequencing:		*BRAF V600E* Digital PCR			*CTNNB1* sanger sequencing
				Mutation	Average Mutation allele frequency	Mean mutant copies/µL	Mean wild-type copies/µL	Mean % mutant	
87	PCP	70	2087	BRAF-V600E	22%	252.5	655	27.60%	No mutation
91	PCP	70	6653	BRAF-V600E	23%	1262.5	3302.5	27.70%	No mutation
96	PCP	70*	360	BRAF-V600E	9%	36	240	13.00%	No mutation
97	PCP	50	262	BRAF-V600E	16%	11.8	72.5	14.20%	No mutation
101	PCP	60	1978	BRAF-V600E	19%	122.5	395	23.60%	No mutation

* includes significant areas of anuclear necrosis/degenerative change.

Figure 4-2: *BRAF* V600E mutation specific antibody staining of PCP. Tumour epithelia (*), but not fibro-vascular core ($) stains for V600E mutation. Scale bar =100um.

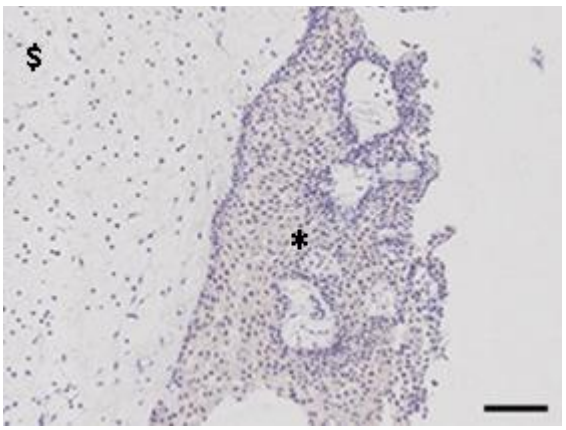

4.3 *CTNNB1* mutations are clonal and mutated β catenin is expressed by all tumour tissue

4.3.1 Laser capture microdissection (LCM) and targeted sequencing

The mutation allele frequencies identified in the series of un-dissected FFPE cases are consistent with the presence of heterozygous *CTNNB1* mutation throughout all tumour epithelial cells; e.g. results where the variant allele frequency was 39% would suggest that 78% of cells sequenced harboured a heterozygous mutation.

To confirm the presence of *CTNNB1* mutations in both clusters and non-cluster ACP tissue, we performed LCM on a series of three ACP samples for which fresh frozen material was available and clusters were easily identifiable histologically. DNA was then extracted and targeted next generation sequencing performed by Alice Gutteridge of Tim Forshew's group.

This approach was selected as a previous MSc student had previously attempted to perform laser capture of archival FFPE ACP tissue, followed by a nested PCR approach, to amplify and Sanger sequence *CTNNB1*. This had been unsuccessful, thought possibly due to poor quality of DNA extracted from FFPE tissue. We therefore chose to perform this with frozen tissue, aiming to acquire better quality of DNA. The next generation sequencing approach has the added benefit of, as well as identifying mutations, in also giving a variant allele frequency.

Unfortunately, neither our group, nor others (Annett Hölsken, personal communication) have been able to successfully immuno-stain human frozen tissue for β-catenin. Therefore Haematoxylin and Eosin stained sections were used to identify structures. For each case, we confirmed that there was reasonable correlation between clusters identified on matched FFPE sections stained with either β-catenin antibody or Haematoxylin and Eosin (Figure 4-3).

The three cases underwent LCM of clusters (C), palisading epithelium (PE), stellate reticulum (SR) and glial tissue (G) Figure 4-3. Where available, targeted sequencing was also performed on matched germline DNA extracted from blood. Laser capture

microdissection was performed in duplicate on different occasions with freshly cut sections. Each sequencing reaction was also performed in duplicate.

Full results are presented in Supplementary Table 1 and a summary in Table 4-4.

Initial results showed that in cases JA004, JA061 and duplicate 1 of case JA029, *CTNNB1* mutations could be identified in all (C, PE & SR) tumour compartments with approximately 50% variant allele frequency. This would be consistent with heterozygosity. For the second duplicate of JA029, the mutation was identified, but at more modest variant allele frequencies of 26.8-37%. The sequencing reactions were repeated with the same DNA sample with similar results. However on inspection, the DNA concentrations of these samples were noted to be significantly higher than other samples and it was felt that contamination may have occurred.

Whilst *CTNNB1* mutations were found at 50% allele frequency in tumour compartments, unexpectedly they were also found in several samples of glial tissue ranging from 2% to 21%, though absent from germline DNA in the blood.

Reviewing the experimental approach, LCM of glial tissue was predominantly performed after capture of tumour tissue compartments. When performing laser capture microdissection not all sections that are cut, lift and stick to the appropriate collection tube, and therefore there was potential for contamination of glial samples from tumour tissue. We therefore repeated the laser capture of glial tissue from virgin uncut slides. For case JA004 and JA029 the *CTNNB1* mutation was no longer detectable. For case JA061 the variant allele frequency reduced to 0.65%.

No mutations were identified in *BRAF, H3F3A, H3.1, IDH1,* or *IDH2* were identified in any of the samples.

Figure 4-3: Representative images of laser capture microdissection (LCM) a) Representative images of β catenin immunohistochemistry of FFPE sections of the three cases undergoing LCM. b) Representative images of laser capture microdissection, showing marking of clusters (green), palisading epithelium (blue), stellate reticulum (yellow) and reactive glial tissue (red).c) Collection of samples in adhesive cap. Scale bars= 150um

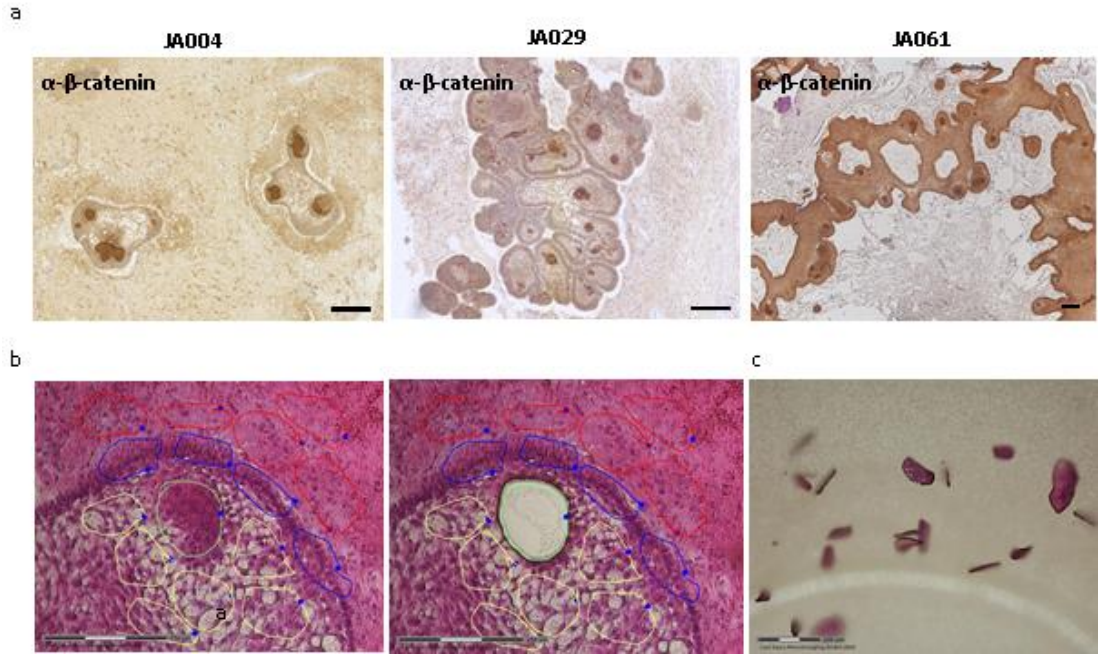

Table 4-4: Summary results of next generation sequencing of laser capture micro-dissected human ACP.

Case	JA004	JA029	JA061
Mutation	CTNNB1-S37F	CTNNB1-G34E	CTNNB1-G34E
Clusters	49%	49%*	52%
Palisading epithelium	47%	49%*	54%
Stellate Reticulum	49%	51%	55%
Glial Tissue*	0%*	0%*	0.65%*
Germline	0%	NA	0%

* only samples where confident of no contamination included. See Supplementary Table 1 for full results, NA indicates sample not available

4.3.2 Mutation specific antibody staining

In parallel to the laser capture microdissection a post-doctoral scientist, Dr Christina Stache, optimised the immuno-staining of ACP using antibodies specific to particular β-catenin mutations, specifically S33F, S37F and T41I. She had performed immunostaining on a cohort of 10 cases of ACP from Erlangen, Germany.

As case JA004 had an S37F mutation, the findings of the laser capture micro-dissection and targeted sequencing were further validated by myself through mutation specific β-catenin immunohistochemistry on a matched FFPE sample of this case. This and previously stained cases were then imaged on the confocal microscope. This confirmed the expression of mutated β-catenin protein in all tumour compartments (Figure 5).

Together these results confirm, by two independent techniques and on two separate, but overlapping, cohorts, that *CTNNB1* mutations are clonal within the tumour epithelia and present in all tumour components. Therefore the mutations are present in cells which have, and those which do not have, nuclear accumulation of β-catenin.

Figure 4-4: Mutation specific antibody staining of human ACP. Mutation specific and mutation non-specific antibody staining perfectly match. Scale bars= 100µm

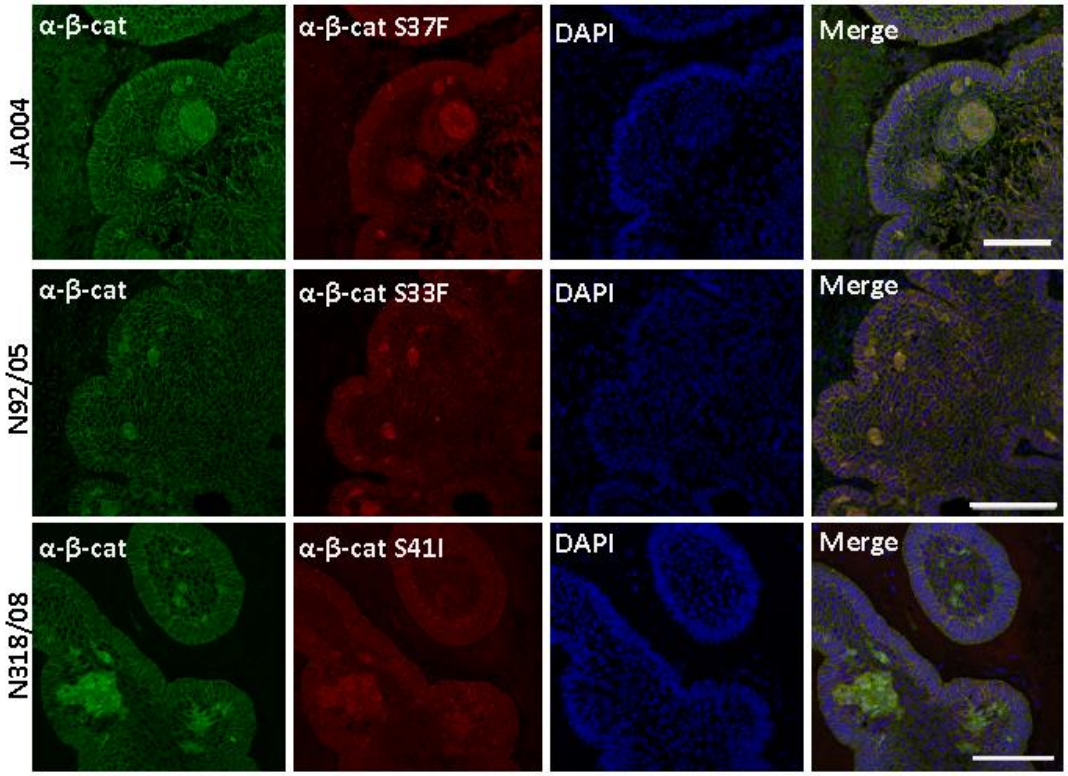

4.4 Chapter summary

In summary, in this chapter I provide further support of mutual exclusivity of *CTNNB1* mutations and *BRAF* mutations in ACP and PCP respectively. Furthermore, I confirm the presence of *CTNNB1* mutations in all epithelial ACP cells using two independent methods.

Chapter 5 Transcriptional profiling of ACP reveals complex tissue architecture and relationship with the developing tooth.

5.1 Introduction

The previous chapter addressed the targeted sequencing of specific genes related to craniopharyngioma. Next we wished to investigate the gene expression landscape of ACP.

To date only three previous publications have investigated the global gene expression patterns in ACP. Gong *et al*. 2014, compared primary and relapse samples of two paediatric ACP patients using expression microarray and identified high levels of CXCL12 and CXCR2 associated with relapse (Gong, Zhang et al. 2014). Gump *et al*. 2015, performed microarray analysis of 15 ACP samples, comparing them with a panel of normal brain tissues and other tumour types (Gump, Donson et al. 2015). Differential expression analysis was performed identifying up-regulation of a number of genes related to epithelial differentiation and odontogenesis as well as a number of potential therapeutic targets including *SHH* and *EGFR (Gump, Donson et al. 2015)*. Similarly, Holsken et al, 2016, performed expression array analysis comparing ACP with PCP showing differences in gene expression patterns, with SHH and WNT pathway genes up-regulated in ACP (Holsken, Sill et al. 2016).

In these publications, correlation between dysregulated gene pathways and tumour architecture has been limited. In this chapter, I use RNA sequencing to further dissect the gene expression of several pathways within the context of tissue architecture and address several biological questions of relevance:

- Are there distinct biological subtypes of ACP?
- What biological pathways are active within human ACP?
    - Specifically, within which tissue compartment? (e.g. cluster, non-cluster tumour, reactive glial tissue)
        - What are the pathways/genes activated in nuclear β-catenin accumulating clusters?
    - Can this inform about the cell of origin of tumours?
    - What therapeutically targetable pathways are active within ACP?

To address these questions we identified a cohort of archival frozen specimens to perform RNA sequencing. Similar to the approach for *CTNNB1* genomic sequencing, we also undertook LCM of two cases to profile the genomic landscape specifically of clusters, palisading epithelium, and glial tissue.

5.2 Identification, quality control and selection of cases for sequencing

5.2.1 ACP Cohort

Frozen ACP cases were sought from national biobanks and national and international collaborators (see Methods). At the time of analysis, 40 frozen samples from 37 cases of craniopharyngioma had been accessed. This included four adult ACP specimens and one childhood case of PCP. No adult PCP frozen material was available. In one ACP case, four separate samples were available. In addition, frozen control samples of three fetal pituitaries (19 weeks gestational age), six non-functioning pituitary adenomas (NFPA) and four post-mortem specimens of adult pituitaries were accessed.

Quality assessment revealed variable quality across samples. All adult post-mortem pituitaries had low quality RNA (RNA integrity number (RIN) <4) and therefore not suitable for RNA sequencing. 19 ACP samples from 17 cases were histologically confirmed as ACP and had adequate RNA quality (RIN >=6). A sample cohort of 18 ACP samples, three fetal pituitaries and three non-functioning adenomas was therefore selected for sequencing. Two samples from one case of ACP were included to assess for intra-tumoural heterogeneity. One case of adult ACP was included. The summary details of the included cases are shown in (Table 5-1). Of note the epithelial tumour content varied considerably across the samples with estimates ranging from 20-90%. Histological images of each case are shown in Figure 5-1.

RNA sequencing was performed to a depth of 50 million paired-end reads per sample (see Methods). This depth was selected to give sufficient coverage to detect sequence variants (mutations) and fusion genes, in addition to gene expression data only. This was successfully performed and the resultant data presented below.

Table 5-1: Characteristics of samples included in RNA Sequencing cohort. ACP = Adamantinomatous craniopharyngioma; NFPA = Non-functioning pituitary adenoma; GA= Gestational age. Tumour content was assessed histologically as percentage of nuclei. The presence or absence of wet keratin and glial reactive tissue on the frozen section is also indicated. NA* indicates unable to assess histologically, usually due to extensive freezing artefact on frozen section.

Sample ID	Type	Age of patient at sample collection	Tumour content (% nuclear)	Glial reactive tissue	Wet keratin	*CTNNB1* mutation	*CTNNB1* RNA mutation allele frequency (%)
JA002[#]	ACP	10yrs	60	Yes	Prominent	Ser37Phe	25
JA004[#]	ACP	10yrs	40	Yes	Minimal	Ser37Phe	16
JA005	ACP	13yrs	60	Yes	Minimal		0
JA008	ACP	8yrs	60	NA*	Prominent	Gly34Arg	27
JA009	ACP	13yrs	90	NA*	Prominent	Ser37Phe	48
JA010	ACP	13yrs	40	Yes	None	Asp32Gly	6
JA011	ACP	15yrs	20	Yes	Minimal	Gly34Arg[$]	5[$]
JA013	ACP	8yrs	90	No	None	Thr31Ile	47
JA014	PCP**	3yrs	90	No	None	Ser45Phe	42
JA020	ACP	7yrs	70	Yes	None	Ser37Phe	9
JA023	ACP	16yrs	90	No	Prominent	Thr31Ile	41
JA026	ACP	3yrs	90	No	Prominent	Gly34Arg	37
JA029	ACP	8yrs	70	Yes	Prominent	Gly34Glu	13
JA030	ACP	2yrs	90	No	None	Gly34Glu	42
JA036	NFPA	adult	0	NA	None		0
JA037	NFPA	adult	0	NA	None		0
JA038	NFPA	adult	0	NA	None		0
JA051	ACP	50yrs	80	Yes	None	Ser33Cys	36
JA053	ACP	8.8yrs	80	No	Prominent	Asp32Arg	41
JA054	ACP	13.1yrs	NA*	NA*	NA*	Asp32Tyr	13
JA056	ACP	8.4yrs	80	No	Prominent	Ser33Cys	36
JA058	Fetal Pituitary	21/40 GA	0	No	None		0
JA059	Fetal Pituitary	21/40 GA	0	No	None		0
JA060	Fetal Pituitary	21/40 GA	0	No	None		0

NB JA002 and JA004 were two separate samples collected from one tumour in the same surgery $ Not detected by RNA sequencing but detected by targeted next generation sequencing of DNA of adjacent frozen tumour sample.** reclassified as ACP based on presence of *CTNNB1* mutation and clustering with other ACPs. Histology review inconclusive.

Figure 5-1: Histology of matched frozen sections to ACP samples undergoing RNA sequencing. For cases JA005 and JA011, where *CTNNB1* mutations were not identified, only solitary small islands of tumour epithelia (arrow) were seen. (Scale bars = 500um and 100um)

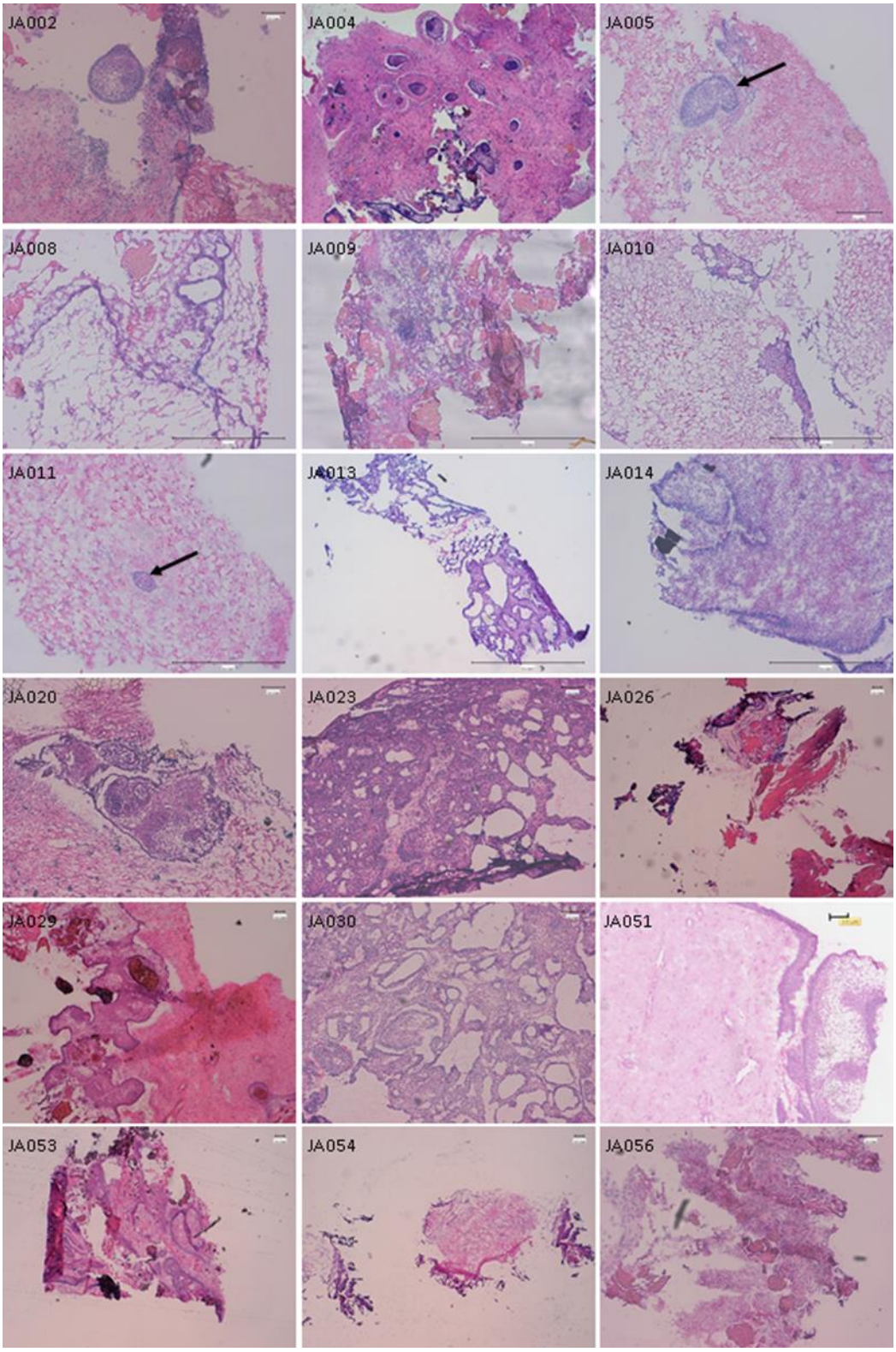

5.2.1.1 Successful RNA sequencing of laser capture micro-dissected tissue

In two samples (JA004, JA029) LCM was also performed, isolating clusters (C), palisading epithelium (NC/PE) and glial (G) tissue. In case JA004 duplicates of clusters and palisading epithelium tissue were collected. Case JA061, which also underwent LCM and targeted DNA sequencing, was not available at the time these experiments were performed and thus not included.

RNA was analysed by Bioanalyser which demonstrated the presence of only very small quantities of RNA (9-66pg/µl) (Table 5-2). Such low quantities precluded assessment of RNA integrity. Following conversion to cDNA and amplification, concentrations ranged from 52-727pg/µl and this cDNA underwent 76bp single-ended sequencing to a depth of 15 million reads (Table 5-2). Adapter contamination was identified in FASTQ files processed by UCL genomics standard pipeline. These were removed prior to alignment (performed by Nital Jani).

Table 5-2: Laser capture microdissection samples: RNA concentration after extraction and cDNA concentration following amplification.

Sample ID	Case	Cell type	RNA conc (pg/µl)	cDNA concentration (pg/µl)
4C	JA004	Cluster	66	727.8
4NC	JA004	Palisading epithelium	53	74.09
4C-2	JA004	Cluster	22	175.93
4NC-2	JA004	Palisading epithelium	35	95.04
4G	JA004	Reactive glia	17	52.43
29C	JA029	Cluster	72	424.91
29NC	JA029	Palisading epithelium	9	138.37
29G	JA029	Reactive glia	34	121.30

5.3 *CTNNB1* mutations identified by RNA sequencing

To assess the presence of *CTNNB1* mutations, reads mapping to exon 3, where the vast majority of the *CTNNB1* mutations lie, were analysed. This revealed several known activating mutations in 16 out of 18 craniopharyngioma samples, with one mutation per tumour (Table 5-1). The mutational allele frequency ranged between 6 to 48%. This significantly correlated with the estimated histological tumour content ($r=0.88$, $p=6.61 \times 10^{-8}$) and was consistent with the mutation being present in heterozygosity within all of the tumour epithelia (Figure 5-2).

Failure to identify the *CTNNB1* mutations in cases JA005 and JA011 most likely suggests that not enough tumour RNA material was represented in the total RNA isolated from these specimens. In agreement with this possibility, targeted next generation DNA sequencing of an adjacent frozen sample of case JA011 revealed a *CTNNB1* p.Gly34Arg mutation with a variant allele frequency of 4.7%. There was insufficient material to perform targeted sequencing on JA005, but the histological assessment showed only a very small island of tumour in the section (Figure 5-1).

The mutations identified in cases JA004 and JA029 were also confirmed within the LCM cluster tissue. Unfortunately, there was insufficient or no reads to assess these loci in the palisading epithelium or glial tissue.

Figure 5-2: *CTNNB1* mutations in ACP. a) Example trace from integrative genomic viewer showing reads with p.S37F *CTNNB1* mutation. b) Correlation between mutation allele frequency and histologically-assessed tumour content.

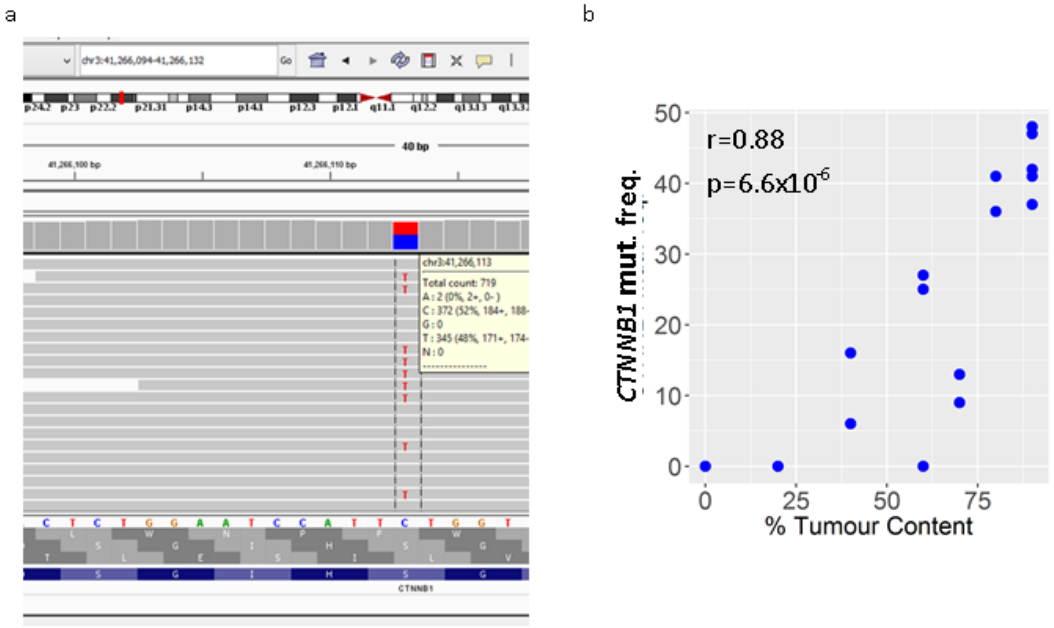

5.4 Clustering of samples identifies relationship with tumour content

Next to assess the overall patterns of gene expression across the samples, Principal Component Analysis (PCA) and Hierarchical Clustering was performed. This confirmed the separation of tumours (including JA005 and JA011) from controls (Figure 5-3). Of note, sample JA051, the adult ACP case, grouped within the other paediatric cases. Similarly JA014, reported as a childhood PCP, clustered with the ACP cases. Given this case harboured a *CTNNB1* mutation, no *BRAF* mutation and inconclusiveness of histology to differentiate between ACP and PCP in the available sample, coupled with the extreme rarity of PCP in childhood, this case was reclassified as an ACP. Samples JA002 and JA004 grouped together.

Whilst tumour cases grouped separately from control tissues, considerable variance in tumours was also apparent. Clustering revealed this to relate to the tumour content and the *CTNNB1* mutation allele frequency (Figure 5-3). Samples JA26, 56, 14, 13, 9, 30, 51, 23 and 53 had high tumour contents and high *CTNNB1* mutational allele frequencies (>30%), whereas samples JA005, 11, 19, 20, 29, 2, 4, 8 and 54 had low tumour contents, lower *CTNNB1* mutation allele frequencies and were more likely to include reactive glial tissue.

To assess the stability of this clustering a class discovery tool, Consensus Clustering, was performed. Using the 5000 most variably expressed genes, this approach repeatedly selects a random subset of 250 genes to perform clustering and assess the stability of the resulting groups. This confirmed that the most stable clustering was with three groups (K=3), corresponding to the control samples and the two subgroups identified by hierarchical clustering (Figure 5-4).

To investigate whether such a dichotomy of ACP samples is seen over a larger cohort I integrated the variant allele frequencies from the RNA sequencing cohort with that of the DNA targeted sequencing cohort. In samples JA004, 5, 8, 9, 10 and 11, where both RNA and DNA sequencing data was available, variant allele frequencies for RNA and DNA analysis was comparable, suggesting this approach is valid in this cohort (Table 4-2, Table 5-1).

Histograms showed that whilst there are two peaks at low and high allele frequency in the RNA cohort, there was one of intermediate frequency in the DNA cohort (Figure 5-5). Combining the cohorts showed equal distribution across allele frequencies. To further investigate whether our RNA sequencing cohort had sampling bias we reviewed the histology of a larger cohort of cases across GOSH and the National Hospital for Nervous Diseases (approximately a further 70 cases), this identified cases where different blocks, and even occasionally the same block, included areas corresponding to both histological phenotypes (Figure 5-5b). Therefore it was concluded that the sample groups identified by RNA seq and clustering analysis most likely represent sampling variation, as opposed to true biological variation between tumours.

Whilst this does not therefore support the identification of ACP subgroups, this variation in tumour content facilitated *in silico* molecular dissection of the gene expression pathways in ACP.

Figure 5-3: Principal Component Analysis (PCA) and Hierarchical Clustering of samples. a) PCA plot showing separation of tumours from controls and variance amongst tumours. b) Hierarchical Clustering of samples showing the separation of controls from tumours. Note that samples JA002 and JA004, both from the same patient, group together and that JA051, the only adult ACP sample, groups with other paediatric ACP samples. The dendrogram is further annotated with sample information. Blue indicates the presence of a trait. For instance, JA005 includes reactive glia. For wet keratin, dark blue indicates prominent wet keratin and light blue minimal wet keratin. The assessment of tumour content and *CTNNB1* mutation allele frequency is represented in red colour, the higher the value the more intense the red. For instance, tumour JA009 shows both high tumour content and *CTNNB1* mutation allele frequency. Values are available in Table 1. Grey indicates that tissue could not be assessed for a given trait, usually due to freezing artefact. NFPA = non functioning pituitary adenoma.

a

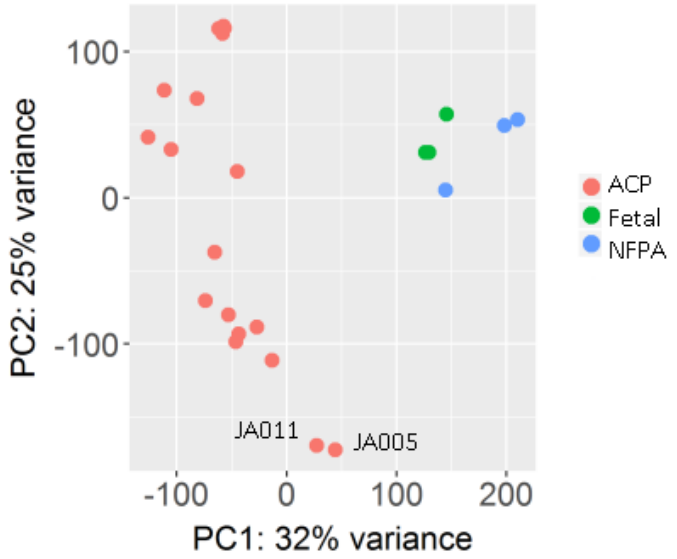

b

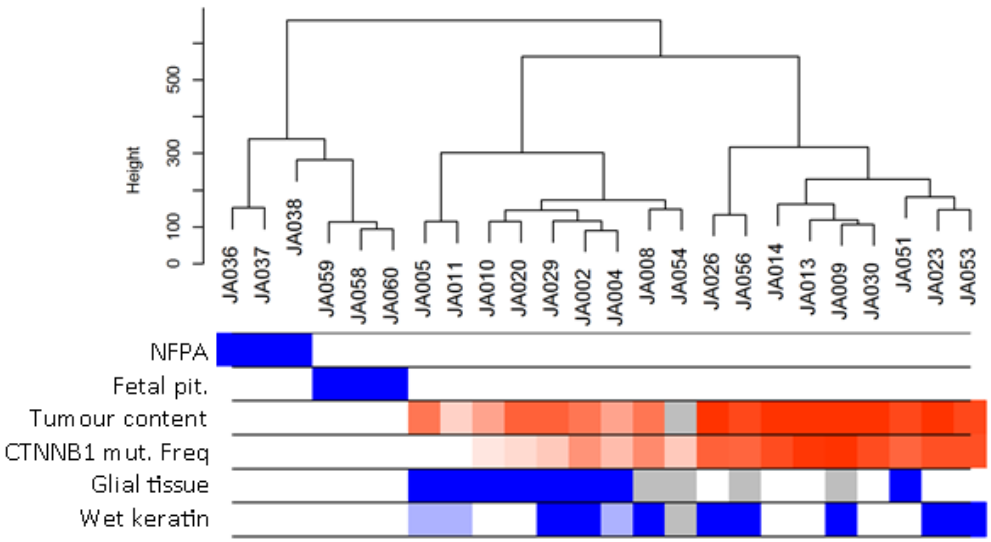

Figure 5-4: Consensus Clustering of 5000 most variably expressed genes. a) Consensus matrix plots for K=2-4. Colour indicates the frequency with which samples group within each group on multiple iterations of clustering. (deep blue = strong group membership). b) & C) The consensus distribution function plot and delta area plot indicate that the most stable clustering is with k=3

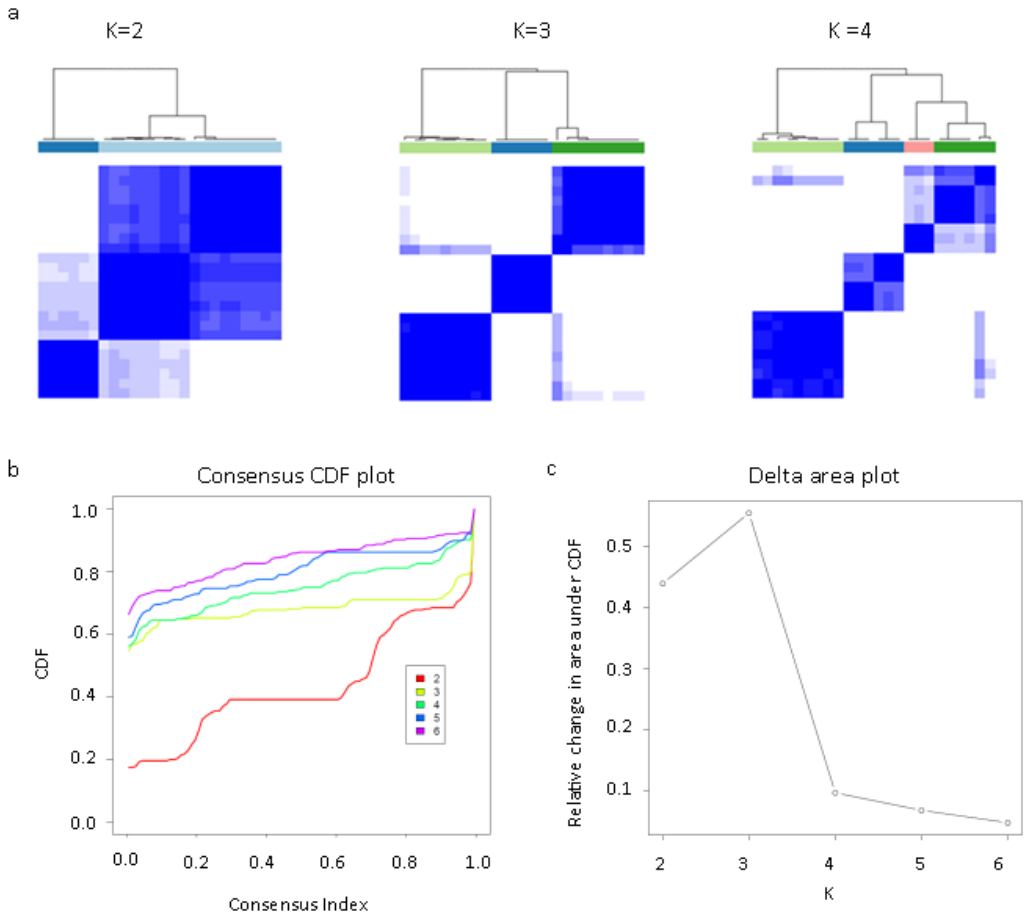

Figure 5-5: *CTNNB1* mutation allele frequencies. a) Histograms of *CTNNB1* mutation allele frequency across targeted DNA sequencing, RNA sequencing cohorts and all samples. B) Histological images of FFPE block of case JA025 where varying tumour content is found within two areas of a single tissue block. In the upper half of the block almost all cells are tumour epithelia, whereas in the lower half ther is only a solitary island of tumour (arrow), surrounded by reactive glial tissue. Scale bar = 500um.

a

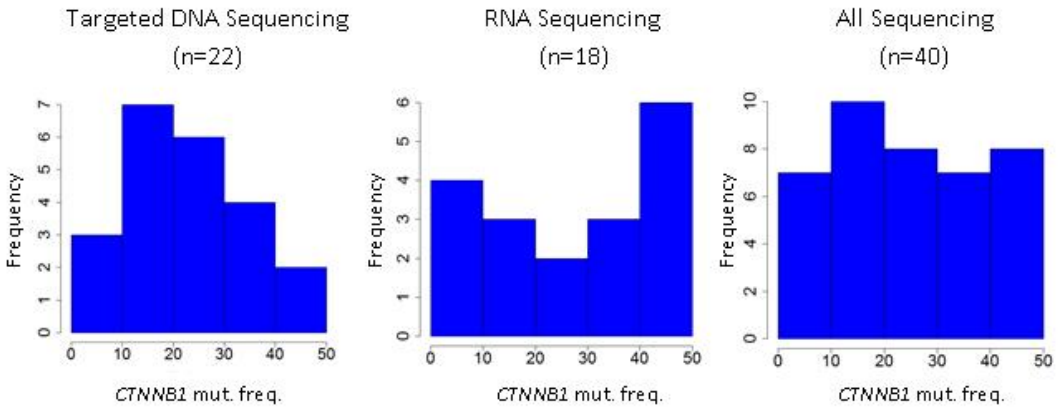

b

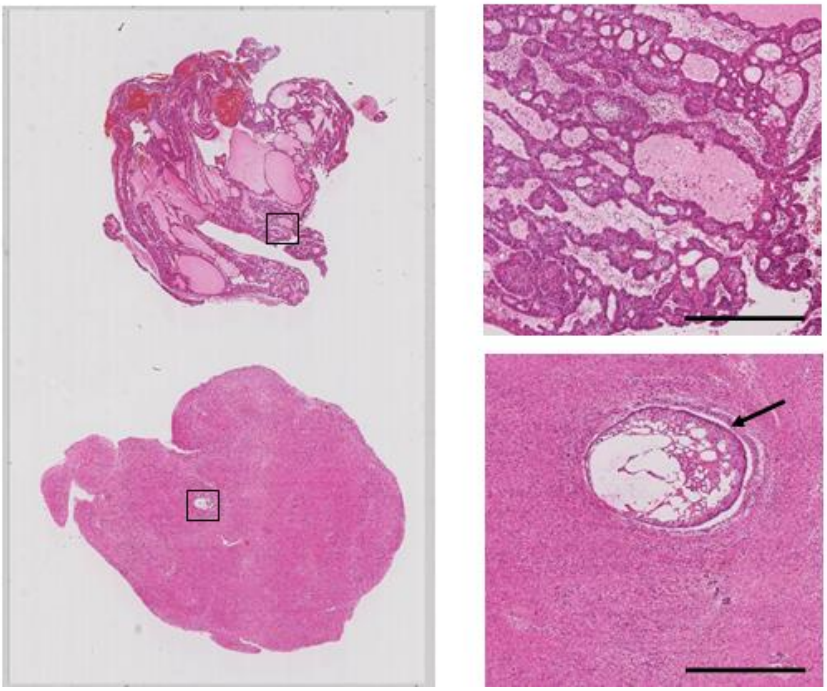

5.5 Differential gene expression analysis demonstrates WNT pathway activation and epithelial differentiation in ACP

To understand the gene expression patterns within ACP, I began by performing differential expression analysis between tumours and controls. This revealed that a total of 6099 genes were up-regulated and 5211 genes down-regulated in the tumours relative to control tissues (adjusted p-value <0.1) (Supplementary Table 2). Keratins *KRT75* and *KRT5* were the most up-regulated genes (1888 and 1788 fold, respectively), consistent with epithelial histological features of ACP and previous immuno-histochemical studies (Buslei, Holsken et al. 2007) (Figure 5-6).

Consistent with the activating *CTNNB1* mutation identified in most tumours, several WNT target genes and WNT ligands were also up-regulated in the tumours including *LEF1* (8.12 fold), *AXIN2* (3.87 fold), *NOTUM* (114 fold), *WNT3a* (522 fold) and *WNT7A* (459 fold) (Figure 5-6). Other genes known to be highly expressed in ACP were also found up-regulated in the tumours relative to the control tissues, including *FGF4* (760 fold), *FGF3* (47 fold), *BMP7* (36 fold) and *BMP4* (7 fold) (Figure 5-6). Likewise, a number of previously suggested therapeutic targets including *SHH* (35 fold), *MMP12* (417 fold) *MMP9* (64 fold) and *EGFR* (9 fold) were also up-regulated in the tumours (Holsken, Gebhardt et al. 2011, Gomes, Jamra et al. 2015, Gump, Donson et al. 2015) (Figure 5-6).

As expected, pituitary transcription factors (e.g. *LHX3* (236 fold), *POU1F1* (646 fold) were down-regulated in the tumours relative to the controls (Figure 5-6). In agreement with the non-hormone secretory phenotype of human ACP, pituitary markers of terminal differentiation, such as *GH*, *TSH*β, *FSH*β were also down-regulated in the tumours (512 fold, 544 fold and 547 fold, respectively) (Figure 5-6). These results are consistent with published RNA and immuno-histochemical ACP expression data and support that the data set is robust and biologically meaningful (Buslei, Holsken et al. 2007, Holsken, Gebhardt et al. 2011, Andoniadou, Gaston-Massuet et al. 2012, Andoniadou, Matsushima et al. 2013, Gomes, Jamra et al. 2015, Gump, Donson et al. 2015).

To further understand the functional significance of the genes up-regulated in tumours, gene ontology analysis was performed. This analysis revealed that the 1000 genes most up-regulated in the tumours were enriched for ontologies relating to development of the skin (e.g. GO:00425288, keratinocyte differentiation, adjusted p-value = $2.43x10^{-20}$), tooth (e.g. GO: 0042476: odontogenesis adjusted p-value = $2.02x10^{-20}$) and hair (e.g. GO:0042633: Hair cycle, adjusted p-value $1.42x10^{-12}$) as well as the inflammatory response (GO:0006954, adjusted p-value= $8.52x10^{-12}$) (Supplementary Table 2, Figure 5-6b). Of note, skin, teeth and hair follicles are derived from embryonic non-neural ectoderm, and ACP is thought to derive from remnants of Rathke's pouch, an oral ectoderm derivative. This suggests that normal development of skin, hair follicle and tooth and the pathogenesis of human ACP may share common molecular mechanisms and is explored further in section 5.10.

Table 5-3: Top 15 most up-regulated genes in human ACP compared with controls.

Gene Symbol	Fold Change (log2)	Adjusted p-value
KRT75	10.88312	6.45E-34
KRT5	10.80425	1.01E-44
CALML3	10.41795	3.43E-33
KRT6C	10.38228	7.51E-26
KRT16	10.36806	3.28E-30
SERPINB5	10.366	5.63E-36
KRT14	10.31731	5.15E-37
KRT85	10.31375	5.44E-20
KRTAP3-1	10.30121	2.68E-25
COL17A1	10.2852	3.10E-35
KRT31	10.24653	2.75E-24
KRT6A	10.23574	1.15E-24
FDCSP	9.966995	1.56E-20
MSX2	9.957839	4.19E-48
KRT15	9.896415	1.01E-37

Table 5-4: Top 15 most down-regulated genes in ACP compared with controls.

Gene Symbol	Fold Change (log2)	Adjusted p-value
GH1	-9.0006	5.12E-12
TSHB	-9.08938	7.84E-10
FSHB	-9.09542	6.01E-12
C18orf42	-9.14156	1.56E-17
GHRHR	-9.18615	8.09E-19
HEPACAM2	-9.22051	2.93E-24
SCRT1	-9.2947	1.31E-34
GJD2	-9.33303	7.47E-26
POU1F1	-9.33816	4.41E-14
DGKK	-9.35132	1.96E-36
MS4A8	-9.36783	5.56E-67
BPIFA1	-9.3739	NA
NR5A1	-9.51748	1.48E-33
TRPC7	-9.63265	2.15E-20
CGA	-10.0933	5.31E-23

Figure 5-6: Differential expression results between tumours and controls. a) Bar plot of selected differentially expressed genes. Log2 fold change indicates expression in tumours compared with controls. Error bars = 1 standard error. b) Ancestor chart showing hierarchy of the top 20 enriched biological process ontology terms of the top 1000 most up-regulated genes in ACP compared with controls. Enriched ontologies are indicated by a coloured box. Note there are multiple enriched ontologies within the same hierarchies relating to tooth and skin development, the hair cycle and the immune response.

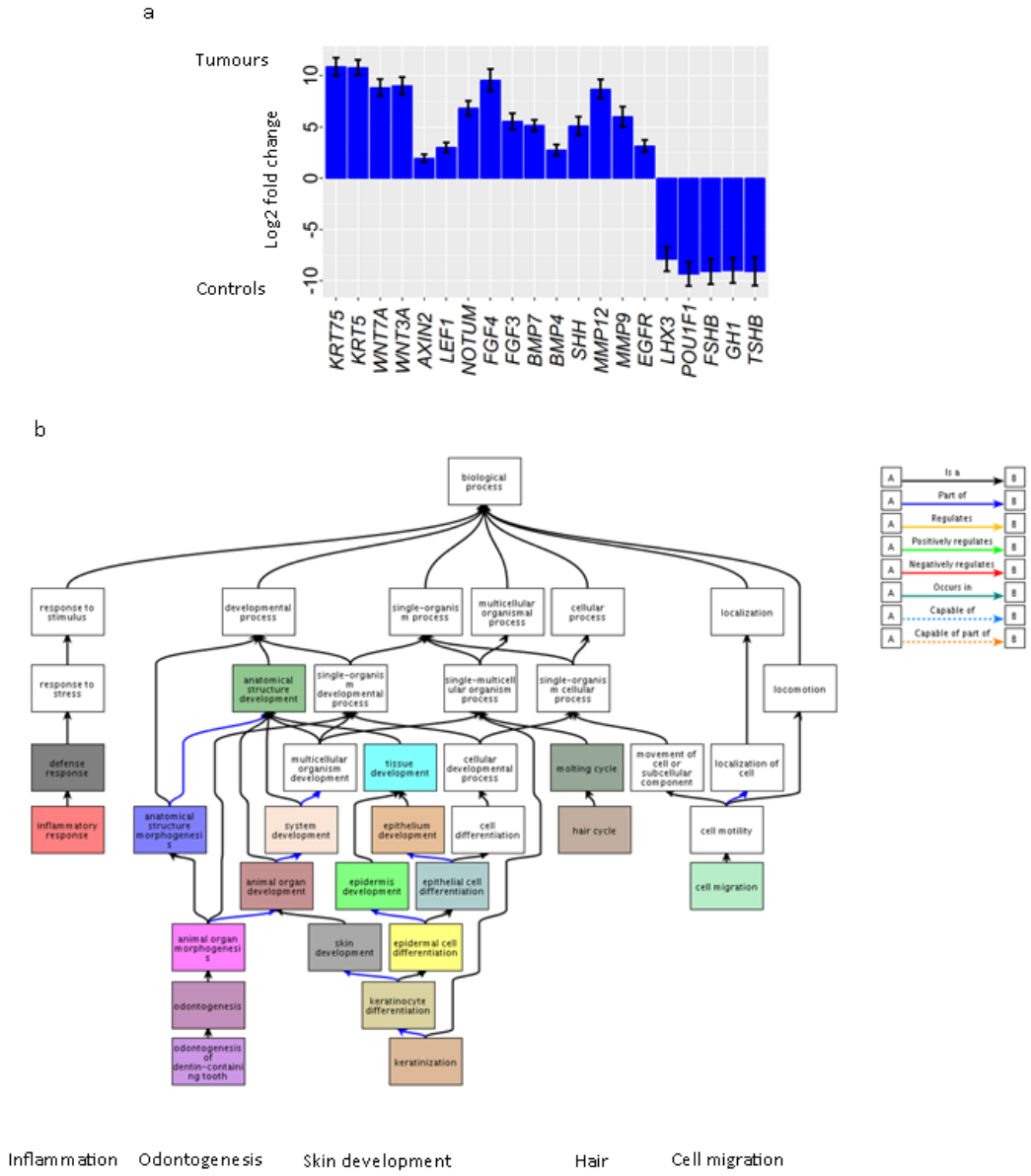

5.5.1 Differential expression within groups suggests complex reactive tissue comprising of nervous system and inflammatory components

In addition to performing differential expression between all tumours and controls, differential expression analyses were also performed between:

- High tumour content tumours vs controls
- Low tumour content tumours vs controls (fetal pituitaries only, as NFPA samples clustered across groups when analysis limited to low content tumours and were therefore excluded).
- High tumour content tumours vs low tumour content tumours

Full results are presented in Supplementary Table 2. As expected, genes expressed by high tumour content tumours in comparison with either controls, or low tumour content tumours, were enriched for genes relating to epidermis development, keratinocyte differentiation, odontogenesis and hair cycle and included Keratins, WNT targets, FGFs and other genes known to be expressed in ACP.

In contrast, genes expressed by low tumour content samples were enriched for genes relating to the immune response, (GO: 000695, adjusted p-value =2.91E-45) and nervous system development (GO:0007399, adjusted p-value= 1.91E-19) and included immune system genes, e.g. immunoglobulin heavy chains (e.g. IGHA1, 3700 fold up-regulated in low tumour content tumours compared with fetal pituitaries, 8 fold compared with high tumour content tumours), and glial markers such as GFAP (941 fold up-regulated compared with fetal pituitaries, 24 fold compared with high tumour content tumours). This suggests distinct processes and genes expressed within the reactive tissue component of these samples. This is further explored below using other approaches.

5.6 WGCNA identifies 12 modules of co-expressed genes

To further analyse patterns of gene expression across the cohort, I used an approach known as weighted gene correlation network analysis (WGCNA) (see Methods for full details). This identifies patterns of gene expression in a hypothesis-independent manner based on the Pearson correlation co-efficient of expression patterns between genes. These expression patterns can be statistically summarised as a vector (Eigen vector) and themselves correlated with sample characteristics, including diagnosis, percentage of tumour content, *CTNNB1* mutation allele frequency and the presence of specific histological features.

Analysis of the 5000 most variably expressed genes across all samples by WGCNA identified 12 distinct groups, each one containing between 69 and 958 genes sharing similar expression patterns. These were each assigned a colour as a reference/name and will be referred to hereafter as modules (Figure 5-7, Table 5-5)

I confirmed that each module had a specific expression pattern through plotting expression heatmaps of all the genes within each module (Figure 5-8). The relationship of modules was also plotted on a multidimensional scale plot where genes were annotated by the colour of the module to which they belonged (Figure 5-7). This showed three major distinct patterns of gene expression across the samples, the brown, blue/dark turquoise and magenta modules with the green module overlapping blue/dark turquoise and brown modules.

5.6.1 Modules are preserved in an independent dataset

WGCNA was also performed on the human ACP microarray data published by Gump *et al.* to assess whether the co-expression modules observed in our cohort were also present in this independent data set (Gump, Donson et al. 2015). Of the 5000 genes included in our WCGNA analysis, the expression patterns of 2963 were available but the other genes were not present in the microarray data provided (Gump, Donson et al. 2015). Multidimensional scale plotting and hierarchical clustering of the genes expression patterns showed consistency with the modules identified in our cohort (Figure 5-7). Moreover, statistical assessments of module preservation, which measure how well patterns of gene co-expression are maintained in independent sample sets, revealed a strong preservation of the brown, blue, magenta, pink and green modules between the two data sets (Zsummary > 10) and weak to moderate preservation for the others (Zsummary 2-10) (Figure 5-7).

These analyses demonstrate that the patterns of gene expression that we have identified in our RNA-Seq data are also present in an independent dataset, and therefore of likely biological significance.

5.6.2 Modules correlate with specific tumour cell compartments:

Next, I explored further this modular analysis in an attempt to establish whether specific modules may correlate with phenotypic information. Heatmaps identified that patterns of gene expression correlated with sample information. To further investigate this, I performed correlation analysis between the module eigen vectors and phenotypic information. This identified that the brown module showed the strongest positive correlation with histological tumour content ($r=0.88$, $p=1x10^{-8}$) and *CTNNB1* mutational allelic frequency ($r=0.89$, $p=4x10^{-9}$) (Figure 5-9). Inspection of the module expression heatmap confirmed that the genes of this module exhibited the highest expression in those tumour samples with the most tumour content and greatest *CTNNB1* mutational allelic frequency and the lowest expression in controls and JA005 and JA011 (Figure 5-8). Moreover, the genes included in this module were enriched for functions related to WNT pathway activation, as well as odontogenesis, hair cycle and development of the epidermis ($p< 7x10^{-10}$) (Supplementary Table 3).

In contrast, the blue and dark turquoise modules were highly correlated with the presence of glial reactive tissue and showed enrichment of genes related to central nervous system development (blue: $r=0.93$, $p=3x10^{-11}$; dark turquoise: $r=0.68$, $p=3x10^{-4}$) (Supplementary Table 3). This suggests that this module contains genes expressed by the reactive brain tissue within the tumour samples, an idea supported by the strong correlation with *GFAP* expression ($r=0.94$, $p=6x10^{-12}$), a known marker of astrocytes representing glial tissue infiltrated by ACP. The magenta module was enriched for genes related to the immune response and correlated with the expression of immune cell markers such as *CD14* ($r=0.97$, $p=1x10^{-14}$) and *CD3E* ($r=0.87$, $p=3x10^{-8}$).

Together, these *in silico* analyses suggest that most of the identified modules represent expression patterns relating to specific functions of particular cell types within the tumour samples. Therefore, they could provide insights into the molecular signatures of specific cell compartments. I next discuss individual modules in further detail.

Table 5-5: Summary of WGCNA modules

Module	Number of genes	Expression pattern	Ontology Enrichment	Comment
Brown	829	High expression in tumours with high tumour content/*CTNNB1* allele frequency	Skin development, Odontogenesis, hair cycle and WNT signalling	Represents genes expressed by tumour epithelia, e.g. *BCL11B*
Black	394	Highest expression in ACPs with prominent wet keratin	Keratinisation	Includes keratins, keratin associated proteins and enamel genes and proteinases (e.g. *AMELX, ENAM, MMP20*)
Dark grey	69	High expression in tumours with high tumour content/*CTNNB1* allele frequency	Skin development and cell jucntions	
Magenta	958	Low in controls, Variable expression across ACP samples	Immune response	Includes immune cell markers (e.g. *CD14*) and pro and anti-inflammatory cytokines (e.g. *TNF, IL10*)
Blue	793	High in those ACP tumours with reactive glial tissue	Nervous system development	Includes glial genes *GFAP*, *S100B*. Enriched for signature of astrocytes
Dark turquoise	338	High in those ACP tumours with reactive glial tissue and fetal pituitaries	Nervous system development	Includes *NKX2.2*. Enriched for oligodendrocyte lineage gene sets
Green	730	High in those ACP tumours with reactive glial tissue, fetal pituitaries and NFPA	Microtubules and cilia	
Light yellow	89	High in fetal pituitaries and some ACP	Extracellular matrix	
Pink	443	High in controls	Hormone signalling	
Cyan	133	High in fetal pituitaries	Cell cycle	Fetal pituitaries are known to be highly proliferative
Light green	93	High in fetal pituitaries and one NFPA	Hormone signalling	
Grey	131	Majority of no genes show no pattern, a small subset are expressed based on sex		

Figure 5-7: WGCNA Module detection and preservation: a) Network heatmap plot. Heatmap of the adjacency measure of the 5000 most variably expressed genes. Dendrograms show the hierarchical clustering of genes which are annotated as modules by colour bar. In the heatmap, high co-expression is indicated by more saturated colour b) Multidimensional scaling plot of expression patterns of the 5000 most variably expressed genes. The colour of each gene indicates it membership to a co-expressed gene expression module. c) Hierarchical clustering of module eigengenes, e.g. brown, dark grey and black modules have similar expression patterns d) Multi-dimensional scaling of the expression pattern 2963 matched genes from Gump *et al*, 2016 annotated with the colours of module identified in the UCL cohort. e) Hierarchical clustering of the expression pattern of the genes in both UCL and Gump et al cohorts annotated by module colour. f) Assessment of module preservation in the dataset of Gump *et al*., 2016. Modules are plotted by colour. Values over 10 (green line) indicate strong evidence module is preserved. Values between 2 (blue line) and 10 indicate weak to moderate evidence of preservation. The pink, magenta, brown, blue and green are the most preserved modules. The cyan module is the least preserved. This represents cell cycle genes expressed by proliferating fetal pituitary tissue. As the normal pituitary tissue analyzed in Gump *et al*., 2016 is adult, it is expected that this module would be the least preserved

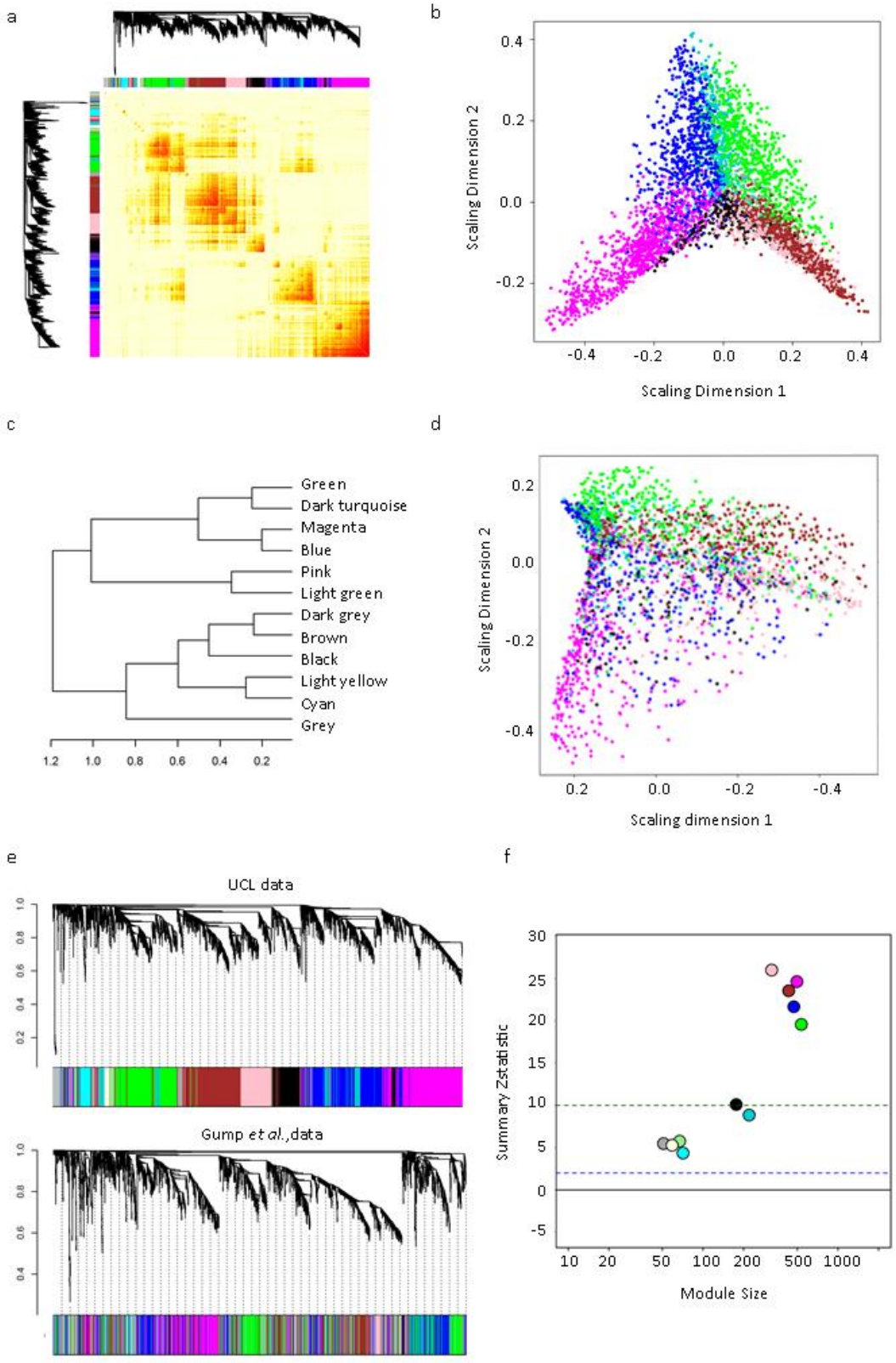
a
b
Scaling Dimension 2
Scaling Dimension 1
c
Green
Dark turquoise
Magenta
Blue
Pink
Light green
Dark grey
Brown
Black
Light yellow
Cyan
Grey
d
Scaling Dimension 2
Scaling dimension 1
e
UCL data
Gump et al., data
f
Summary Zstatistic
Module Size

Figure 5-8: Heatmaps of WGCNA modules. Heatmaps of variance stabilised counts of genes within each module. Heatmaps are scaled by row highlighting patterns of expression, scale represents row Z-score with high expression in yellow, and low expression in red. Where relevant samples are also annotated with phenotypic information.

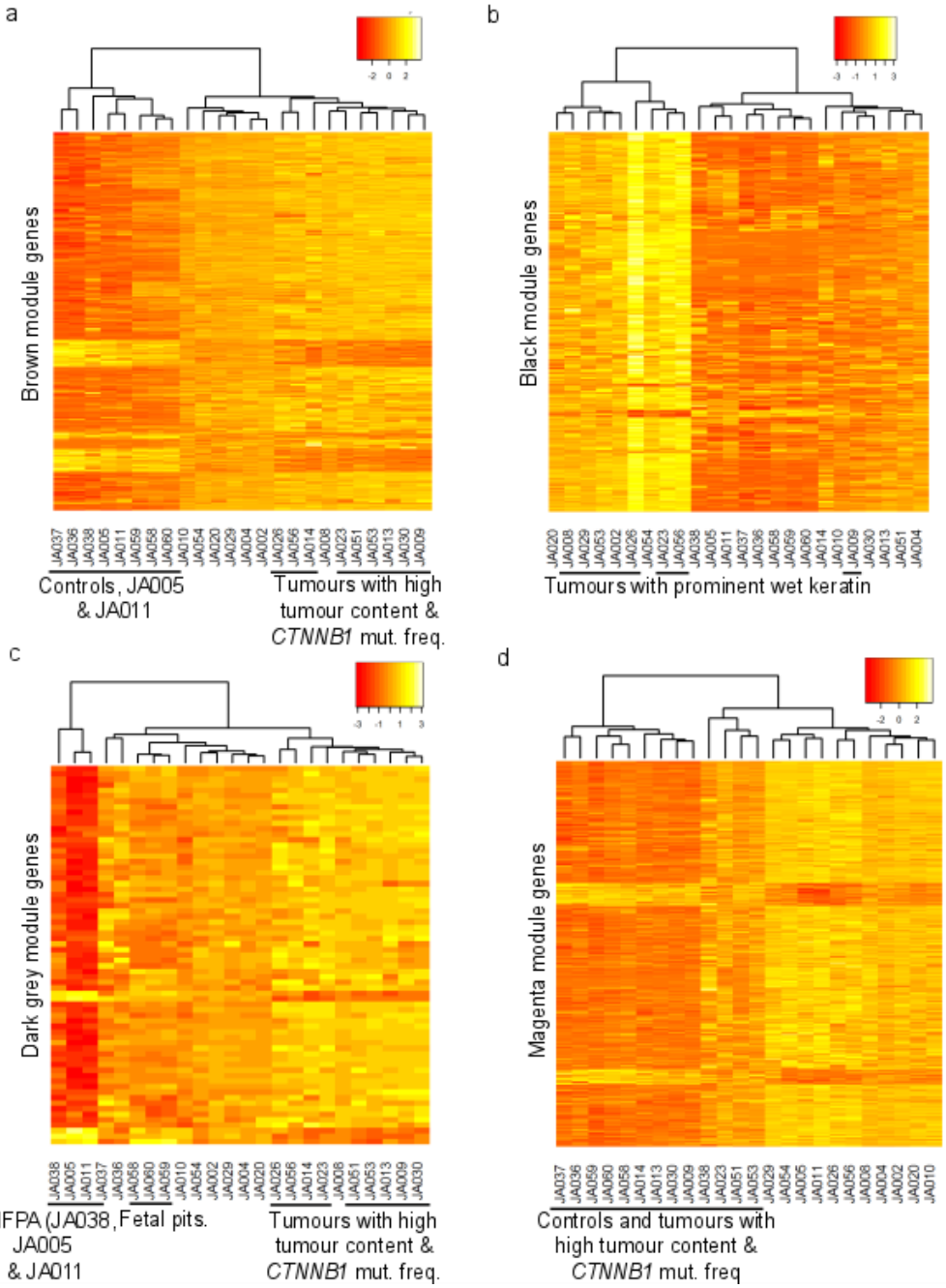

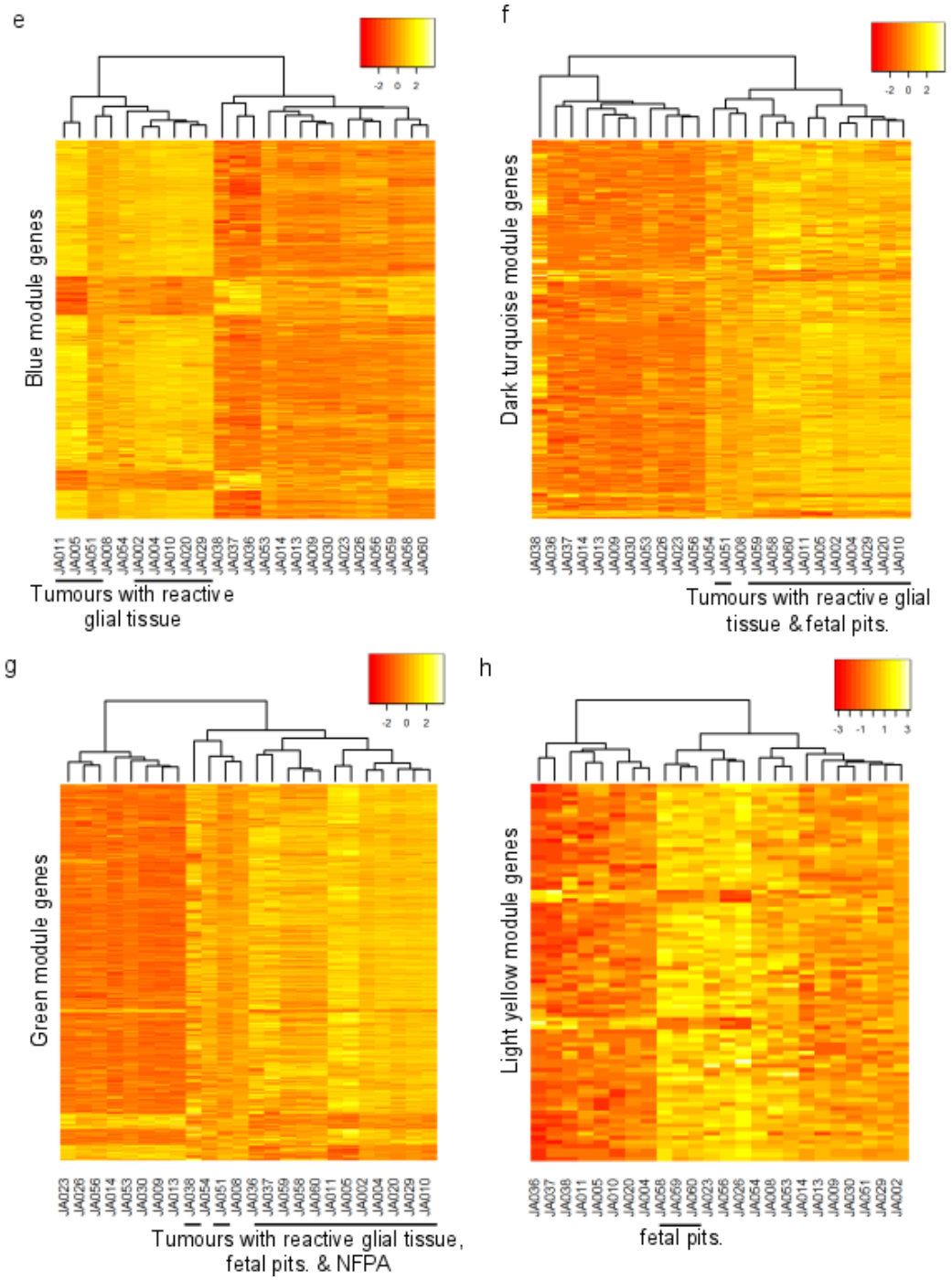
e
Blue module genes
-2 0 2
JA011 JA005 JA051 JA008 JA054 JA002 JA004 JA010 JA020 JA029 JA038 JA037 JA036 JA053 JA014 JA013 JA009 JA030 JA023 JA026 JA056 JA059 JA058 JA060
Tumours with reactive glial tissue
f
Dark turquoise module genes
-2 0 2
JA038 JA036 JA037 JA014 JA013 JA009 JA030 JA053 JA026 JA023 JA056 JA054 JA051 JA008 JA059 JA058 JA060 JA011 JA005 JA002 JA004 JA029 JA020 JA010
Tumours with reactive glial tissue & fetal pits.
g
Green module genes
-2 0 2
JA023 JA026 JA056 JA014 JA053 JA030 JA009 JA013 JA038 JA054 JA051 JA008 JA036 JA037 JA059 JA058 JA060 JA011 JA005 JA002 JA004 JA020 JA029 JA010
Tumours with reactive glial tissue, fetal pits. & NFPA
h
Light yellow module genes
-3 -1 1 3
JA036 JA037 JA038 JA011 JA005 JA010 JA020 JA004 JA058 JA059 JA060 JA023 JA056 JA026 JA054 JA008 JA053 JA014 JA013 JA009 JA030 JA051 JA029 JA002
fetal pits.

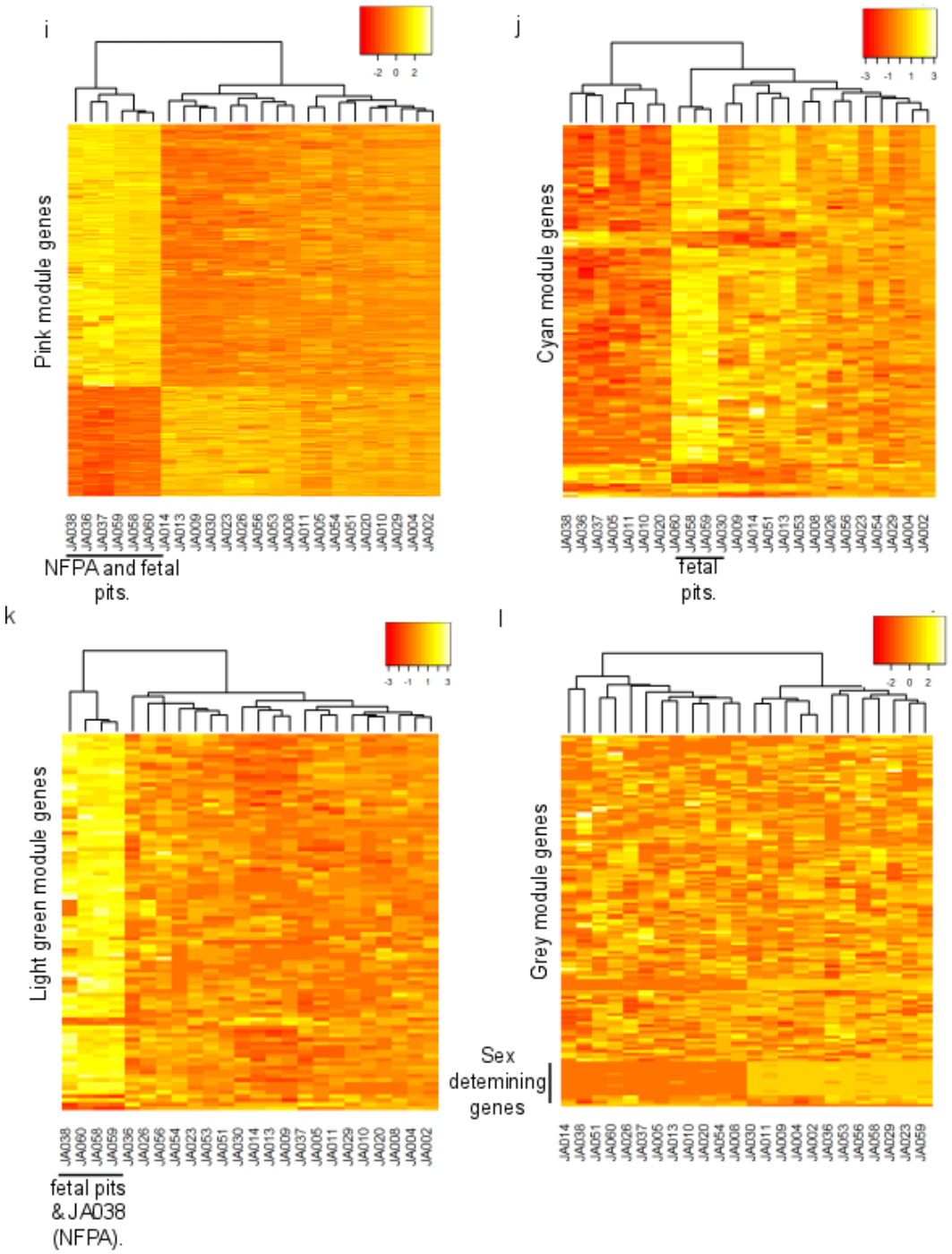
i
Pink module genes
NFPA and fetal pits.
j
Cyan module genes
fetal pits.
k
Light green module genes
fetal pits & JA038 (NFPA).
l
Grey module genes
Sex determining genes

Figure 5-9: Heatmap of correlations between each module's eigengenes and phenotypic information. Scale bar indicates r-value -1 to +1. For instance, the brown module shows a strong correlation with tumour content and mutational frequency, whilst the blue module correlates with the presence of glial reactive tissue and GFAP. A summary of ontology enrichment analysis for each module is highlighted. NB the grey module includes genes not fitting into a specific co-expression module.

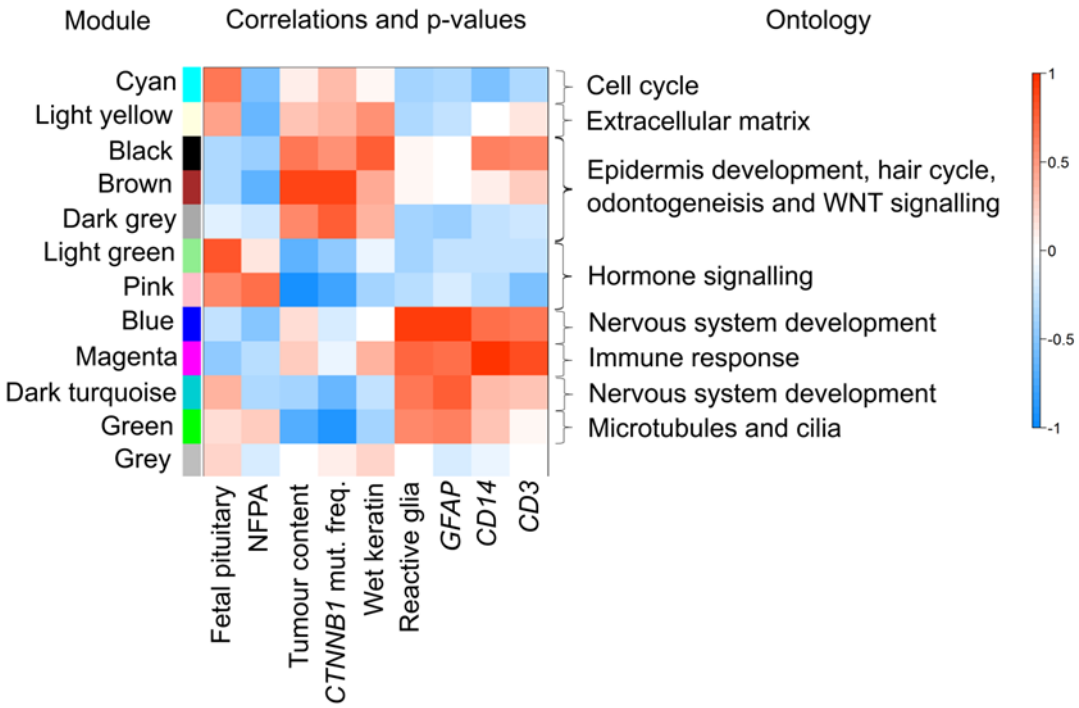

5.7 Expression of novel ACP genes in tumour epithelium identified by WGCNA and laser capture microdissection

5.7.1 The brown module identifies novel ACP genes expressed within tumour epithelium

Given the strong positive correlation of the brown module with tumour content and *CTNNB1* mutation allele frequency, it could be expected that this module includes genes and pathways known to be dysregulated in human ACP, as well as other yet unidentified genes.

First, I identified the three genes with the strongest module membership, a measure of the degree of co-expression. This revealed *APCDDL1, BCL11B*, and *TP63* as the most co-expressed genes. Plotting the normalised expression levels against the *CTNNB1* mutation allele frequency confirmed the relationship of these brown module genes with *CTNNB1* mutation allele frequency, further supporting that these genes are expressed exclusively within the tumour cells (r=0.83, 0.95, 0.96 respectively for each gene, $p<1x10^{-5}$) (Figure 5-10). Expression of TP63 has previously shown to be widespread throughout the tumour tissue in human ACP, but *APCDDL1* and *BCL11B* are genes not previously associated with human ACP (Momota, Ichimiya et al. 2003, Cao, Lin et al. 2010, Esheba and Hassan 2015). Immunostaining of ACP histological sections revealed the expression of BCL11B and TP63 exclusively in tumour cell compartments, including clusters, palisading epithelium and stellate reticulum, but not within surrounding reactive tissue (Figure 5-10). The expression of *APCDDL1* was not investigated due to the absence of a specific antibody.

Having validated that the brown module genes are expressed in tumour tissue, I interrogated which genes were included within this module. This included WNT targets (including *AXIN2, NOTUM),* consistent with WNT pathway activation within the tumour. In addition to genes previously shown to be expressed in ACP (e.g. *FGF3, FGF4, BMP4, EGFR*), others not previously implicated in ACP (e.g. *APCDDL1,*

BCL11B, and many others included in Supplementary Table 2a) were also identified within this module (Full module list in Supplementary Table 2a).

Figure 5-10: Brown module. a) Scatter plots of normalised expression counts for *APCDD1L, BCL11B* and *TP63* with *CTNNB1* mutation allele frequency. Note the significant correlation between gene expression and mutation allele frequency. b) Double immunofluorescence staining against BCL11B and TP63 with β-catenin in ACP showing expression in all tumour cells (including clusters) but not in reactive glial tissue. Scale bars indicate 100µm.

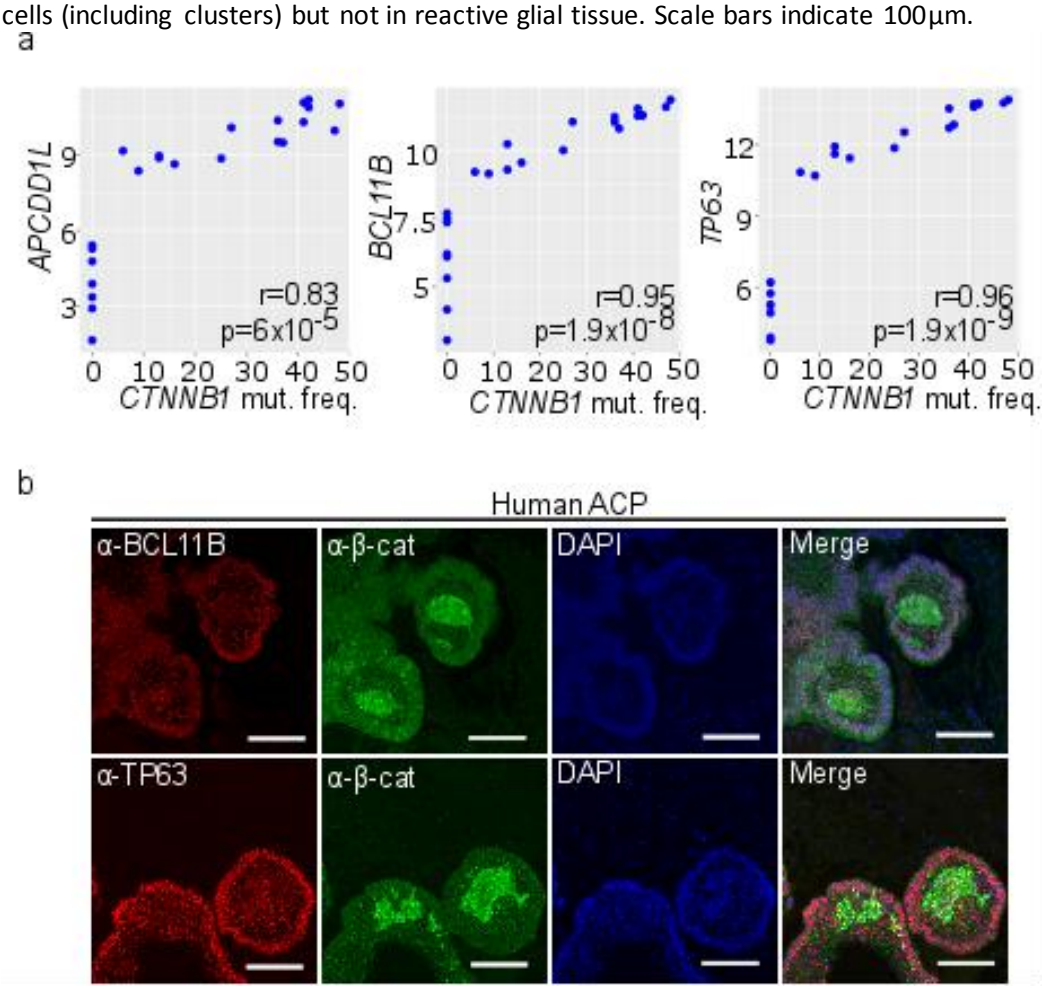

5.7.2 Laser capture microdissection reveals genes expressed by tumour epithelium

Next, I integrated the results of the WGCNA with those results of the RNA sequencing of LCM tissue compartments of cases JA004 and JA0029. First I performed Principal Component Analysis of this data set, which revealed grouping of different cell populations (i.e. clusters (C), palisading epithelium (NC) and glial (G) tissue), confirming the success of the experimental approach (Figure 5-11).

To assess which genes were expressed within the tumour epithelia, differential expression analysis was performed between tumour (C+NC) and reactive glial (G) components (Full results Supplementary Table 2).

This identified up-regulation of 2347 genes in tumour compartments compared with glial tissue and 1406 genes up-regulated in glial tissue (adjusted p-value <0.1). WNT inhibitor *DKK4* was the most up-regulated gene in tumour tissue (9881 fold). Other genes up-regulated in tumour tissue included keratins (e.g. *KRT18*, 3884 fold). Gene ontology enrichment of the 1000 genes most up-regulated in tumour compartments revealed the most enriched ontology was tooth mineralisation, GO:0034505 (p-value 4.84x10-5) however this was non-significant after adjusting for multiple testing (adjusted p-value 0.48) (Supplementary Table 2). Further additional pairwise differential expression analyses from this data set are presented later (Section 5.11)

5.7.3 Validation of WGCNA by laser capture microdissection

Using the LCM data it was possible to validate the results of the WGCNA modular analysis, confirming that brown module genes were expressed in the tumour epithelium. This was performed using Gene Set Enrichment Analysis (GSEA), a tool that explores the distribution of genes of interest, (a so called gene set, e.g. targets of a signalling pathway), within a list of ranked genes (e.g. by differential expression between two conditions). Genes were ranked from highest expression in the LCM tumour compartments to highest in the reactive glial tissue. This analysis confirmed the expression of brown module genes predominantly in the tumour compared

with reactive glial tissue (normalised enrichment score (NES) = 2.24, false discovery rate (FDR) <0.001) (Fig. 3d).

This, and the immuno-histochemical validation, gives confidence in the interpretation of the brown WGCNA module as representing tumour tissue compartments.

Figure 5-11: Laser capture microdissection and RNA sequencing of ACP. a) PCA of the 500 most variably expressed genes showing grouping of clusters (C), non-clusters (NC) and glial (G) tissue. b) GSEA barcode plot showing enrichment of brown genes within the expression signature of tumour compartment and c) the blue and dark turquoise modules in the reactive glia. d) Immunohistochemistry of GFAP showing GFAP positive cells in sample JA004, but not JA030. NES = normalised enrichment score, FDR = false discovery rate

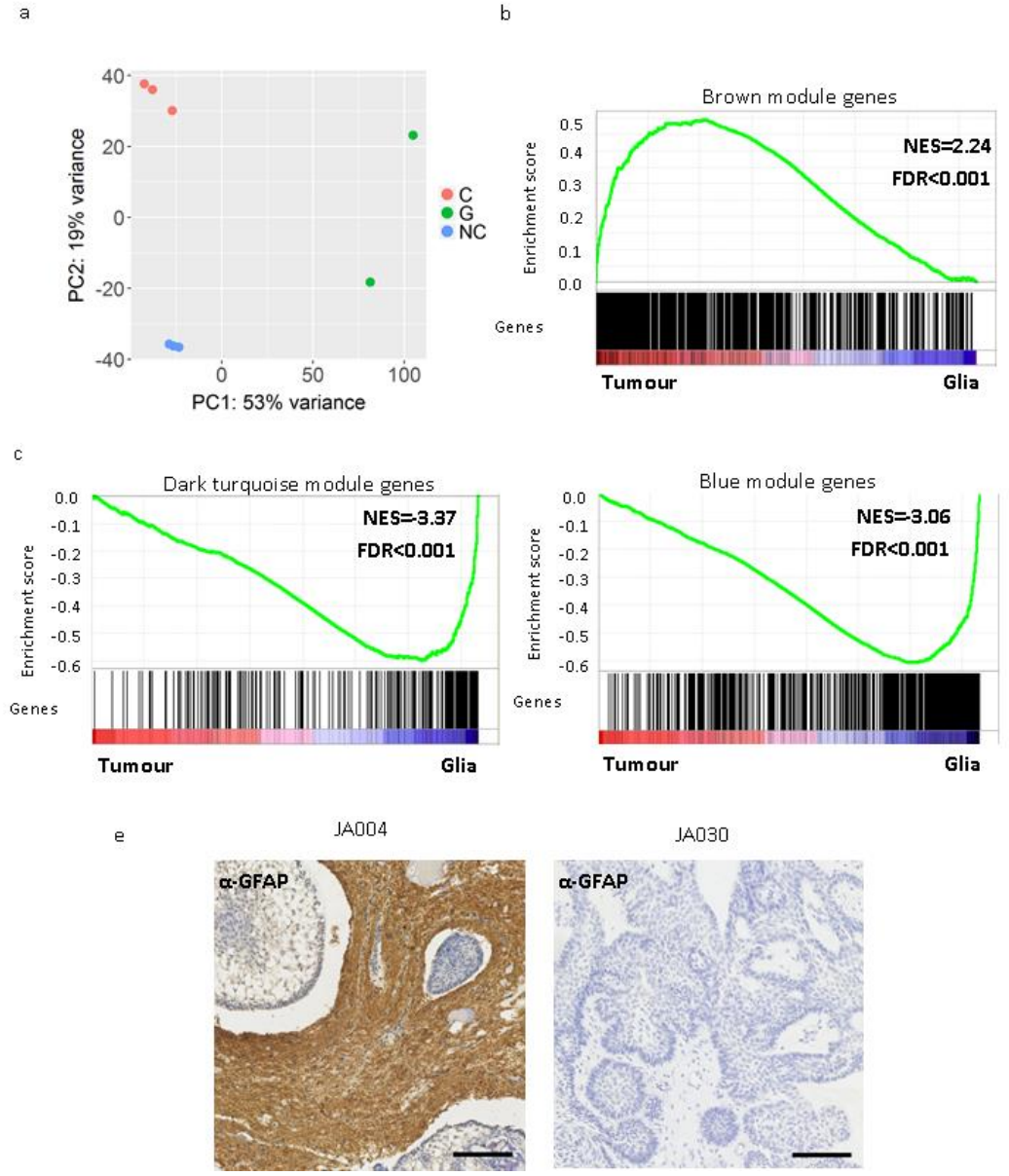

Table 5-6: Top 15 most up-regulated genes in tumour compared with glial tissue

Gene Symbol	Fold Change (log2)	Adjusted p-value
DKK4	13.27046942	9.78E-10
TSPAN8	12.0799091	1.38E-08
KRT18	11.92333508	2.34E-08
CXADR	11.36100456	2.97E-07
MFAP2	11.26188379	1.00E-07
NA*	11.19452436	6.21E-07
ZNF410	11.12581236	2.75E-07
SDC1	11.05399877	3.14E-14
SMYD2	10.97945649	4.28E-07
ST6GALNAC2	10.89742087	4.62E-07
PVRL1	10.83354123	1.26E-06
SLC25A39	10.82869648	1.13E-06
GPX2	10.79301045	4.45E-06
PTGES2	10.73801215	1.21E-06
APTR	10.70799631	2.11E-06

*NA = entrez gene 100507493, no gene symbol available.

Table 5-7: 15 most down-regulated genes in tumour compared with glia (i.e. up-regulated in glia)

Gene Symbol	Fold Change (log2)	Adjusted p-value
CSPG5	-12.66308699	1.44E-08
KCNQ2	-12.67096627	1.74E-08
GALNT15	-12.71242125	2.20E-08
COL9A1	-12.77243047	3.93E-11
GRIK3	-12.866078	1.44E-08
GBP4	-12.99939861	2.85E-09
PKNOX2	-13.09868603	5.22E-09
CADM2	-13.1116304	3.72E-13
TM4SF18	-13.12830032	1.70E-09
OLIG1	-13.160598	5.37E-14
SCN1A	-13.21634549	2.99E-09
MRO	-13.40441549	1.93E-09
LRP1B	-13.53237844	9.04E-10
LHFPL3	-14.30087614	2.80E-11
FABP7	-14.6219676	1.04E-11

5.8 The reactive glial tissue has signature of both astrocyte and oligodendrocyte lineages

Both the blue and dark turquoise modules, which closely correlated with the presence of glial tissue, were enriched for genes implicated in central nervous system development (Figure 5-9). This suggests that these genes are expressed by the reactive glial component of the specimen. This was also supported by laser capture microdissection and GSEA (blue module NES -3.37, FDR<0.001, dark turquoise module NES = -3.06 FDR<0.001) (Figure 5-11).

Gene expression heatmaps confirmed that genes within each module were highly expressed by tumours with glial tissue (Figure 5-8). However their expression varied across the control tissues. Blue module genes were only highly expressed in tumours with glial tissue, whereas dark-turquoise genes were also highly expressed in fetal pituitaries (Figure 5-8). This suggests that the genes in these modules may indicate different biological functions.

Genes with strong membership of the blue module included the astrocytic markers *S100B* and *GFAP,* whose expression in reactive glial tissue was confirmed immune-histochemically (Figure 5-11). In contrast, the gene with the highest module membership score for the dark turquoise module is *NKX2.2*, a transcription factor involved in oligodendrocyte differentiation, suggesting these modules represent different glial cell types [65]. Barcode plots of each module with published gene sets of genes specifically up-regulated in different glial, neuronal and endothelial components shows the blue module being more enriched for astrocyte genes (enrichment score (ES)= 3.3, p=0.0001) and the dark turquoise for oligodendrocyte lineage genes (oligodendrocyte precursor cells ES=3.4, $p=6.8x10^{-5}$, newly formed oligodendrocytes ES=3.9, p=0.0012, myelinating oligodendrocytes ES=3.5, $p=5.7x10^{-5}$) [65] (Supplementary Fig. 6c). Together this suggests that both astrocyte and oligodendrocyte lineage genes are expressed within the reactive glial tissue of ACP tumours with a proportion, predominantly oligodendrocyte genes, also expressed in the developing pituitary, possibly the posterior lobe.

Figure 5-12: Barcode plots of blue and dark turquoise modules with gene sets of genes expressed by differing cell types within the central nervous system. Genes were ranked by their membership of either the blue or dark turquoise modules and the presence of genes in published gene sets corresponding to different glial cell types are plotted as vertical lines. The top part of the graph shows the enrichment at each part of the ranked list, the higher the value the greater the enrichment. For instance, for astrocytes the majority of the lines are at the left hand of the plot indicating they are among the most connected members of the blue module. The astrocyte signature has a greater enrichment in the blue module compared with dark turquoise, whereas for the OPCs it is more enriched in the dark turquoise module. OPC = oligodendrocyte precursor cell, NFO = newly formed oligodendocyte, MO = myelinating oligodendrocyte.

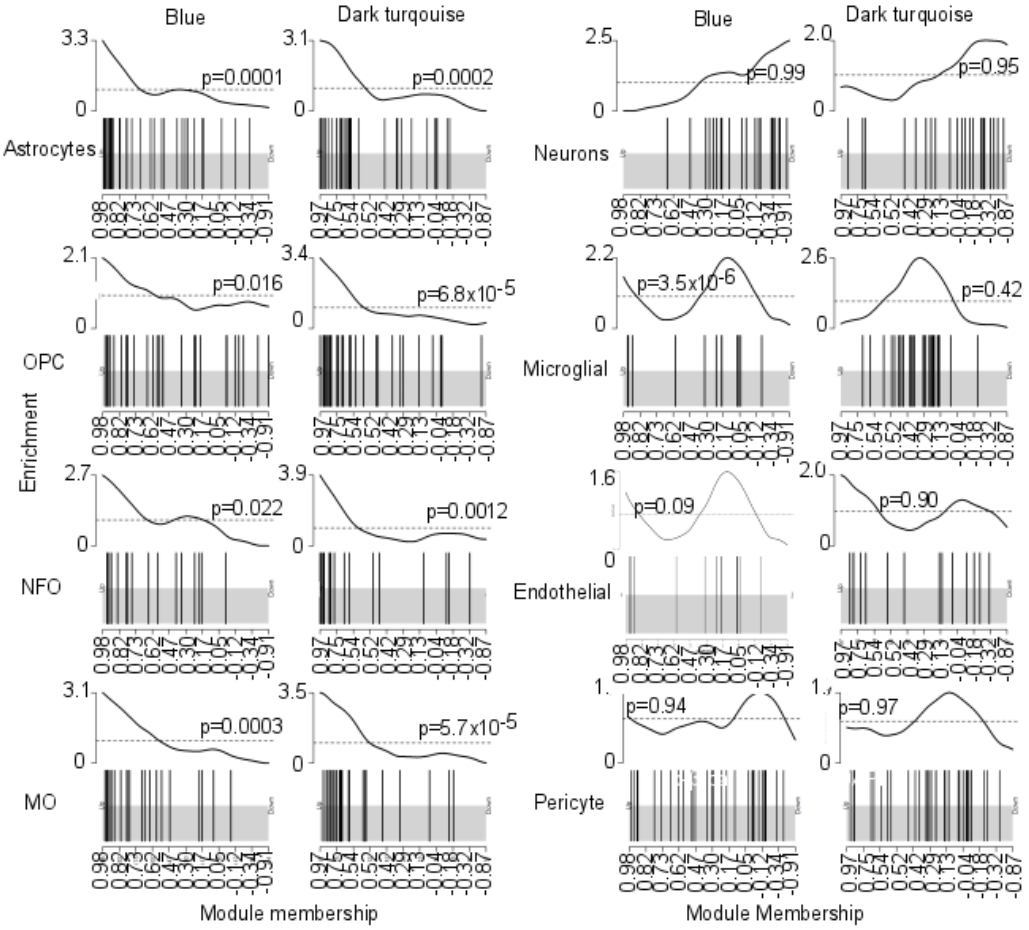

5.9 Other WGCNA modules

5.9.1 Black and dark grey modules

Similar to the brown module, WGCNA analysis showed that the black module also correlated with tumour content ($r=0.65$, $p=6x10^{-4}$) and in addition, with the presence of wet keratin ($r=0.73$, $p=5x10^{-5}$) (Figure 5-9). The heatmap showed the highest expression of the black module genes predominantly in those tumour cases where wet keratin had been identified (Figure 5-8). This module includes several keratins, keratin associated proteins and of particular note enamel proteins (*ENAM, AMELY, AMELY, AMBN*) and proteinases (*KLK4, MMP20*).

Likewise, the dark grey module also correlated with *CTNNB1* mutation allelic frequency ($r=0.78$, $p=6x10^{-6}$), but some genes were also expressed in control tissues (Figure 5-8). This was enriched for genes relating to cell junctions. Among the brown, black and dark grey module, the brown module is more likely to specifically represent the molecular signature of the tumour cell compartment, hence excluding host-derived reactive tissue.

5.9.2 Green module

The green module genes are expressed by tumours with glial tissue and also by control tissues (Figure 5-8). Expression correlated inversely with tumour content ($r=-0.9$, $p=2x10^{-9}$) and broadly with *GFAP* expression ($r=0.64$, $p=8x10^{-4}$) and was enriched for genes of microtubules and cilia (Figure 5-9, Supplementary Table 3).

5.9.3 Pink, cyan and light green modules: signatures of control tissues

Genes of the pink, cyan and light green modules are expressed by the fetal pituitaries and/or NFPA and were enriched for genes related to hormone processing and release (pink, light green) or cell cycle (cyan), which are cellular processes relevant to these control tissues (Supplementary Table 3).

5.9.4 Light yellow module

Genes in this module were expressed by fetal pituitaries and variably across ACPs (Figure 5-8h). Genes included collagen and extracellular matrix genes and may reflect contamination of fetal pituitary samples with surrounding connective tissue (e.g. cartilage).

5.9.5 Grey module

The grey module contains the remaining 131 genes that could not be grouped into a distinct co-expression module. Within this module was a small number of sex determining genes, e.g. *XIST*

5.9.6 Magenta module

The magenta module is considered in detail in section 5.16.

5.10 Expression analysis highlights the close relationship of ACP with tooth development.

Odontogenesis is a recurrent theme in several of the ontology analyses. In addition, both the black and the brown modules, which correlate with tumour but not glial tissue, include several genes that are required for normal tooth development. For instance, enamel protein genes *(*e.g. *AMELX, AMBN* and *ENAM*), ameloblast secreted proteinases *(MMP20* and *KLK4)* and the odontogenic ameloblast-associated protein gene *ODAM* were contained within the black module, expressed in association with wet keratin. Likewise, many transcription factors required for inner enamel epithelium/ameloblast differentiation such as *BCL11B*, *TP63*, *MSX2, DLX* family members and *SP6*, were part of the brown module.

5.10.1 Ameloblast genes are up-regulated in ACP

Differential expression analysis confirmed a significant up-regulation of these ameloblast-related genes in ACP tumours compared with control tissue (Figure 5-13) [16]. In contrast, *MSX1*, a regulator of odontoblast differentiation and the odontoblast specific gene *DSPP*, encoding dentin sialoprotein, were not up-regulated in ACP tumours (Figure 5-13).

To further investigate the molecular connection between ACP tumourigenesis and amelogenesis, we used publicly available lists of genes experimentally confirmed in human or other species to be expressed in the inner enamel epithelium and ameloblasts. This found a significant enrichment of these genes in ACP tumours compared with control tissue by gene set enrichment analysis (NES= 2.79 and 2.57 respectively, FDR<0.001) (Fig. 5b) (Helsinki 1996-2007). This evidence suggests that the gene expression programme that is triggered during normal ameloblast induction and differentiation is also activated in the tumour cells in human ACP.

Despite the proposed common origin of ACP and PCP (i.e. oral ectoderm derivatives), histological similarities have been observed between ACP, odontogenesis and odontogenic tumours, but no such similarity has been reported for PCP (Paulus, Stockel et al. 1997, Louis, Ohgaki et al. 2016).

To explore further the degree of molecular connection between PCP and odontogenesis, we analysed the expression of ameloblast and odontoblast genes in ACP relative to PCP (rather than to control tissue as previously performed) using data from Holsken *et al.,* 2016 (Holsken, Sill et al. 2016). This analysis showed the up-regulation of enamel genes, ameloblast secreted proteinases and several DLX transcription factors specifically in ACP (Fig. 5c). GSEA confirmed that a proportion of amelogenesis-related genes were overall up-regulated in ACP compared with PCP, though many were not differentially expressed (IEE, NES=1.30 FDR=0.29, ameloblast genes, NES=1.20, FDR=0.20) (Figure 5-13).

5.10.2 *BCL11B* and *MSX2* Expression

BCL11B and *MSX2*, two critical regulators of ameloblast development, were highly up-regulated in ACP compared with control (15 fold and 995 fold) and only modestly up-regulated in ACP compared with PCP (1.7 fold and 3.8 fold respectively), suggesting that they may be expressed also in PCP tumours. To assess this possibility, we performed immunohistochemistry with specific antibodies. Having previously confirmed the presence of BCL11B in ACP we confirmed the presence of BCL11B in PCP (Figure 5-10, Figure 5-13). Specifically, BCL11B expression was widely observed in ACP tumour cells, and predominantly the basal epithelial layers of PCP. MSX2 expression (performed by Annett Holsken) was broadly expressed in tumour cells in both ACP and PCP (Fig. 5e). Therefore, although overall ACP has a greater signature of ameloblast development, particularly the expression of enamel genes, there is a partial overlap between ACP and PCP tumourigenesis.

Figure 5-13: Expression of tooth related genes in ACP. Differential expression of tooth related genes in a) ACP compared with controls and b) ACP compared with PCP. Error bars = 1 standard error. Gene set enrichement analysis plots of genes expressed in inner enamel epithelium (IEE) and ameloblasts in ACP compared with c) controls, d) PCP, e) *BCL11B* expression in PCP, f) *MSX2* expression in ACP and PCP.

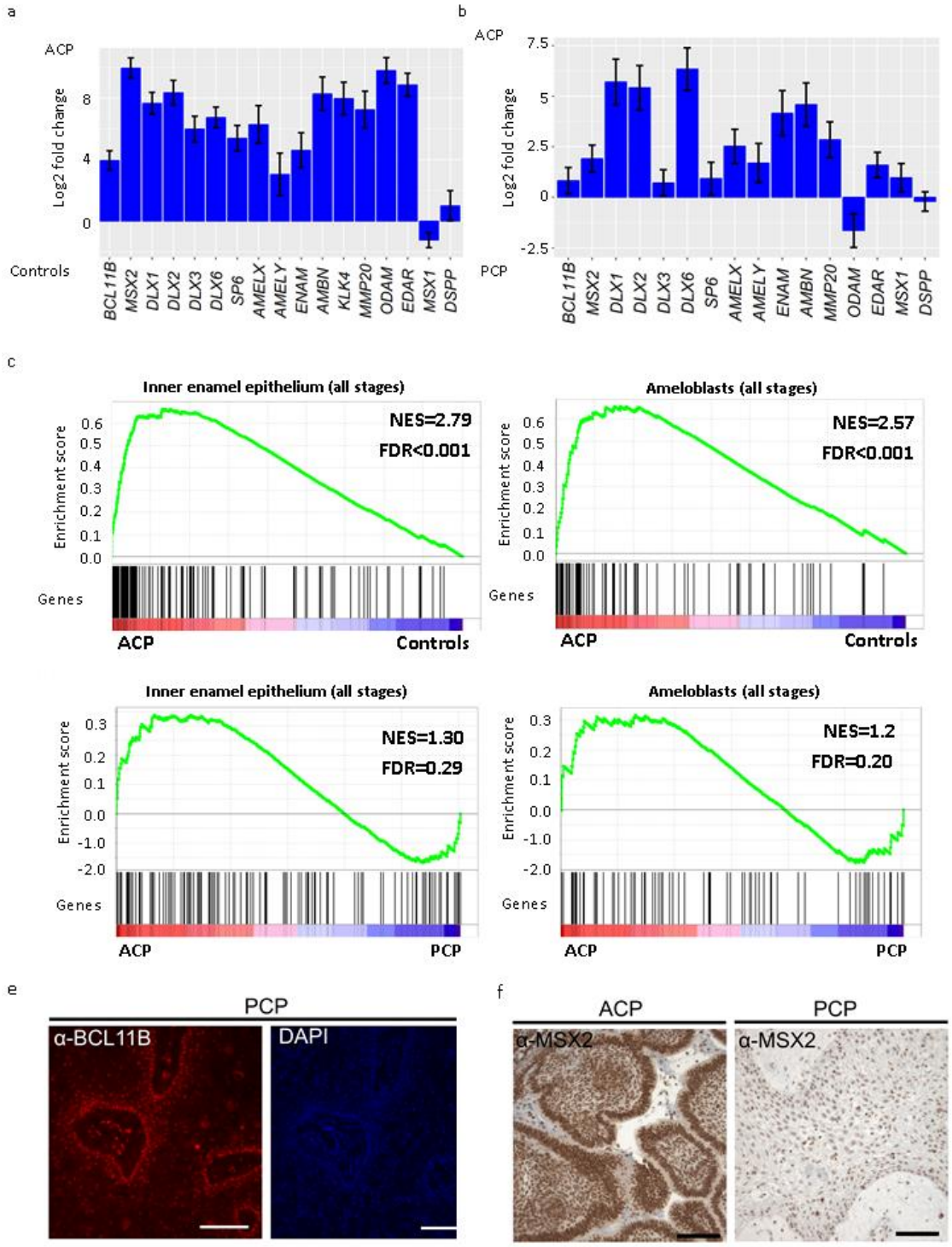

5.11 Laser capture microdissection reveals signature of clusters

To investigate the molecular signature of clusters, differential expression analysis was performed between clusters and palisading epithelium. This identified 647 genes up-regulated in clusters compared with palisading epithelium and 310 in palisading epithelium compared with clusters. The most up-regulated genes in clusters were *CHRNA3*, *GAD1* and *CA6* (1696, 1009 and 495 fold, respectively). Genes up-regulated in clusters were enriched for genes relating to cell migration (GO:0016477, adjusted p-value 0.000144). This is consistent with data from Stache *et al.*, where it was proposed that clusters play an active role in invasion/infiltrative behaviour of human ACP in a xenograft murine model, and with the distribution of clusters at the leading edge of tissue invasion as discussed in Chapter 3 (Andoniadou, Gaston-Massuet et al. 2012, Stache, Holsken et al. 2015).

Genes up-regulated in palisading epithelium were enriched for ontologies of extracellular matrix (GO:0031012) (adjusted p-value 1.98x10-7) and tissue development (GO:0009888, adjusted p-value 4.13x10-6).

5.11.1 Clusters exhibit transcriptional signature of WNT pathway activation

Clusters are characterised by their nuclear accumulation of β-catenin and activation of the WNT pathway, as evidenced by over expression of WNT pathway targets. Differential expression analysis showed the up-regulation of WNT pathway target genes such as *LEF1* (9 fold), *AXIN2* (3.75 fold,) and *NOTUM* (51 fold) in clusters relative to palisading epithelium and gene set enrichment analysis confirmed that clusters exhibit a molecular signature strongly associated with activation of the WNT pathway (NES= 1.81, FDR=0.013) (Figure 5-14).

Other genes known to be expressed specifically in clusters from in *situ* hybridisation and immunohistochemical studies, were also up-regulated in clusters compared with palisading epithelium (e.g. *FGF3* (33 fold), *BMP4* (9.8 fold), *WNT5A* (4.9 fold), *CD44* (6.6 fold)) (Supplementary file 2).

These results support that clusters were successfully isolated and that these results can inform on their biology.

Table 5-8: Top 15 most up-regulated genes in clusters compared with palisading epithelium.

Gene Symbol	Fold Change (log2)	Adjusted p-value
CHRNA3	10.72856982	3.32E-27
GAD1	9.978881961	2.15E-26
CA6	8.951353678	4.39E-15
TNFRSF11B	8.799594904	3.15E-14
ITLN2	8.777772856	3.26E-14
ALDH1A1	8.777763239	3.15E-14
ERVMER34-1	8.586760306	3.08E-13
CHST11	8.471032085	1.04E-12
EPS8	8.302451483	4.38E-16
GYG1	8.273363338	8.37E-12
PPAP2A	8.023429034	1.15E-10
GRM8	8.004905374	1.15E-10
ABHD12B	7.972940022	1.54E-10
HSPB8	7.916412468	2.94E-10
KCNN4	7.901935424	3.21E-10

Table 5-9: Top 15 genes most down-regulated in clusters compared with palisading epithlium (most up in palisading epithelium).

Gene Symbol	Fold Change (log2)	Adjusted p-value
NA	-5.507529618	0.000604893
CPVL	-5.818262674	1.61E-05
SULT1E1	-5.827626376	0.000118317
UPK3B	-5.831622022	0.000149803
ABI3BP	-5.860104534	1.80E-15
CRISP2	-5.867271511	8.06E-05
SERPINE2	-6.343519618	4.79E-08
COL6A6	-6.393948864	1.02E-05
PTER	-6.408716695	4.20E-06
THSD7B	-6.420229391	1.24E-09
STRC	-6.56843238	3.98E-06
FST	-6.883612018	1.49E-07
SPTBN4	-7.394648059	1.95E-08
HSD17B2	-7.432187512	2.32E-10
LY75	-7.471878849	2.24E-28

Figure 5-14: Clusters compared with palisading epithelium. a) Principal component analysis plot of gene expression patterns of laser captured samples of clusters and palisading epithelium, 4 indicates case number, C = cluster, NC = palisading epithelium, for 4C2, and 4NC2 are independent replicates of 4C and 4NC. b) Enrichment of gene signature of WNT signalling within human ACP clusters.

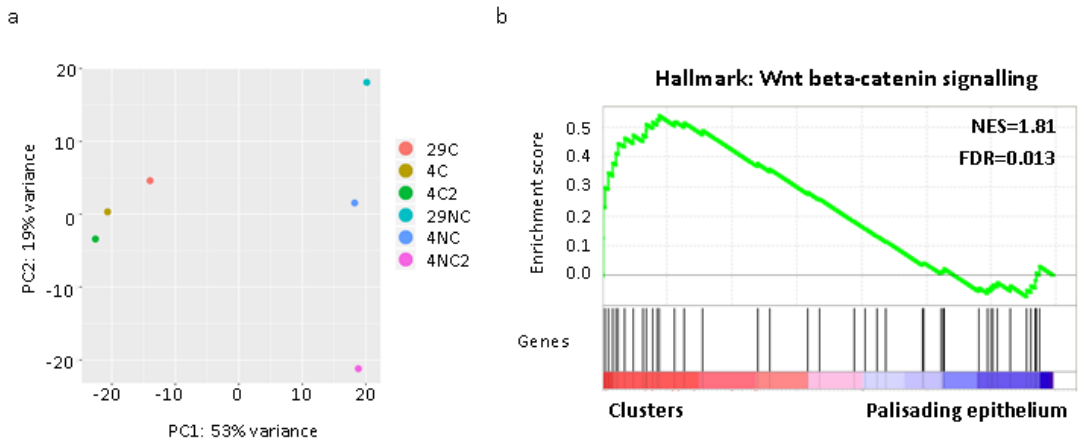

5.12 ACP clusters in human and mouse ACP share an expression profile with the enamel knot

The enamel knot is a critical signalling centre at the cap stage of the developing tooth. Morphologically it is similar to human ACP clusters and it also accumulates nuclear-cytoplasmic β-catenin (Obara and Lesot 2004). To further assess the molecular similarities we used a gene set of genes known to be expressed by the enamel knot. GSEA showed a significant enrichment in ACP clusters when compared with palisading epithelium (NES=1.98, FDR<0.001) or glial tissue, suggesting that these are highly analogous structures (Figure 5-15) (Helsinki 1996-2007).

The enamel knot occurs at the cap stage of development and the palisading epithelium was most enriched for the gene set of the inner enamel epithelium at this stage (NES=-1.85, FDR=0.008) (Figure 5-15), further highlighting the relationship between tooth development and ACP.

The enamel knot forms a signalling centre inducing dental mesenchyme to condense and differentiate into odontoblasts. GSEA suggested some enrichment of genes specifically expressed in these compartments, but not within the inner enamel epithium/enamel knot or ameloblasts, to be enriched within the glial tissue (NES =-1.41, FDR=0.23) (Figure 15) suggesting there could be some analogy in processes between condensation of dental mesenchyme and activation of glia. This is further explored with respect to specific pathways below.

p21/CDKN1A is often used as a marker of the enamel knot known to be expressed within ACP clusters. Another enamel knot marker is the ectodysplasin receptor (EDAR), which has not previously been implicated in ACP (Tucker, Headon et al. 2000, Tucker and Sharpe 2004). My analysis revealed that EDAR was up-regulated in ACP tumours compared with controls (382 fold) and in clusters relative to palisading epithelium (10 fold). Immunostaining confirmed the expression of EDAR in human cluster cells (Figure 5-15).

In summary this data confirm at the molecular level the relationship between tooth development and ACP tumourigenesis and highlight that the enamel knot and the β-catenin accumulating cell clusters are analogous structures.

Figure 5-15: ACP clusters share expression signatures with the enamel knot. Gene set enrichment plot showing enamel knot signature enriched in ACP clusters compared with a) palisading epithelium b) glial tissue. c) Inner enamel epithelium signature enriched in palisading epithelium, d) Expression of a proportion of genes expressed within dental mesenchyme and odontoblasts in glia. e) Double immunostaining of p21, EDAR and EDA in human ACP. Scale bars = 100µm

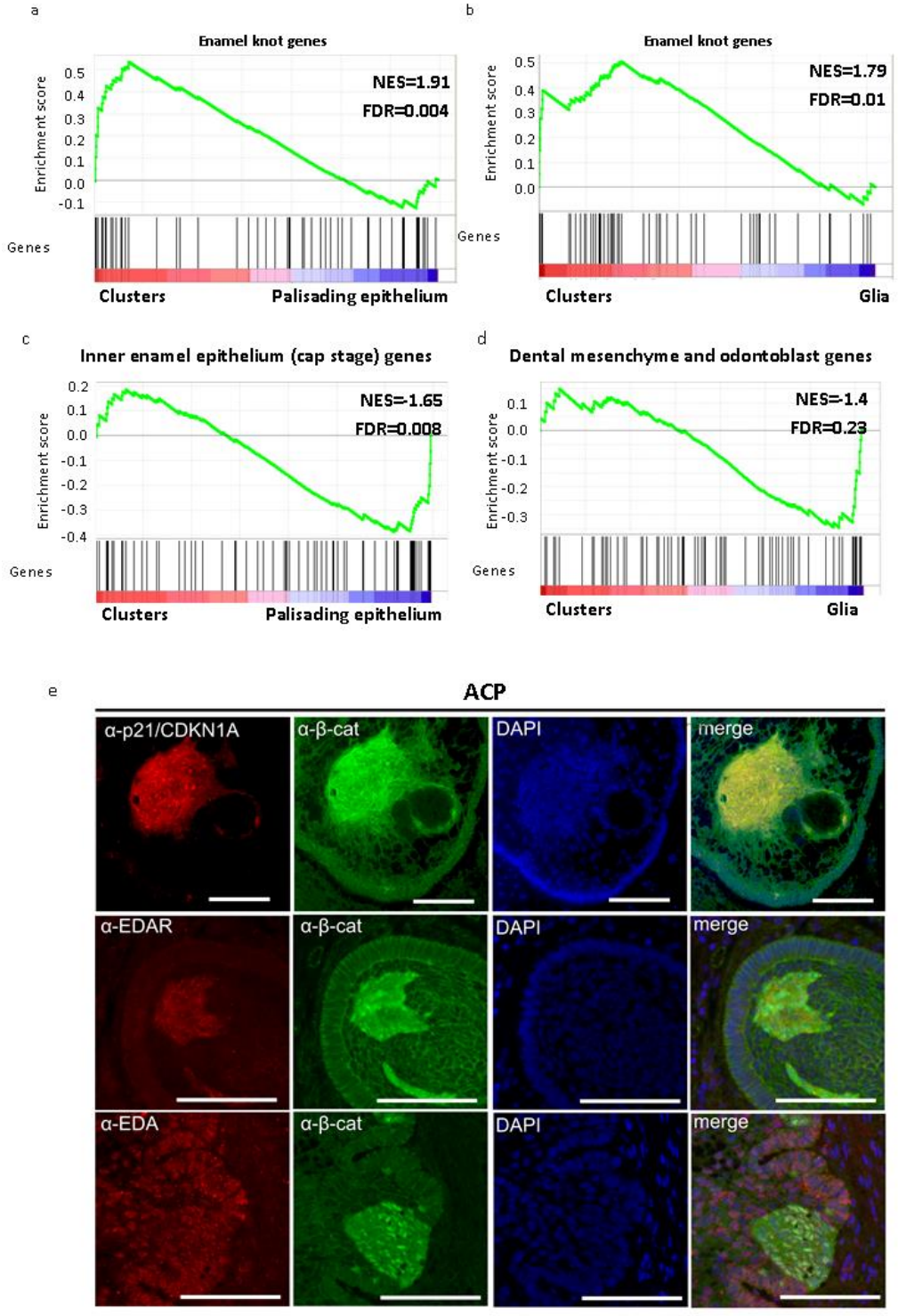

5.13 Autocrine and paracrine signalling between cell types

During odontogenesis, the enamel knots acts as a signalling hub by secreting several signals of the WNT, FGF, BMP and SHH families that induce surrounding dental mesenchyme to condense and form the odontoblasts of the dental papilla (Tucker and Sharpe 2004, Jussila and Thesleff 2012). These transient structures also control proliferation and epithelial bending, driving normal morphogenesis of the tooth. Studies on mouse models for human ACP, have reported that autocrine and paracrine signalling may be important for tumour development (Andoniadou, Gaston-Massuet et al. 2012, Andoniadou, Matsushima et al. 2013). Specifically, it was hypothesised that the β-catenin-accumulating cell clusters may act as signalling centres affecting tumour cell behaviour (Andoniadou, Gaston-Massuet et al. 2012, Andoniadou, Matsushima et al. 2013, Xavier, Patist et al. 2015). I therefore decided to further explore the possibility that human clusters are signalling centres using the RNA-Seq datasets of human ACP.

Differential expression analysis identified that many secreted factors were up-regulated by clusters relative to palisading epithelium (Supplementary Table 1d). These included: (i) several ligands that have previously been shown to be expressed in human ACP, such as *SHH* (3 fold) *BMP4* (10 fold), *BMP7* (2 fold), *FGF3* (33 fold), *FGF4* (22 fold) (Andoniadou, Gaston-Massuet et al. 2012, Gomes, Jamra et al. 2015, Gump, Donson et al. 2015); (ii) others previously identified as up-regulated in murine ACP clusters including *WNT16* (6 fold), *WNT5A* (5 fold), *TGFB1* (5 fold) and *TGFA* (7 fold) (Andoniadou, Gaston-Massuet et al. 2012); (iii) additional genes not previously described in human ACP e.g. *FGF12* (34 fold), *FGF8* (3 fold), *FGF19* (3 fold), *BMP8A* (38 fold), *BMP6* (3 fold) and *LIF* (7 fold)). These genes were also up-regulated in clusters when compared with glial tissue (Supplementary Table 2). A few secretory factors were also identified as expressed by both clusters and palisading epithelium (e.g. *WNT6, WNT10A*), or predominantly by reactive glial tissue (e.g. *FGF1, PDGFA*) (Figure 7c, Supplementary Fig. 8, 11). Similarly the receptors of several of these secreted signals were also expressed in specific tumour cell compartments.

In the following sections I further investigate specific pathways of interest in ACP, (e.g. having previously been suggested as therapeutic targets) as well as those relating to tooth development.

5.13.1 WNT pathway

Clusters are defined by their activation of the WNT/β-catenin pathway and in 5.11.1 we show transcriptional evidence of activation of the WNT pathway within ACP clusters. Clusters have also been shown to express a range of WNT ligands and FZD receptors. WNTs 4, 5A, 10B and 16 were most highly expressed by clusters. In contrast *WNTs 3A, 6, WNT10A* were more evenly expressed by clusters and palisading epithelium. FZD receptors were variably expressed across all 3 compartments with FZD1, 2, 6 and 7 most highly expressed by clusters. WNT inhibitors, e.g. DKK4 are also highly expressed by clusters (21000 fold in clusters compared with glia and 11 fold in clusters compared with palisading epithelium).

Why β-catenin pathway activation is limited to clusters, despite the presence of *CTNNB1* mutations in all epithelia, remains uncertain.

5.13.2 Sonic Hedgehog (SHH) Pathway

Sonic Hedgehog was up-regulated in clusters, in concordance with previously published *in situ* hybridisation and immunohistochemistry by another laboratory member, Gabriela Carreno (Andoniadou, Gaston-Massuet et al. 2012).

In contrast, the receptor *PTCH1*, and *SMO*, a critical pathway component, were up-regulated 1.7 and 2 fold, respectively, in the palisading epithelium relative to the clusters. Likewise, *GLI1* and *GLI3*, two pathway targets were up-regulated 2 and 3 fold, consistent with paracrine signalling from the clusters [1]. Plotting of the normalised counts also identified the up-regulation of *GLI1* (95 fold) and *GLI3* (33 fold) within the clusters themselves when compared with the glial tissue suggesting additional autocrine signalling (Figure 5-17).

mRNA in situ hybridisation previously published and by Gabriela Carreno confirmed the expression of *PTCH1* and *GLI1* in all tumour cells, supporting the presence of both autocrine and paracrine signalling within the tumour epithelium (Figure 5-17). Sonic hedgehog is known to be highly expressed by the enamel knot, and manipulation of the pathway results in abnormalities of growth and tooth shape (Dassule, Lewis et al. 2000, Cobourne and Sharpe 2005).

The SHH pathways has previously been suggested by several groups as a possible therapeutic targeted in ACP (Gomes, Jamra et al. 2015, Gump, Donson et al. 2015, Coy, Du et al. 2016, Holsken, Sill et al. 2016). We further explore this in Chapter 8.

5.13.3 Fibroblast Growth Factor (FGF) Pathway

FGFs 3, 4, 9, 12, 13, 19 were highly expressed by clusters. In contrast FGF2 and 20 were expressed across all tissue compartments with FGF20 highest in clusters, and FGF1 highly by reactive glia (Figure 5-18). The receptors FGFR1-3 were expressed across all tissue compartments (Figure 5-18). The expression of FGF3, 4, 9 and 20 by ACP clusters mirrors that of their expression by the enamel knot. Of note FGF19, hormone like FGF which binds with high affinity to FGFR4 was predominantly expressed in clusters, whilst its receptor's expression was predominant in reactive glial tissue.

The MAPK pathway is a major downstream target of the FGF signalling and to assess activation within tumours, immunostaining of the phosphorylated form of ERK1/2 (pERK1/2) was performed. This identified variable activation in non-cluster tumour tissue and in the reactive glial tissue (Figure 5-18). Of note, areas of pERK1/2 staining at the leading edge of tumour invasion was apparent in a proportion of case, suggesting a possible role in tissue invasion.

5.13.4 Epithelial Growth Factor Receptor (EGFR) Pathway

The EGFR pathway has been suggested as a possible therapeutic target in ACP. Examination of the EGFR pathway ligands revealed high expression of *TGFA* in clusters and *HB-EGF* in glial tissue (Figure 5-18). *EGFR* expression was limited to

tumour compartments, whereas *ERBB2* and *ERBB3* were expressed in all compartments and ERBB4 limited to the reactive glia (Figure 5-18).

EGFR activation requires phosphorylation and whilst EGFR receptor has been shown to be phosphorylated specifically in the clusters, downstream activation of the pathway in clusters has not been demonstrated (Holsken, Gebhardt et al. 2011). Like the FGFR pathway, EGFR activates the MAPK pathway. The relative absence of pERK staining in clusters suggests that this is not a major feature of ACP.

5.13.5 Transforming Growth Factor β (TGFβ) Pathway

The hallmark gene set for TGFβ pathway signalling was enriched in tumours compared with control (NES= 2.1, FDR<0.001), suggesting activation of the pathway within ACP (Figure 5-19). *TGFB1* and *INHBB* are specifically expressed by clusters whereas *TGFB2*, *TGFB3* and the receptors *TGFBR1-3* and *ACVR1, ACVR2A* and *ACVR2B*, are more ubiquitously expressed (Figure 5-19).

To investigate this pathway further, immunostaining against the activated (phosphorylated) SMAD3 (pSMAD3) was performed. This confirmed activation of the pathway (Figure 5-19). pSMAD3 staining was observed within the tumour, particularly in areas of stellate reticulum close to clusters. It was also observed within the reactive glial tissue, in an apparent dose-dependent manner around areas of tumour. This pattern is consistent with paracrine signalling between tumour and reactive glial tissue.

5.13.6 Bone Morphogenic Protein Pathway

BMP4 and *7* were found to be highly expressed by clusters and to a lesser extent other compartments, consistent with previous *in situ* hybridisation. Both BMP4 and 7 are known to be critical regulators of tooth development. The receptors *BMPR1A* and *BMPR2* are expressed across compartments and *BMPR1B* was found to be expressed in only one of the two glial tissue samples (Figure 5-20). This would be consistent with signalling across compartments through a *BMPR1A/BMPR2* heterodimer.

To assess the downstream activation pSMAD1,5,8/9 immunohistochemistry was performed. This confirmed activation across tumour and reactive glial compartments (Figure 5-20).

5.13.7 Ectodysplasin (EDAR) pathway

The expression of the ectodysplasin receptor, *EDAR*, in clusters supports the molecular analogy with the enamel knot. Ectodysplasin (*EDA*) is the ligand for this receptor and immunostaining showed expression in all tumour cells, consistent with its expression in the tooth epithelium (Figure 5-15). This is consistent with both autocrine and paracrine signalling.

EDAR signalling activates the NF-kB signalling pathway. This has separately been confirmed to be activated specifically in clusters through immunostaining against phosphorylated IKB (M. Gonzalez-meljem, G. Kauskal, personal communication).

5.13.8 Other factors/pathways

A range of additional factors were also assessed. *LIF* was specifically expressed by clusters, with its receptor, *LIFR*, expressed by glial tissue, suggesting paracrine signalling between clusters and the surrounding glia (Figure 5-21). In contrast, *OSM* was expressed specifically by glia and its receptor, *OSMR*, across all compartments (Figure 5-21). *PDGFA* was predominantly expressed by the glial reactive tissue and its receptor *PDGFRA* was most highly expressed by clusters (Figure 5-21)

Glial cell derived neurotrophic factor, *GDNF* was specifically expressed by clusters with its co-receptor *GFRA1* expressed across compartments (Figure 5-21). In contrast, the brain derived neurotrophic factor, *BDNF*, was expressed predominantly by clusters and palisading epithelium, and its receptor, *NTRK2,* was expressed very highly by reactive glial tissue (Figure 5-21).

In summary, these analyses reveal a complex system of autocrine and paracrine signalling between tissue compartments and support the role of clusters as a signalling hub with similarities to the enamel knot.

5.14 Proliferation in ACP

To assess the functional significance of clusters on tissue proliferation, Ki67 immunostainings was performed on ACPs. As previously described in the literature, this revealed proliferation predominantly within the palisading epithelium and absent in clusters and minimal in the reactive tissue (Raghavan, Dickey et al. 2000). Double immunostaining revealed areas of Ki67 expression to frequently be in close association with clusters. This would be consistent with paracrine signalling from clusters driving proliferation of epithelium in a manner similar to that of signalling from the enamel knot in the developing tooth.

Figure 5-16: Heatmap of normalised expression values of WNT ligands and FZD receptors in laser capture micro-dissected human ACP tissues. Yellow indicates higher expression, red lower.

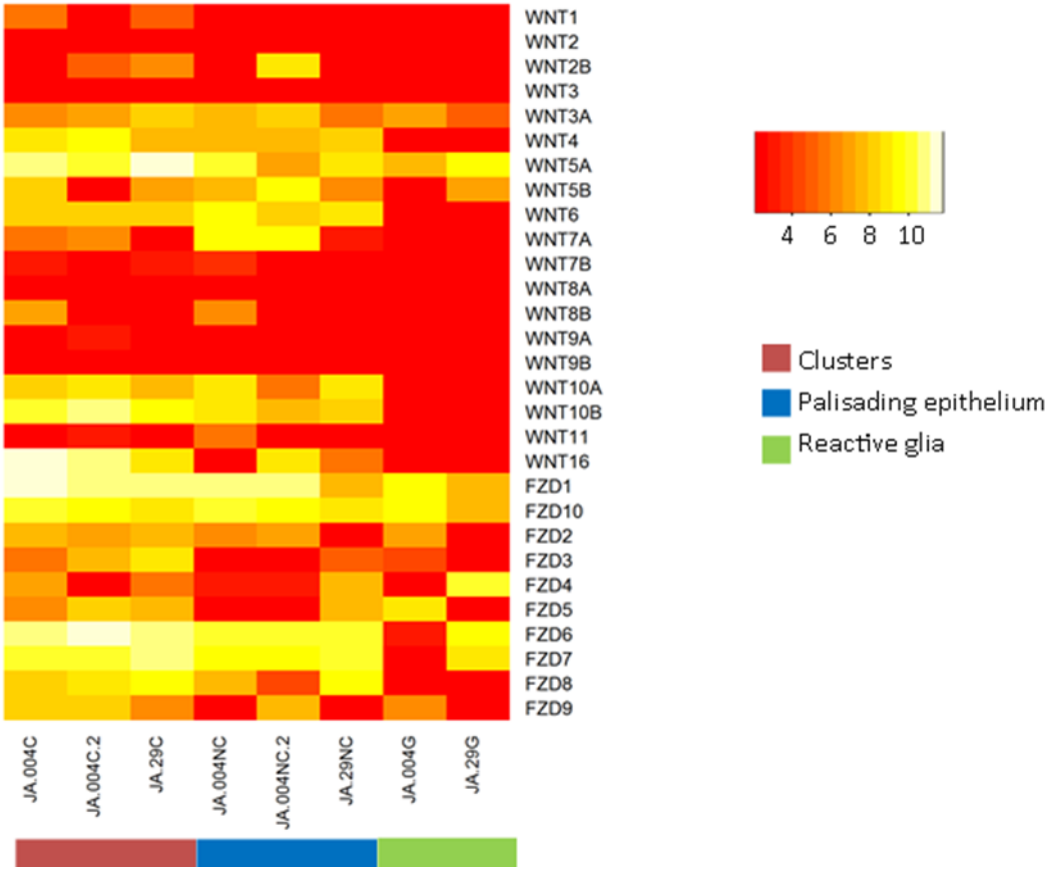

Figure 5-17: Expression of Sonic Hedgehog pathway components in ACP. a) Plots of normalised expression counts for SHH pathway members b) Immunohistochemistry demonstrating expression of SHH in ACP clusters (G.Carreno) and c) in situ hybridisation of *PTCH1* and *GLI1* (G Carreno).

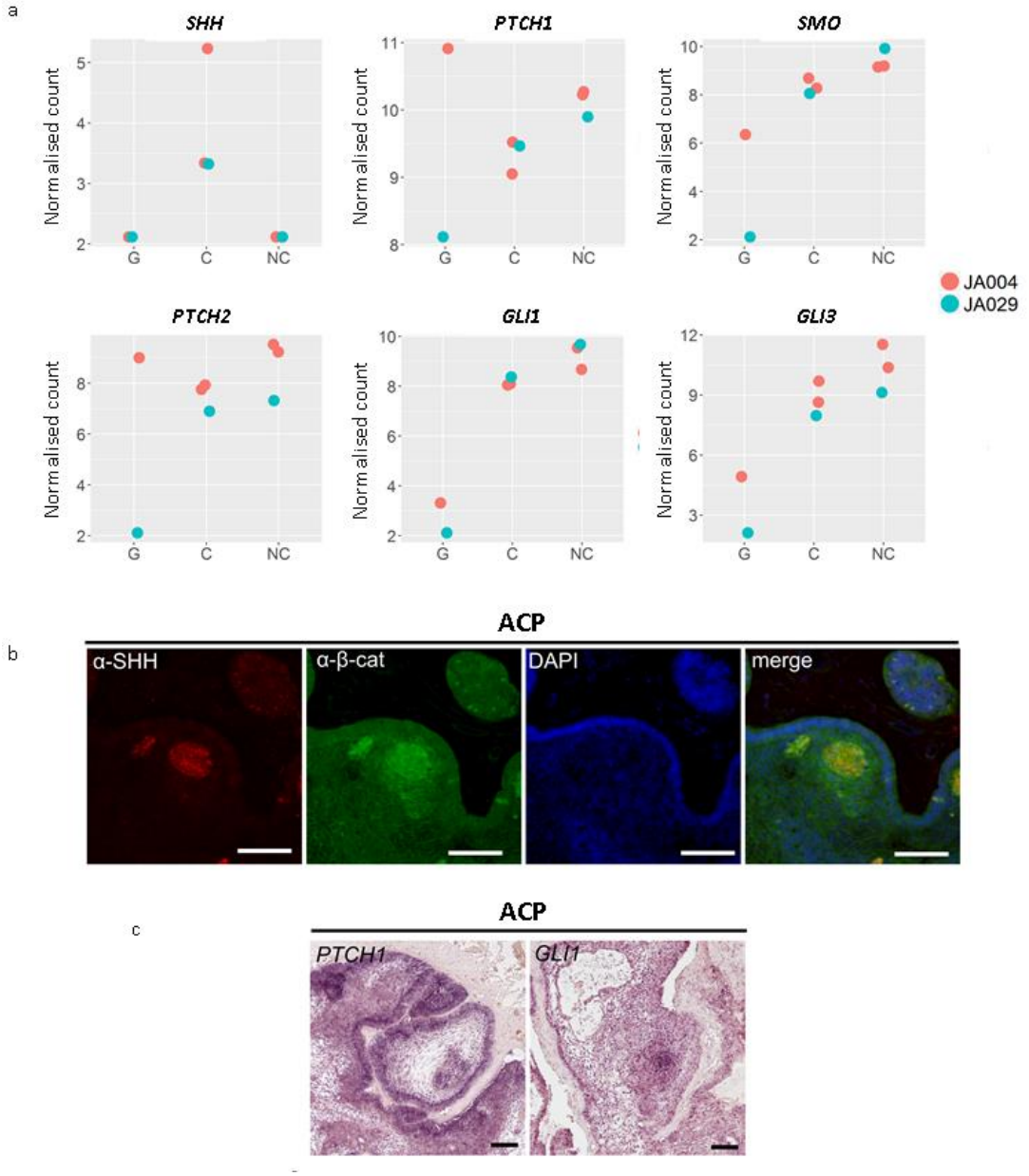

Figure 5-18: Fibroblast growth factor and epidermal growth factor signalling. Heatmaps of normalised expression of a) FGF ligands and receptors b) EGF family receptors and ligands c) Double immunofluorescence and immune-histochemical staining of the phosphorylated forms of ERK1/2 in 2 cases of ACP. Scale bars =100µm and 500µm.

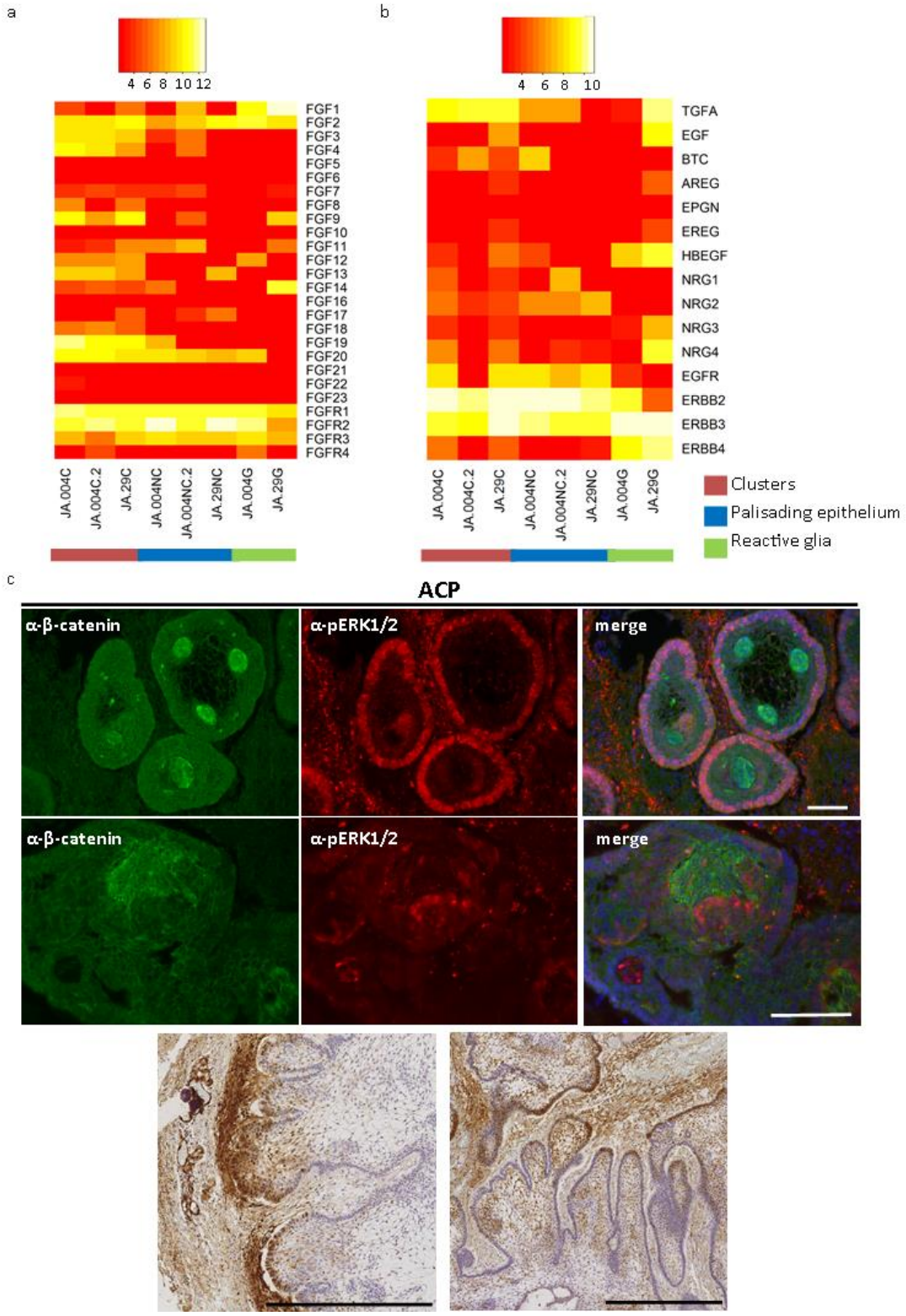

Figure 5-19: TGFβ pathway signalling. a) Normalised expression of TGFB1 by clusters b) Heatmap of normalised expression of TGFB, activin and inhibin ligands and receptors, c) GSEA plot showing enrichment of TGFB signalling in ACP. d) Double immunofluorescence showing activated p-SMAD3 in 2 cases of ACP. Scale bars =100µm.

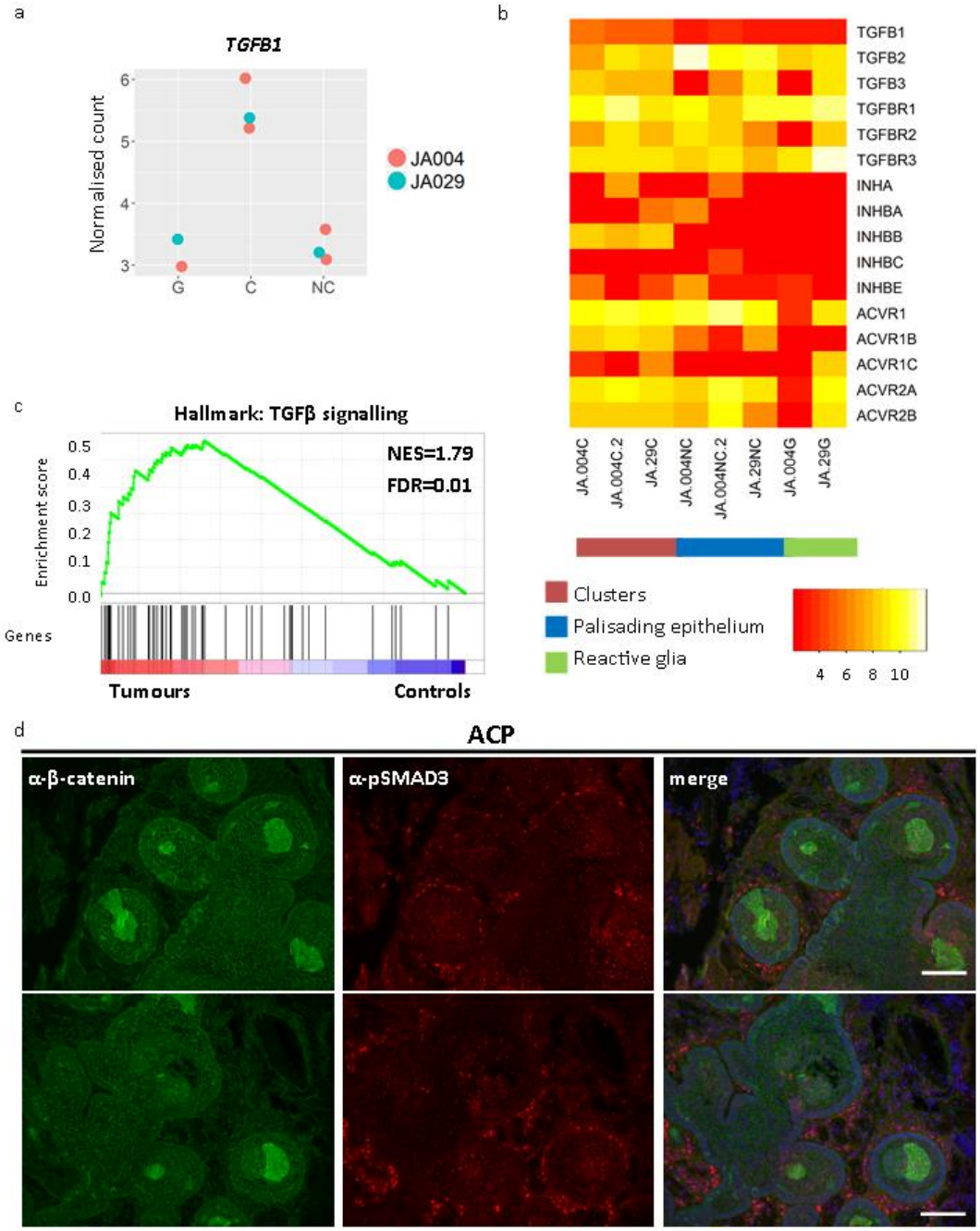

Figure 5-20: BMP pathway signalling. a) Heatmap of normalised expression of BMP ligands and receptors b) Double immunofluorescence staining showing activation of SMADs1,5,8/9 double check. Scale bars=100um.

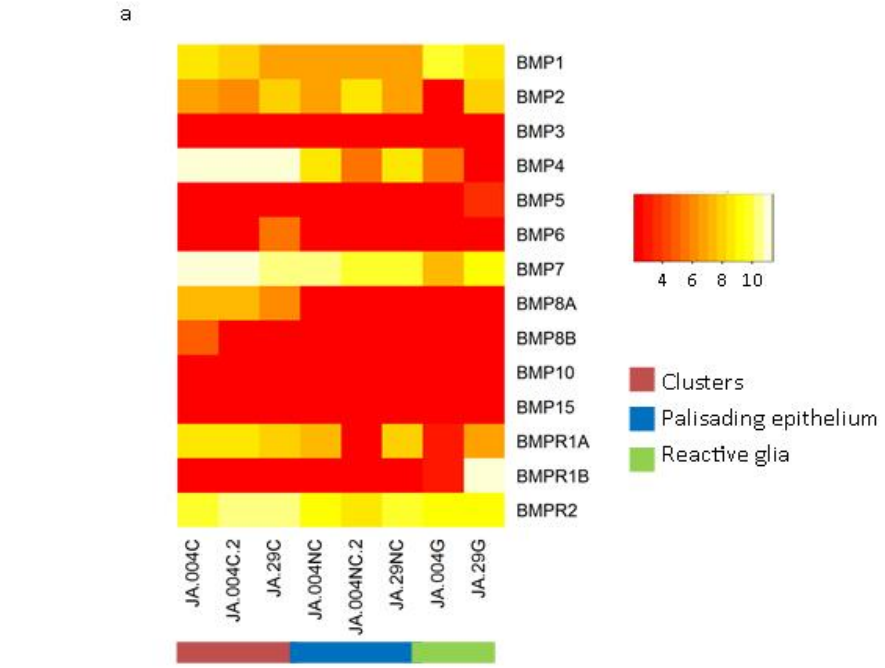

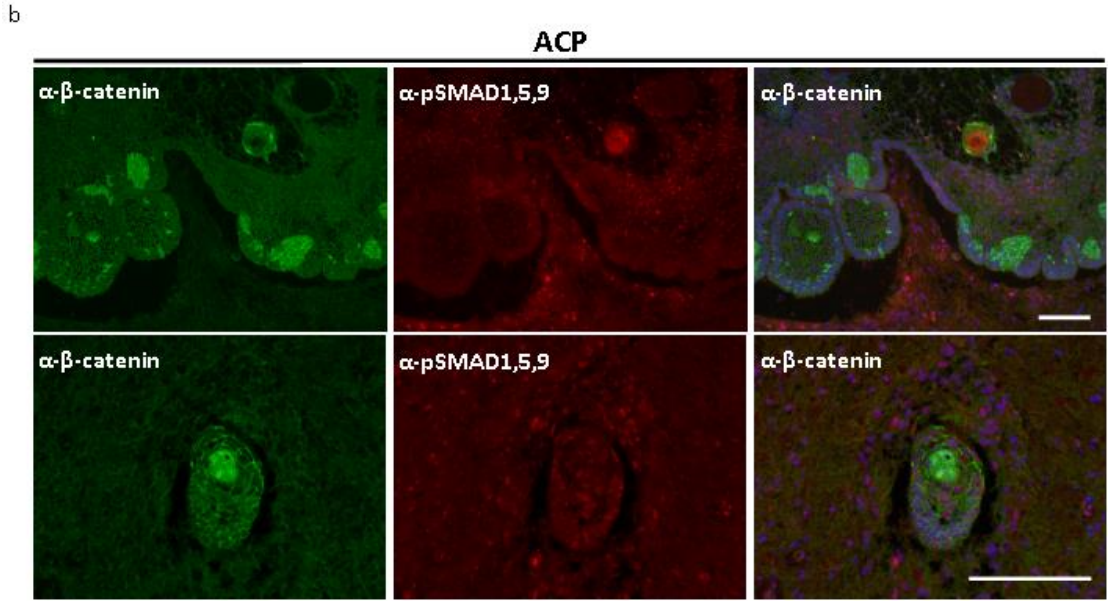

Figure 5-21: Other signalling pathways. Plots of normalised expression values of selected members of other signalling pathways.

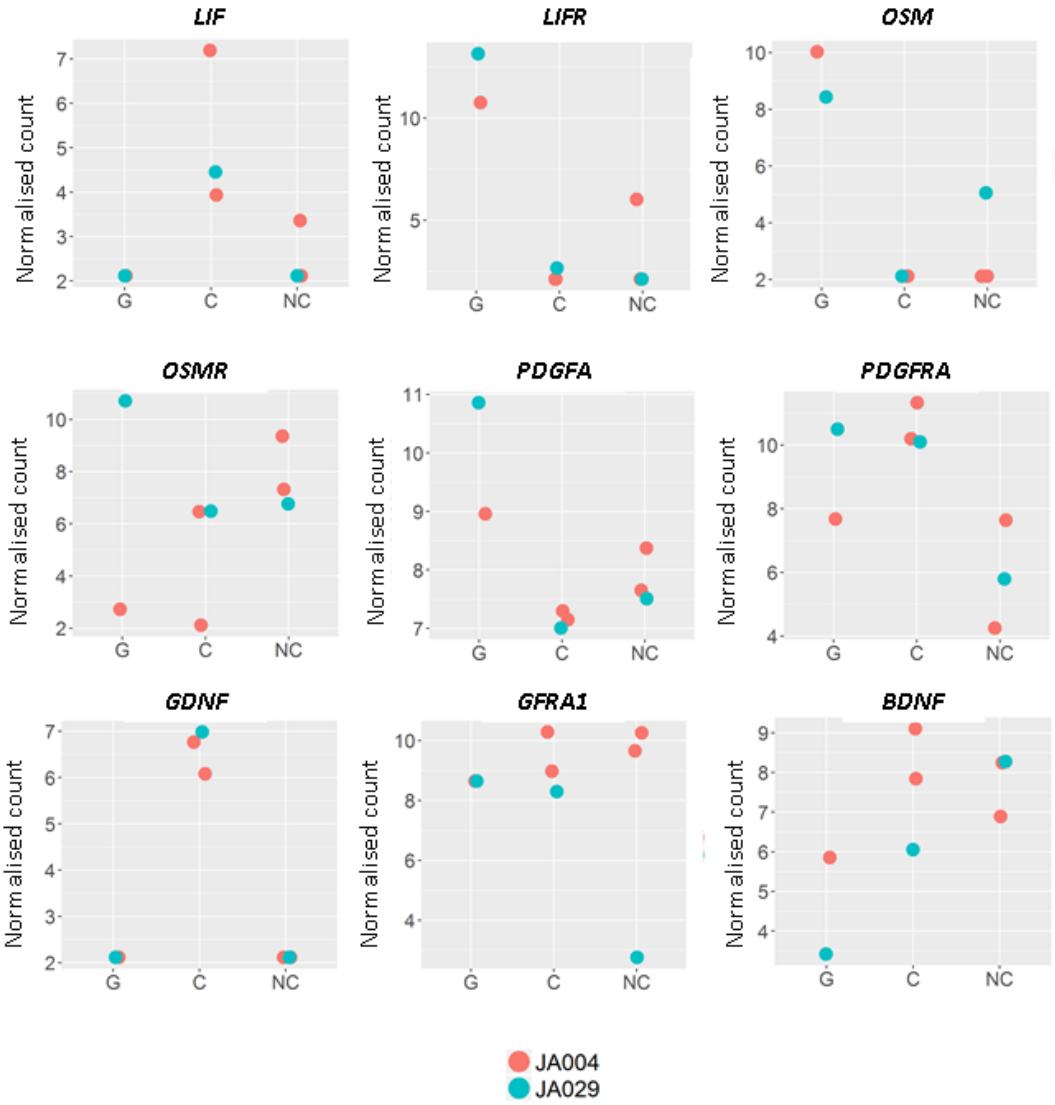

Figure 5-22: Proliferation in ACP. Double immunofluorescence for the proliferation marker Ki67 and β-catenin in 3 cases of ACP. Proliferation is predominantly limited to the palisading epithelium, close to clusters. The top panel is a serial section of the pERK staining presented in Figure 5-19. Scale bars =100µm.

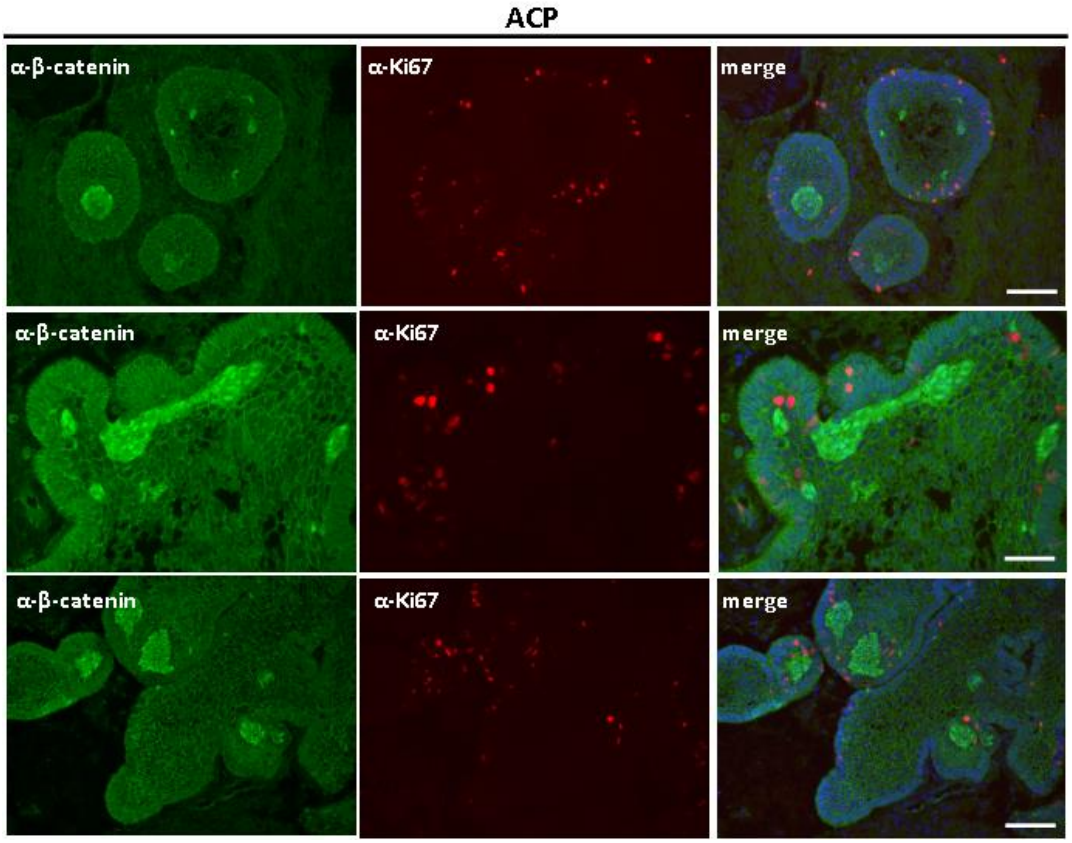

5.15 ACP clusters exhibit the expression signature of cellular senescence and SASP

Immunohistochemical studies by Mario Gonzalez-Meljem have shown that ACP clusters undergo cellular senescence, as evidenced by a lack of proliferation markers, expression of GLB1, activation of mTOR and NF-kB pathways. Using GSEA I compared the gene expression profile of clusters with a previously established transcriptional signature for oncogene-induced senescence (OIS) obtained from human IMR90 ER:RAS fibroblasts. These cells express an Esteroid Receptor-$KRAS^{V12D}$ chimaeric fusion protein that triggers growth arrest, senescence and SASP (Acosta, Banito et al. 2013). This confirmed enrichment of the senescence gene signature in human ACP clusters (NES=1.44, FDR=0.14) (Figure 5-23)/

RT-PCR and ELISA analyses had also confirmed that murine ACP clusters exhibit activation of the Senescence Associated Secretory Phenotype (SASP). To assess the expression of this in human clusters, using a gene set derived from proteomic analysis of cultured media of the IMR90 ER:RAS induced senescent fibroblasts GSEA was performe and confirmed enrichment in clusters (NES=1.41, FDR=0.09) (Figure 5-23).

Section 1.13 describes the expression of many growth factors including members of the SASP (e.g. TGFβ). Inflammatory cytokines IL6 and CXCL8 (IL8), IL1A and IL1B, in addition to their established roles in inflammation (discussed below in section 5.16) are important members of the SASP. *IL1A* (18 fold), *IL1B* (7 fold) and *IL8* (3 fold) were all significantly up-regulated in tumours vs controls (*IL6* 1.7 fold up-regulated, non- significant). Within the laser capture micro-dissected RNA seq dataset there were insufficient or no reads to assess expression of these cytokines. These genes are typically small, have high homology and therefore challenging to align. Due to the single-end, short length and relatively shallow sequencing used the lack of reads in these genes may reflect experimental design rather than true biology.

Immunohistochemistry for cytokines is challenging due to their secretory nature and often short half-lives. Immunohistochemistry for the IL6 receptor subunit

IL6RA confirmed expression within ACP, particularly the stellate reticulum, but also within the reactive tissue (Figure 5-23).

Activation of STAT3 by phosphorylation is a major downstream signalling pathway of the IL6 receptor complex. Consistent with the expression of IL6RA, pSTAT3 immunohistochemistry had previously been observed in both tumour and reactive glial compartments (Donson, Apps et al. 2017).

Figure 5-23: Senescence and ACP a) Enrichment of transcriptional signatures of senescence and SASP within human ACP clusters b) Immunohistochemistry showing expression of IL6RA within ACP, particularly the stellate reticulum, and also in cells within the reactive tissue. Scale bars=100µm.

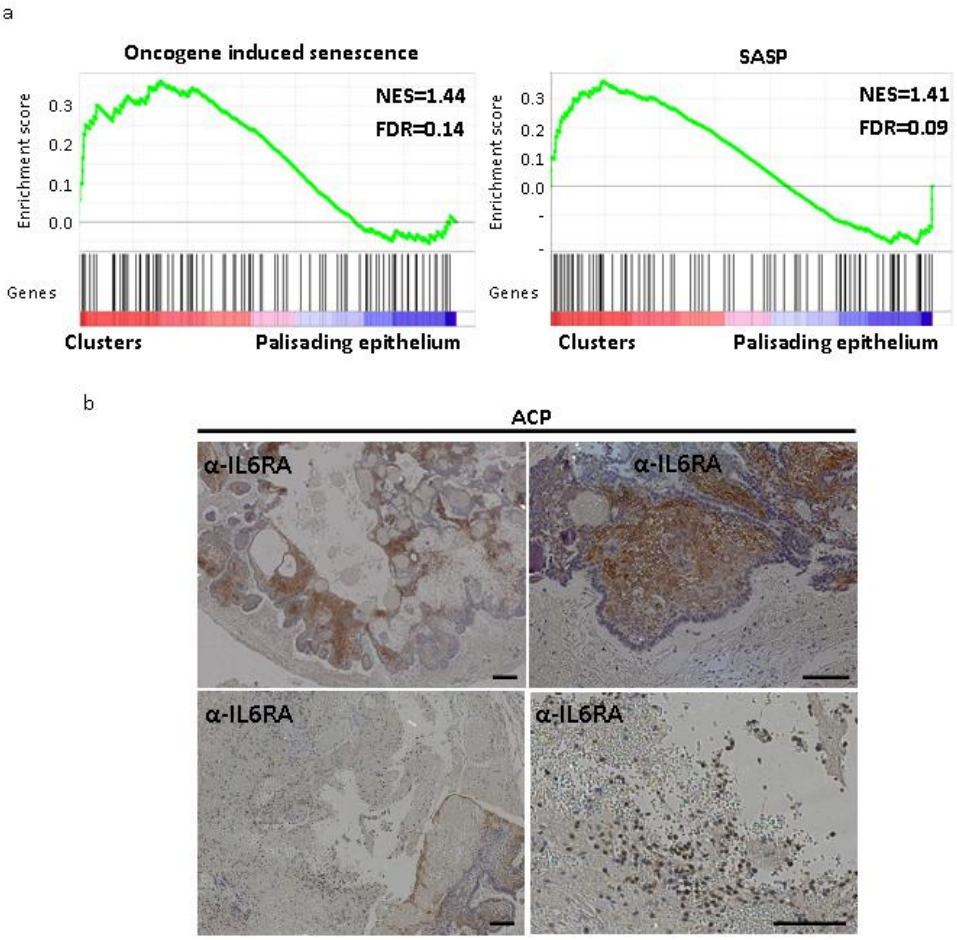

5.16 The signature of the ACP immune infiltrate highlights a complex immune microenvironment with expression of pro- and anti-inflammatory cytokines

In addition to these signatures of tumour and reactive glial tissue, WGCNA identified a third major pattern of gene co-expression, the magenta module containing 958 genes (Figure 5-7, Supplementary Table 3). An overall positive correlation was observed with reactive glial tissue ($r=0.74$, $p=4x10^{-5}$) and GFAP expression ($r=0.69$, $p=2x10^{-4}$), but not with tumour content or *CTNNB1* mutation allele frequency, suggesting that the magenta module is not related to tumour cells (Figure 5-9). In agreement with this notion, gene ontology assessment revealed a significant enrichment for genes associated with the immune response and module genes included cell surface markers (e.g. *CD14, CD68, CD3*), MHC class II proteins, as well as several cytokines comprising both pro- (e.g. *IL18, TNF*) and anti-inflammatory mediators (e.g. *IL10*) (Table 5-10). This analysis suggests that the magenta module may represent the immune infiltrate/response frequently observed in ACP tumours.

This was further supported by GSEA which showed enrichment for the microglial gene signature (ES=5.4, p=2.8x10-13) (Figure 5-24) (Zhang, Chen et al. 2014). Microglia are CD68+ve bone marrow derived inflammatory cells in the CNS.

To dissect further this module, we assessed the differential expression and correlation of expression patterns of myeloid and lymphoid immune cell markers. CD14 (6.2 fold), CD68 (11.9 fold) and CD3E (3.6 fold) were all up-regulated in ACPs compared with controls. Strong correlations were observed between myeloid markers CD14 and CD68 ($r= 0.94$, $p=7x10^{-12}$) as well as with the T cell receptor component CD3E (CD14: $r=0.81$, $p=1.2x10^{-6}$, CD68: $r=0.82$, $p=9x10^{-7}$). The variable presence of CD68 positive and CD3 positive cells within ACP samples was confirmed by immunohistochemistry in three cases (JA005, JA029, JA054) and also an existing tissue microarray of ACP tissue (Figure 5-24).

To further characterise the T cells present in the tumour specimens, we compared the expression of *CD8*, a marker of cytotoxic T cells, and *CD4*, a marker of helper T cells, to reveal that CD4 was up-regulated in tumours relative to control tissues (11 fold), whilst CD8 was not significantly differentially expressed (1.1 fold). Additionally, expression of *CD4* correlated better with *CD3* ($r=0.87$, $p=4x10^{-8}$) and other immune cell markers than *CD8a* ($r=0.55$, $p=0.004$), suggesting a predominantly CD4+ T cell response. Immunohistochemistry in cases JA054 and JA029 confirmed the variable presence of both CD4+ve and CD8+ve cells in ACP (Figure 5-24).

Histological review of ACP cases has also suggested the possible presence of plasma cells. B cell markers CD20 (*MS4A1*) and CD79a (*CD79a*) and the majority of immunoglobulin genes were not overall up-regulated in ACP tumours compared with controls. Immunostaining confirmed the relative paucity of CD79a positive cells, with presence observed in only 4/60 tissue cores on a tissue microarray (Figure 5-24). As highlighted in section 5.5.1, immunoglobulin genes were up-regulated in low tumour content tumours compared with controls. Together these results suggest that a humoral immune response can occur within ACP tissue.

The magenta module included several cytokines highly up-regulated in tumours compared with controls, including potential therapeutic targets such as *TNF* and *IL1A*. We examined these in more detail showing that for *TNF, IL10, IL18, IL1A* and *IL1B* and several chemokines, e.g. *CCL2*, expression correlated closely with the expression of immune cell markers *CD14, CD68* and *CD4* ($r>0.7$, $p<0.0001$), but not with the *CTNNB1* mutation frequency ($r<0.2$) (Table 5-10). This is consistent with these cytokines being expressed predominantly by immune cells, in line with a recent limited immunohistochemical study of the immune infiltrate in ACP (Tena-Suck, Citlaltepelt et al. 2015).

To validate the presence of these cytokines in human ACP, protein lysates were extracted from matched frozen samples of eight tumours. Multiplex ELISA against IL1β, IL6, IL8, IL10, IL18, TNFα and IFNγ confirmed the expression of all of these but IFNγ (Figure 5-24).

5.16.1 Cystic fluid and inflammation

Cystic fluid has been shown to include inflammatory mediators (Pettorini, Inzitari et al. 2010). Recent cytometric bead analysis of cytokines within cystic fluid has also confirmed expression of many cytokines, including IL6, CXCL8 (IL8), IL1a, IL1b and TNFα (Donson, Apps et al. 2017). We confirmed this using multiplex ELISA to reveal the presence of IL6, IL8, IL18, IL1B, IFNy and TNF in the cystic fluid of 10 patients from GOSH (Figure 5-24). This showed particularly high levels of IL6 and IL8 (median 3342pg/ml and 3927pg/ml respectively), comparable to those identified by cytometric bead analysis.

Independently, mass spectroscopy analysis of human ACP fluid from six patients has also recently been performed identifying the presence of 461 proteins (Benedetta Pettorini, personal communication). The most abundant of these were apolipoprotiens (particularly APOA1 and APOA2). Other proteins identified included; complement proteins, coagulation cascade proteins, immunoglobulins, keratins (1, 2, 5, 6A, 7,8, 10, 14,16, 17, 18, 19) (Benedetta Pettorini, personal communication).

To assess the origin of the proteins in cystic fluid, gene set enrichment analysis was performed. Using the LCM RNA seq dataset highlighted that whilst some proteins (e.g. keratins) were likely epithelial derived, overall the proteins were predominantly expressed by the reactive tissue (NES=-1.60, FDR<0.001) (Figure 5-25). When considering the WGCNA modules, this showed the black and magenta modules were most enriched for expression of genes. These results are consistent with a mixed, tumour (particularly wet keratin associated) and reactive immune cell origin of proteins within cystic fluid (Figure 5-25).

5.16.2 The immune signature of ACP suggests activation of inflammasomes

The up-regulation of several IL1 family members (IL1A, IL1B, IL18) and their presence in cystic fluid is suggestive of a relationship with inflammasome-mediated inflammation. Inflammasomes are innate immune response complexes activated through a range of danger signals (Guo, Callaway et al. 2015). The complexes, the

most common of which is the NLRP3 inflammasome, result in activation of caspase 1, which in turn cleaves members of the IL1 family (particularly IL1b and IL18) to the active form driving an inflammatory response. Targets include expression of other inflammatory mediators such as cytokines (including IL6, IL8, TNF), chemokines (e.g. CCL2), Cyclo-oxygenase-2 (COX2) and inducible nitric oxide synthase (iNOS) as well as other factors such as MMPs and VEGF (Hoffman, Rosengren et al. 2004, Lewis, Varghese et al. 2006, Apte and Voronov 2008, Guo, Callaway et al. 2015).

Analysis of the cytokines present in ACP cystic fluid identified strong correlation between IL1β and IL6, 8 and TNF (IL6 r=0.91, p=0.0002, IL8, r=0.95, p=2.4x10-5, TNF, r=0.96, p=1.41x10-5) (Figure 5-26).

Activation of the inflammasome is associated with many diseases. Of note, lipids, e.g. in atherosclerosis, and crystals (e.g. in crystal arthropathies) are potent activators of the inflammasome. Cholesterol clefts are not infrequently observed in ACP tissue and negatively birefringent cholesterol crystals are a pathognomonic feature of ACP fluid. Immunohistochemistry for CD68 and CCL2 of a case with cholesterol clefts highlighted a spatial relationship of inflammatory cells and chemokines to lipid in ACP (Figure 5-26).

To further investigate the relationship between inflammasomes and ACP, GSEA was performed confirming i) expression of IL1β response genes by human ACP tumours, using gene sets from cell culture experiments where IL1β was added to macrophages, chondrocytes or uterine muscle (Vincenti and Brinckerhoff 2001, Chevillard, Derjuga et al. 2007, Jura, Wegrzyn et al. 2008) and ii) enrichment of genes expressed in atherosclerotic arteries (NES=2.12, NES<0.001) (Sulkava, Raitoharju et al. 2017). This signature was significantly enriched within human ACP tissue suggesting molecular analogies between the processes.

Activation of inflammasomes by cholesterol crystals requires additional mechanisms, one of which is activation of the complement cascade (Niyonzima, Halvorsen et al. 2017). Gene set enrichment analysis had highlighted expression of complement components in ACP tumours (NES=2.09, FDR<0.001), particularly in the reactive component compared with the tumour epithelia. All core canonical and

non-canonical complement proteins have also separately been identified within ACP cystic fluid (Benedetta Pettorini, personal communication). Other mechanisms include through TLR4, which is also up-regulated in ACP tumours compared with controls (5 fold) (Supplementary Table 2).

In addition to pro-inflammatory cytokines anti-inflammatory cytokines were also identified, particularly *IL10*, whose expression correlated with the immune cell infiltrate (Table 5-10). Others, e.g. TGFβ appear to be predominantly expressed by tumour (section 5.13.5).

Together these results also highlight the complex local immune environment with the presence of both pro-inflammatory (e.g. *TNF, IL18, IL1A, IL1B*) and anti-inflammatory (e.g. *IL10*) mediators.

Table 5-10: Correlation of expression of tumour up-regulated cytokines of the magenta module with *CTNNB1* mutation allele frequencies and immune cell markers.

Gene Symbol	Differential expression results		Correlation with CTNNB1 mut allele freq		Correlation with CD14		Correlation with CD68		Correlation with CD3E		Correlation with CD4		Correlation with CD8A	
	log2FC	Padj	r	p	r	p	R	p	r	p	r	p	r	p
IL1A	4.180456	2.99E-11	0.457088	0.024732	0.728229	5.48E-05	0.831374	4.84E-07	0.684772	0.000223	0.809621	1.65E-06	0.018407	0.931968
IL1B	2.814562	0.004409	-0.10557	0.623476	0.851123	1.36E-07	0.72189	6.83E-05	0.676671	0.000283	0.775218	8.63E-06	0.372277	0.073222
IL10	4.071387	1.04E-07	0.148307	0.489185	0.90128	1.88E-09	0.863031	5.74E-08	0.784304	5.74E-06	0.878822	1.61E-08	0.365705	0.07885
IL16	1.837601	0.001424	-0.25213	0.234619	0.934398	2.46E-11	0.846896	1.81E-07	0.810102	1.61E-06	0.91506	3.85E-10	0.520537	0.009113
IL18	3.893901	1.35E-07	0.101299	0.637653	0.91319	4.85E-10	0.920587	1.88E-10	0.844334	2.14E-07	0.908365	8.59E-10	0.398997	0.053432
IL32	1.324885	0.012781	-0.09127	0.671446	0.794491	3.55E-06	0.776968	7.99E-06	0.751461	2.31E-05	0.854753	1.05E-07	0.448074	0.028104
CCL2	4.043857	8.42E-11	0.202457	0.342742	0.814754	1.25E-06	0.838249	3.17E-07	0.760925	1.58E-05	0.882254	1.19E-08	0.248567	0.241513
CCL3	3.218444	0.000257	-0.03584	0.867962	0.89264	4.55E-09	0.811135	1.52E-06	0.72607	5.91E-05	0.816726	1.13E-06	0.43621	0.033092
CCL4	2.919365	0.000948	-0.0818	0.703952	0.875707	2.10E-08	0.763637	1.41E-05	0.686265	0.000213	0.78354	5.95E-06	0.442284	0.030457
CCL5	1.326884	0.096813	-0.06848	0.750527	0.886379	8.23E-09	0.835729	3.71E-07	0.928813	5.88E-11	0.865809	4.65E-08	0.654354	0.000523
CCL8	2.715066	0.001207	0.084345	0.695172	0.82913	5.54E-07	0.783256	6.02E-06	0.724543	6.23E-05	0.782659	6.19E-06	0.434666	0.03379
CCL20	3.66574	4.26E-05	0.222122	0.296862	0.834656	3.96E-07	0.855468	9.99E-08	0.701466	0.000134	0.844602	2.10E-07	0.241146	0.25631
TNF	3.380521	1.69E-05	0.01929	0.928715	0.804407	2.17E-06	0.772626	9.67E-06	0.701721	0.000133	0.791097	4.18E-06	0.310326	0.139986

Figure 5-24: The immune environment of ACP. a) Enrichment plot showing enrichment of magenta module with gene signature of microglia b) Immune-histochemistry of case JA029 showing variable infiltrate of CD68, CD3, CD4 and CD68 positive cells. c) CD79 positive cells within reactive tissue of a case of ACP. d) Correlation of IL18, IL1B and IL10 expression with CD14 expression. e) Detection of cytokines in solid tumour lysates, results adjusted to total protein added to assay. f) Concentration of cytokines in ACP cystic fluid. Scale bars=100µm.

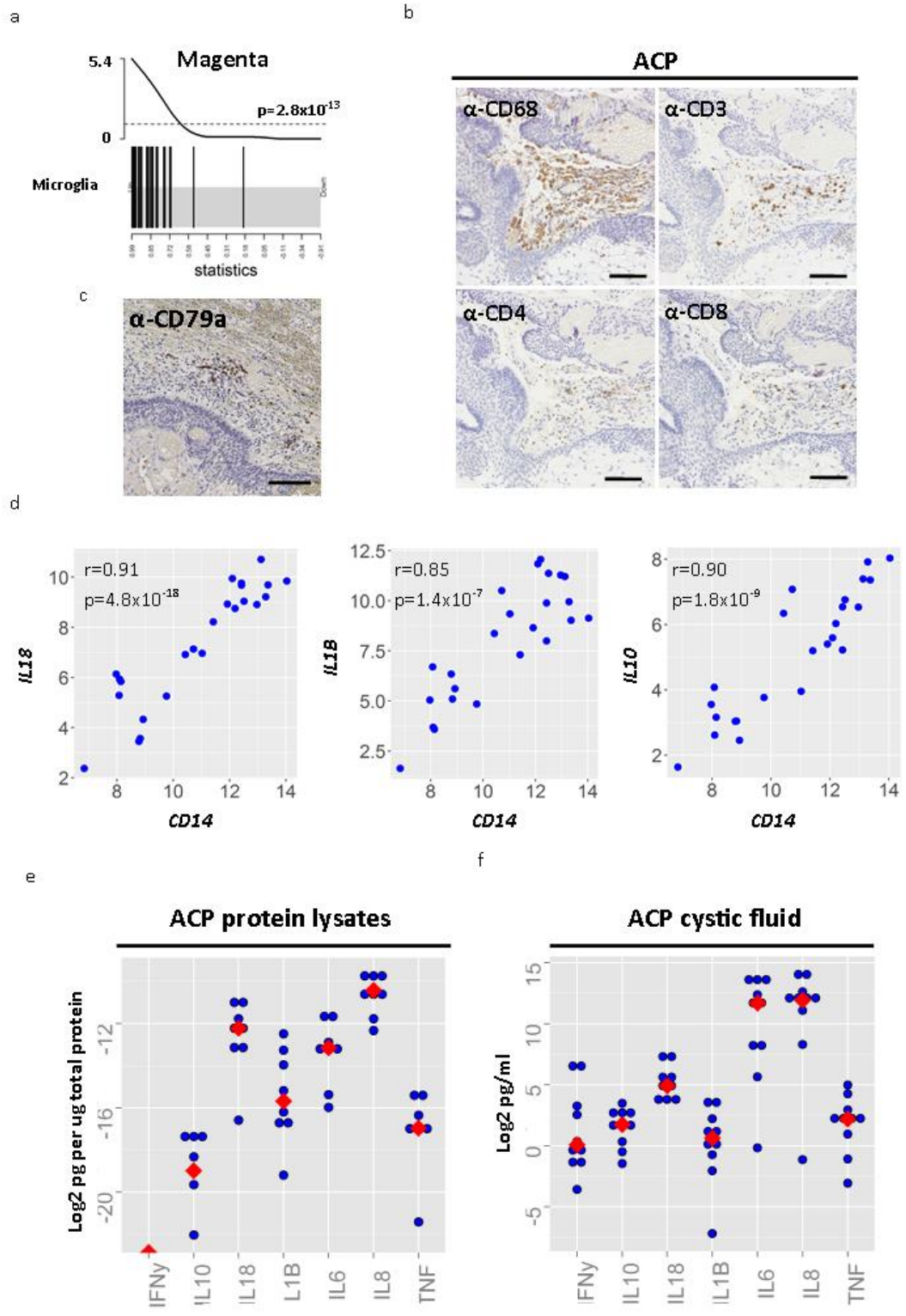

Figure 5-25: Proteins in cystic fluid derive from tumour epithelia and reactive tissue. a) GSEA plot showing that cystic fluid protein genes are overall expressed more highly in the reactive tissue rather than tumour. B) Barcode plots showing that cystic fluid proteins are expressed within the black module (associated with wet keratin) and magenta module (inflammatory infiltrate).

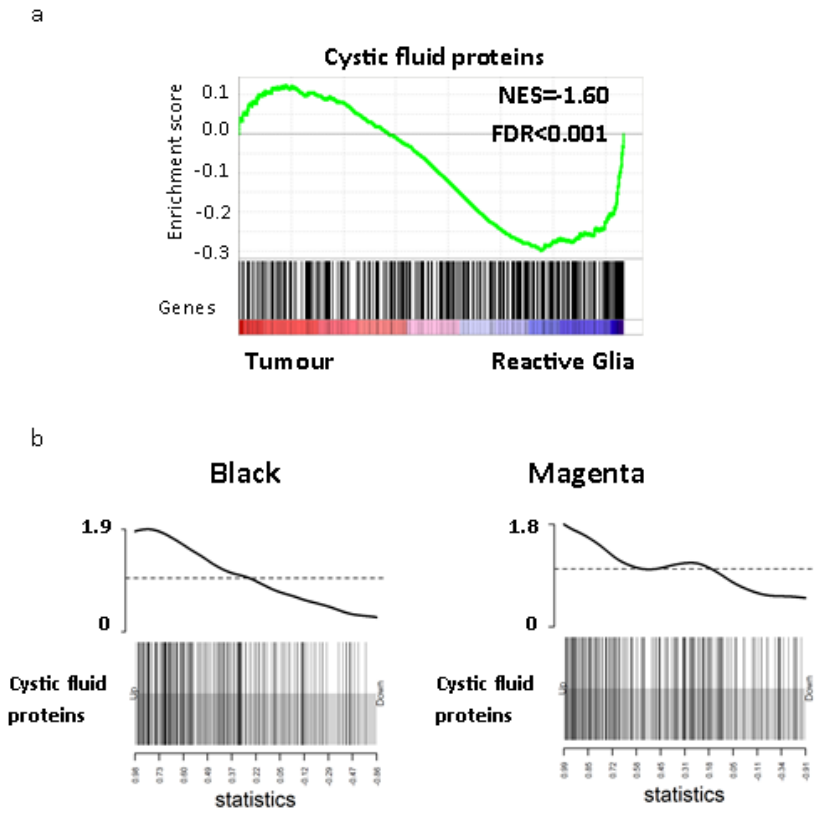

Figure 5-26: Inflammasome activation underlies inflammation in ACP. a) Correlation between IL6, IL8 and TNF in cystic fluid with IL1β. b) CD68+ve cells and CCL2 expression around cholesterol clefts (arrow) within ACP. c) GSEA plots showing enrichment of IL1β response signatures and atherosclerosis gene expression in ACP.

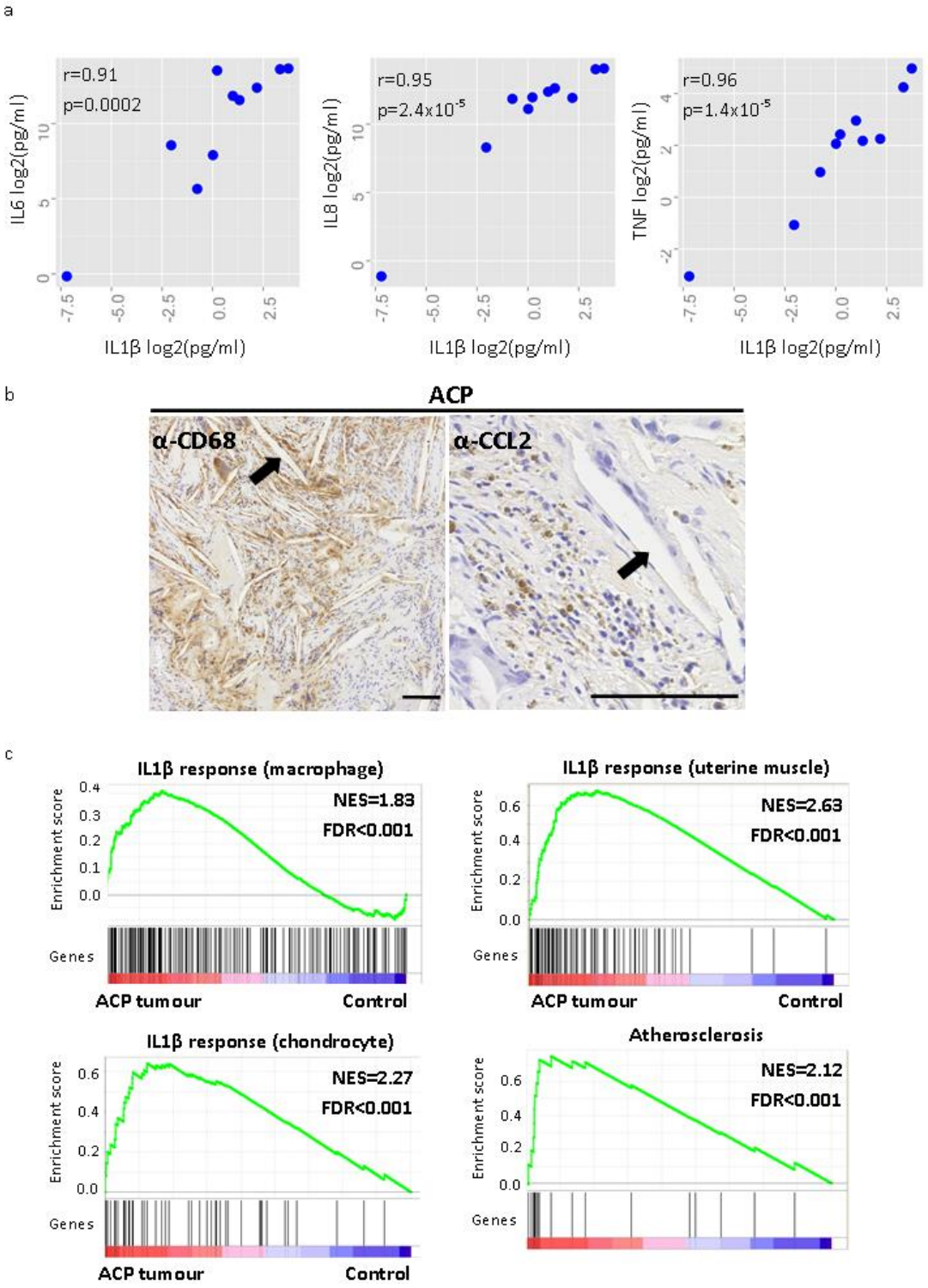

5.17 Chapter summary/Discussion

The expression analyses presented in this chapter significantly advance our understanding of the molecular profiles of ACP. They highlight a complex transcriptional landscape, which reflects the underlying histology and a complex autocrine and paracrine signalling network between various tumour, glial and immune cell types.

The expression and activation of many of the genes and pathways identified by these analyses are consistent with the published literature and/or have been confirmed by immunohistochemistry, or by independent experiments within the group. In addition novel ACP genes (e.g. *BCL11B*) genes and pathways (e.g. ectodysplasin) have been identified and validated by immunohistochemistry.

Returning to the specific scientific questions highlighted on page 132.

5.17.1 Are there distinct biological subtypes of ACP?

Whilst clustering analyses initially suggested two subgroups, further analysis suggested that this related to sampling as opposed to true biological subgroups. These results highlight the challenges of such clustering analyses in small sample cohorts, and the caution required in interpretation of results.

Despite this negative result, ACPs remain clinically heterogeneous tumours, both in their clinical course but also in histology. Dissecting the molecular basis of this is likely to require larger cohorts, and accurate integration of clinical and histological features.

5.17.2 What biological pathways are active within human ACP?

The results highlight a number of pathways active within ACP and a complex pattern of autocrine and paracrine signalling. Activation of an inflammasome-mediated response is apparent within the tumour microenvironment and activation of a senescent phenotype amongst ACP clusters.

5.17.3 Can this inform about the origin of tumours?

In this chapter, the molecular relationship of ACP with tooth development has also begun to be unravelled, particularly the similarities with amelogenesis, with clusters closely resembling the enamel knot, a critical signalling centre of the developing tooth. The developing pituitary shares an oral ectoderm origin with enamel epithelium and these results would be consistent with both theories of origin, that either pituitary precursor cells have been diverted down an ameloblast lineage differentiation programme, or that tumours derive from enamel rests. The cell of origin is further addressed in Chapter 6, with relation to the murine ACP models.

5.17.4 What therapeutically targetable pathways are active within ACP?

This analysis has identified several therapeutically targetable pathways. These will be considered in more detail in later chapters and in the discussion. Briefly, of the paracrine signalling pathways, the sonic hedgehog pathway inhibitors are in clinical use for other malignancies and will be discussed further in Chapter 8. The FGFR and MAPK pathways are targetable by a number of agents, the most advanced of which are MEK inhibitors, for which favourable responses are seen in other paediatric brain tumours (Zhao and Adjei 2014). The EDAR pathway is also therapeutically attractive due to its less pleiotropic activities. WNT, TGFb and BMP pathways have not been successfully targeted clinically to date, but remain of interest therapeutically.

In addition to targeting the paracrine signalling pathways, interrogation of the immune microenvironment suggests several novel therapeutic approaches. Specifically targeting of the IL1β, but also targeting of other inflammatory mediators, e.g. IL6, TNFa, complement. Finally, the work in this thesis supports work by others of a role of senescence and SASP in driving tumourigenesis and there is considerable interest in developing targeted therapies to eliminate senescent cells.

Chapter 6 Characterising the mouse models of ACP

6.1 Introduction

In Chapter 3, the non-linear growth dynamics of *Hesx1*$^{Cre/+}$*;Ctnnb1*$^{lox(ex3)/+}$ mice were revealed by serial MRI imaging. Dr Mario Gonzalez-Meljem, using lineage tracing, has shown the non-cell autonomous origin of tumour cells in the post-expansion and late-stage tumours (Figure 1-2), but the cell of origin and exact signalling mechanisms underlying this have not been elucidated. In this chapter I use RNA sequencing of *Hesx1*$^{Cre/+}$*;Ctnnb1*$^{lox(ex3)/+}$ pituitaries and tumours at various stages of development to explore and address:

- The temporal dynamics of gene expression across tumour stages, including of specific pathways explored in human ACP in Chapter 5.
- The relationship of murine ACP to odontogenesis.
- The cellular phenotype and cell of origin of late stage tumours.
- Whether murine ACP clusters exhibit a transcriptional signature of cellular senescence.
- The relationship of murine clusters and tumours with human ACP clusters and tumours.

6.2 Samples and datasets

Hesx1$^{Cre/+}$*;Ctnnb1*$^{lox(ex3)/+}$ pituitaries were collected at birth (P1), at humane end-point (late stage tumours) and at mid stages (9.9 & 13.4 weeks) referred to as 'pre-expansion', meaning macroscopically enlarged but without any discrete lesion (as in Figure 1-2and Figure 3-3), or 'post-expansion', where there was enlargement of a defined area, but pituitary tissue could still be identified macroscopically. In addition *Ctnnb1*$^{lox(ex3)/+}$ mice, functionally wild-type due to the lack of Cre-recombinase expression, adult and P1 pituitaries were collected as controls (Table 6-1). Of note methodologically, the small size of the P1 samples required them to be extracted by the Qiagen RNeasy micro-kit, rather than the mini-kit, and the low RNA yield (31-88ng/µl) required amplification prior to sequencing.

In addition to the samples of wildtype and *Hesx1*$^{Cre/+}$*;Ctnnb1*$^{lox(ex3)/+}$ pituitaries, further samples of late stage tumours from *Hesx1*$^{Cre/+}$*;Ctnnb1*$^{lox(ex3)/+}$*;Trp53*$^{fl/fl}$ mice were also included in this study. These were provided by Dr Mario Gonzalez-Meljem, who had recently demonstrated using lineage tracing that, in contrast to the *Hesx1*$^{Cre/+}$*;Ctnnb1*$^{lox(ex3)/+}$ tumours, tumours in the p53-deficient mice developed in a cell-autonomous manner (M. Gonzalez-Meljem, personal communication).

The expression microarray profile of clusters in E18.5 *Hesx1*$^{Cre/+}$*;Ctnnb1*$^{lox(ex3)/+}$ mice has previously been published and I further analysed this dataset to gain insight into the processes and signalling pathways (Andoniadou, Gaston-Massuet et al. 2012). Separately another PhD student, Scott Haston, had performed RNA sequencing on flow cytometry separated adult pituitary stem cells with and without activation of oncogenic β catenin (YFP positive *Sox2*$^{CreERT2/+}$*;Ctnnb1*$^{lox(ex3}$*;Rosa26*$^{YFP/+}$ and *Sox2*$^{CreERT2/+}$*;Rosa26*$^{YFP/+}$ cells respectively). This dataset is also analysed and interrogated.

Table 6-1: Samples undergoing RNA sequencing.

Sample Name	Sequencing ID	Genotype	Sample	Age	Extraction/ Amplification
WTP1.1	WT1P0.1	$Ctnnb1^{lox(ex3)/+}$	Wildtype pituitary	P1	Micro/Yes
WTP1.2	WT1P0.2	$Ctnnb1^{lox(ex3)/+}$	Wildtype pituitary	P1	Micro/Yes
WTP1.3	WT1P0.3	$Ctnnb1^{lox(ex3)/+}$	Wildtype pituitary	P1	Micro/Yes
WTP1.4	WT1P0.4	$Ctnnb1^{lox(ex3)/+}$	Wildtype pituitary	P1	Micro/Yes
PTP1.1	MP0.1	$Hesx1^{Cre/+}$;$Ctnnb1^{lox(ex3)/+}$	Pre-tumoural pituitary	P1	Micro/Yes
PTP1.2	MP0.2	$Hesx1^{Cre/+}$;$Ctnnb1^{lox(ex3)/+}$	Pre-tumoural pituitary	P1	Micro/Yes
PTP1.3	MP0.3	$Hesx1^{Cre/+}$;$Ctnnb1^{lox(ex3)/+}$	Pre-tumoural pituitary	P1	Micro/Yes
WT1	WT1	$Ctnnb1^{lox(ex3)/+}$	Normal pituitary	9.1 weeks	Mini/No
WT2	WT2	$Ctnnb1^{lox(ex3)/+}$	Normal pituitary	9.1 weeks	Mini/No
WT3	WT4	$Ctnnb1^{lox(ex3)/+}$	Normal pituitary	9.1 weeks	Mini/No
LST1	10.5.1	$Hesx1^{Cre/+}$;$Ctnnb1^{lox(ex3)/+}$	Late stage tumour	11.1weeks	Mini/No
LST2	10.5T	$Hesx1^{Cre/+}$;$Ctnnb1^{lox(ex3)/+}$	Late stage tumour	12.6weeks	Mini/No
LST3	2.3T	$Hesx1^{Cre/+}$;$Ctnnb1^{lox(ex3)/+}$	Late stage tumour	40.7weeks	Mini/No
LST4	3.2.2.T2	$Hesx1^{Cre/+}$;$Ctnnb1^{lox(ex3)/+}$	Late stage tumour	12.4weeks	Mini/No
LST5	7.5T	$Hesx1^{Cre/+}$;$Ctnnb1^{lox(ex3)/+}$	Late stage tumour	14weeks	Mini/No
LST6	B429T	$Hesx1^{Cre/+}$;$Ctnnb1^{lox(ex3)/+}$	Late stage tumour	22.7weeks	Mini/No
LST7	J13.2.1	$Hesx1^{Cre/+}$;$Ctnnb1^{lox(ex3)/+}$	Late stage tumour	12.9weeks	Mini/No
LST8	J3.3.3.FD	$Hesx1^{Cre/+}$;$Ctnnb1^{lox(ex3)/+}$	Late stage tumour	17.7weeks	Mini/No
PreExp 1	J1	$Hesx1^{Cre/+}$;$Ctnnb1^{lox(ex3)/+}$	Midstage "pre-expansion" pituitary	9.9 weeks	Mini/No
PreExp 2	J2	$Hesx1^{Cre/+}$;$Ctnnb1^{lox(ex3)/+}$	Midstage "pre-expansion" pituitary	9.9 weeks	Mini/No
PreExp 3	J5	$Hesx1^{Cre/+}$;$Ctnnb1^{lox(ex3)/+}$	Midstage "pre-expansion" pituitary y	13.4 weeks	Mini/No
PostExp 1	J3	$Hesx1^{Cre/+}$;$Ctnnb1^{lox(ex3)/+}$	"Post expansion" pituitary. 2mm lesion	9.9 weeks	Mini/No
PostExp 2	J4	$Hesx1^{Cre/+}$;$Ctnnb1^{lox(ex3)/+}$	"Post expansion" pituitary 2mm lesion, bigger	13.4 weeks	Mini/No
PostExp 3	J6	$Hesx1^{Cre/+}$;$Ctnnb1^{lox(ex3)/+}$	"Post-expansion" pituitary 3.5mm lesion	13.4 weeks	Mini/No
LST-p53.1	M1	$Hesx1^{Cre/+}$;$Ctnnb1^{lox(ex3)/+}$; $Tp53^{fl/fl}$	Mutant tumour without p53	44.7 weeks	Mini/No
LST-p53.2	M2	$Hesx1^{Cre/+}$;$Ctnnb1^{lox(ex3)/+}$; $Tp53^{fl/fl}$	Mutant tumour without p53	37.7 weeks	Mini/No
LST-p53.3	M3	$Hesx1^{Cre/+}$;$Ctnnb1^{lox(ex3)/+}$; $Tp53^{fl/fl}$	Mutant tumour without p53	44.4 weeks	Mini/No

MSP-p53.1	P1	$Hesx1^{Cre/+}$;$Ctnnb1^{lox(ex3)/+}$; $Tp53^{fl/+}$	Midstage pituitary with single copy of p53	18 weeks	Mini/No
MSP-p53.2	P2	$Hesx1^{Cre/+}$;$Ctnnb1^{lox(ex3)/+}$; $Tp53^{fl/+}$	Midstage pituitary with single copy of p53	18 weeks	Mini/No
MSP-p53.3	P3	$Hesx1^{Cre/+}$;$Ctnnb1^{lox(ex3)/+}$; $Tp53^{flf+}$	Midstage pituitary with single copy of p53	19 weeks	Mini/No

6.3 Overall distribution of samples

Initial analysis of all samples by Principle Component Analysis and Clustering highlighted separation of P1 samples (Figure 6-1). As these had undergone RNA amplification and therefore changes may reflect technical biases, they are thereafter considered separately. In addition, this analysis showed a complex relationship between other samples which will be dissected and discussed further below.

Initial analysis focused on samples from *Hesx1*$^{Cre/+}$*;Ctnnb1*$^{lox(ex3)/+}$ mice where pairwise analyses were performed between:

- P1 mutant vs wildtype pituitaries
- *Hesx1*$^{Cre/+}$*;Ctnnb1*$^{lox(ex3)/+}$ late stage tumours vs wildtype pituitaries
- Post-expansion vs pre-expansion pituitaries

As per the human analyses, differential expression analysis was performed using DESeq2. To functionally assess the resultant differentially expressed gene lists, I performed gene ontology enrichment using GOseq and gene set enrichment analysis using the Hallmark gene sets. Where pathways of interest were identified they were further analysed by interrogating genes of interest and validating expression using immunostaining.

Below are described the results of these pairwise analyses, followed by more integrated analysis, bringing together the results of several of these and exploring patterns across the sample sets using WGCNA. Full results of the pairwise analyses are presented in Supplementary Table 4.

Figure 6-1: Principal component analysis (PCA) and Hierarchical Clustering of expression signatures of all murine samples undergoing RNA sequencing. Note how on PCA (highlighted with circle) and clustering that P1 samples group separately. Other samples show a complex relationship which will be dissected in following sections and figures. Key to samples in Table 6-1.

a

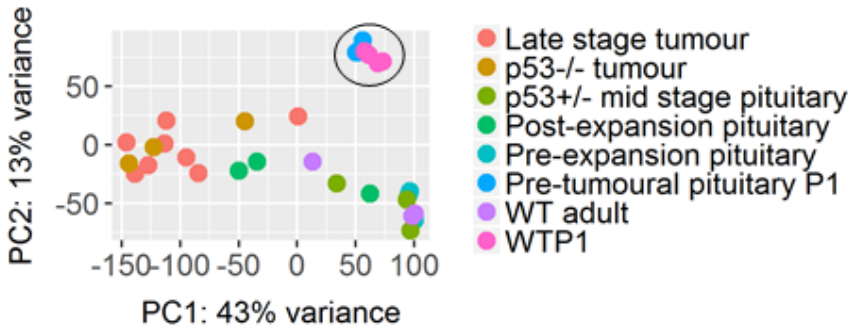

b

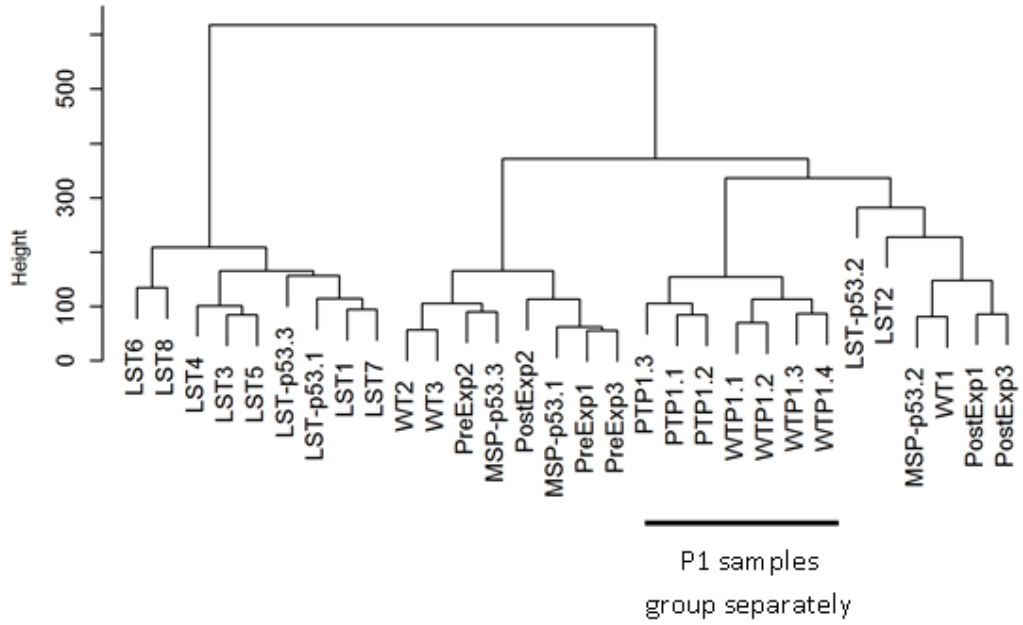

6.3.1 P1 pre-tumoural *Hesx1$^{Cre/+}$;Ctnnb1$^{lox(ex3)/+}$* vs WT pituitaries

Clustering analysis confirmed separation of WT and *Hesx1$^{Cre/+}$;Ctnnb1$^{lox(ex3)/+}$* P1 pituitaries (Figure 6-2). Differential expression analysis identified 1472 genes up-regulated and 1323 genes down-regulated in mutants (P1) compared with control (adjusted p-value <0.1). The most up-regulated genes in mutants were 4921525O09Rik (40 fold), a poorly characterised RNA, Dkk4 (27 fold), dickkopf WNT signalling pathway inhibitor 4, with *Fgf20* (17 fold), *Fgf3* (13 fold), *Fgf4* (10 fold) and *Shh* (10 fold) also among the 20 most up-regulated genes. These genes are known to be highly expressed in human tumours and murine ACP clusters (Andoniadou, Gaston-Massuet et al. 2012).

The most down-regulated genes were pituitary hormones, growth hormone (*Gh*) and thyroid stimulating hormone (*Tshb*) (10.5 and 10.1 fold respectively), consistent with pituitary differentiation defects and the growth hormone deficient phenotype of mice as previously described (Gaston-Massuet, Andoniadou et al. 2011). Gene ontology enrichment analysis identified enrichment of over 500 gene ontologies in tumours. These included a range of processes including many relating to developmental processes (Supplementary Table 4). To further refine the specific pathways activated in the expression signature of mutant pituitaries, gene set enrichment analysis (GSEA) was performed using the hallmark gene sets from the Broad Institute. Of these 50 gene sets, 20 were enriched with a false discovery rate <0.25 (Table 6-3). Of note there was enrichment of the WNT and SHH signalling within the mutant pituitary (NES =1.90, 1.88 respectively, FDR<0.001). The most enriched gene set in mutant pituitaries was for an epithelial to mesenchymal (EMT) transition signature within the mutant pituitaries.

Angiogenesis was also enriched (NES=2.01, FDR<-0.001), consistent with the influx of endomucin positive cells observed at this stage.

Figure 6-2: Analysis of P1 *Hesx1*$^{Cre/+}$*;Ctnnb1*$^{lox(ex3)/+}$ pre-tumoural pituitaries compared with p1 WT pituitaries. a) PCA and hierarchical clustering showing separation of mutant and WT pituitaries b) GSEA showing enrichment of gene signatures of EMT, angiogenesis, WNT and HH signalling within *Hesx1*$^{Cre/+}$*;Ctnnb1*$^{lox(ex3)/+}$ pre-tumoural pituitaries.

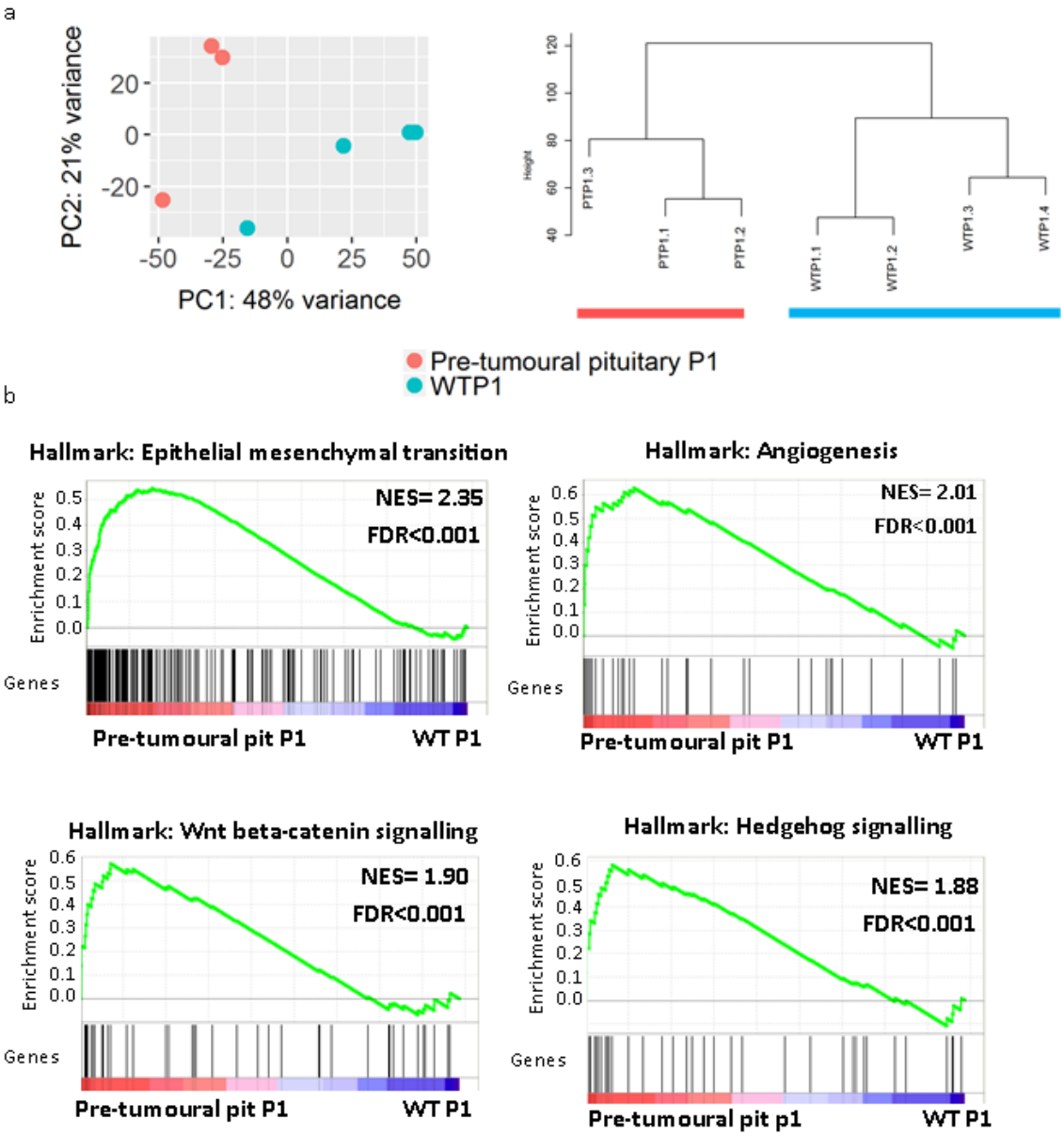

Table 6-2: Top 15 most up-regulated genes in P1 mutant pituitaries compared with controls.

Gene Symbol	Fold Change (log2)	Adjusted p-value
4921525O09Rik	5.306164	2.25E-48
Dkk4	4.780541	1.32E-38
Fgf20	4.094317	2.81E-23
Cdx1	4.064522	1.74E-24
Fgf3	3.774897	1.79E-19
Zfp385c	3.732687	5.69E-30
Fgf4	3.703927	1.42E-19
Notum	3.435146	1.22E-53
Foxa2	3.39915	1.89E-21
Pglyrp1	3.362144	6.22E-23
Shh	3.360002	1.54E-20
S100a14	3.303215	3.43E-34
Col9a1	2.980082	5.78E-41
S100a6	2.978218	5.60E-43
Fndc1	2.951818	7.70E-30

Table 6-3: 20 Hallmark gene sets enriched in mutant pituitaries. Where FDR=0.000, this indicates level <0.001.

Gene set	Size	Normalised Erichment Score (NES)	False disocvery rate (FDR)
HALLMARK_EPITHELIAL_MESENCHYMAL_TRANSITION	191	2.36	0.000
HALLMARK_ANGIOGENESIS	33	2.01	0.000
HALLMARK_APICAL_SURFACE	44	1.95	0.000
HALLMARK_APICAL_JUNCTION	191	1.94	0.000
HALLMARK_WNT_BETA_CATENIN_SIGNALING	41	1.90	0.000
HALLMARK_HEDGEHOG_SIGNALING	35	1.88	0.000
HALLMARK_NOTCH_SIGNALING	31	1.87	0.000
HALLMARK_COAGULATION	131	1.79	0.001
HALLMARK_ESTROGEN_RESPONSE_EARLY	195	1.74	0.003
HALLMARK_XENOBIOTIC_METABOLISM	184	1.70	0.004
HALLMARK_ESTROGEN_RESPONSE_LATE	190	1.69	0.004
HALLMARK_IL6_JAK_STAT3_SIGNALING	85	1.67	0.004
HALLMARK_UV_RESPONSE_DN	141	1.61	0.006
HALLMARK_P53_PATHWAY	193	1.60	0.007
HALLMARK_MYOGENESIS	197	1.59	0.007
HALLMARK_KRAS_SIGNALING_DN	182	1.58	0.007
HALLMARK_FATTY_ACID_METABOLISM	146	1.57	0.007
HALLMARK_TGF_BETA_SIGNALING	54	1.57	0.007
HALLMARK_KRAS_SIGNALING_UP	190	1.51	0.013
HALLMARK_INFLAMMATORY_RESPONSE	194	1.45	0.023

6.3.2 Post-expansion vs Pre-expansion *Hesx1$^{Cre/+}$;Ctnnb1$^{lox(ex3)/+}$* pituitaries

Next pre- and post- expansion mid-stage pituitaries were compared. PCA and Clustering suggested that sample J4 overall grouped more closely with pre-expansion pituitaries than post expansion pituitaries (Figure 6-3). I therefore removed sample J4 and performed differential expression between the remaining samples. This identified 5322 genes up-regulated and 5023 genes down-regulated in post-expansion samples. The most overexpressed gene was *Dspp* (1335 fold) encoding Dentin sialophosphoprotein, which as discussed in Chapter 5 is expressed within odontoblasts. Other genes expressed by odontoblasts were also markedly up-regulated including *Ibsp* (bone sialoprotein, 384 fold), *Sp7* (Osterix, 166 fold), *Dmp1* (dentin matrix protein, 164 fold), *Bglap* (osteocalcin, 39 fold), *Runx2* (12 fold).

Inspecting the expression of *Dspp* and *Ibsp* across all samples demonstrated upregulation of *Dspp* in post expansion pituitaries but not late stage tumours suggesting that expression is transient for this stage (Figure 6-3). Sample J4 exhibited intermediate expression between pre and post expansion stages consistent, consistent with an intermediate stage of tumourigenesis.

Gene set expression analysis identified enrichment of 36/50 of the Hallmark gene sets (Figure 6-3, Table 6-5: Hallmark gene sets enriched in post expansion *Hesx1$^{Cre/+}$;Ctnnb1$^{lox(ex3)/+}$* pituitaries. Table 6-5). These are similar to those subsequently identified comparing late stage tumours with wild type pituitaries, the significance of which will be discussed in section 6.3.3.

Figure 6-3: Post- vs pre- expansion mid stage *Hesx1*$^{Cre/+}$;*Ctnnb1*$^{lox(ex3)/+}$ pituitaries. a) Principal Component Analysis and Hierarchical Clustering showing separation of pre- and post- expansion pituitaries with sample PostExp2/J4 at intermediate stage. b) Normalised expression values of *Dspp* and *Ibsp* across tumour stages.

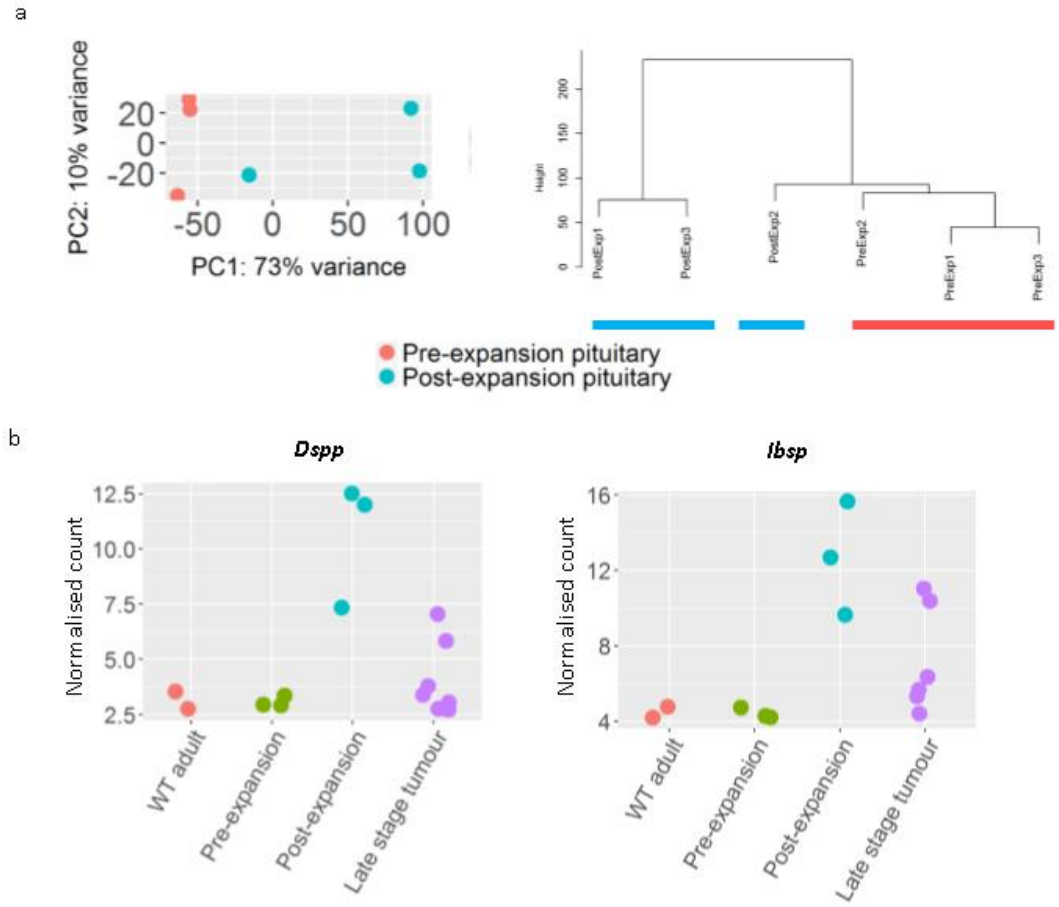

Table 6-4: Top 15 up-regulated genes in post-expansion compared with pre-expansion *Hesx1$^{Cre/+}$;Ctnnb1$^{lox(ex3)/+}$* pituitaries.

Gene Symbol	Fold Change (log2)	Adjusted p-value
Dspp	10.38293	3.76E-112
Lrrc15	8.586415	1.14E-37
Ibsp	8.327409	2.53E-24
Panx3	8.175649	2.25E-27
Hoxd9	8.013229	5.80E-121
Prdm6	7.907269	1.75E-129
Hoxd8	7.744906	1.66E-119
Dkk1	7.721082	6.65E-36
Apela	7.653791	2.9E-61
Sp7	7.377877	1.49E-46
Prss35	7.370249	7.51E-35
Dmp1	7.362322	1.54E-45
Ifitm5	7.297831	1.02E-29
Hoxd4	7.294897	1.4E-46
Prph	7.282815	3.92E-115

Table 6-5: Hallmark gene sets enriched in post expansion *Hesx1$^{Cre/+}$;Ctnnb1$^{lox(ex3)/+}$* pituitaries.

Gene set	Size	Normalised Erichment Score (NES)	False disocvery rate (FDR)
HALLMARK_MYC_TARGETS_V1	197	2.69	0.000
HALLMARK_E2F_TARGETS	194	2.54	0.000
HALLMARK_EPITHELIAL_MESENCHYMAL_TRANSITION	191	2.46	0.000
HALLMARK_G2M_CHECKPOINT	194	2.41	0.000
HALLMARK_MYC_TARGETS_V2	58	2.24	0.000
HALLMARK_TGF_BETA_SIGNALING	54	2.22	0.000
HALLMARK_WNT_BETA_CATENIN_SIGNALING	41	1.99	0.000
HALLMARK_MITOTIC_SPINDLE	196	1.90	0.000
HALLMARK_TNFA_SIGNALING_VIA_NFKB	195	1.87	0.000
HALLMARK_APICAL_JUNCTION	190	1.81	0.000
HALLMARK_ANGIOGENESIS	35	1.79	0.000
HALLMARK_COAGULATION	123	1.70	0.002
HALLMARK_IL2_STAT5_SIGNALING	190	1.69	0.002
HALLMARK_APOPTOSIS	155	1.66	0.003
HALLMARK_MYOGENESIS	196	1.59	0.007
HALLMARK_P53_PATHWAY	193	1.56	0.010
HALLMARK_IL6_JAK_STAT3_SIGNALING	84	1.56	0.010
HALLMARK_UV_RESPONSE_DN	141	1.52	0.017
HALLMARK_HYPOXIA	192	1.48	0.024
HALLMARK_MTORC1_SIGNALING	193	1.45	0.029
HALLMARK_ADIPOGENESIS	193	1.44	0.033
HALLMARK_NOTCH_SIGNALING	31	1.44	0.032
HALLMARK_OXIDATIVE_PHOSPHORYLATION	192	1.43	0.031
HALLMARK_ESTROGEN_RESPONSE_EARLY	194	1.40	0.041
HALLMARK_DNA_REPAIR	139	1.39	0.042
HALLMARK_CHOLESTEROL_HOMEOSTASIS	67	1.37	0.053
HALLMARK_INFLAMMATORY_RESPONSE	194	1.36	0.056
HALLMARK_GLYCOLYSIS	192	1.35	0.055
HALLMARK_COMPLEMENT	177	1.34	0.058
HALLMARK_ANDROGEN_RESPONSE	95	1.33	0.065
HALLMARK_UV_RESPONSE_UP	150	1.24	0.142
HALLMARK_ALLOGRAFT_REJECTION	180	1.24	0.139
HALLMARK_UNFOLDED_PROTEIN_RESPONSE	112	1.23	0.145
HALLMARK_PI3K_AKT_MTOR_SIGNALING	102	1.19	0.183
HALLMARK_HEME_METABOLISM	181	1.19	0.187
HALLMARK_KRAS_SIGNALING_UP	190	1.17	0.198

6.3.3 Late stage *Hesx1*$^{Cre/+}$;*Ctnnb1*$^{lox(ex3)/+}$ tumours vs wild-type adult pituitaries

Next, late stage tumours and wild-type adult pituitaries were compared. Clustering revealed that the majority of tumours separated from controls with the exception of LST2/10.5T (Figure 6-4). Review of histology of this sample revealed that in addition to tumour tissue, neighbouring normal brain had also been collected. Similarly, it was later shown that WT1 expression pattern resembled that seen in post-expansion *Hesx1*$^{Cre/+}$;*Ctnnb1*$^{lox(ex3)/+}$ pituitaries (despite review of genotyping confirming WT expression) and therefore this was also excluded (see Section 6.3.4). Differential expression was therefore performed between the remaining seven tumours and two wild type pituitaries.

This identified 4565 genes up-regulated and 4585 down-regulated in the murine ACP tumours. The most up-regulated genes are shown in Table 6-6. The non-coding RNA *Fendrr* was the most up-regulated in tumours (765 fold). The notochord/chordoma marker Brachyury (*T*) was the third most up-regulated gene (510 fold) (Figure 6-4b). *Smco2* was the most down-regulated (265 fold) whilst Growth hormone (*Gh)* was the ninth most down-regulated (159 fold).

Ontology enrichment of the top 1000 up-regulated genes identified enrichment of developmental processes, including terms specific to many organs (e.g. skin, teeth, heart, kidney, muscle, pancreas) (Supplementary Table 4). Gene set enrichment identified upregulation of 37 hallmark gene sets in tumours of which EMT, MYC, E2F, TGFB and WNT signalling were the most up-regulated (Table 6-7).

The high expression of EMT gene sets suggest these tumours exhibit a predominantly mesenchymal phenotype, possibly indicating a mesenchymal cell of origin. The enrichment of MYC, E2F targets, G2M checkpoint, mitotic spindle gene-sets may reflect the proliferative nature of late stage tumours.

Further visual inspection of the genes up-regulated within the tumours compared with WT controls identified genes including FGFs (e.g. *Fgf4*, 110 fold), BMPs (e.g.

Bmp4, 55 fold), TGFB (e.g *Tgfb1,* 10 fold), and the germ cell tumour and hepatoblastoma marker *Afp* (Alpha feto-protein, 150 fold) (Figure 6-4b).

Figure 6-4: Late stage *Hesx1*$^{Cre/+}$;*Ctnnb1*$^{lox(ex3)/+}$ tumours . a) PCA and hierarchical clustering showing separation of late stage and WT tumours. Outliers LST2 and WT1 are highlighted and were not included in differential expression analysis. b) Normalised expression values of *T* and *Afp* across tumour stages. c) GSEA plots showing enrichment of signatures of EMT, Myc, TGFb and Wnt signalling in tumours compared with wild-type pituitaries.

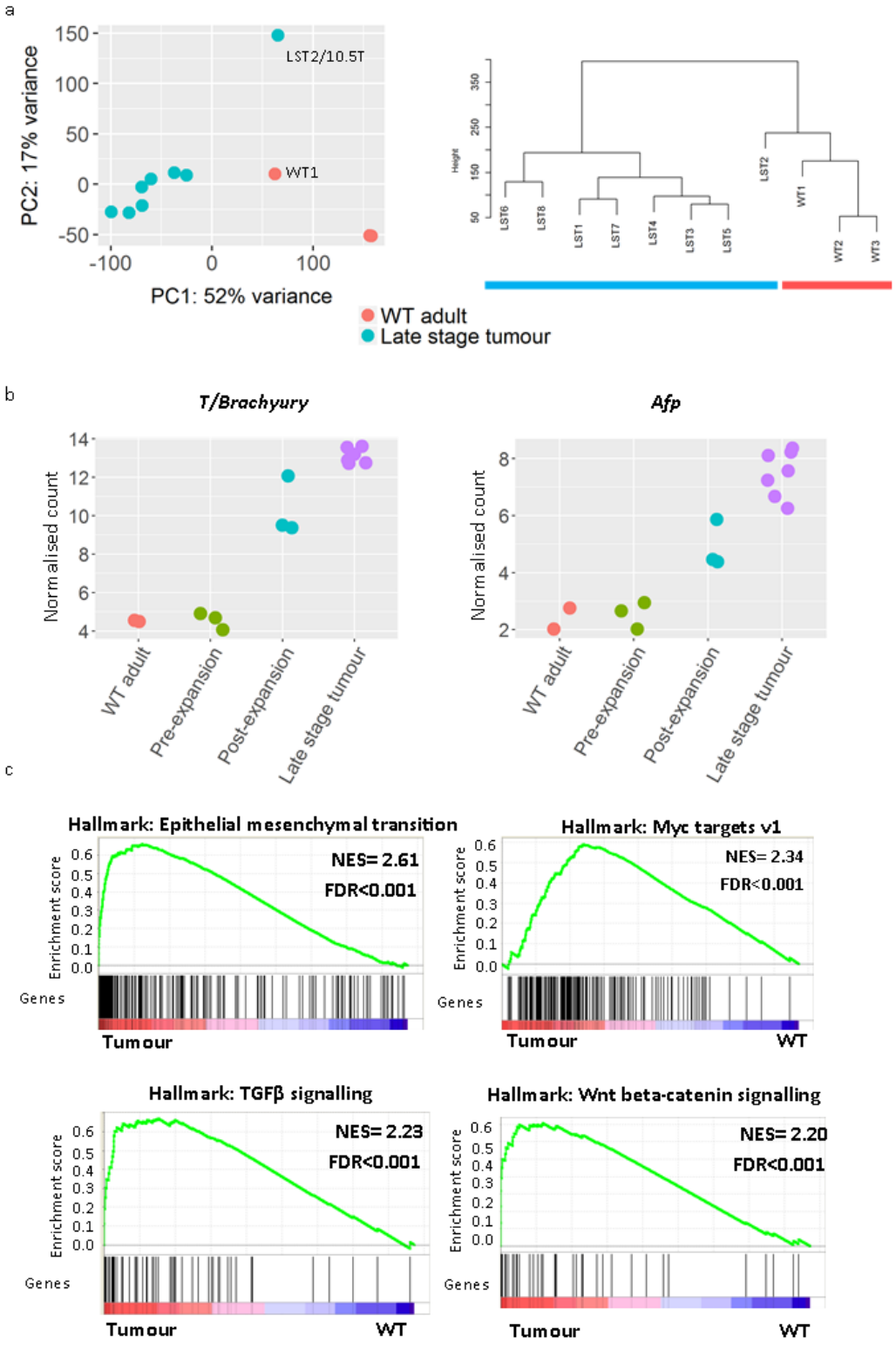

Table 6-6: 15 most up-regulated genes in late stage *Hesx1$^{Cre/+}$;Ctnnb1$^{lox(ex3)/+}$* tumours compared with controls.

Gene Symbol	Fold Change (log2)	Adjusted p-value
Fendrr	9.580897	1.02E-47
Gbx2	9.317008	1.18E-74
T	8.994956	1.02E-109
R3hdml	8.820336	5.77E-55
Tbx4	8.788391	9.97E-107
Wif1	8.742061	3.13E-257
Hoxd3	8.731874	3.33E-18
Hoxd9	8.688136	3.45E-52
Notum	8.65695	2.00E-281
Foxa2	8.604187	7.25E-48
Camkv	8.557676	1.85E-71
Adra2a	8.529267	1.77E-89
Slc35f2	8.486406	1.45E-53
Igfn1	8.481606	2.84E-30
Tnnt2	8.423523	6.02E-26

Table 6-7: 37 Hallmark gene sets up-regulated in late stage *Hesx1$^{Cre/+}$;Ctnnb1$^{lox(ex3)/+}$* tumours compared with wild-type adult pituitaries.

Gene set	Size	Normalised Erichment Score (NES)	False disocvery rate (FDR)
HALLMARK_EPITHELIAL_MESENCHYMAL_TRANSITION	191	2.612846	0.000
HALLMARK_MYC_TARGETS_V1	197	2.343957	0.000
HALLMARK_E2F_TARGETS	194	2.342108	0.000
HALLMARK_TGF_BETA_SIGNALING	54	2.235166	0.000
HALLMARK_WNT_BETA_CATENIN_SIGNALING	41	2.200653	0.000
HALLMARK_G2M_CHECKPOINT	193	2.185311	0.000
HALLMARK_APICAL_JUNCTION	191	2.04943	0.000
HALLMARK_MITOTIC_SPINDLE	197	2.014696	0.000
HALLMARK_COAGULATION	127	1.987355	0.000
HALLMARK_MYOGENESIS	196	1.964852	0.000
HALLMARK_MYC_TARGETS_V2	58	1.941042	0.000
HALLMARK_ANGIOGENESIS	35	1.929029	0.000
HALLMARK_NOTCH_SIGNALING	31	1.913098	0.000
HALLMARK_UV_RESPONSE_DN	141	1.812816	5.99E-04
HALLMARK_IL6_JAK_STAT3_SIGNALING	84	1.799928	5.59E-04
HALLMARK_P53_PATHWAY	193	1.793195	5.25E-04
HALLMARK_TNFA_SIGNALING_VIA_NFKB	195	1.780684	5.91E-04
HALLMARK_IL2_STAT5_SIGNALING	189	1.774185	5.58E-04
HALLMARK_APOPTOSIS	155	1.768525	5.29E-04
HALLMARK_APICAL_SURFACE	44	1.734614	8.94E-04
HALLMARK_COMPLEMENT	178	1.545644	0.009134
HALLMARK_HYPOXIA	192	1.538911	0.00955
HALLMARK_ADIPOGENESIS	193	1.341692	0.061569
HALLMARK_GLYCOLYSIS	192	1.286769	0.096111
HALLMARK_UV_RESPONSE_UP	150	1.236009	0.131886
HALLMARK_HEME_METABOLISM	183	1.226492	0.137333
HALLMARK_KRAS_SIGNALING_UP	190	1.219113	0.140897
HALLMARK_MTORC1_SIGNALING	193	1.146634	0.227027

6.3.4 Weighted gene correlation network analysis reveals patterns of expression across samples

The pairwise analyses demonstrated enrichment of signatures of MYC, WNT, TGFβ, EMT pathway activation in post expansion pituitaries and late stage tumours, suggesting common mechanisms between stages of tumour development and consistent with the progressive increases in expression of specific genes (Figure 6-4). However, analysis of a limited number of genes, e.g. *Dspp*, also exhibited non-linear patterns of expression during tumour growth, with peaks at the post-expansion stage (Figure 6-3).

To explore these patterns of expression across the samples at different stages, I performed WGCNA of the wild-type adult pituitaries, pre-expansion, post-expansion and late stage *Hesx1*$^{Cre/+}$*;Ctnnb1*$^{lox(ex3)/+}$ samples. Initial analysis highlighted 10.5T as an outlier and so this was not included in the analysis. From the remaining 16 samples, the 5000 most variably expressed genes were selected and 9 patterns of gene expression identified (Table 6-8, Figure 6-5).

Of particular note, the brown module genes were most highly expressed by tumours and there was moderate expression of the two post expansion pituitaries PostExp1/J3 and PostExp3/J6, and surprisingly of 1 adult WT (WT1) (hence its exclusion in differential expression in section 6.3.3). This module included 704 genes which were enriched from developmental pathways. Using gprofiler, to analyse the 500 genes with the highest module membership score for the brown module, also identified enrichment of KEGG pathways in cancer, Wnt signalling, Hippo signalling, TGFβ signalling and proteoglycans in Cancer. Genes within this module included *Bmp4, Bmp7, Fgf11, Fgf11, TGFβ*, as well as several of their receptors (*Fgfr1,2,3, Bmpr2)*. As expected from their expression pattern discussed in 6.3.3, *T and Afp* were also in this module.

The green module genes were also identified as highly expressed in the tumours, particularly a subset. This module was enriched for cell cycle/mitosis genes. This is consistent with variable proliferation, as evidenced by Ki67 staining, observed in late stage tumours.

The pink module of 91 genes identified genes with an expression pattern matching that of *Dspp* and *Ibsp*, high in post expansion pituitaries, but not tumours. This module was most highly enriched for genes relating to odontogenesis, including specifically of dentin-containing teeth, ossification and bio-mineral tissue development. I discuss the potential significance of this later in section 6.4 with relation to murine ACP and odontogenesis.

The remaining modules included genes predominantly expressed within the pre-expansion and wild-type pituitaries. These modules are enriched for varying biological processes and structures. The turquoise module included pituitary hormone and was enriched for neuron and endocrine organ development, the blue for synaptic signalling. The red module was enriched from keratins and skin development genes and the yellow for cilia and microtubules. Of note the black module included genes highly expressed in pre expansion and WT pituitaries and lowly expressed in tumours relate to lipid catabolism genes. It is tempting to hypothesize that low expression of such genes could relate to poor clearance of lipids and accumulation of cysts within tumours, however this would require further examination.

As with the human WGCNA analysis, the grey module includes remaining genes, a subset of which includes sex determining genes such as *Xist.*

Table 6-8: WGCNA identified nine patterns of gene expression.

Module	No. Genes	Expression pattern	Gene Ontology Enrichment	Genes of Interest
Brown	704	High expression in tumours, medium expression in post-expansion pituitaries	Developmental processes Pathways in Cancer, WNT signalling, Hippo Signalling, TGFB Proteoglycans in cancer	*T* (brachyury) Afp, Ret Bmp4,7, Tgfβ, Fgf11
Green	435	High expression in tumours, medium expression in post-expansion pituitaries	Cell cycle/Mitosis	
Pink	91	High expression in post expansion pituitaries PostExp1 & 3	Odontogenesis ossification	Dspp, Msx2, Sp6, Sp7, Fgf3, Fgf4, Dlx2, Osr1
Turquoise	1585	High expression in WT and pre-expansion pituitaries	Neuron differntiation Synaptic transport Endocrine organ development	Pituitary hormones
Blue	1316	High or low expression in WT and pre-expansion pituitaries	Synaptic signalling	
Yellow	459	Mostly high expression in WT and pre-expansion pituitaries	Cilia and microtubules	
Black	143	Mostly high expression in WT and pre-expansion pituitaries	Lipid breakdown	Includes *GFAP*
Red	212	Highest in pre-expansion pituitaries	Skin development keratinisation	Many keratins
Grey	55	Variable expression clusters based on sex		Includes sex genes e.g. *Xist*.

Figure 6-5: Weighted gene co-expression network analysis of Hesx1Cre/+;Ctnnb1lox(ex3)/+ samples. a) MDS plot highlighting expression patterns of 5000 most variably expressed genes. Genes are labelled by their module colour. Expression heatmaps of b) brown, c) green, d) pink modules.

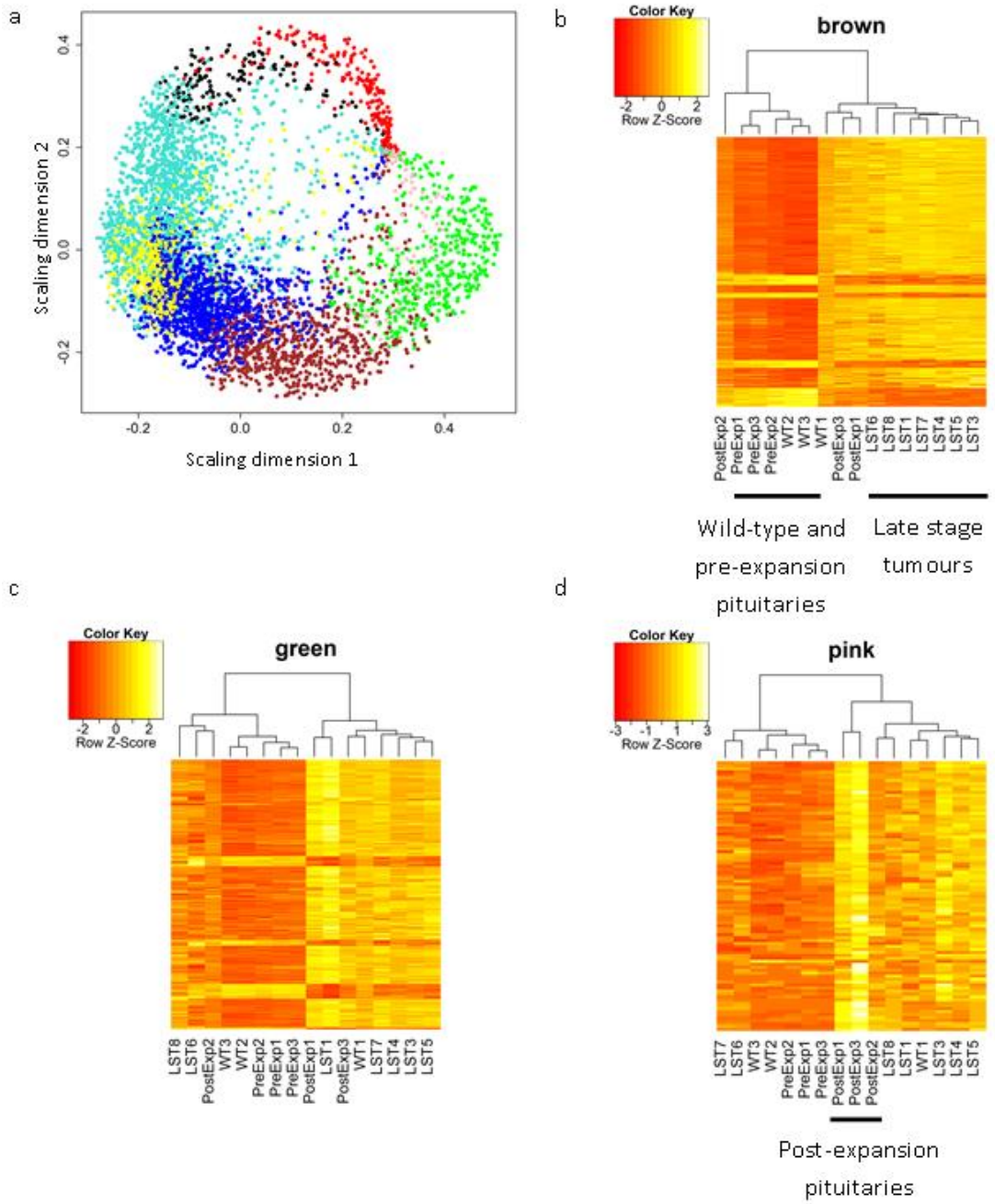

Figure 6-6: Heatmaps of remaining WGCNA modules.

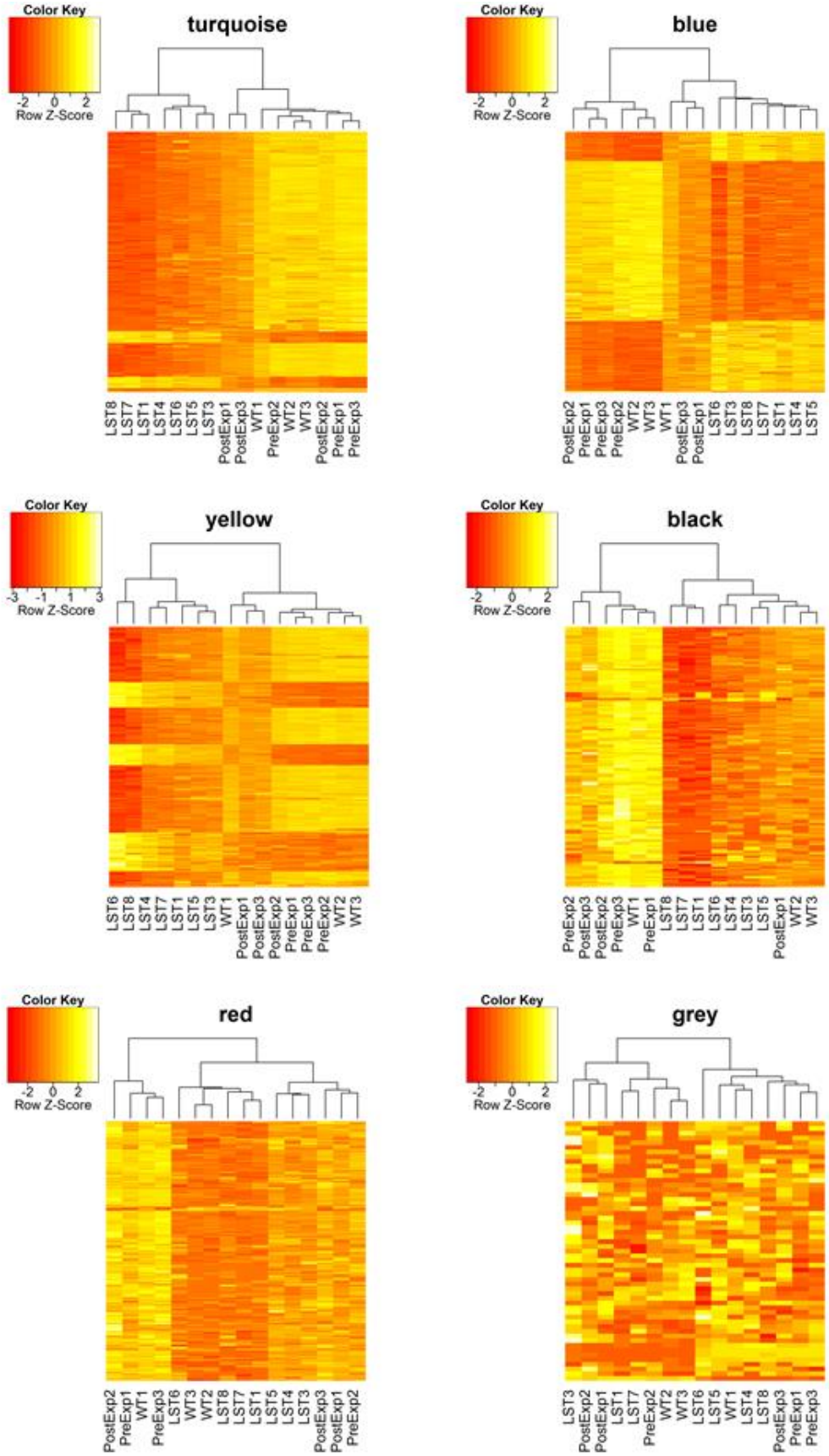

6.4 Murine ACP and odontogenesis

Results presented in Chapter 5 highlight the relationship between human ACP and odontogenesis, specifically the activation of an inner enamel epithelium and ameloblast gene signatures within human ACP and molecular similarities between the enamel knot and human ACP clusters.

Analysis of murine ACP had highlighted expression of odontoblast genes in post expansion pituitaries (section 6.3.2). In this section I further explore the relationship of the mouse models with odontogenesis.

6.4.1 *Ctnnb1* mutation activates ameloblast differentiation profile in Rathke's pouch derivatives

Analysis of P1 *Hesx1*$^{Cre/+}$;*Ctnnb1*$^{lox(ex3)/+}$ pituitaries showed upregulation of several of the ameloblast genes shown in Figure 5-13 (Supplementary Table 4), though not of enamel genes themselves. Of note *Msx2* (3.5 fold), *Dlx3* (5 fold), *Sp6* (2.8 fold) and *Edar* (2.7 fold) were all significantly up-regulated (adjusted p-value <0.01). Gene set enrichment analysis also showed activation of the inner enamel epithelium and ameloblast signatures in mutant P1 pituitaries (NES = 2.61 and 2.38 respectively, FDR< 0.001) suggesting that *Ctnnb1* mutation alone is sufficient to induce an enamel epithelium/ameloblast like differentiation programme in Rathke's pouch (

Figure 6-7).

6.4.2 Murine ACP clusters are analogous to the enamel knot

Many of the factors known to be expressed by the enamel knot have previously been shown to be expressed by murine clusters (e.g. p21, SHH, FGFs, BMPs). To further assess whether murine β-catenin accumulating clusters transcriptional profile also resembled the enamel knot, GSEA was performed, comparing clusters from both the embryonic and the inducible ACP model. In the first instance, clusters are compared with non-cluster pituitary tissue, whereas in the inducible model, Sox2 positive pituitary cells with activation of β-catenin are compared with wild-type Sox2 positive cells. In both cases the signature of the enamel knot was

enriched within β-catenin accumulating clusters (NES=2.47 & 2.47 respectively, FDR <0.001) (Table 6-7).

6.4.3 Odontoblast genes expressed in post expansion mid stage *Hesx1*$^{Cre/+}$;*Ctnnb1*$^{lox(ex3)/+}$ pituitaries

Lineage tracing highlights that at early stages of murine tumourigenesis, the majority of pituitary tissue is derived from *Hesx1* expressing tissue, other than the endomucin positive cells (Figure 1-2).

At the development of tumour growth and enlargement however the pituitary tissue becomes taken over by non *Hesx1* derived tissue. Both pairwise analysis and WGCNA highlighted the expression of odontoblast genes at the post expansion stage of tumourigenesis. Odontoblasts are neural crest derived mesenchymal cells that produce dentin. In the developing tooth their differentiation is induced through signals from the enamel epithelium and particularly signalling from the enamel knot (Balic and Thesleff 2015).

GSEA was performed to assess the expression of genes known to be expressed by dental mesenchyme or odontoblasts within post expansion *Hesx1*$^{Cre/+}$;*Ctnnb1*$^{lox(ex3)/+}$ pituitaries. This confirmed enrichment (NES 2.57 and 2.47 respectively, FDR<0.001) supporting a relationship of these non-pituitary derived cells with dental mesenchyme (Figure 6-7).

Considering the relevance of this to human ACP, case reports were reviewed where whole teeth had been reported in human ACP patients (Seemayer, Blundell et al. 1972, Muller, Adroos et al. 2011, Beaty and Ahn 2014). Where histology was reported, or available, dentin producing cells were observed, and these may reflect the non-cell autonomous processes observed in the mouse model. More common than observing the presence of complete teeth in ACP is the presence of bone like differentiation. Osteogenesis and odontogenesis are closely related processes induced by many of the same signalling pathways (e.g. BMP signalling) and so these murine results may be of relevance to this process (Kim, Kim et al. 2013).

6.4.4 Summary

Together these results suggest that similar processes are occurring during murine ACP formation as in tooth development. In murine ACP, at early stages, pituitary derived epithelium and clusters resemble IEE/ameloblasts and the enamel knot, similar to that observed in human ACP. Later, during the expansion stage, there is a non-cell autonomous accumulation of cells resembling dental mesenchyme/odontoblasts, for which analogous processes have been described in human ACP.

Figure 6-7: Relationship of *Hesx1*$^{Cre/+}$;*Ctnnb1*$^{lox(ex3)/+}$ tumourigenesis with odontogenesis. a) enrichment of inner enamel epithelium signature and ameloblast signature in P1 mutant pituitaries b) Enrichment of enamel knot genes in murine clusters from embryologic and inducible ACP models. c) Enrichment of dental mesenchyme and odontoblast signatures in post expansion stage pituitaries

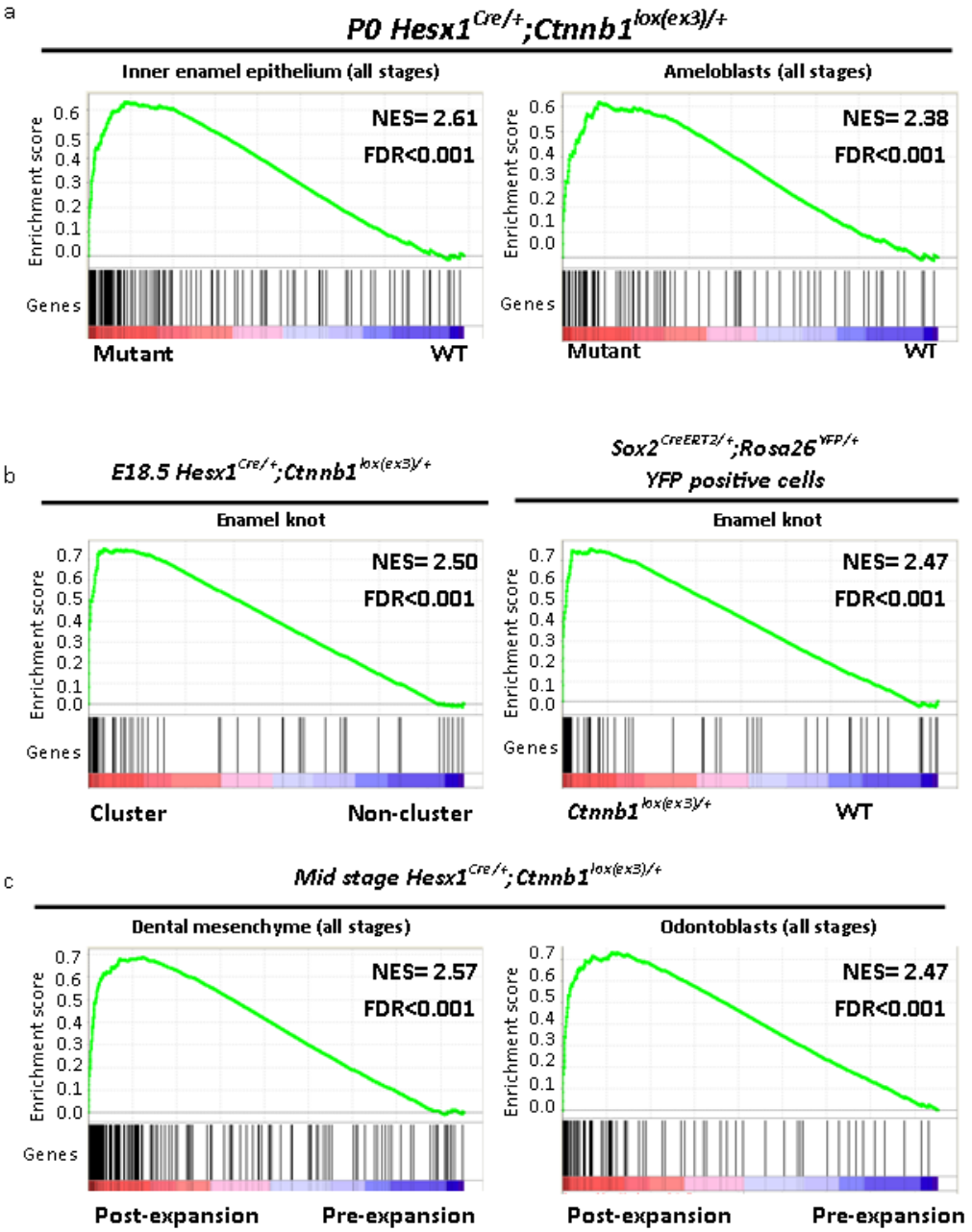

6.5 Late stage murine tumours express markers of mesenchymal stem cells

Surprisingly, the expression of odontoblast genes identified by WGCNA appears to be specific in timing to the post expansion pituitaries and these genes are not expressed/expressed less in late stage murine tumours.

Late stage tumours appear to express genes enriched for roles in developmental processes, including several different organ systems, suggesting a less differentiated state (Supplementary Table 4).

In contrast to ameloblasts and enamel, dentin can be repaired and replaced in fully developed teeth. This is due the presence of dental mesenchymal stem cells. These cells share many feature of bone marrow derived mesenchymal stem cells and are of considerable interest in regenerative medicine (Huang, Gronthos et al. 2009, Sharpe 2016). For the most part, these stem cells are likely to be pericyte derived neural crest cell derivatives, as evidenced by Ng2-Cre labelled lineage tracing experiments, but there is also increasing evidence of contribution of other cell lineages, e.g. glia (Sharpe 2016). There are several distinct types of dental mesenchymal stem cells, varying in location and function and the markers are increasingly being refined. Many are in common with other mesenchymal stem cell elsewhere in the body (Huang, Gronthos et al. 2009). Markers typically used to characterise mesenchymal stem cells are CD146 (Mcam), CD90 (Thy1), CD105 (Eng), CD13 (Anpep), CD73 (Nt5e) and the absence of haematopoetic stem cells markers (e.g. CD34, CD45 (Ptprc)) (Huang, Gronthos et al. 2009, Sharpe 2016).

Expression of these markers in murine ACP was interrogated. High CD146, CD105, CD13 and CD73 expression was observed in post-expansion pituitaries with highest expression in *Hesx1*$^{Cre/+}$*;Ctnnb1*$^{lox(ex3)/+}$ tumours (Figure 6-8). CD90 expression in contrast was low, and CD45 showed no upregulation and CD34 had variable expression (Figure 6-8).

To further investigate whether *Hesx1*$^{Cre/+}$*;Ctnnb1*$^{lox(ex3)/+}$ tumours exhibited a MSC signature the literature was searched for MSC related gene sets. Roson-Burgo *et al*,.

have recently integrated previously published an analysis of RNA sequencing and expression array datasets to identify 489 core genes expressed by mesenchymal stem cells from several organs, though not including teeth (Roson-Burgo, Sanchez-Guijo et al. 2016). Gene set enrichment analysis showed enrichment of this signature in both post-expansion pituitaries (NES=2.22, FDR<0.001) and late stage tumours (NES=2.14, FDR<0.001) (Figure 6-8).

Together, these results suggest that lesions in post expansion pituitaries express mesenchymal stem cell markers and markers of odontoblast differentiation, whereas late stage tumours are less differentiated and express other developmental genes such as *Afp* and *T (*brachury).

6.5.1 High expression of AFP suggests some similarities with intracranial germ cell tumours

The high expression of *Afp* by late stage tumours suggested a possible similarity between murine ACP and germ cell tumours. These heterogeneous tumours arise most commonly in the testis and ovary, with a subset arising in the central nervous system. Intracranial germ cell tumours typically arise in supra-sellar and pineal regions and can occur after a prolonged period of thickened pituitary stalk, a possible analogy with murine ACP tumourigenesis (Bettendorf, Fehn et al. 1999). Traditionally, these tumours are thought to have arisen from primordial germ cells that have aberrantly migrated to the CNS (Louis, Perry et al. 2016). Alternative suggestions are that they may form from native stem cell populations of embryonic or neural type and indeed have been generated in animal models from neural stem cells by overexpression of *Oct4* (Louis, Perry et al. 2016).

Intracranial germ cell tumours can be divided into several types, histologically into germinomas and non-germinomatous, which include embryonal carcinoma, yolk sac tumours, choriocarcinoma and teratomas (mature and immature) based on the secretion of tumour markers and histological features. A raised serum or CSF β-HCG is consistent with choriocarcinoma whereas embryonal cell carcinomas, immature teratomas and yolk sac tumours secrete AFP. There are also mixed types.

Given the high expression of AFP in late stage tumours, and possible mesenchymal stem cell like phenotype, the transcriptional relationship between murine ACP and intracranial germ cell tumours was further explored.

Whilst gene set enrichment using genes expressed by non germinomatous malignant germ cell tumours were enriched in murine ACP tumours (NES=2.26, FDR<0.001) (Figure 6-8), suggesting some similarity, murine ACP lack expression of embryonal stem cell markers ((Oct4 (POU5F1), Nanog, Lin28) suggesting that they are not bona fide germ cell tumours (Wang, Wu et al. 2010).

Review of the literature separately suggested rare coexistence of germ cell tumours, with craniopharyngioma, including based on high expression of AFP (Plowman, Besser et al. 2004, Moschovi, Alexiou et al. 2010, Tsoukalas, Tolia et al. 2013). Whilst full details for these cases are not available, it is possible that these rare cases could resemble the processes observed in *Hesx1*$^{Cre/+}$*;Ctnnb1*$^{lox(ex3)/+}$ tumourigenesis.

To further investigate the relationship of murine ACP with germ cell tumours the murine data included in this chapter will be integrated with the paediatric brain tumour expression dataset at the German Cancer Research Center (DKFZ) in Heidelberg (by Dr David Jones).

Figure 6-8: Mesenchmyal stem cell markers in murine ACP. a) Expression of mesenchymal stem cell markers b) GSEA shows enrichment of MSC gene set in post expansion and late stage *Hesx1*$^{Cre/+}$;*Ctnnb1*$^{lox(ex3)/+}$ tumours. c) Late stage tumours are also enriched for a signature of non germinomatous malignant germ cell tumours

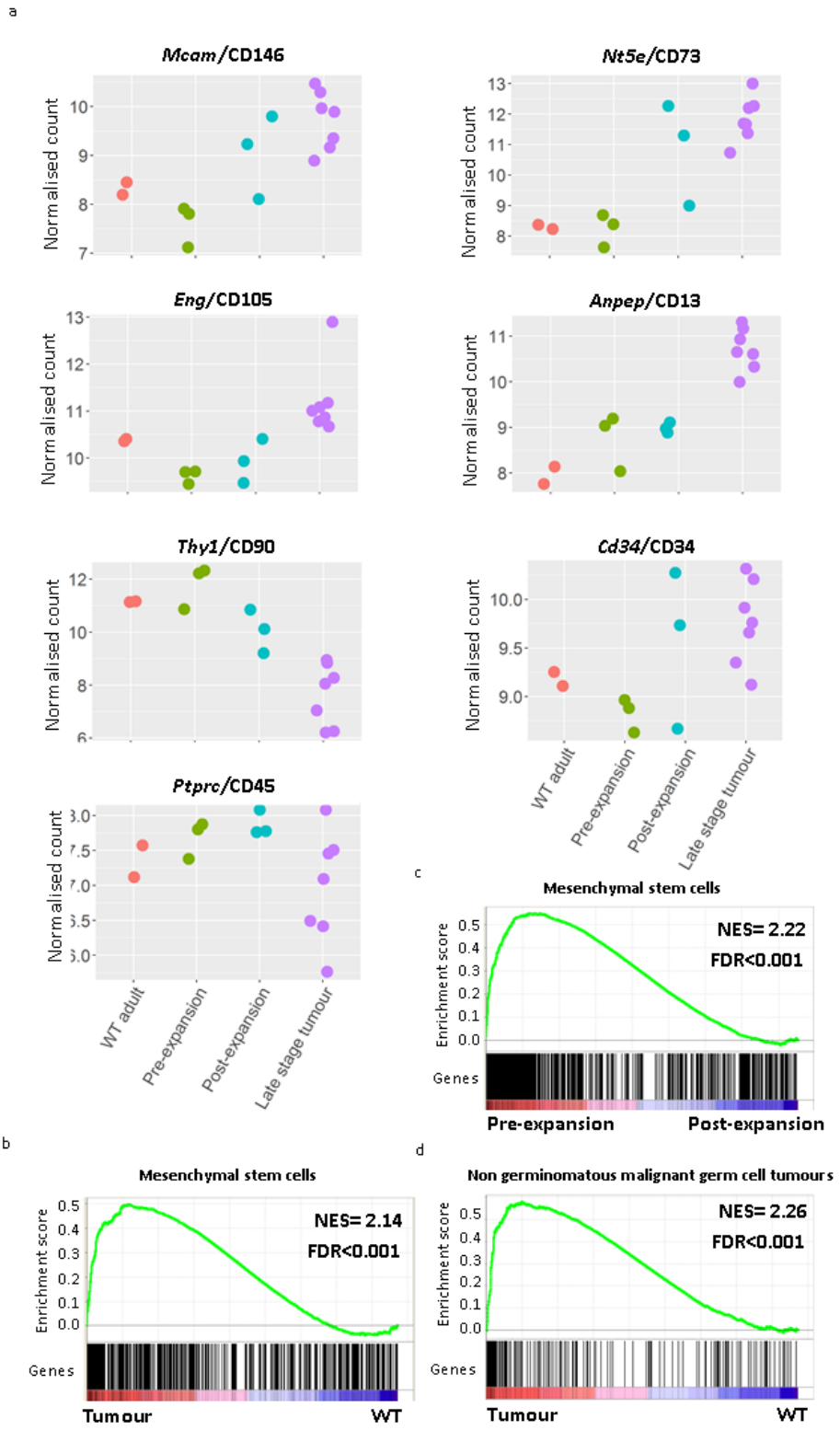

6.6 Specific pathways and processes in human and murine ACP tumourigenesis

The expression of many secreted factors by clusters has previously been well described in murine ACP, including by expression microarray (Andoniadou, Gaston-Massuet et al. 2012). In this section, the expression of genes in pathways relevant to tooth development, or of particular interest in ACP, are further explored, both within clusters, but also in pre-and post-expansion pituitaries and late stage murine ACP tumours.

As described in the introduction, during tooth development the expression and activation of these signalling pathways is a dynamic process with secretion of ligands alternating between epithelial and mesenchymal components. This is observed within the murine ACP model, with many ligands expressed within the clusters at E18.5, analogous to the enamel knot, but later becoming expressed in post-expansion and late stage tumours, more analogous to dental mesenchyme/odontoblasts.

6.6.1 WNT pathway

Previously published microarray analysis, qRT-PCR and *in situ* hybridisation of *Hesx1*$^{Cre/+}$;*Ctnnb1*$^{lox(ex3)/+}$ mice at E18.5 had confirmed the expression of WNT targets, e.g. *Lef1*, A*xin2* in clusters compared to non-cluster pituitary as well as expression of WNT ligands (e.g. WBT6 (4.9 fold), Wnt5a (2.7 fold), Wnt16 (1.6 fold), Wnt4 (1.6 fold) and Wnt9b (1.6 fold) (Andoniadou, Gaston-Massuet et al. 2012). GSEA of the microarray data from clusters in these mice also confirmed enrichment for the gene signature of activation of the WNT pathway within clusters (NES 2.31, FDR<0.001) (Figure 6-9).

Similarly, late stage tumours have previously been shown to have nuclear-accumulation of β-catenin. Wnt targets such as *Axin2* (19 fold), *Sp5* (304 fold) were up-regulated in tumours compared with control and GSEA confirmed enrichment of the signature of activation at this stage (NES=2.11, FDR<0.001) (Figure 6-4).

Assessment of results shows statistically significant (adjusted p-value <0.1) upregulation of *Wnt6* (92 fold), *11* (42 fold), *2* (19 fold), 10a (15 fold), *9b* (15 fold), *7a* (12.4 fold), *5a* (11 fold), *5b* (6.9 fold), *10b* (4.4 fold) *3* (3 fold) and *4* (2.9 fold) in post-expansion pituitaries. In late stage tumours compared with WT adult pituitaries, *WNTs 6, 7a, 10b, 5a, 11, 9b, 16, 10a, 2, 5b, 7b, 4, 3* were also all up-regulated (339, 206, 82, 42, 36, 27, 26, 20, 12, 10, 9, 9, 7 fold respectively). These results are presented visually in a heatmap in (Figure 6-9).

In the *Hesx1*$^{Cre/+}$*;Ctnnb1*$^{lox(ex3)/+}$ model, the activating β-catenin mutation is present in all the epithelial cells of the pituitary, however activation of the pathway is limited to a subset of cells (clusters). As in human ACP, the mechanisms of this remain unclear.

6.6.2 Sonic hedgehog pathway

Expression of *Shh* in E18.5 murine clusters by *in situ* hybridisation and its receptor, *Ptch1*, in surrounding pituitary has previously been published following identification of 10 fold upregulation by expression microarray (Andoniadou, Gaston-Massuet et al. 2012). As shown in Figure 6-2, P1 *Hesx1*$^{Cre/+}$*;Ctnnb1*$^{lox(ex3)/+}$ pituitaries are enriched for the gene signature of hedgehog signalling consistent with this.

Between pre- and post- expansion stages, whilst *Shh* was not significantly up-regulated, *Ptch1* (1.9 fold), *Gli1* (5.1 fold), *Gli3* (1.5 fold) were all up-regulated. In late stage tumours *Gli3* (2.5 fold) was the only member to be significantly up-regulated (adjusted p-value <0.1) (Figure 6-10).

The expression of members of the SHH signalling pathway have also been further studied by *in situ* hybridisation, RNA scope and immunostaining by Gabriela Carreno who has demonstrated expression of *Shh* and downstream targets up to 2 months of post-natal age.

I explore the therapeutic potential of targeting the SHH pathway in Chapter 8.

6.6.3 Fibroblast growth factor pathway

Fgfs 3, 4, 15 and *20* have previously been shown to be particularly up-regulated in ACP clusters (7 fold, 20 fold, 5 fold, 16 fold respectively) and expression of *Fgf3* confirmed by *in situ* hybridisation. Immunostaining for activation of the downstream target ERK1/2 identified widespread activation in the E18.5 $Hesx1^{Cre/+};Ctnnb1^{lox(ex3)/+}$ pituitaries (Figure 6-11).

Between pre and post expansion stages, *Fgfs 3* (15 fold), *4* (13 fold), *8* (9 fold), *20* (3.4 fold), *2* (3.4 fold), *11* (3.1 fold) and *18* (2.6 fold) were all significantly up-regulated (adjusted p-value<0.1), as were *Fgfrs 1-4* (2.7, 4.3, 4.4, 2.6 fold). Similarly in late stage tumours, *Fgf8* (11 fold), *18* (6 fold), *3* (5 fold), *11* (4 fold), *22* (2.6 fold) were all significantly up-regulated in late stage tumours (adjusted p-value<0.1) as were the receptors *Fgfr1, 2, 3* (1.9 fold, 7 fold and 6, fold) (Figure 6-10).

Immunostaining shows phosphorylation/activation of downstream targets ERK1/2 within three late stage tumours consistent with activation of the FGF pathway (Figure 6-11).

6.6.4 Transforming growth factor β pathway

Tgfb1, *Tgfb*2 and *Inbb* and *Inhba* (5.7fold, 5.2 fold, 9.7 fold, 7.3 fold) have previously been shown to be up-regulated in murine ACP clusters. To investigate activation of downstream signalling pSMAD3 stainings were performed on E18.5 mutant pituitaries. This confirmed activation in cells abutting and nearby clusters, but not clusters themselves (Figure 6-12).

Between pre and post expansion stages, *Tgfb1* (18 fold), *Tgfb2* (4.7 fold), *Tgfb3* (2.7 fold) *Inhba* (15 fold), *Inhbb* (2.8 fold) and *Tgfbr2*(1.3 fold) were all up-regulated. In contrast *Inha* (3 fold), *Acvr2a*(1.3 fold), *Acvr1c*(4.7 fold) were down-regulated (Figure 6-13).

Similarly, *Tgfb1* (6 fold), *Tgfb2* (3 fold), *Inhba*(4.3 fold), *Inhbb* (5.3 fold) and *TGFBR2* (2.1fold) but not *Tgfb3* were up-regulated in late stage tumours and *Inba* (4 fold), and *Acvr1c* (28 fold) down-regulated. Gene set enrichment identified enrichment of

TGFβ signalling at all stages (P1 mutant vs WT, post vs pre expansion, late stage tumour vs WT), with the greatest enrichment in late stage tumours (NES=2.44, FDR<0.001) (Figure 6-13). pSMAD3 immunostaining also confirmed heterogeneous activation of the TGFβ pathway in late stage tumours (Figure 6-12).

6.6.5 Bone morphogenic protein pathway

*BMP*s *3,7,2, 8b* and *5* had previously been shown to be up-regulated in murine clusters (9.5, 5.7, 3.7, 1.9, 1.8 fold respectively). To investigate activation of downstream signalling pSMAD1,5,8/9 stainings were performed on E18.5 mutant pituitaries. Similar to pSMAD3 staining this confirmed activation in cells abutting and nearby clusters, but not clusters themselves (Figure 6-14).

Between pre and post expansion stages, *Bmp8a* (36 fold), *2* (24 fold), *7* (23 fold), *4* (15 fold), *3* (15 fold), *8b* (10 fold), *5*(7.2 fold), *1* (5 fold) were all significantly (adjusted p-value <0.1) up-regulated as was *Bmpr2* (2.8 fold). Similarly, *Bmp3* (7.8 fold), *4* (5.5 fold), *7* (4.7 fold), *1* (4.5 fold), *8b* (4.3) *8a* (4.0 fold) and *Bmpr2* (2.2 fold) were also up-regulated in late stage tumours compared with controls (Figure 6-15). pSMAD1,5,8/9 immunostaining confirm heterogeneous activation of the BMP pathway in late stage tumours (Figure 6-14).

6.6.6 Ectodysplasin signalling

The expression of Ectodysplasin family members was explored in all datasets. At E18.5 microarray analysis of clusters revealed 3.9 fold upregulation of EDAR and 1.3 fold of *EDA*. Consistent with these results at P1 EDAR and EDA were significantly up-regulated (2.7 fold, 1.7 fold, adjusted p-value <0.1), respectively, compared with controls.

Following expansion, *EDAR* was 2 fold further up-regulated (adjusted p-value<0.1), though at late stages *EDAR* was not significantly differentially expressed and EDA was down-regulated 1.9 fold (adjusted p-value <0.1).

To further investigate the expression of EDA and EDAR, immunohistochemistry was performed (Figure 6-16). At E18.5 stage, expression was observed EDAR was

observed throughout the pituitary, with possible higher expression within clusters. EDA was similarly expressed throughout the pituitary, with possible higher expression peri-clustrerally. Nf-kB signalling has previously been demonstrated within murine clusters consistent with activation of this pathway in clusters, but could equally be activated by other means.

In view of the expression of EDA within the normal pituitary in the mouse model the expression within normal adult and fetal pituitary was also explored. This confirmed expression, though the absence of a pituitary phenotype in hypohidrotic ectodermal dysplasia suggests this may not be functionally important.

6.6.7 Summary

In summary. these results suggest that whilst at early stages expression of the secreted factors is predominant in the clusters, at later stages their expression shifts to the non-epithelial derived tumour. This shift is reminiscent of tooth development where these signals are dynamically expressed in different cell types at different stages of development.

Figure 6-9: WNT pathway activation and expression in murine ACP. a) GSEA confirming enrichment of the hallmark wnt signalling signature in clusters and late stage tumours. b) heatmap showing high expression of many wnt ligands in late stage tumours and associated expression of FZD receptors across stages.

a

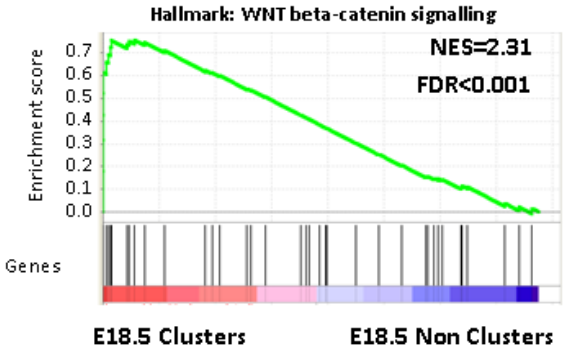

b

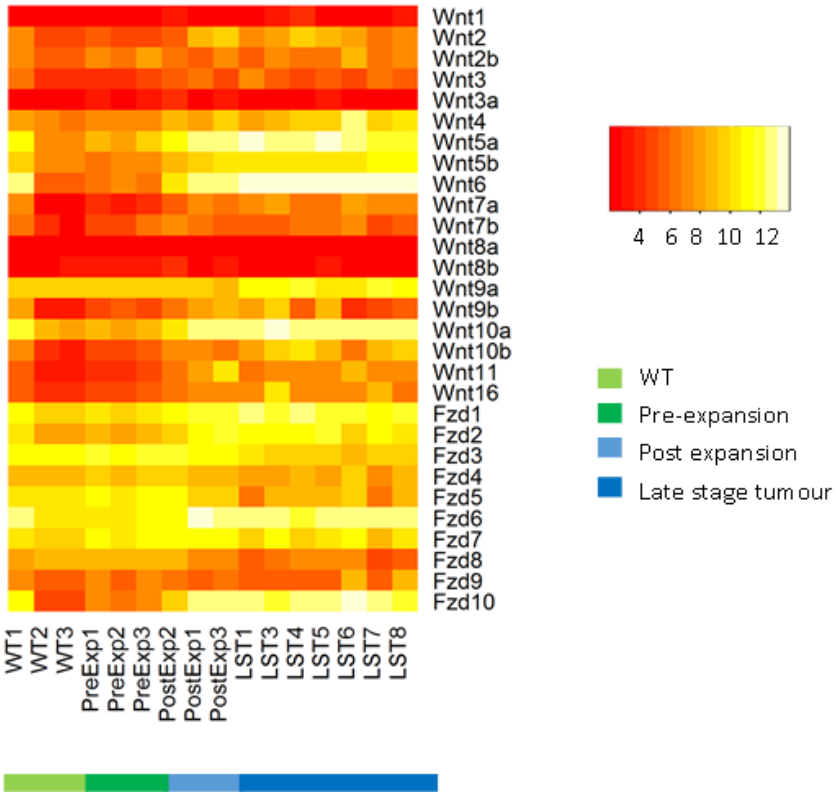

Figure 6-10: Heatmaps of expression of a) SHH pathway and b) FGF pathway members in murine ACP.

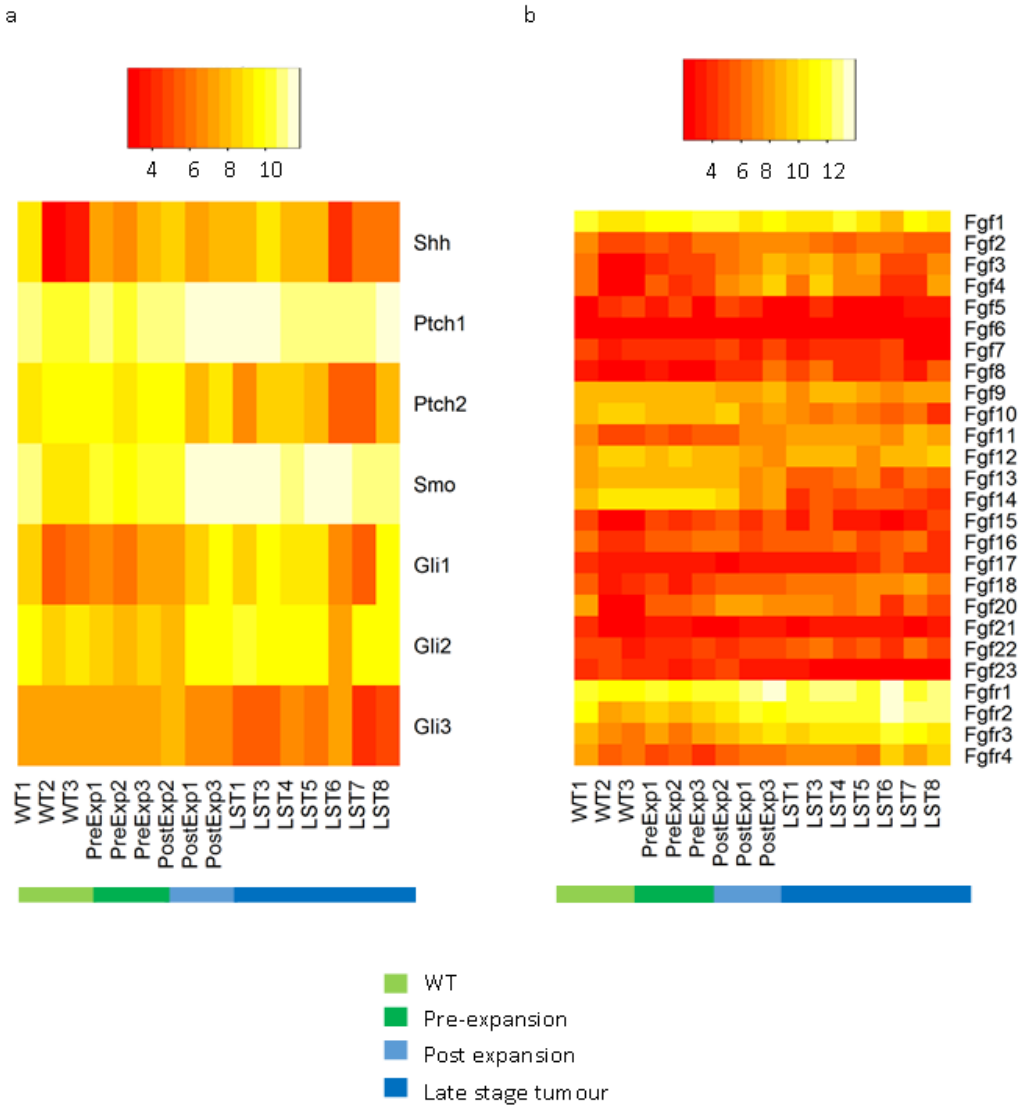

Figure 6-11: Double immunofluorescence showing activated pERK1/2 in a) E18.5 pituitaries and b) late stage tumours of *Hesx1*$^{Cre/+}$;*Ctnnb1*$^{lox(ex3)/+}$ mice.

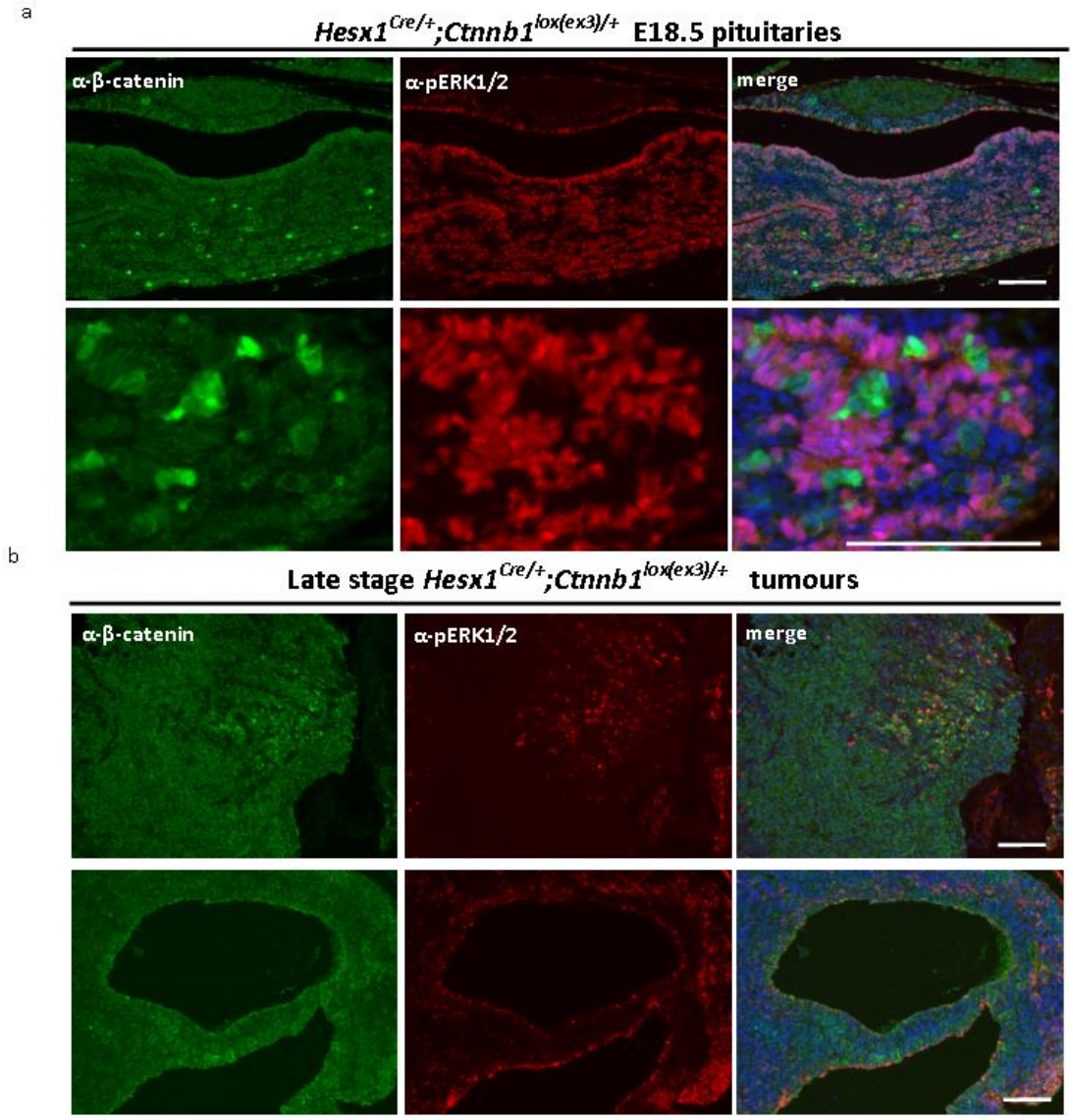

Figure 6-12: Double immunofluorescence showing activated p-SMAD3 in a) E18.5 pituitaries and b) late stage tumours of *Hesx1*$^{Cre/+}$;*Ctnnb1*$^{lox(ex3)/+}$ mice.

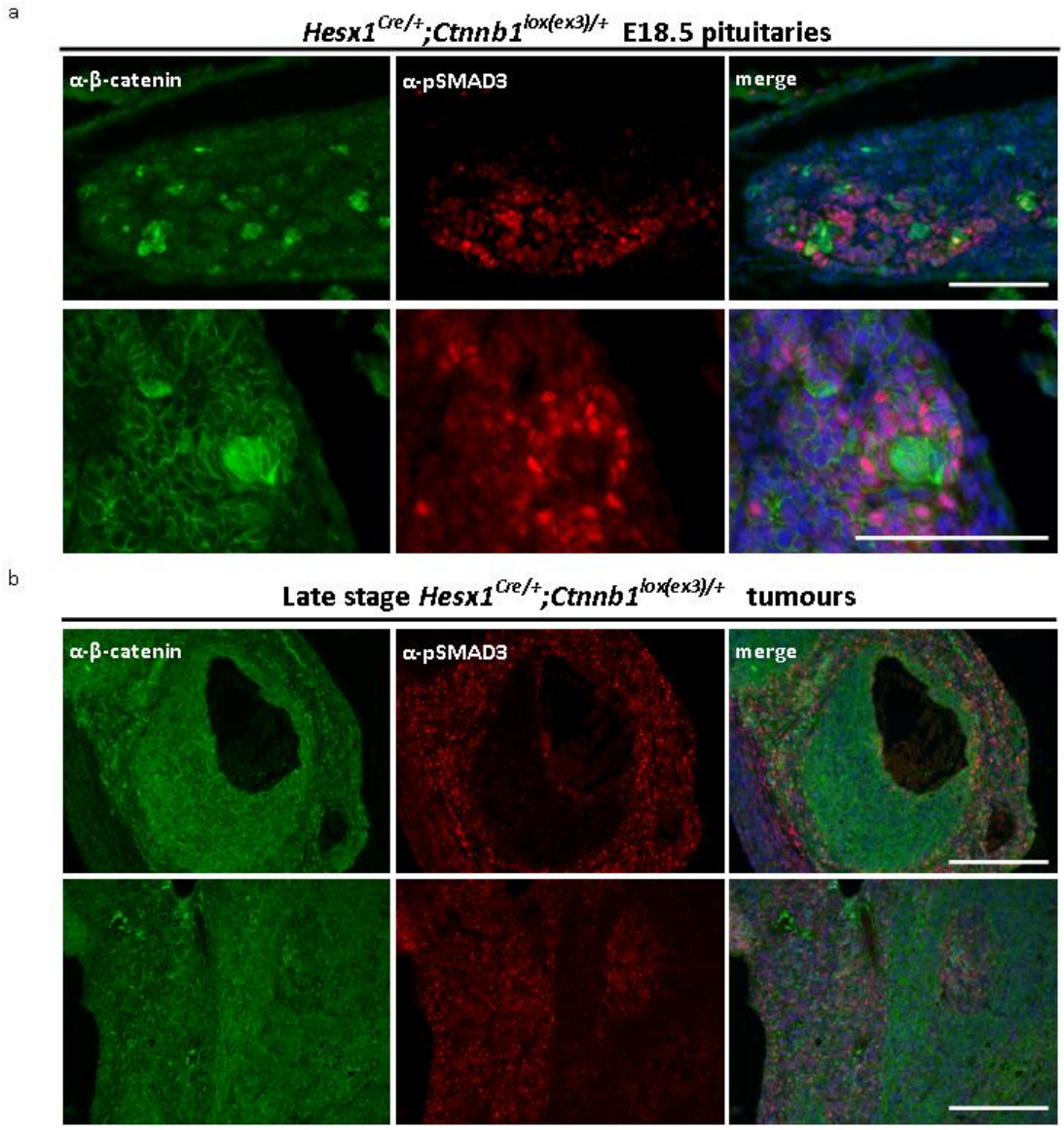

Figure 6-13: TGFβ signalling in of *Hesx1*$^{Cre/+}$;*Ctnnb1*$^{lox(ex3)/+}$ tumours . a) heatmap of expression of TGFB, inhibin and activing ligands and receptors. B) GSEA plots of TGFβ signalling signature at various stages of tumour development.

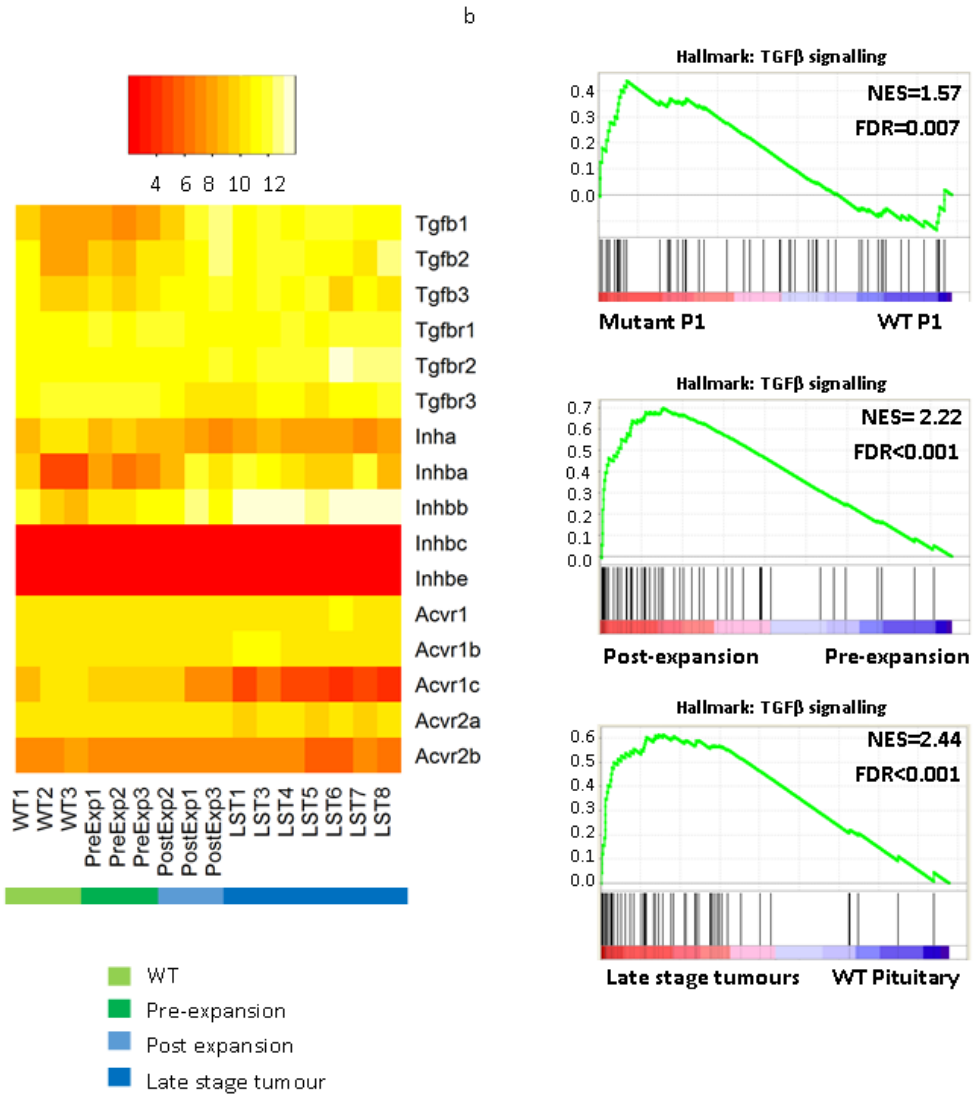

Figure 6-14: Double immunofluorescence showing activated p-SMAD1,5,8/9 in a) E18.5 pituitaries and b) late stage tumours of *Hesx1*$^{Cre/+}$;*Ctnnb1*$^{lox(ex3)/+}$ mice.

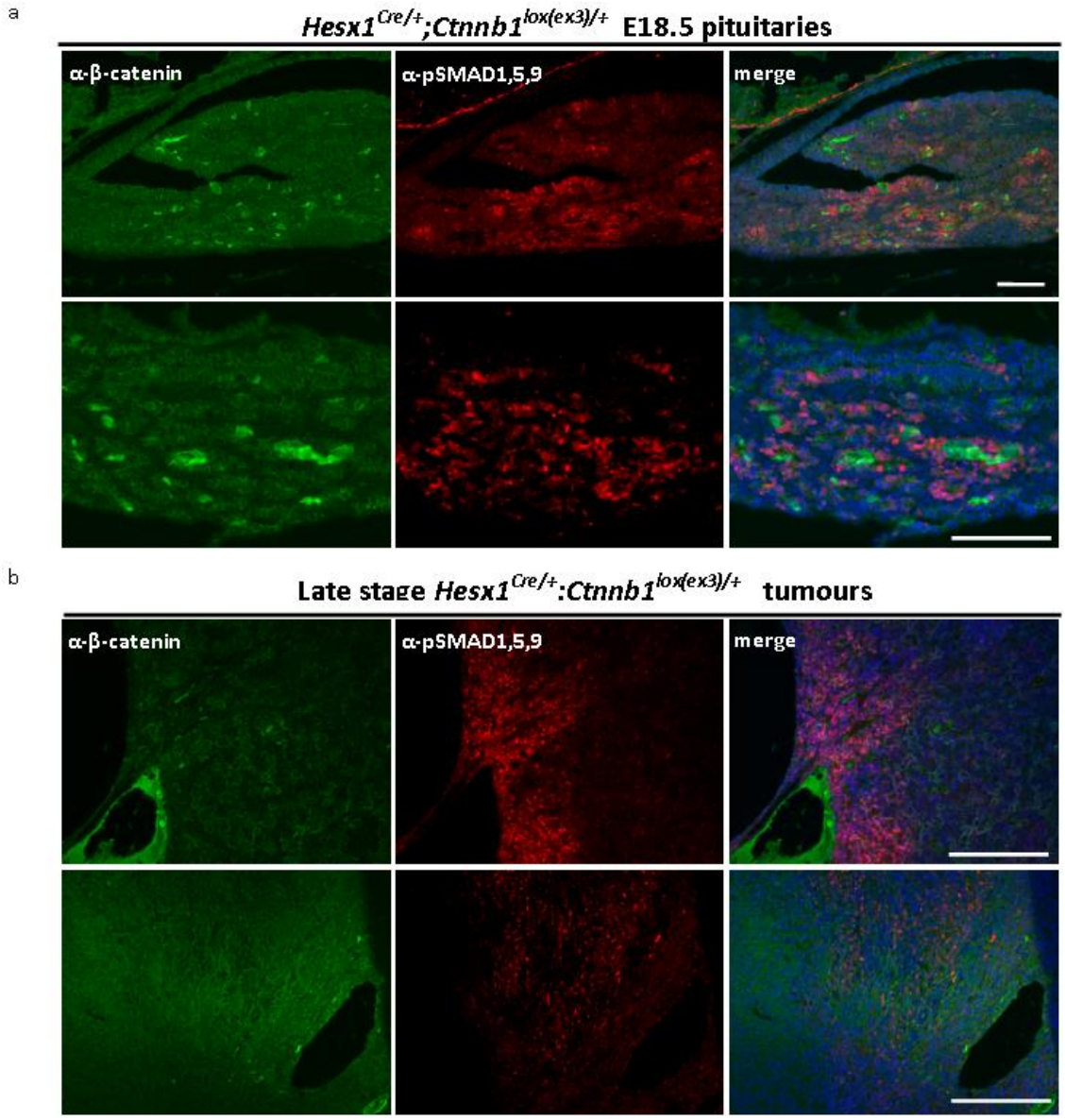

Figure 6-15: Heatmaps of expression of BMP pathway members in murine ACP.

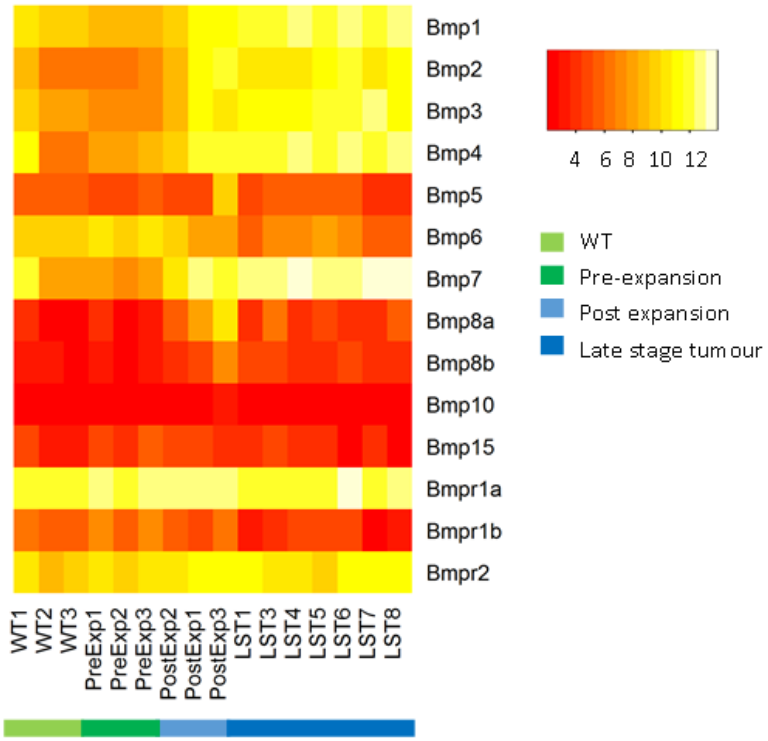

Figure 6-16: Double immunofluorescence of Ectodysplasin pathway members EDA and EDAR in murine ACP and adult human pituitaries. (Images Helen Fraser).

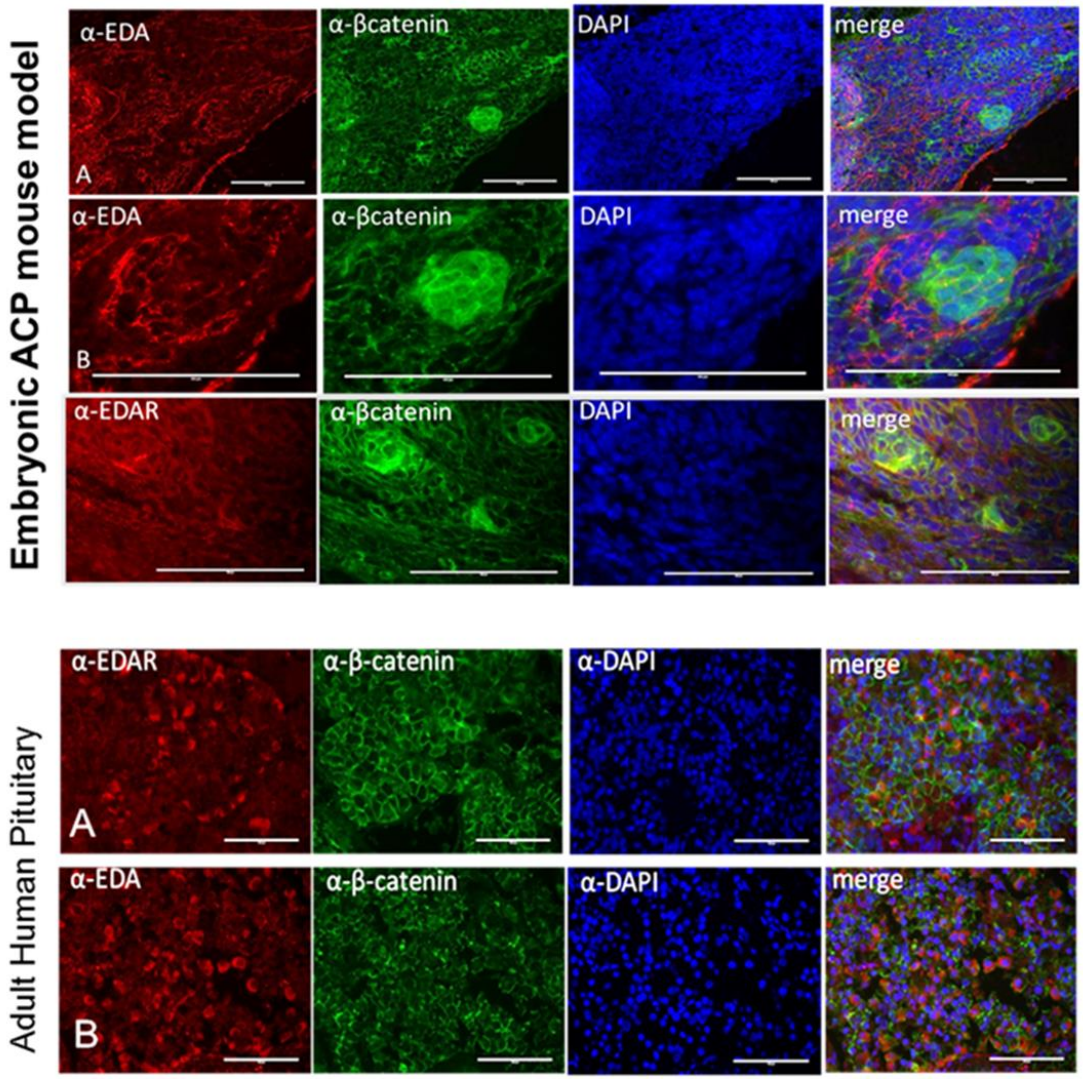

6.7 Murine clusters exhibit transcriptional profile of senescent cells

Immunohistochemistry and qRT-PCR have shown that murine clusters, like human clusters, have features of senescent cells and express the SASP. Similarly to the human RNA sequencing data (Section 5.15), I performed GSEA to assess expression of the transcriptional profile of oncogene induced senescence (OIS) and the ssenescence associated secretory phenotype (SASP) on the gene expression signatures of murine clusters. This demonstrated enrichment of both OIS and SASP in clusters from both the embryonic (OIS: NES=1.23, FDR=0.12, SASP: NES=1.52, FDR=0.01) and inducible (OIS: NES=1.3, FDR=0.01, SASP: NES=1.57, FDR=0.007) murine ACP models. These results add additional support that there is activation of OIS and SASP within clusters.

Figure 6-17: GSEA plots of OIS and SASP gene sets in murine ACP clusters. a) embryonic model, b) inducible model.

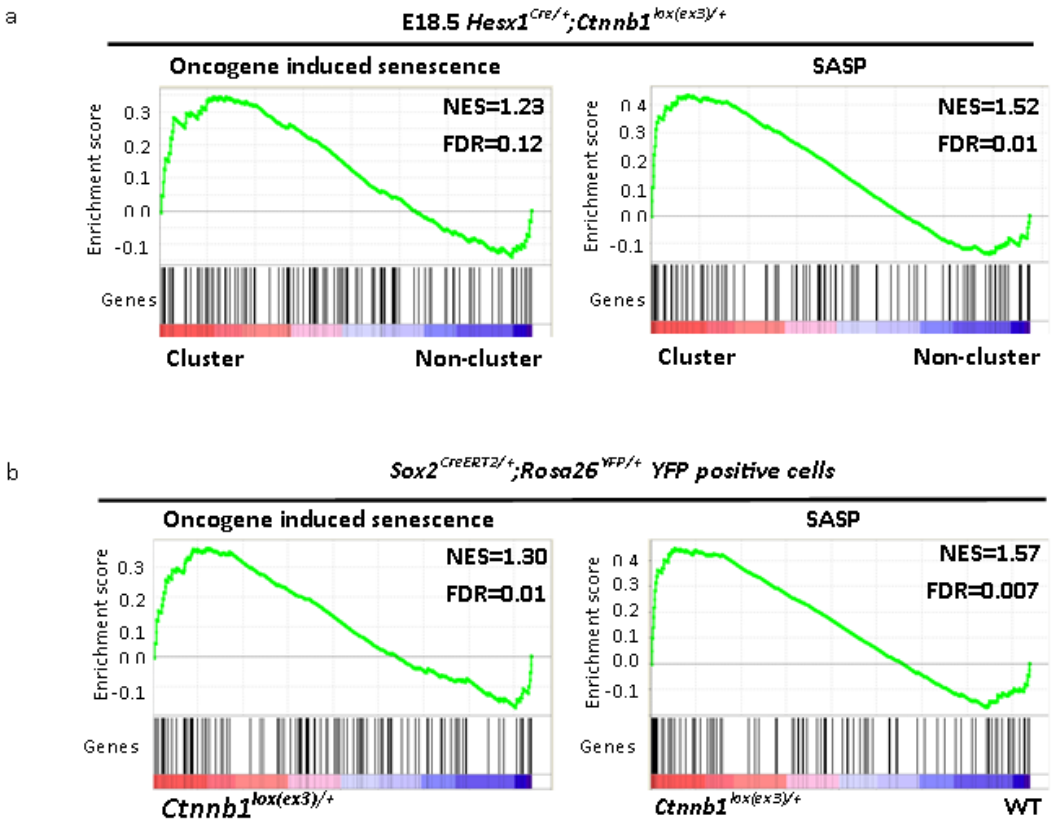

6.8 Tumours without p53

6.8.1.1 Two distinct forms of tumour in Hesx1$^{Cre/+}$;Ctnnb1$^{lox(ex3)/+}$;Trp53$^{fl/fl}$ mice

Having established the signatures of different stages and processes of tumourigenesis in the *Hesx1$^{Cre/+}$;Ctnnb1$^{lox(ex3)/+}$* model, next I analysed the tumours from animals where *Trp53* (encoding p53) had been knocked out (samples LST-p53.1-3 also known as M1-3) and mid-stage lesions from animals heterozygous for *Trp53*. (MST-p531-3/P1-3).

Firstly, plotting of expression of *Trp53* expression confirmed absence of expression in all three tumour cases. Mid-stage *Hesx1$^{Cre/+}$;Ctnnb1$^{lox(ex3)/+}$;Trp53$^{fl/+}$* mice had Trp53 expression equivalent to pre-expansion *Hesx1$^{Cre/+}$;Ctnnb1$^{lox(ex3)/+}$* mice (Figure 6-18).

To further explore the relationships between samples as identified by Principal Component Analysis and in initial Clustering analysis (Figure 6-1), heatmaps of the genes of each module identified in section 6.3.4 (mouse WGCNA) were replotted with all murine samples (Figure 6-18).

Of note, plotting of the heatmap of brown module genes (highly expressed by late stage *Hesx1$^{Cre/+}$;Ctnnb1$^{lox(ex3)/+}$* tumours), highlighted that the *Hesx1$^{Cre/+}$;Ctnnb1$^{lox(ex3)/+}$;Tp53^{fl+}* samples MSP-p53.2/P1 and MSP-p53.3/P3 grouped with pre-expansion pituitaries and adult WT samples WT2, WT4. MSP-p53.3/P2 grouped with J4 and WT1. Similar patterns were seen for P1, 2 and 3 across other modules. These results would be consistent with no effect of loss of a single copy of Trp53. I will not consider these samples further.

Of the *Hesx1$^{Cre/+}$;Ctnnb1$^{lox(ex3)/+}$;Trp53$^{fl/fl}$* tumours, two, LST-p53.1/M1 and LST-p53.3/M3, grouped with *Hesx1$^{Cre/+}$;Ctnnb1$^{lox(ex3)/+}$* tumours, suggesting these are molecularly analogous tumours, despite lineage tracing showing differing cells of origin (Figure 6-18). As well as expressing brown module genes, these samples also highly expressed genes in the green module, suggesting activation of the cell cycle (data not shown).

In contrast, as per original clustering, tumour LST-p53.2/M2 clustered separately. This was particularly in the red module, which is enriched for genes relating to epithelial differentiation (Figure 6-18). This suggests that M2 has a more epithelial transcriptional profile.

To further explore the expression profiles of samples, differential expression analyses were performed between samples M1 and M3 and *Hesx1*$^{Cre/+}$*;Ctnnb1*$^{lox(ex3)/+}$ tumours and sample M2 and *Hesx1*$^{Cre/+}$*;Ctnnb1*$^{lox(ex3)/+}$ tumours.

Figure 6-18: Relationship of *Hesx1$^{Cre/+}$;Ctnnb1$^{lox(ex3)/+}$;Trp53$^{fl/fl}$* tumours with *Hesx1$^{Cre/+}$;Ctnnb1$^{lox(ex3)/+}$* samples. a) Expression of Trp53. b) Principal Component Analysis plot showing relationship of p53 null tumours with other samples. c) Heatmaps of WGCNA modules detected in Hesx1Cre/+;Ctnnb1lox(ex3)/+ samples (Figure 6-5, Figure 6-6) with inclusion of p53 null samples (highlighted by arrows). M1=LST-p53.1, M2=LST-p53.2, M3=LST-p3.3.

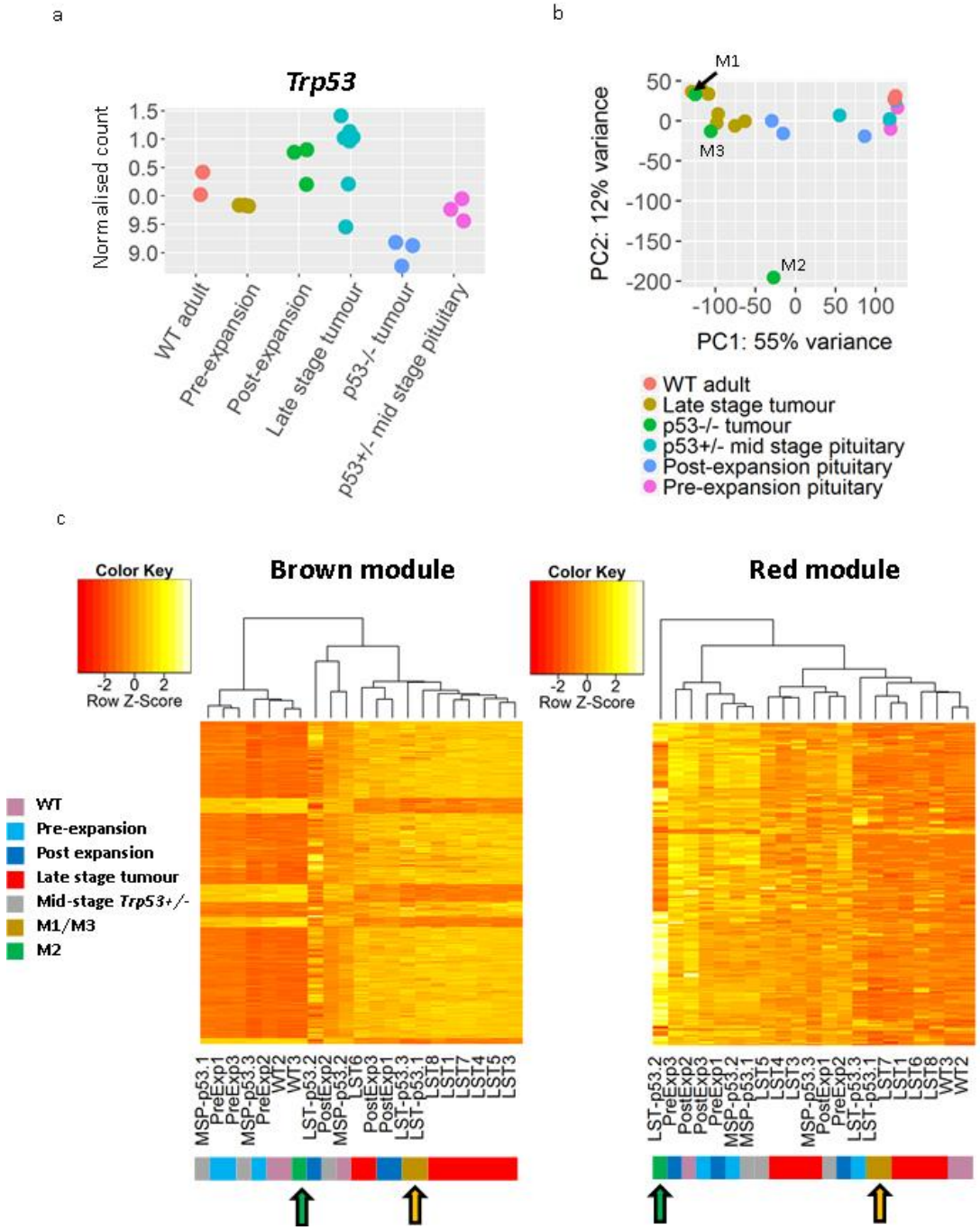

6.8.1.2 Tumours M1 and M3

Despite clustering showing considerable overlap between M1 and M3 and *Hesx1*$^{Cre/+}$;*Ctnnb1*$^{lox(ex3)/+}$ tumours, to understand whether there were differences between M1 and M3 and the *Hesx1*$^{Cre/+}$;*Ctnnb1*$^{lox(ex3)/+}$ tumours a pairwise analysis was performed. This showed 331 genes up-regulated in the p53fl/fl tumours and 759 down-regulated.

As expected, *Trp53* was down regulated (2.8 fold) in trp53fl/fl tumours. Full differential expression results are in Supplementary Table 4. *CD146, CD73, CD13, CD90* were not differentially expressed suggesting that, like *Hesx1*$^{Cre/+}$;*Ctnnb1*$^{lox(ex3)/+}$ tumours, M1 and M3 express markers of MSCs (Figure 6-19).

6.8.1.3 Tumour M2 has an epithelial phenotype

To further explore the signature of sample M2, differential expression analysis was performed comparing sample M2, with *Hesx1*$^{Cre/+}$;*Ctnnb1*$^{lox(ex3)/+}$ tumours (excluding LST2/10.5T). This identified 2437 genes up-regulated and 2254 down-regulated. Ontology enrichment analysis highlighted that these were enriched for genes relating to epithelial development. Genes highly up-regulated included many keratins, e.g. *Krt6a* (370 fold), *Krt6b* (317 fold). This would be consistent will cell autonomous epithelial derived tumourigenesis and the epithelial phenotype identified by WGCNA (Section 6.8.1.1). Gene set enrichment analysis identified inflammation related genes set to be the most enriched within genes up-regulated in M2.

The genes most up-regulated in *Hesx1*$^{Cre/+}$;*Ctnnb1*$^{lox(ex3)/+}$ tumours compared to M2 included *T(* brachyury) (328 fold), *AFP* (80x), whereas WNT signalling and EMT were the only two sets enriched in *Hesx1*$^{Cre/+}$;*Ctnnb1*$^{lox(ex3)/+}$ tumours.

Together these suggest that M2 has an epithelial phenotype, distinct from the other *Hesx1*$^{Cre/+}$;*Ctnnb1*$^{lox(ex3)/+}$ and *Hesx1*$^{Cre/+}$;*Ctnnb1*$^{lox(ex3)/+}$;*Trp53*$^{fl/fl}$ tumours.

Figure 6-19: Expression of *Afp*, *T*, MSC markers and keratins in p53 null samples.

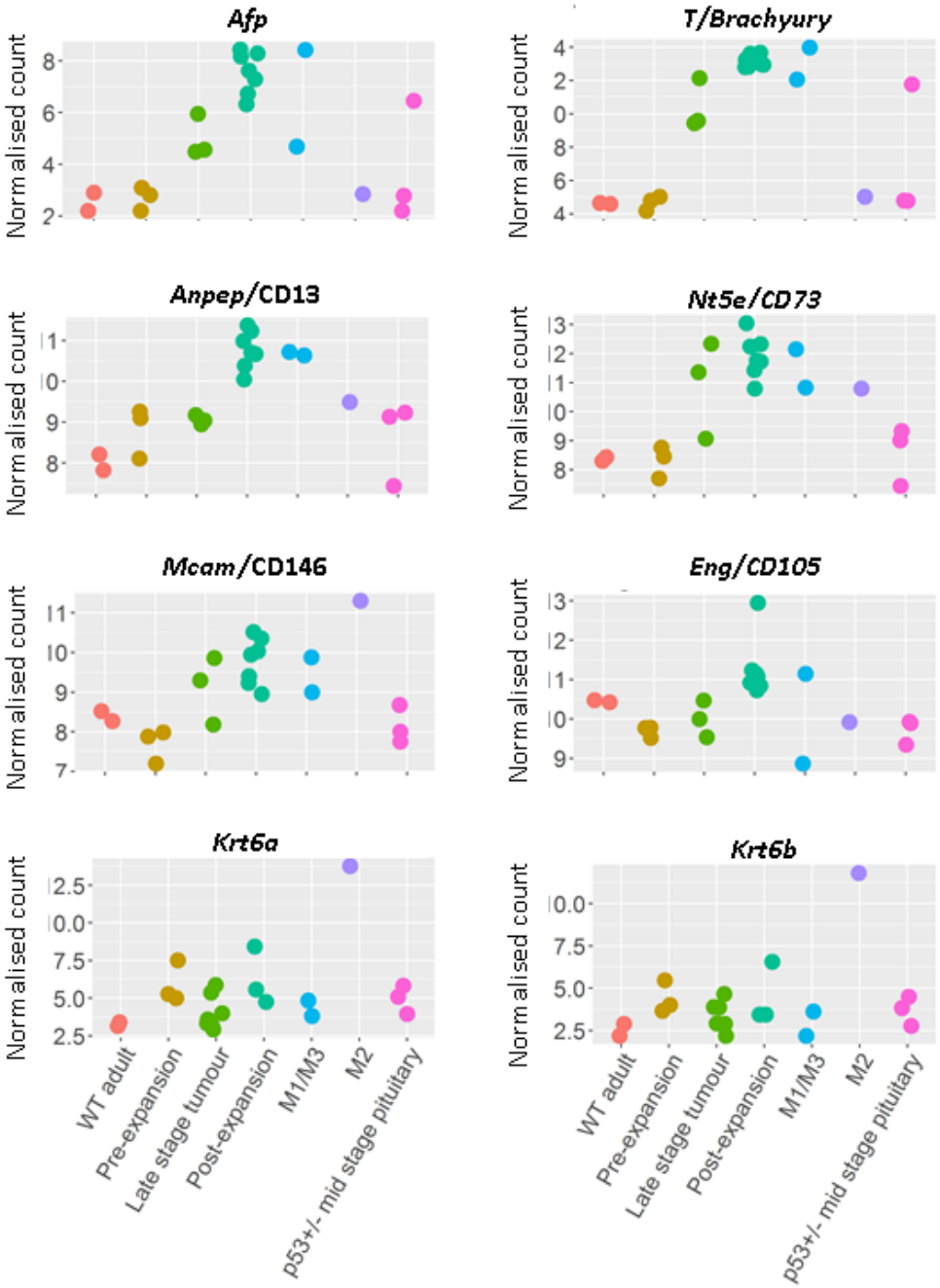

Table 6-9: Top 10 up-regulated genes in M2 compared with *Hesx1$^{Cre/+}$;Ctnnb1$^{lox(ex3)/+}$* tumours.

Gene Symbol	Fold Change (log2)	Adjusted p-value
Prss27	11.14944	2.74E-69
Tmprss11g	10.80775	1.02E-40
Ltf	10.22852	3.87E-31
2010300F17Rik	10.20344	1.26E-46
Vwde	9.89337	7.93E-28
Dsg1b	9.665081	1.87E-26
Tmprss11d	9.595727	2.27E-40
Tchh	9.556121	3.06E-33
Tmprss11b	9.528398	3.38E-34
D630010B17Rik	9.485047	3.38E-34

Table 6-10: Top 10 ontologies enriched in *Hesx1$^{Cre/+}$;Ctnnb1$^{lox(ex3)/+}$;Tp53$^{fl/fl}$* tumour M2 compared with *Hesx1$^{Cre/+}$;Ctnnb1$^{lox(ex3)/+}$* tumours.

Category	Term	Padj
GO:0043588	skin development	5.63E-26
GO:0030216	keratinocyte differentiation	1.86E-24
GO:0008544	epidermis development	4.40E-24
GO:0060429	epithelium development	7.34E-23
GO:0009888	tissue development	2.41E-22
GO:0009913	epidermal cell differentiation	2.81E-21
GO:0030855	epithelial cell differentiation	5.38E-21
GO:0031424	keratinization	1.50E-16
GO:0048513	animal organ development	2.61E-15
GO:0018149	peptide cross-linking	8.85E-11
GO:0050891	multicellular organismal water homeostasis	1.13E-10

Table 6-11: 26 gene sets enriched in genes up-regulated in M2 compared with *Hesx1$^{Cre/+}$;Ctnnb1$^{lox(ex3)/+}$* tumours.

Gene set	Size	Normalised Erichment Score (NES)	False disocvery rate (FDR)
HALLMARK_INTERFERON_GAMMA_RESPONSE	184	1.99	0.001
HALLMARK_INFLAMMATORY_RESPONSE	194	1.98	0.001
HALLMARK_ALLOGRAFT_REJECTION	180	1.81	0.003
HALLMARK_TNFA_SIGNALING_VIA_NFKB	195	1.72	0.005
HALLMARK_IL6_JAK_STAT3_SIGNALING	84	1.72	0.004
HALLMARK_INTERFERON_ALPHA_RESPONSE	88	1.70	0.005
HALLMARK_COMPLEMENT	178	1.64	0.009
HALLMARK_ESTROGEN_RESPONSE_LATE	189	1.56	0.019
HALLMARK_KRAS_SIGNALING_UP	190	1.55	0.018
HALLMARK_P53_PATHWAY	193	1.50	0.028
HALLMARK_IL2_STAT5_SIGNALING	190	1.47	0.033
HALLMARK_ESTROGEN_RESPONSE_EARLY	193	1.47	0.031
HALLMARK_PROTEIN_SECRETION	94	1.47	0.029
HALLMARK_GLYCOLYSIS	192	1.42	0.046
HALLMARK_COAGULATION	127	1.40	0.052
HALLMARK_ANDROGEN_RESPONSE	95	1.37	0.064
HALLMARK_XENOBIOTIC_METABOLISM	182	1.36	0.065
HALLMARK_HYPOXIA	192	1.33	0.080
HALLMARK_KRAS_SIGNALING_DN	184	1.25	0.151
HALLMARK_APICAL_SURFACE	44	1.23	0.173
HALLMARK_NOTCH_SIGNALING	31	1.17	0.248

Table 6-12: Top 10 most up-regulated in *Hesx1$^{Cre/+}$;Ctnnb1$^{lox(ex3)/+}$* tumours compared with M2.

Gene Symbol	Fold Change (log2)	Adjusted p-value
Calcr	-8.43879	3.59E-24
T	-8.35914	4.6E-57
Pax1	-8.27091	3.18E-24
Grid1	-7.98196	1.33E-26
Cntnap4	-7.92809	2.24E-34
Slc44a5	-7.89039	1.32E-30
Calb2	-7.87996	4.19E-14
Mnx1	-7.87903	7.01E-15
Hoxd9	-7.85953	1.03E-28
Sorcs3	-7.84962	1.73E-21

Table 6-13: Gene sets enriched in genes expressed in Cre gof tumours compared with M2.

Gene set	Size	Normalised Erichment Score (NES)	False disocvery rate (FDR)
HALLMARK_WNT_BETA_CATENIN_SIGNALIN G	41	1.46	0.166
HALLMARK_EPITHELIAL_MESENCHYMAL_TRA NSITION	191	1.44	0.103

6.9 Correlation of human and murine ACP

The mouse models of ACP are intended to model the human disease, therefore the relationship between murine and human ACP transcriptional profiles was assessed.

Specifically:

- How well murine clusters compare with human ACP clusters?
- How well murine tumours compare with human ACP tumours?

6.9.1 Murine clusters closely resemble human ACP clusters.

To compare the transcriptional signatures of murine clusters and human clusters two methods were used: Gene set enrichment analysis and hierarchical clustering.

For gene set enrichment, gene sets were generated of the 100 and 500 genes most up-regulated as assessed by Wald statistic in human clusters. This confirmed enrichment for the human cluster signature in both *Hesx1*$^{Cre/+}$*;Ctnnb1*$^{lox(ex3)}$ and *Sox2*$^{CreERT2/+}$*;Ctnnb1*$^{lox(ex3}$*;Rosa26*$^{YFP/+}$ clusters (Table 6-14, Table 6-15, Figure 6-20). To cluster the data, per gene expression values from each of the heterogeneous datasets had to be integrated (human RNA seq, murine RNA seq and murine expression array). To achieve this, normalised (variance stabilised transformed) counts from human cluster and non-cluster tissue were median scaled within sample pairs, then median averaged across samples. For the *Hesx1*$^{Cre/+}$*;Ctnnb1*$^{lox(ex3)}$ cluster vs non cluster microarray data, MAS5 normalised intensity values log2 scaled then median scaled. For Sox2 samples, as samples were not paired, variant stabilised counts were averaged (median) and then median scaled. To merge the datasets murine gene names were converted to capital letters and the data sets merged, this gave 11347 genes on which expression data was available in all three datasets.

Clustering was performed using correlation distance and showed grouping of clusters and non- clusters further confirming that murine clusters closely resemble those of human ACP (Figure 6-20).

Table 6-14: Enrichment of human cluster signature in *Hesx1$^{Cre/+}$;Ctnnb1$^{lox(ex3)}$* clusters.

	NES	FDR
Human clusters top 100	2.36	0.000
Human clusters top 500	2.15	0.000

Table 6-15: Enrichment of human cluster signature in *Sox2$^{CreERT2/+}$;Ctnnb1$^{lox(ex3}$;Rosa26$^{YFP/+}$* clusters.

	NES	FDR
Human clusters top 100	2.37	0.000
Human clusters top 500	2.17	0.000

Figure 6-20: Murine clusters share transcriptional profile with human clusters. a) Gene set enrichment plots showing enrichment of human cluster signatures in clusters (top 100 or 500 genes as ranked by Wald statistic) from the embryonic and inducible murine models ACP ACP.b)Hierarchical clustering of gene expression signatures of clusters and non-clusters across species and models.

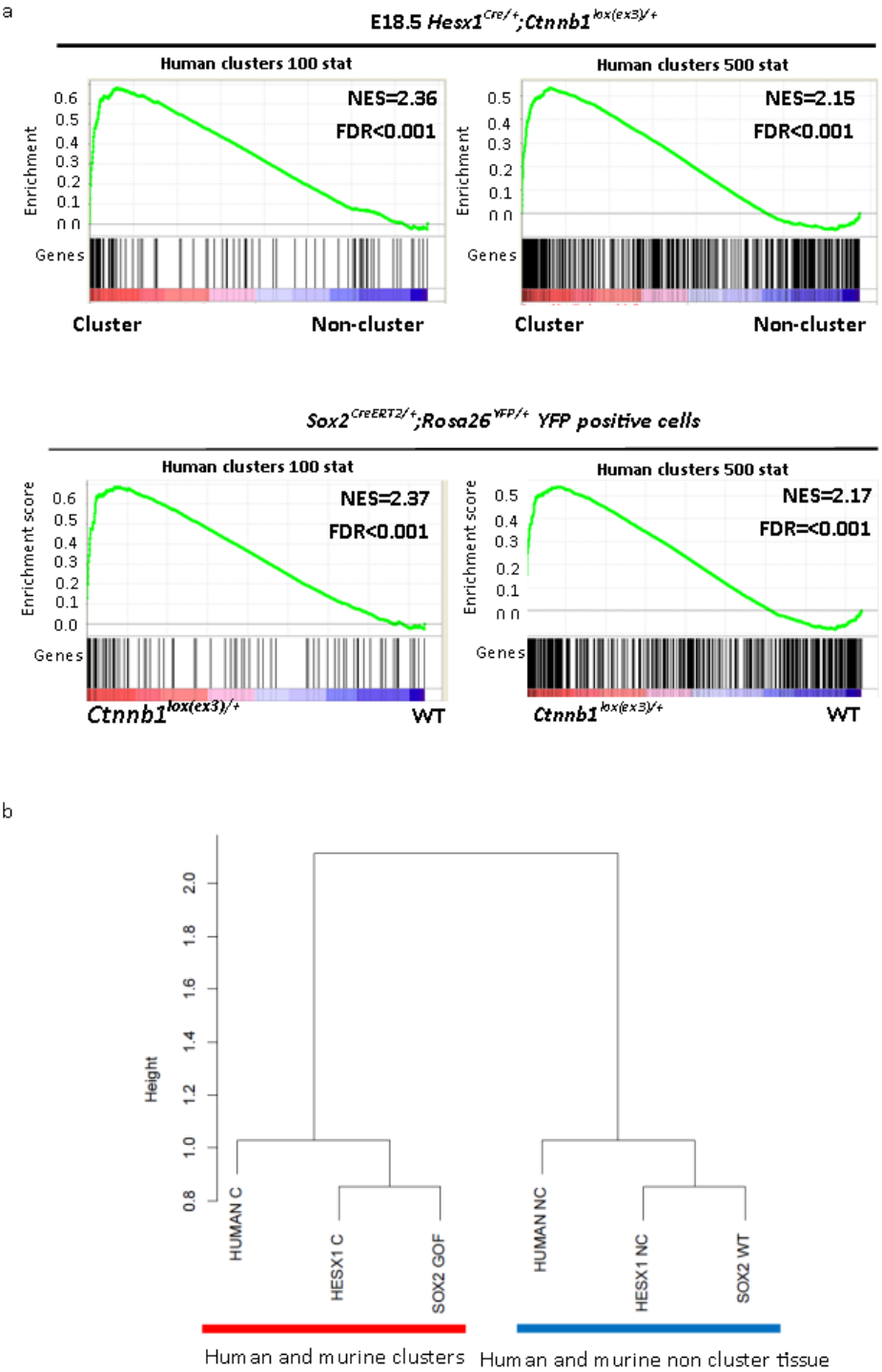

6.9.2 Murine ACP tumours share signatures of human ACP

6.9.2.1 Gene set enrichment analysis of human ACP signature

Similar to assessing the relationship between human and murine clusters, gene sets of the 500 genes most up-regulated in human ACP compared with controls was generated.

Assessment of *Hesx1*$^{Cre/+}$*;Ctnnb1*$^{lox(ex3)}$ tumours vs controls showed enrichment of the human tumour signature (NES=2.57, FDR<-0.001) as did analysis of post-expansion vs pre-expansion mid stage pituitaries. (NES=2.20, FDR <0.001) (Figure 6-21).

Considering the relationships between human and murine ACP with the tooth, it is likely that it is at the earlier stages of murine ACP tumourigeneis that it most closely resembles the epithelial component of human ACP (with clusters, and expanded epithelia analgous to the enamel knot and palisading epithelium respectively). Supporting this, gene set enrichment analysis confirmed even greater enrichment of the signature of human ACP at this stage (NES=2.87, FDR<-0.001) than post-expansion or late stage tumours (Figure 6-21).

Next, we explored the relationship of sample LST-p53.2/M2 with human ACP. When compared to *Hesx1*$^{Cre/+}$*;Ctnnb1*$^{lox(ex3)}$ tumours this also showed enrichment of the signature of human ACP in M2 (NES=2.24, FDR<0.001), suggesting that while many genes of human ACP are up-regulated in *Hesx1*$^{Cre/+}$*;Ctnnb1*$^{lox(ex3)/+}$ tumours, this epithelial *Hesx1*$^{Cre/+}$*;Ctnnb1*$^{lox(ex3)}$ *;Trp53*$^{fl/fl}$ tumour more closely recapitulates the transcriptional landscape of human ACP (Figure 6-21).

Figure 6-21: Enrichment of human ACP signature in murine ACP. Top 500 genes in human ACP compared with control as assessed by Wald statistic.

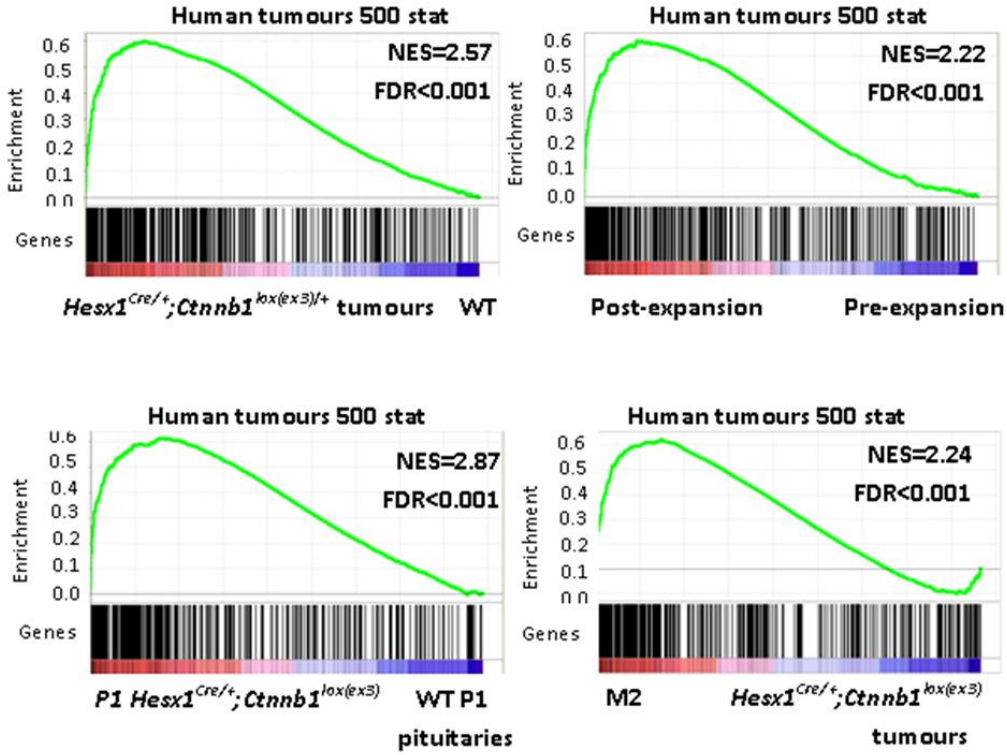

6.9.2.2 Expression of human WGCNA module genes by murine ACP

As described in Chapter 5, WGCNA had identified several transcriptional patterns across human ACP samples, representing different tissue compartments and processes. To assess whether these were expressed by murine ACP, heat maps of each modules genes were plotted.

Unsurprisingly, the brown, black and dark grey genes, which correlated with tumour content and *CTNNB1* variant allele frequency, were highly expressed by tumour LST-p53.2/M2, and otherwise variably by WT and *Hesx1*$^{Cre/+}$*;Ctnnb1*$^{lox(ex3)}$ mice. The cyan module representing cell cycle was highly expressed by a subset of tumours, including LST-p53.1/M1 and LST-p53.3/M3, consistent with the variable proliferation across sample. Other modules, representing glial tissue, immune cells and control tissues were predominantly expressed by wildtype and pre-expansion pituitaries (data not shown).

6.9.2.3 Expression of murine WGCNA module genes by human ACP

In a similar way, heatmaps of human genes were also plotted for the modules identified by WGCNA of murine samples. In the murine analysis the brown (different to the human brown genes) and green modules were expressed by *Hesx1*$^{Cre/+}$*;Ctnnb1*$^{lox(ex3)}$ tumours. The brown module genes included developmental genes and was most expressed by human tumour samples JA005, and JA011, which were predominantly reactive glial tissue. This suggests activation of similar gene expression profiles in theses samples to those observed in murine ACP.

The green module, of cell cycle genes was most up-regulated in fetal pituitary samples, consistent with the findings of the WGCNA analysis of human ACP.

A subset of pink genes, expressed by post expansion pituitaries and including *Dspp,* were most highly expressed in samples JA023, JA026 and JA056. These samples had the highest expression in the black module of human WGCNA analysis which expression correlated with the presence of wet keratin. This suggests that these human tumours may represent a more advanced developmental stage of odontogenesis than others, as evidenced by increased expression of enamel and dental mesenchyme/odontoblast genes.

Figure 6-22: Expression of human WGCNA module genes by murine ACP. The brown, black and dark grey modules are groups of genes highly expressed by the epithelial content of human ACP. High expression of these genes ins observed in sample *Hesx1*$^{Cre/+}$*;Ctnnb1*$^{lox(ex3)}$ *;Trp53*$^{fl/fl}$ tumour M2 (arrow) with variable expression in other tumours.

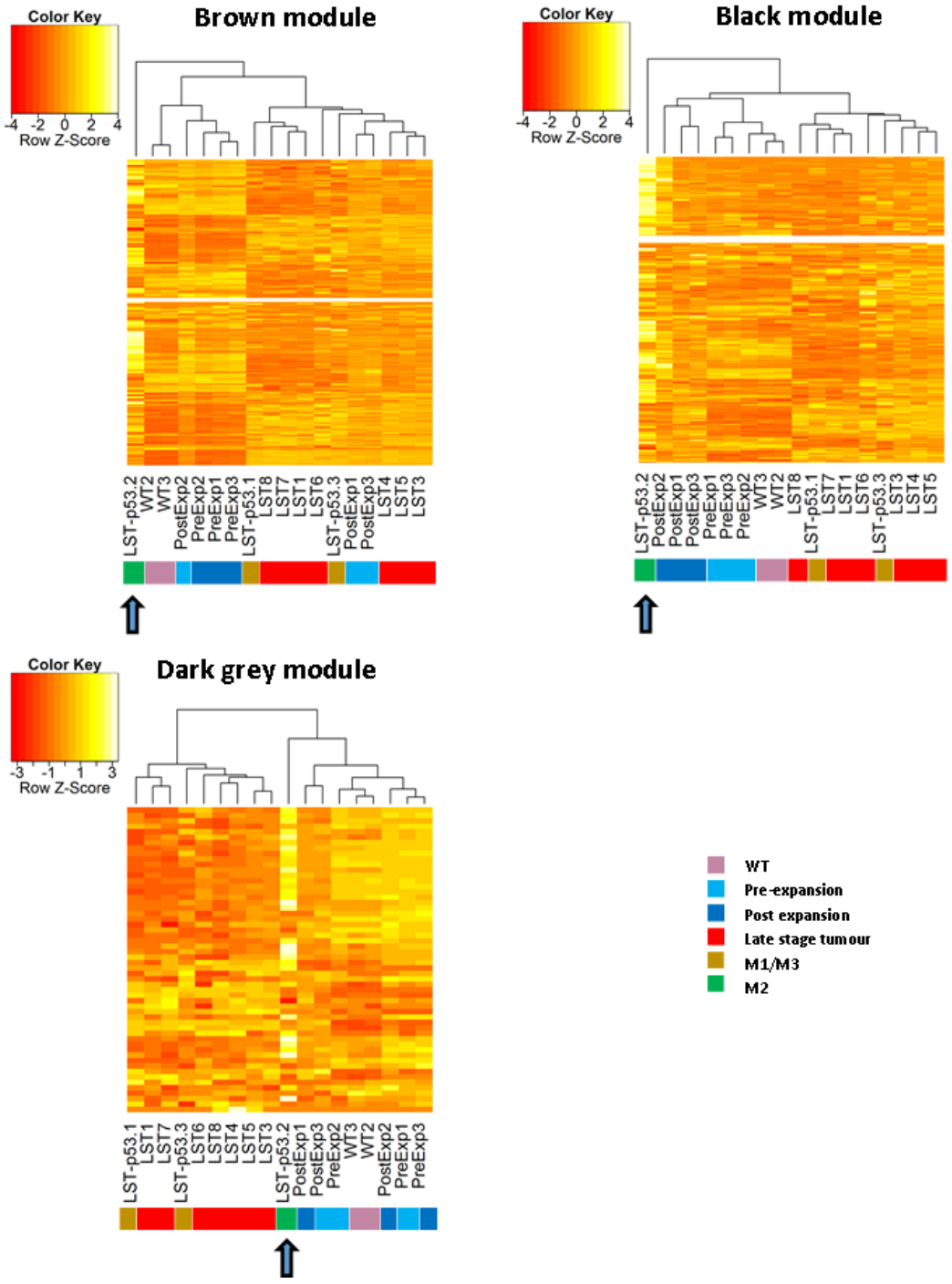

Figure 6-23: Expression of murine WGCNA modules by human ACP. The brown module gens are highly expressed by *Hesx1*$^{Cre/+}$;*Ctnnb1*$^{lox(ex3)/+}$ tumours and are variably expressed by human ACP. The green module of cell cycle genes is most highly expressed by fetal pituitaries. The pink modules of genes, expressed by post-expansion mid-stage *Hesx1*$^{Cre/+}$;*Ctnnb1*$^{lox(ex3)}$ pituitaries and including dental mesenchyme/odontoblast genes are most highly expressed by a subset of human ACP with wet keratin.

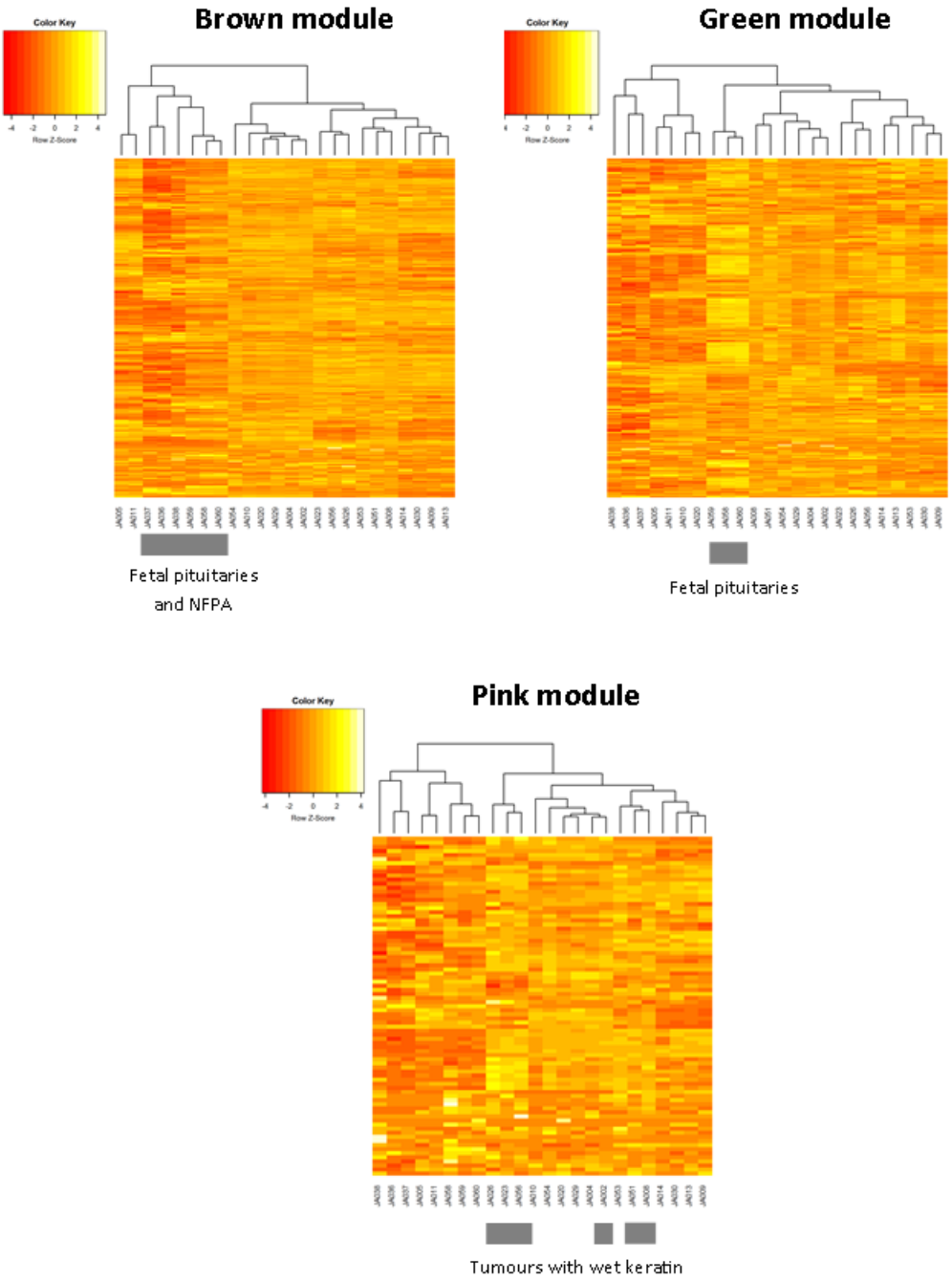

6.9.3 Summary

Together, these results suggest considerable overlap between the processes of human ACP tumourigenesis and those observed in *Hesx1*$^{Cre/+}$*;Ctnnb1*$^{lox(ex3)}$ tumourigenesis.

6.10 Inflammation in murine ACP

Inflammatory cells have not been observed within murine ACP. To further investigate the cytokine milieu within *Hesx1*$^{Cre/+}$*;Ctnnb1*$^{lox(ex3)/+}$ tumours, the expression patterns of a subset of cytokines was plotted (Figure 6-24).

This showed high expression of *Il6* amongst late stage tumours, with *IL6RA* broadly expressed across stages. *IL1a*, *1l1b* and *Il10* were highly expressed by the late stage tumour without p53, LST-p53.2/M2, whilst *IL18* was highly expressed by late stage tumours but not LST-p53.2/M2.

Figure 6-24: Expression of selected cytokines in murine ACP tumours.

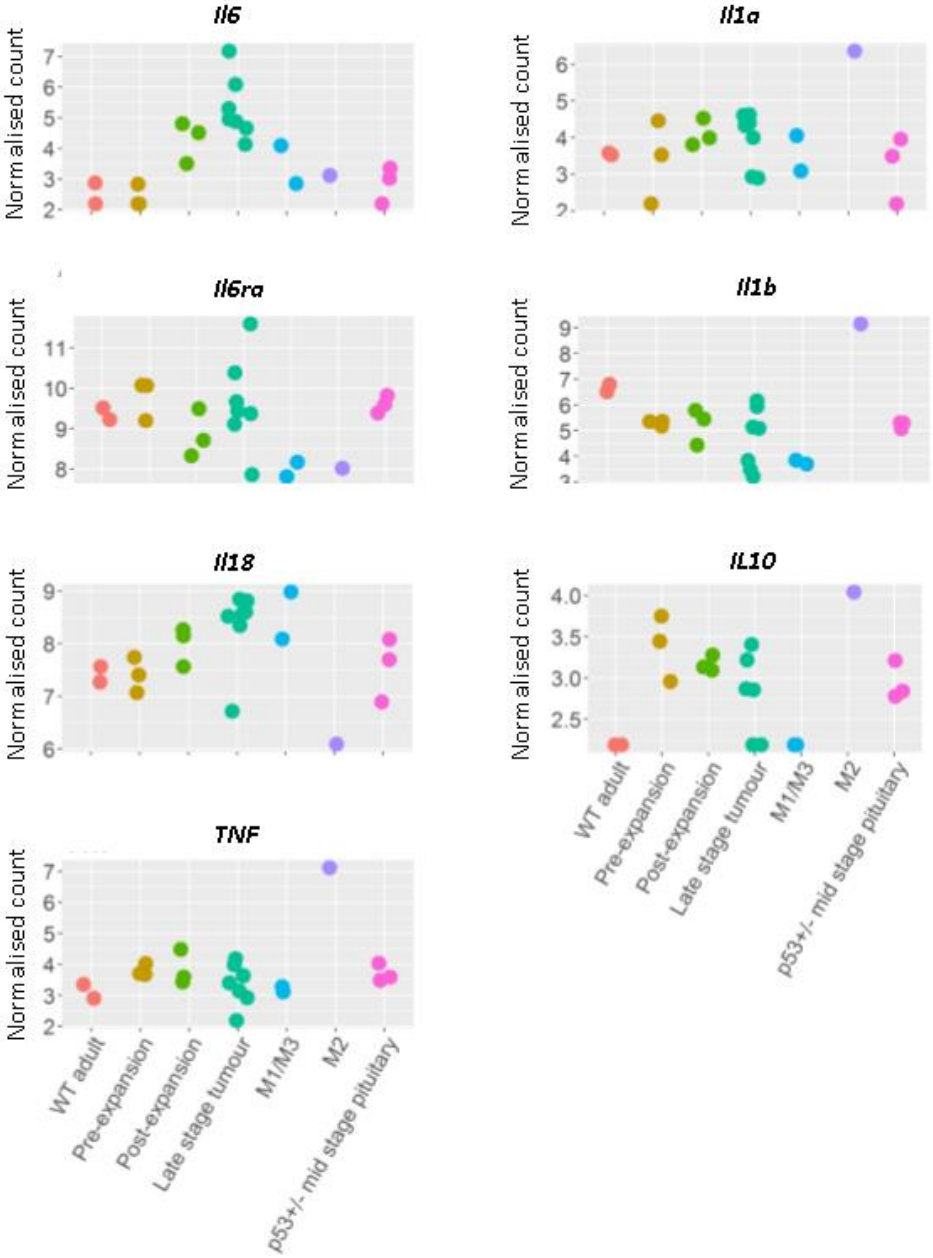

6.11 Chapter summary

The results of this chapter highlight the complex transcriptional dynamics that occur during murine ACP tumourigenesis.

At early stages (E18.5/P1), activation of β-catenin in the developing pituitary induces activation of the IEE/ameloblast differentiation signature and a proportion of cells form a structure similar to the enamel knot of the developing tooth. This accumulates nucleo-cytoplasmic β-catenin and has previously been shown to express genes of secreted members of the WNT, HH, TGFB, BMP family and I show also expresses the ectodysplasin receptor, *Edar*. These clusters are molecularly analogous to human ACP clusters and can also be directly induced by activation of β-catenin in Sox2 positive adult stem cells.

At the expansion stage, there is an influx and expansion of cells which has previously been shown by lineage tracing to not be derived from the pituitary epithelium. The data presented identifies upregulation of markers of odontoblasts, e.g. *DSPP*, suggesting that these cells may be derived from similar, i.e. neural crest, origin.

At late stages, the pituitary epithelium has been replaced by non-pituitary derived cells. These do not express odontoblast genes, however express several mesenchymal stem cells and other developmental genes such as *Afp* and *T*. Whether these cells represent a de-differentiation of the cells observed at the post expansion stage or an expansion of a sub population of these cells is unknown. These cells also express large amounts of several signalling family members and a proportion are observed to activation of downstream signalling.

Deletion of *Trp53* has been shown to result in cell autonomous tumours, and surprisingly two tumours profiled had transcriptional profiles closely related to those of $Hesx1^{Cre/+};Ctnnb1^{lox(ex3)/+}$ tumours. This suggests that the characteristics of these late stage tumours can be preserved despite a different cell of origin (Hesx1 lineage or non Hesx1 lineage derived). This suggests that the local tissue environment is more important the cell or origin in determining final tumour

phenotype. A third tumour, LST-p53.2/M2, in contrast exhibited a more epithelial phenotype.

Comparison with human ACPs showed some similarities between murine ACP, but also differences. Clusters showed similar features and activation of similar processes, e.g. analogies to the enamel knot, activation of senescence and SASP. Indeed early stages show the strongest similarities with human ACP. Late stage tumours also showed similarities, with tumour M2, showing the strongest similarity, likely reflecting the epithelial phenotype.

These results will be integrated with those from Chapter 5, to propose a novel model of ACP tumourigenesis as a recapitulation of tooth development in the Discussion (Chapter 9).

Chapter 7 Exome sequencing of murine ACP and whole genome sequencing of human ACP

7.1 Introduction

Lineage tracing experiments have demonstrated the non-cell autonomous origin of late stage murine tumours and in Chapter 6 the gene expression changes underpinning this begin to be unravelled. However, it remains unclear whether these tumours harbour the somatically acquired mutations expected of transformed cells. To assess this, we performed exome sequencing of a cohort of 15 late stage murine tumours, including the eight which underwent RNA sequencing (Chapter 6), and compared with their matched germline DNA.

Similarly, whilst in Chapter 4 we confirm the presence of *CTNNB1* mutations, the absence of *BRAF* and selected other mutations, the overall genomic landscape of human ACP remains unclear. In particular, the presence and functional significance of any additional somatic mutations remains unknown. To further assess this, we performed whole genome sequencing of five human ACP tumours and matched germline DNA.

7.2 Exome sequencing reveals acquisition of somatic mutations within murine ACP tumours

In the mouse models, activation of β-catenin in Rathke's pouch progenitors or adult SOX2 stem cells, results in the formation of clusters resembling those in human ACP. Late stage tumours subsequently develop, but are not derived from these *CTNNB1* recombined cells (Figure 1-2). Whether these late stage tumours acquire somatic mutations has not previously been investigated.

Somatically acquired mutations are a defining characteristic of most tumours and in a similar model of leukaemogenesis, Kode *et al*., expressed the same oncogenic β-catenin in osteoblasts and the subsequent leukaemia was found to have acquired somatic changes (particularly translocations) (Kode, Manavalan et al. 2014). This supports the potential acquisition of somatic mutations in late stage murine ACP tumours.

To address whether *Hesx1*$^{Cre/+}$;*Ctnnb1*$^{lox(ex3)/+}$ late stage tumours harbour somatic mutations, I established a collaboration with Dr David Adams, (Wellcome Sanger Centre, Cambridge) to perform exome sequencing on 15 tumour and germline (tail) paired DNA samples collected from mice with end stage tumours.

In addition to informing about craniopharyngioma biology, these experiments also have wider relevance to the field of senescence. Whilst there is accumulating evidence of a pro-tumourigenic role of SASP, whether SASP can induce cell transformation and tumour initiation of non-tumourigenic cells *in vivo* has not previously been demonstrated in the literature (Coppe, Desprez et al. 2010).

7.2.1 Exome sequencing confirms somatic mutation in late stage murine ACP

Initial single nucleotide variant analysis identified 848 variants across the 15 tumours. However, manual review of the mutations revealed that several variants, while present only in the sequencing of the tumour of a matched tumour and germline pair, were identifiable within the germline of other mice within the cohort, suggesting that these were not true somatically acquired mutations.

To further filter the results, the analysis was rerun, both with updated versions of the Sanger Cancer Genome Project pipeline, but also with the addition of a filter to removing all variants identified within any of the germline samples. This identified 273 mutations, of which 131 were within coding regions (non-sense, missense or silent). There was a median of eight coding region mutations per tumour (range 4-14) (Table 7-1) (Full results in Supplementary Table 6).

Variant allele frequencies of changes were distributed as plotted in Figure 7-1. The median allele frequency was 21% (range 4.4%-100%). Due to the variable sequencing depth across mutations and the relatively low number per case it was not possible form the data to assess whether the mutations are within a clonal population.

Table 7-1 Murine ACP samples undergoing exome and transcriptome sequencing

Sample Label	Sanger centre ID	Sex	Age at death (weeks)	RNA sequencing performed	Number of coding mutations detected by exome sequencing
2.3	MD5190	F	40.7	Yes	4
B429	MD5198	M	22.7	Yes	5
1.1	MD5185	F	15.7	No	8
3.1.7	MD5193	F	20.1	No	14
25-Nov	MD5191	F	21.7	No	8
1.2	MD5184	M	16.0	No	13
27-Oct	MD5192	F	13.1	No	8
10.5.1	MD5186	F	11.1	Yes	8
10.5	MD5187	F	12.6	Yes	5
16.1	MD5189	F	30.4	No	12
7.5	MD5197	M	14.0	Yes	12
4.2.2.	MD5196	M	9.7	No	8
13.2.1	MD5188	M	12.9	Yes	9
3.2.2	MD5194	M	12.4	Yes	10
3.2.2FD	MD5195	M	17.7	Yes	7

Figure 7-1: Distribution of variant allele frequencies and number of mutant allele reads in *Hesx1*$^{Cre/+}$;*Ctnnb*$^{lox(ex3)/+}$ tumours. Note the majority of mutations have low read numbers and allele frequency.

a

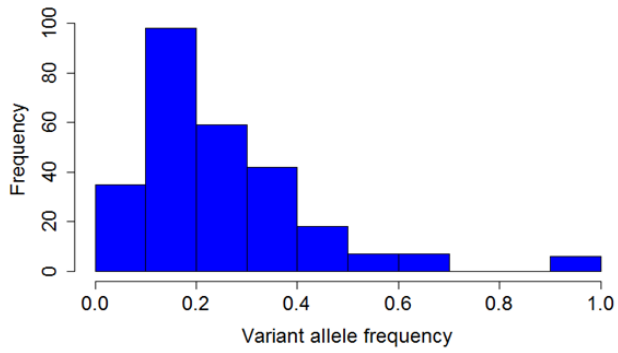

b

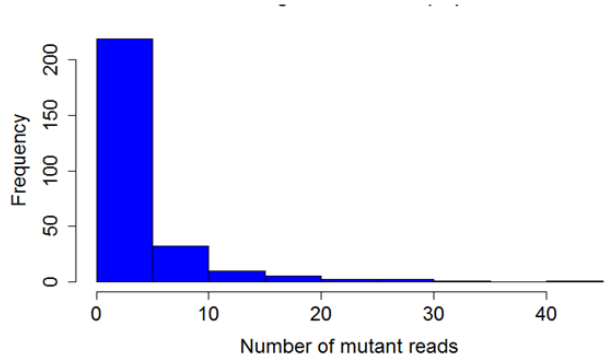

7.2.2 Validation of exome sequencing results

To validate these results, Sanger sequencing was performed for 14 of these mutations. This was performed in DNA from tumours and matched germline for the relevant case.

As discussed in Chapter 4, Sanger sequencing only reliably detects variants with an allele fraction greater than approximately 20%. Consequently, the 14 genes were selected such that they had allele frequencies greater than this, and with moderate (>3) numbers of mutant reads. This confirmed the mutations in 12 of the 14 genes sequenced (Figure 7-2, Table 7-2).

RNA sequencing data was available for 8 of the tumours (59 of the 131 mutations). This was assessed for the expression of mutations. In 27/59 there were 3 or less reads at the mutation loci, therefore it was not possible to assess mutation status. Of the remaining 32, expression of the mutation was confirmed in 9 (28%).

Figure 7-2: Validation of mutations by Sanger sequencing. a) IGV trace showing A to G Trappc11 mutation b) Sanger sequencing electropherograms confirming presence of mutation in tumour, but not germline DNA.

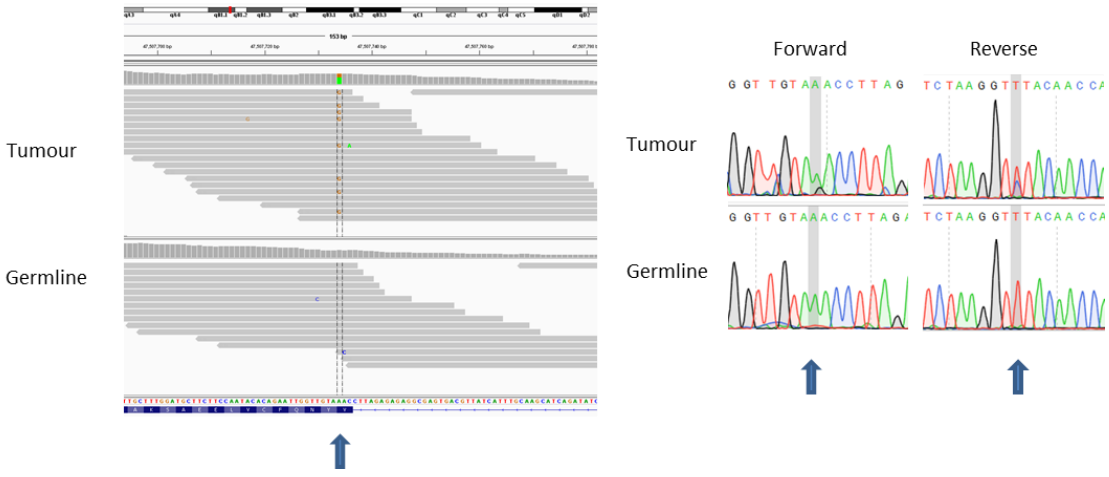

Table 7-2: Details of 14 mutations where Sanger sequencing validation was performed. This confirmed the presence of mutations in 12/14 cases. Chr=Chromosome, WT=Wild-type allele, V=Variant allele

Case	Gene	Chr	Locus	WT	V	cDNA change	Protein change	Type	Variant allele depth	Variant Allele frequency	Confirmed by Sanger sequencing	Identified on RNA seq
90	Apcs	1	1.73E+08	G	A	c.324C>T	p.Y108Y	silent	12	0.39	Yes	No coverage
94	Sohlh2	3	55204396	G	A	c.938G>A	p.R313Q	missense	11	0.48	Yes	no coverage
84	Kcnd3	3	1.05E+08	C	T	c.621C>T	p.C207C	silent	28	0.39	Yes	N/A
96	Col9a2	4	1.21E+08	A	C	c.1280A>C	p.D427A	missense	18	0.56	No	N/A
86	Ncdn	4	1.27E+08	C	T	c.833G>A	p.R278H	missense	11	0.35	Yes	55/103
95	Kmt2c	5	25385687	T	C	c.1254A>G	p.Q418Q	silent	14	0.26	Yes	1/7 reads
97	Pak1	7	97866200	A	C	c.430A>C	p.S144R	missense	6	0.24	No	0/17
86	Slco2b1	7	99686093	G	T	c.479C>A	p.A160E	missense	15	0.33	Yes	0/3
94	Trappc11	8	47507734	A	G	c.1896T>C	p.V632V	silent	8	0.38	Yes	10/12 reads
93	Sipa1l2	8	1.25E+08	T	A	c.2089-2A>T	p.?	ess_splice	16	0.64	Yes	N/A
86	Efcab6	15	83872246	A	C	c.3892T>G	p.S1298A	missense	11	0.27	Yes	no coverage
89	Nell2	15	95232597	G	C	c.1894C>G	p.R632G	missense	25	0.31	Yes	N/A
96	Spsb3	17	24891494	C	T	c.1294C>T	p.R432C	missense	43	0.45	Yes	N/A
89	Olfr137	17	38305263	T	G	c.197A>C	p.N66T	missense	11	0.32	Yes	N/A

7.2.3 Recurrent murine mutations

Only 4 mutations were found recurrently in two or more tumours (Table 7-3). For *Col9a2,* the mutation was not validated by Sanger sequencing. Similarly, *Olfr54* encodes an olfactory receptor and the change was thought to be neutral and therefore unlikely to be of functional significance.

The *L1td1* gene encodes LINE-1 type transposase domain containing 1, an RNA binding protein highly and specifically expressed in pluripotent cells (Emani, Narva et al. 2015). It has also recently been shown to be expressed in medulloblastoma cells and required for cell viability, neurosphere formation and chemoresistance (Santos, Silva et al. 2015). Whilst potentially of interest, functional prediction suggested that this mutation would be tolerated and inspection of the reads with the mutation identified additional changes, including in some germline reads suggesting that this mutation may not be true and relate to technical artefacts, e.g. mapping (Figure 7-3).

The *Vps8* gene encodes a CORVET complex subunit, a protein complex which regulates endosomal tethering and therefore endosomal trafficking. Mutation prediction software suggested a deleterious effect to the two mutations identified in this gene, however, its functional significance in these tumours is unclear.

Table 7-3: Recurrent mutations identified in murine ACP

Gene	Sample	cDNA change	Protein change	Variant classification	Mutant Allele Fraction	Provean Prediction	Sift prediction
Col9a2	MD5196a	c.1280A>C	p.D427A	Missense	0.56	Deleterious	Tolerated
Col9a2	MD5192a	c.1634G>T	p.R545L	Missense	0.14	Deleterious	Damaging
L1td1	MD5192a & MD5194a	c.1466A>G	p.H489R	Missense	0.14	Neutral	Tolerated
Olfr54	MD5193a	c.375T>C	p.F125F	Silent	0.17	Neutral	Tolerated
Olfr54	MD5193a	c.400T>C	p.Y134H	Missense	0.27	Neutral	Tolerated
Olfr54	MD5185a	c.456G>A	p.M152I	Missense	0.5	Neutral	Tolerated
Olfr54	MD5184a	c.913C>A	p.L305I	Missense	0.17	Neutral	Tolerated
Olfr54	MD5184a	c.916C>T	p.L306F	Missense	0.19	Neutral	Tolerated
Olfr54	MD5184a	c.936C>T	p.S312S	Silent	0.19	Neutral	Tolerated
Vps8	MD5194a	c.1063C>A	p.H355N	Missense	0.11	Deleterious	Damaging
Vps8	MD5187a	c.3653A>T	p.N1218I	Missense	0.11	Deleterious	Damaging

Figure 7-3: L1td1 mutation in case MD5192a. Note other changes identified in reads containing suggested mutation. A similar read is also identified in the germline DNA suggestive that this mutation is an artefact.

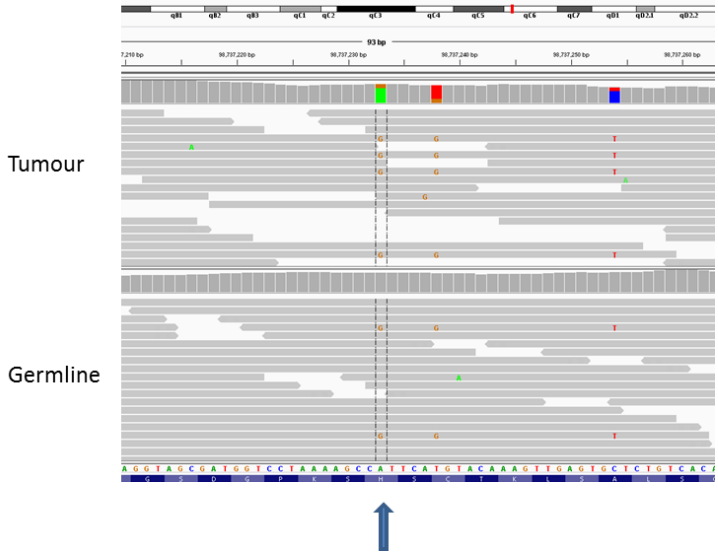

7.2.3.1 Recurrent mutations between murine and human ACP

Comparison was also made with the published exome sequence results of 12 human ACP (Brastianos, Taylor-Weiner et al. 2014). This revealed 12 genes to be mutated in both human and mouse tumours, of which five of which were non silent/intronic in both species (Table 7-4).

7.2.3.2 Known cancer genes

Within established cancer genes, only two coding mutations were identified, p.K400I mutation in the isocitrate dehydrogenase gene *Idh1*, and a p.P466Q mutation in *Recql4* a DNA repair genes. Both were of low allele frequency 9.5 and 8.9% respectively). Results presented in Chapter 4 suggest *IDH1* hotspot mutations are not observed/common in human ACP.

7.2.4 Summary

These results demonstrate that late stage murine ACPs acquire somatic mutations, though with low levels of overlap between individual cases and with human ACP. The functional significance of these mutations is currently unclear.

Exome sequencing approaches are able to establish single nucleotide variants and small insertions and deletions, but not copy number changes and rearrangements. Thus this experiment would not detect translocations of the type observed by Kode *et al.* in their model of leukaemogenesis (Kode, Manavalan et al. 2014).

Table 7-4: Mutation in genes in both human and murine ACP

Human ACP				Murine ACP			
Gene	cDNA change	Protein change	Variant classification	Gene	cDNA change	Protein change	Variant classification
ASCC2	c.1861G>A	p.D621N	Missense	Ascc2	c.1016+10G>A	NA	splice_region
DNAJC3	c.1243C>T	p.R415*	Nonsense	Dnajc3	c.1381G>T	p.G461*	Nonsense
KIF1C	c.2087G>A	p.R696Q	Missense	Kif1c	c.474G>T	p.L158F	Missense
PKD1L1	c.3862C>T	p.R1288C	Missense	Pkd1l1	c.55G>T	p.W19C	Missense
TGFBI	c.1286C>T	p.A429V	Missense	Tgfbi	c.662A>C	p.D221A	Missense

7.3 Whole genome sequencing of human ACP

To understand the wider genomic landscape of human ACP, whole genome sequencing (WGS) of a limited cohort of tumours was performed. In comparison to the previously published 12 exome sequences of ACP, WGS gives further information, both about changes within intronic regions (99% of the genome), but also about copy number changes, for which previous studies have been inconclusive (Table 7-5).

In order to separate somatically acquired genomic variants within the tumour from background germline genomic variation, matched germline DNA samples from the patient is required. The collection of such samples was not routine practice in most UK centres at the start of this project and so only a limited number of samples were available for analysis, particularly once tumour histology and DNA quality had been reviewed.

Consequently, only five tumour and germline sample pairs were available at the time of sequencing (March 2015). Of these, the *CTNNB1* mutational status later became available from targeted DNA sequencing in 4 cases and RNA sequencing of a neighbouring specimen in all five (Chapters 4 and 5) (Table 7-6).

7.3.1 WGS results

No pipeline for analysis of cancer genome sequencing data was available at the Institute of Child Health at the time of this project and so the whole genome sequencing data was analysed through the Wellcome Sanger centre Cancer Genome Project (CGP) pipeline, through collaboration with Dr Sam Behjati. Summary results are presented in Table 7-6 (Full results Supplementary Table 7).

7.3.2 *CTNNB1* mutations confirmed in four of five cases

Whole genome sequencing identified the known *CTNNB1* mutations in four out of five cases. In case JA011 no mutation was identified. As discussed in Chapter 5, this case predominantly consisted of reactive glial tissue and had low tumour content and targeted NGS sequencing had identified a low variant allele frequency. WGS is

less sensitive than the targeted NGS sequencing, due to a lower depth, and this may explain the failure to detect this mutation. All other mutations were in line with the results of targeted sequencing and RNA sequencing, though the allele frequency observed in case JA056 was lower than expected (7% compared to 36%).

7.3.3 Wide variation in mutation number identified across samples

A wide variety in the number of somatic changes was identified across the samples. Of particular note, both cases with relatively high tumour content (JA009 and J0056) had relatively low mutation rates (3009 and 692 respectively, equivalent to 1 and 0.6 per Mb). This is consistent with the results presented by Brastianos *et al*. of 0.9 per Mb (Brastianos, Taylor-Weiner et al. 2014). In contrast, cases JA004, 008 and 011 had much higher mutation burdens (4.6-6.3 per Mb), but low tumour content and low or absent *CTNNB1* mutation allele frequencies. In contrast to cases JA009 and JA056 genomic rearrangements/break points were identified in these cases. These are theoretically considered 'validated' *in silico,* as they have been detected by two independent means; the presence of read pairs at different sites in the genome and identification of split reads spanning the newly created join.

These results suggest that the high mutation burden identified in the three cases with low tumour content could reflect somatically acquired mutations within the reactive glial component of the tissue sequenced, as opposed to the tumour epithelia. This would be equivalent to the mutations identified in the non-cell autonomous murine tumours. I explore this further below.

Table 7-5: Summary of previous studies addressing chromosomal copy number changes in ACP.

Study	Methods	Findings
Rickert & Paulus, 2003(Rickert and Paulus 2003)	Comparative genomic hybridisation (CGH), tumour microdissection so that 80% tumour content or more	No copy number changes in ACP (n=29)
Rienstein et al, 2003 (Rienstein, Adams et al. 2003)	CGH (n=9)	Chromosomal abnormalities in 6/9 samples
Gorski et al, 1992 (Gorski, McMorrow et al. 1992)	Trypsin G banding after 14 days in culture (n=1)	The cells exhibited the following karyotypes:46,XY/46,XY,t(2;12)(q21;q13) t(3;7)(p11;q36),/46,xY,t(6;14](q21;q32) in a ratio of 16:2:2.
Karnes et al, 1992 (Karnes, Tran et al. 1992)	Trypsin G banding (n=3) 3-10 days in culture	2 WT, 46,XY, t(2;19)[q34;q13.3},t(9;21)(q32;q22),del(12)(q24.1),- 13, +mar.
Griffen et al, 1992 (Griffin, Long et al. 1992)	Trypsin G banding (n=4) 4-9 days in culture	No abnormalities

Table 7-6: Summary results of WGS of human ACP.

Case		JA004	JA008	JA009	JA011	JA056
DNA ID (tumour/germline)		BGI314 /320	BGI315 /321	BGI316 /322	BGI318 /BGI324	BGI319a /325a
Sanger ID		PD30776	PD30777	PD30778	PD30779	PD30780
Tumour content (% nuclear area)		40%	60%	90%	20%	80%
CTNNB1 status	Known mutation	p.S37F	p.G34R	p.S37F	p.G34R	p.S33C
	Allele freq (targeted NGS)	13.6%	23%	45%	5%	Not done
	Allele freq (RNA seq)	16%	27%	48%	Not detected	36%
	CTNNB1 (WGS)	p.S37F	p.G34R	p.S37F	Not detected	p.S33C
	Allele freq(WGS) (%, no reads (mut/WT)	16% (13/68)	8% (6/72)	45% (41/50)	N/A	7% (6/86)
Total Substitutions		15370	14446	3009	19348	692
Single nucleotide changes (CaveMan)	All single nucleotide changes	15010	14115	2647	18849	571
	CA	1639	1587	186	2024	71
	CG	2044	1885	423	2489	69
	CT	3935	3767	686	5190	80
	TA	2083	1901	451	2480	204
	TC	3923	3609	710	4887	100
	TG	1386	1366	191	1779	47
Small insertions and deletions (Pindel)	All Indels	360	499	362	331	121
	Complex rearrangements	8	4	28	16	5
	Deletions	279	385	304	230	94
	Insertions	73	110	30	85	22
Large rearrangements (BRASS)	Validated Break Points	5	7	0	2	0

7.3.3.1 Case JA009

Both JA009 and JA0056 had modest mutation frequencies. In JA009 there were no rearrangements and of the substitutions, 31 (1%) were in coding regions (Table 7-7). Of these, only the *CTNNB1* c.110C>T pS37F mutation was in a known cancer gene. Of other mutations, there were a total of 2 non-sense mutations, 18 missense mutations, 8 silent mutations, 1 non coding variant. There were two deletions; one was at splice region of the uncharacterised gene *AC007795.1* and the other an in-frame deletion p.Q413delQ of *R3HDM2.*

Plotting the variant allele frequencies of the single nucleotide variants identified that the majority had a low allele frequency (median 9%). Of note, within the coding region variants only *CTNNB1* had a variant allele frequency of 45% (Table 7-4)

Taken in the context of the histology these results are highly suggestive that *CTNNB1* is the only driver mutation present in this case.

7.3.3.2 Case JA056

Like case JA009, case JA056 also had a good tumour content histologically and a high (36%) variant allele frequency on RNA sequencing of a neighbouring tumour piece. Surprisingly, the allele frequency of the p.S33C *CTNNB1* mutation identified by WGS was only 7%. Of the 692 somatic variants identified, only 5 (0.7%) were in coding regions. These were a missense p.G282D mutation in *FAM230A*, a silent p.T1315T mutation in *SSC5D*, an 82bp r.1123_1204del82 frame shift deletion in *IRF2BPL* and a 63 bp in frame deletion r.76_138del63 in *RAMP2*. Like case JA009 the majority of substitutions had a low variant allele frequency (median 9%).

As with JA009, of the mutated genes only *CTNNB1* is a known cancer driver gene. The functional significance of the other genes is not known.

Figure 7-4: Variant allele frequencies identified of a) all b) coding, mutations identified in case JA009. Note the *CTNNB1* mutation is the only coding mutation with an allele frequency of 45%.

a

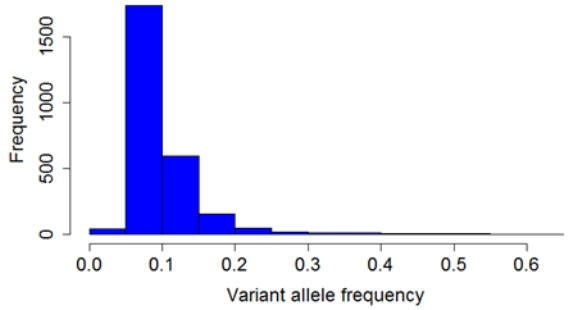

b

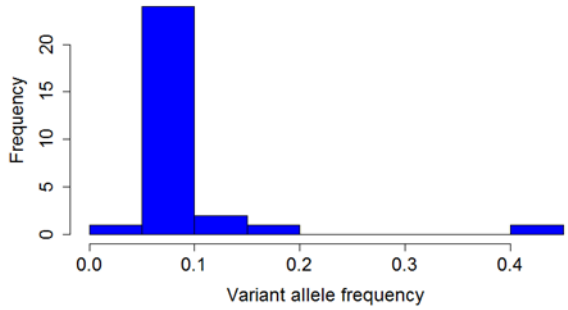

Table 7-7: Thirty-one coding region mutations identified in case JA009 by whole genome sequencing.

Gene	Chr	Locus	Nucleotide change (RNA)	Protein change	Mutation Type	Mutation Effect	Variant allele frequency	RNA seq validation
HRNR	1	247150338	r.4222c>a	p.S1382S	Sub	silent	0.120	0/10 reads
ZNF678	1	152189959	r.1180c>g	p.T343S	Sub	missense	0.052	0/11
ZNF695	1	227842814	r.1627g>a	p.K493K	Sub	silent	0.066	0/1
CTNNB1	3	41266113	r.390c>u	p.S37F	Sub	missense	0.450	345/719 reads
ZNF717	3	75790818	r.450c>u	p.Q43*	Sub	nonsense	0.094	0/12
CMYA5	5	79032447	r.7890a>g	p.H2620R	Sub	missense	0.069	0/4
MDC1	6	30672595	r.5013c>a	p.L1455L	Sub	silent	0.060	6/126 reads
MDC1	6	30672987	r.4621g>c	p.V1325L	Sub	missense	0.062	2/93 reads
DPCR1	6	30919531	r.3318u>c	p.I1097T	Sub	missense	0.078	0/0
NHSL1	6	138763185	r.803g>a	p.R200Q	Sub	missense	0.110	0/41
CSMD1	8	2800017	r.10512u>g	p.F3504L	Sub	missense	0.073	0/2
RP5-903G2.2	11	67707229	r.17c>g	-	Sub	nc_variant	0.053	0/1
CTD-3193O13.9	19	7935108	r.3185c>u	p.P1008S	Sub	missense	0.170	0/17
ZNF93	19	20044577	r.841a>c	p.T271T	Sub	silent	0.072	0/22
ZNF93	19	20044583	r.847u>a	p.T273T	Sub	silent	0.046	0/23 nb 1 G
ZNF93	19	20044585	r.849a>c	p.K274T	Sub	missense	0.092	0/23
ZNF85	19	21132069	r.862a>u	p.K250I	Sub	missense	0.067	1/21 reads
ZNF430	19	21240552	r.1619u>a	p.S480T	Sub	missense	0.081	0/53
ZNF43	19	21990649	r.2360a>g	p.G730G	Sub	silent	0.059	0/56
ZNF43	19	21990655	r.2354u>c	p.H728H	Sub	silent	0.077	0/63
ZNF43	19	21990662	r.2347a>u	p.K726I	Sub	missense	0.079	0/63
ZNF208	19	22154245	r.3740c>g	p.Y1197*	Sub	nonsense	0.065	0/0
ZNF98	19	22574853	r.1306c>a	p.T395K	Sub	missense	0.071	0/1
ZNF98	19	22574857	r.1302a>u	p.T394S	Sub	missense	0.073	0/0
ZNF98	19	22574861	r.1298c>u	p.T392T	Sub	silent	0.082	0/0
ZNF492	19	22847717	r.1490a>u	p.T416S	Sub	missense	0.061	0/5
ZNF345	19	37368618	r.1674a>g	p.N296D	Sub	missense	0.065	0/0
ZNF345	19	37368844	r.1900a>u	p.E371V	Sub	missense	0.059	0/88
FAM47C	X	37027244	r.813a>u	p.Q254L	Sub	missense	0.095	0/0
R3HDM2	12	57674204	r.1627_1629delGCA	p.Q413delQ	Del	inframe	.NA	NA
AC007795.1	19	29360561	r.1_126+74del200	-	Del	nc_ess_splice	NA	NA

7.3.3.3 Cases JA004, JA008, JA011

As highlighted above, in contrast to cases JA009 and JA056, cases JA004, 008 and 011 had relatively low tumour contents, yet much higher number of genomic substitutions. In addition, chromosomal rearrangements were identified in all three of these cases.

Given that the results of JA009 and JA056 are consistent with the published exome sequencing of ACP, and the confirmation of acquisition of somatic mutations in non *CTNNB1* mutation containing cells in murine ACP, these results raise the question as to whether these additional mutations are present in the reactive glial tissue, as opposed to the tumour epithelia.

Of the mutations, 8.5% were identified within coding regions. In case JA004, 132 coding mutations were identified, in case JA008, 124 and in JA011, 159. Other than *CTNNB1,* mutations were identified in seven known cancer driver genes, but none of predicted functional significance (Table 7-8).

Four, seven and two chromosomal alterations were identified in the three cases, respectively. These included inversions, deletion tandem duplications and one translocation between chromosome 3 and 15 (Table 7-9).

Table 7-8: Mutations in known cancer genes.

Case	Chr	Locus	WT	M	Gene	R	Protein change	Type	Consequence	Provean/SIFT prediction
JA004	14	1.03E+08	A	G	HSP90AA1	r.2745u>c	p.D821D	Sub	silent	Neurtral/Tolerated
JA004	11	1.02E+08	G	A	BIRC3	r.3950g>a	p.Q400Q	Sub	silent	Neurtral/Tolerated
JA009	11	65269999	T	A	MALAT1	r.4767u>a	-	Sub	nc_variant	
JA009	5	35874604	G	A	IL7R	r.889g>a	p.A254T	Sub	missense	Neurtral/Tolerated
JA009	13	28622544	T	A	FLT3	r.1155a>u	p.D358V	Sub	missense	Neurtral/Tolerated
JA009	4	54319247	CAG	C	FIP1L1	r.1641_1642delAG	p.R487fs*3	Del	frameshift	
JA009	9	5054611	T	C	JAK2	r.1157u>c	p.Y221Y	Sub	silent	Neurtral/Tolerated

Table 7-9: Chromosomal rearrangements identified in ACP Chr=chromosome

Sample	5' End			3' End			strand1	strand2	Type	Brass Notation – chromosome, breakpoint, microhomology region, breakpoint-chromosome (quality score)	Attempted validation
	Chr	start1	end1	Chr	start2	end2					
JA004	3	38198805	38198806	3	38332023	38332024	+	-	inversion	Chr.3 38198806] TTC [38332024 Chr.3- (score 99)	
JA004	3	178998498	178998502	3	179001458	179001462	+	+	deletion	Chr.3 178998499(502)--TCA--179001459(62) Chr.3 (score 99)	Yes
JA004	16	35018144	35018148	16	35056274	35056278	-	+	inversion	Chr.16- 35018148(45)--TTT--35056275(78) Chr.16 (score 100)	
JA004	13	105462846	105462850	13	105476830	105476834	+	+	deletion	Chr.13 105462847(50)--AAG--105476831(34) Chr.13 (score 100)	Yes
JA008	4	40437858	40437859	4	40469658	40469659	+	+	deletion	Chr.4 40437859] C [40469659 Chr.4 (score 89)	Yes
JA008	22	24312458	24312461	22	24516868	24516871	-	+	inversion	Chr.22- 24312461(59)--CA--24516869(71) Chr.22 (score 100)	
JA008	17	41227450	41227452	17	41342300	41342302	+	+	deletion	Chr.17 41227451(52)--T--41342301(02) Chr.17 (score 98)	Yes
JA008	7	32822894	32822897	7	32824955	32824958	+	+	deletion	Chr.7 32822895(97)--AG--32824956(58) Chr.7 (score 100)	Yes
JA008	7	82973042	82973046	7	82974912	82974916	-	-	tandem-duplication	Chr.7- 82973046(43)--TTG--82974916(13) Chr.7- (score 100)	
JA008	2	44318597	44318604	2	44321179	44321186	+	+	deletion	Chr.2 44318598(604)--AGGAAC--44321180(86) Chr.2 (score 97)	Yes
JA008	14	100782180	100782196	14	100783473	100783489	+	+	deletion	Chr.14 100782181(96)--GTGATCCGCCTGCCT--100783474(89) Chr.14 (score 90)	
JA011	2	212351171	212351172	2	212415755	212415756	+	+	deletion	Chr.2 212351172] TT [212415756 Chr.2 (score 99)	Yes
JA011	3	171753133	171753136	15	99550848	99550851	+	+	translocation	Chr.3 171753134(36)--CC--99550849(51) Chr.15 (score 99)	Yes

7.3.4 Validation of WGS results

To further investigate the results, I aimed to validate a proportion of the mutations identified. I would then performed microdissection of matched sections of these cases, separating tumour epithelia from glia, to identify in which compartment a mutation/chromosomal abnormality was present.

To achieve this, primers were designed to detect eight of the deletions and the translocation as highlighted in Table 7-9. Primers were also designed to amplify the wildtype region across break regions. All primer sequences can be found in the Methods section (Table 2-12).

Wild-type regions were successfully amplified for all the regions surrounding deletions, however in no cases was the deletion detected.

For the translocation, wild-type bands were detected and in the DNA from JA011, a band of approximately the correct molecular weight identified for the translocation (Figure 7-5). Of note, a control sample using PCR using wild-type DNA from non-tumour healthy individuals failed to identify this product.

This band corresponding to the translocation was also present in DNA extracted from micro-dissected glia only from this case. There was insufficient tissue to assess in tumour epithelia alone. Gel extraction was performed from these bands and Sanger sequencing performed. Surprisingly, however, the resultant sequence was not that expected, and indeed could not be accurately mapped in the genome. BLAST of the primers revealed that they also bound other highly homologous areas of the genome, raising concerns that this translocation may not be real, and may have been misidentified due to alignment challenges in highly homologous regions of the genome. In addition, this homology makes design of reliable primers challenging and so this failure to validate may reflect experimental challenges.

Primers were also designed to flank smaller deletions of 337 bp at Chr 17: 39340681 in sample JA004, and 204bp at Chr 1, 244927378 and 342 bp at Chr 19, 1418734 in JA011. Despite successful amplification of wild-type DNA from both controls and cases, no deletion was identified in the cases.

The single nucleotide changes identified in these cases were overwhelmingly of low allele frequency (median 7.8% (IQR 6.7-9.5%)). Consequently, they could not be easily directly validated by Sanger sequencing. I therefore identified a small number of mutations that directly affected restriction enzyme sites. Primers flanking 3 such mutations (Case JA004, Chr 5 65437974 G to A and for JA011, Chr18, 74464442 T to C and Chr 1190532787 C to T) were designed. To improve the variant allele proportion, the DNA underwent restriction digest followed by PCR amplification and then Sanger sequencing. Despite successful amplification for two of the three loci, in neither of the cases were the mutations confirmed.

7.4 Integration of human and murine results

The murine mutations identified in section 7.2 were also further integrated with the WGS results of human ACP. This identified 111 genes with mutations in both human and murine ACP. However, when restricted to coding region mutations this number reduced to coding region mutations this reduced to five genes and in only one gene, *SLITRK2,* was there a missense mutation in both human and murine ACP (Human, pS6010P, Murine p.A732P). Of the genes previously identified in Table 7-4, there were intronic mutations in *ASCC2, DNAJC3, KIF1C* and *PKD1L1*.

Figure 7-5: Attempted validation of translocation in case JA011. a) Primer design strategy, b) PRC products. Arrows indicate products at approximately correct molecular size in DNA from both tumour and from micro-dissected glia. Product not identified in WT control DNA (not shown). Bands highlighted underwent gel extraction and Sanger sequencing, however sequence did not match predicted sequence.

a

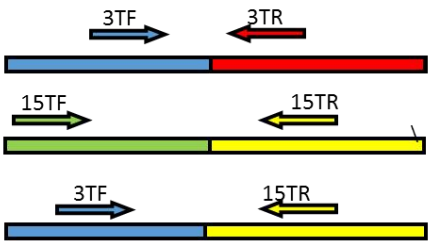

Product	F primer	R primer	Predicted size
WT Chr 3	3TF	3TR	203bp
WT Chr 15	15TF	15TR	587bp
Translocation	3TF	15TR	371bp

b

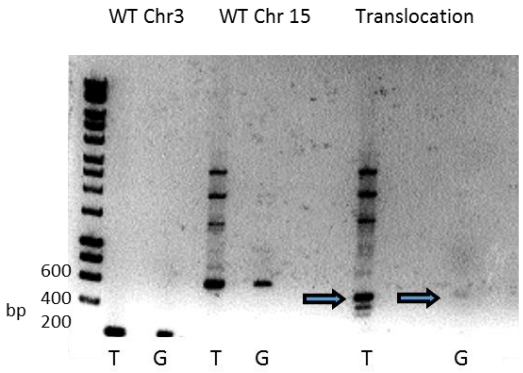

T = whole tumour DNA undergoing WGS
G = DNA from micro-dissected glial tissue only

7.5 Discussion

In summary, whole genome sequencing of ACP has confirmed the presence of *CTNNB1* mutation in four out of the five samples sequenced. The failure to identify the mutation in case JA011 likely reflects the low tumour content. It is recognised that WGS in samples with tumour content <10% is challenging and it is unlikely this experiment had sufficient depth to detect the mutation (Spencer, Tyagi et al. 2014).

For the two cases with high tumour content, the *CTNNB1* mutation was the only one of likely functional significance. This would be consistent with *CTNNB1* mutation alone being sufficient to induce ACP tumourigenesis. The murine models of activation of β-catenin in Rathke's pouch, adult pituitary stem cells, or the embryonic tooth would all further support this.

The significance of the surprising finding of high mutation rates in cases with low tumour content is less clear. Whilst this would be consistent with polyclonal mutations within the reactive glial tissue, attempts to validate this have been unsuccessful. This could reflect i) experimental design – the approach for validation may be less sensitive for identifying small sub-clonal mutations, the primers may have been sub-optimal, ii) Intra-tumoural heterogeneity the low allele frequency suggests that mutations are not present within all cells and therefore there may be multiple clones.. Validation in different DNA aliquots, or neighbouring regions on glial tissue may therefore fail to identify the same mutations as clones may be spatially restricted within the tissue, iii) experimental noise in the WGS data meaning that these "mutations" are false positive results. Why this would occur in these three cases, but not the two with high tumour content is not clear.

To further assess these results a number of options could be pursued. i) Filtering of results using a database of known variants identified in healthy controls sequenced on the same platform at the Beijing Genomics Institute (BGI); The filtering at the Sanger centre is based on their experience with their machines, as the sequencing was performed at BGI filtering using data now available from wider GosGene experience could be used for filtering ii) Next generation sequence validation. (e.g.

targeted amplification and NGS of a number of SNVs). These could be more rationally selected by enriching for those most convincing when reviewing the individual read traces (not available during this project).

Reviewing the previously reported karyotype and comparative genomic hybridisation studies of ACP reveals that chromosomal abnormalities were only identified when microdissection of tumour was not performed, suggesting that these abnormalities may be in the non-tumour epithelia. Indeed, in support of this, the cells presented in Gorski *et al,.* appear markedly astrocytic in their figure (Gorski, McMorrow et al. 1992).

The identification and confirmation of somatic mutations in late stage murine tumours suggests that such acquisition of mutations in the reactive glia could be consistent with analogous processes. Such non-cell autonomous mutagenesis has been observed in other mouse models and these findings would therefore be consistent with and of relevance to a wider literature (Kode, Manavalan et al. 2014). In Chapter 9 (Discussion), I discuss how this may relate to the senescence with SASP resulting in a pro-mutagenic micro-environment.

Even if such mutations were to be confirmed, the functional significance of these mutations in both the mouse and human ACPs however remains unclear. In the absence of direct effects on critical cell regulators (e.g. cell cycle) the presence of such numbers of mutations could have effects on immune activation. Mutation burden is often seen as a biomarker for efficacy of immune checkpoint inhibitors and therefore this could be of therapeutic relevance (Topalian, Taube et al. 2016).

7.6 Summary

In this chapter I confirm that late stage murine ACP acquire somatic mutations, though these are predominantly non recurrent and the functional significance is unclear. WGS sequencing of human ACP identified *CTNNB1* mutations as the only cancer gene to be mutated in two cases with high tumour content, consistent with animal models suggesting that *CTNNB1* mutation is sufficient to induce ACP tumourigenesis. WGS also suggested high mutational burden, of low variant allele frequency, in samples of ACP predominantly consisting of reactive glial tissue. This finding however requires further validation and the functional significance is unclear.

Chapter 8 Pre-clinical testing of targeted therapies

8.1 Introduction

This thesis and previous studies have identified a number of potentially therapeutically targetable pathways in human ACP. In a proportion of these, targeted therapies are currently commercially available and in clinical use for other indications. Of the pathways discussed in this thesis, the SHH pathway is perhaps the best characterised, both in human and murine ACP (see Sections 5.13.2 and 6.6.2). At the time of study, no *in vivo* pre-clinical evaluation of any agents had been performed for ACP. This chapter addresses the pre-clinical testing of the sonic hedgehog pathway inhibitor Vismodegib® (GDC-0449). This experiment gives important information not only about the significance of the SHH pathway, but also acts as a test case for future pre-clinical studies for ACP. Other potentially targetable pathways will be discussed in more detail in the Discussion (Chapter 9).

8.2 Randomised pre-clinical trial of Vismodegib in embryonic ACP model

To test the efficacy of targeting the SHH pathway in murine ACP, Vismodegib was selected as the best agent for testing. This smoothened inhibitor was the first SHH pathway to be licenced (for its use in Basal cell carcinoma) and our collaborators at the ICR had previous experience in using this drug in murine trials (Wong, Alicke et al. 2011, Sekulic, Migden et al. 2012, Hill, Kuijper et al. 2015). Furthermore, this experience was with drug purchased from third party providers, at a reasonable cost, thus avoiding the need to enter into agreements with pharmaceutical companies.

The embryonic model of ACP was felt to be the most appropriate for testing as i) the expression of the SHH pathway members was best characterised in this model ii) the absence of requirement to use tamoxifen induced recombination iii) survival data available at that time suggested a three month median survival with 100% penetrance of tumour development, facilitating a potentially relatively fast experimental duration.

8.2.1 Pharmacokinetic (PK) and pharmacodynamics (PD) analysis

First we wished to confirm the efficacy of Vismodegib *in vivo* by performing limited PK and PD studies. The Home Office project licence, under which the trial was to be conducted, limited drug administration to 56 doses (i.e. 56 days at once a day, or 28 days given twice a day). Previous studies had used varying doses and dosing regimens of Vismodegib, though predominantly twice daily (Wong, Alicke et al. 2011, Gould, Low et al. 2014). We selected the highest published dose (100mg/kg/day) and treated mice with a single dose followed by collection of plasma specimens at 3, 9, 12, or 24 hours post-dose. Mass spectroscopy (by Ruth Ruddle) showed complete elimination of drug by 24 hours (Figure 8-1). Similarly, qRT-PCR of *Gli1* showed reduction in expression within the pituitary at 12 hours but not 24 hours post dose (by Gabriela Carreno), suggesting that 24 hour dosing would not lead to sustained pathway suppression (Figure 8-1). Further PD assessment was performed following seven doses of 100mg/kg. This showed suppression and reduced variation of *Gli1* expression in treated mice (Figure 8-1).

As a result of these experiments, a dosing regimen of 100mg/kg twice a day was selected and a trial designed as per Figure 8-1. Animals were bred by myself at ICH, transferred to ICR, where Home Office regulations required one week period to settle in, followed by randomisation between 100mg/kg Vismodegib, or vehicle alone, twice daily, for 56 doses. After completion of therapy, mice were followed by observation for the development of symptoms, and tumour progression as assessed by MRI, with animals culled at a humane end point.

8.2.2 Vismodegib treated mice have reduced survival

A total of 23 mice were enrolled in the study (12 Vismodegib treated, 11 vehicle treated). The trial was eventually terminated after 19 months, by which time all of the treated mice had died, but four vehicle treated mice remained alive.

Survival analysis showed a median survival in the Vismodegib treated group of 11.9 weeks, whilst the vehicle treated mice had a median survival of 33 weeks. Log-rank test showed this to be a statistically significant difference in survival ($p=0.048$),

Hazard Ratio (2.55, 95% confidence interval: 0.99-6.57) (Figure 8-2). Thus, to our initial surprise, SHH pathway inhibition in murine ACP worsened survival of mice.

8.2.3 MRI analysis shows faster tumour volume doubling time amongst Vismodegib treated mice

Serial MRI scans of trial mice were reviewed. Full data was available for seven mice in each group. These showed heterogeneous progression of cystic and solid components (Figure 8-2). Quantification revealed that Vismodegib treated mice had a faster tumour volume doubling time (mean 8.1=weeks, median=7.4 weeks) compared to vehicle treated mice (mean=15.3 weeks, median=14.2 weeks) (p=0.044) (Figure 8-2) (performed by Jessica Boult).

8.2.4 Additional work (Performed by Gabriela Carreno)

Tissue samples were further analysed by Gabriela Carreno. Whilst morphologically identical, tumours from Vismodegib treated animals showed increased proliferative and mitotic indices and increased expansion of endomucin positive cells compared to those from vehicle treated animals. In addition, samples collected from PD analyses showed tumour lesions present in pituitaries treated with 7 doses of Vismodegib, but not in those from controls. Of note such lesions had never been noted in the pituitaries of *Hesx1*$^{Cre/+}$*;Ctnnb1*$^{lox(ex3)/+}$ mice at this age (1 month). Further analysis showed these pituitaries to have an expanded number of SOX2 positive cells and β-catenin accumulating clusters (data not shown).

Following the finding that Vismodegib treatment lead to an increase in the presence of lesions, cell clusters and proliferation in *Hesx1*$^{Cre/+}$*;Ctnnb1*$^{lox(ex3)/+}$ pituitaries, a clonogenic assay was performed in order to identify if the stem cell compartment of these pituitaries was expanded. Single cell suspensions of anterior pituitaries of mice treated twice daily with either vehicle or 100mg/kg Vismodegib for one week (n=6). Cells were cultured in stem cell promoting media under clonal conditions. This analysis revealed a significant 1.7 fold increase in the numbers of colonies in Vismodegib treated animals compared to vehicles (n=3, p=0.0027, Students t-test) (Fig3 a, b) (data not shown).

Figure 8-1: Pharmacokinetic and pharmacodynamic results of use of Vismodegib in ACP mice a) Plasma concentration following administration of a single dose of Vismodegib (100mg/kg) , b) *Gli1* RT PCR at 12 or 24 hours after administration of Vismodegib (100mg/kg), c) following 7 doses of Vismodegib) Schematic of Visomodegib trial design.

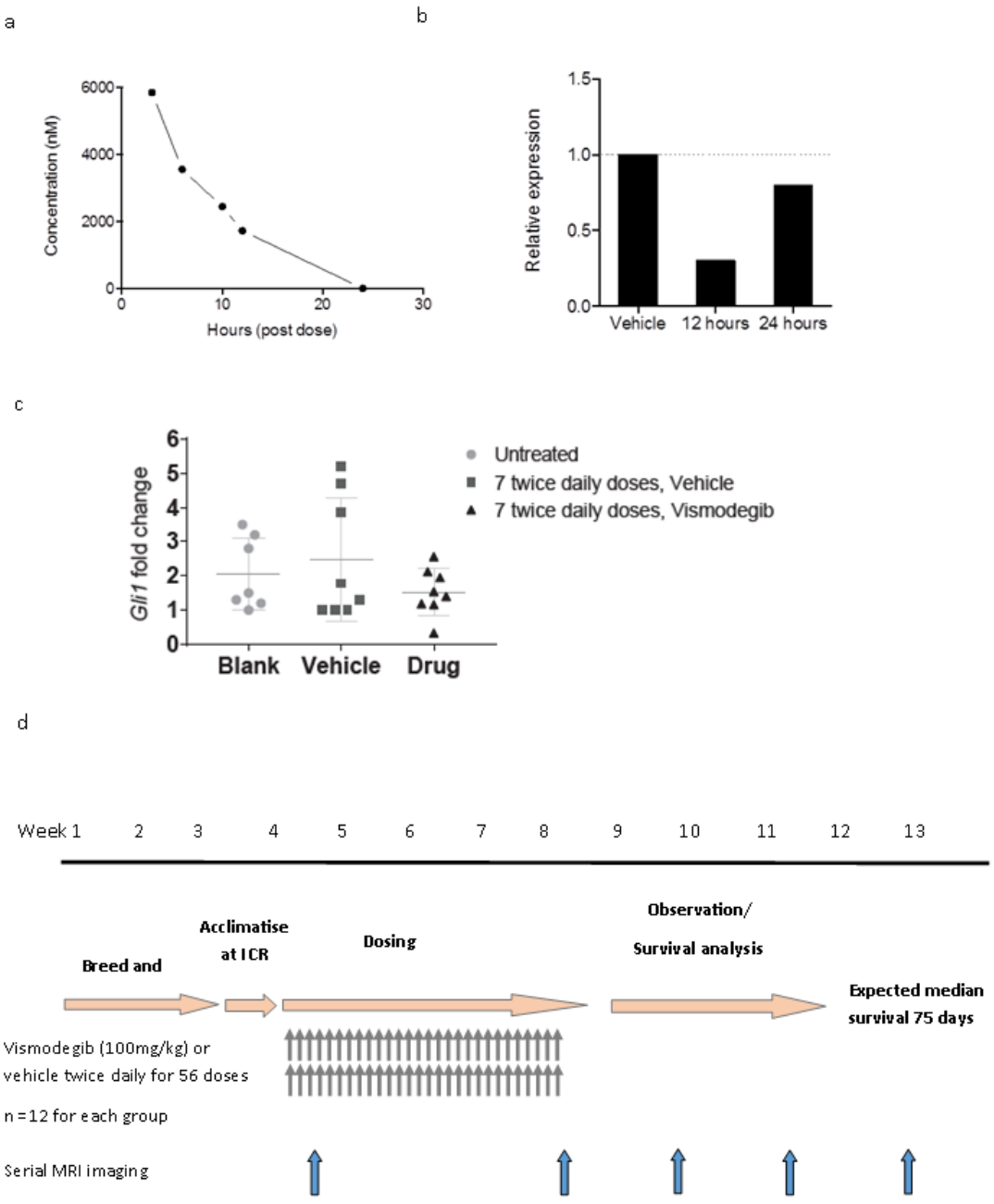

Figure 8-2: Vismodegib trial results. a) Kaplan-Meier showing reduced survival in Vismodegib treated mice (p=0.048) b) example MRIs showing tumour progression (days since treatment initiation), c) Graphical representation of solid tumour growth (days since tumour growth identified).

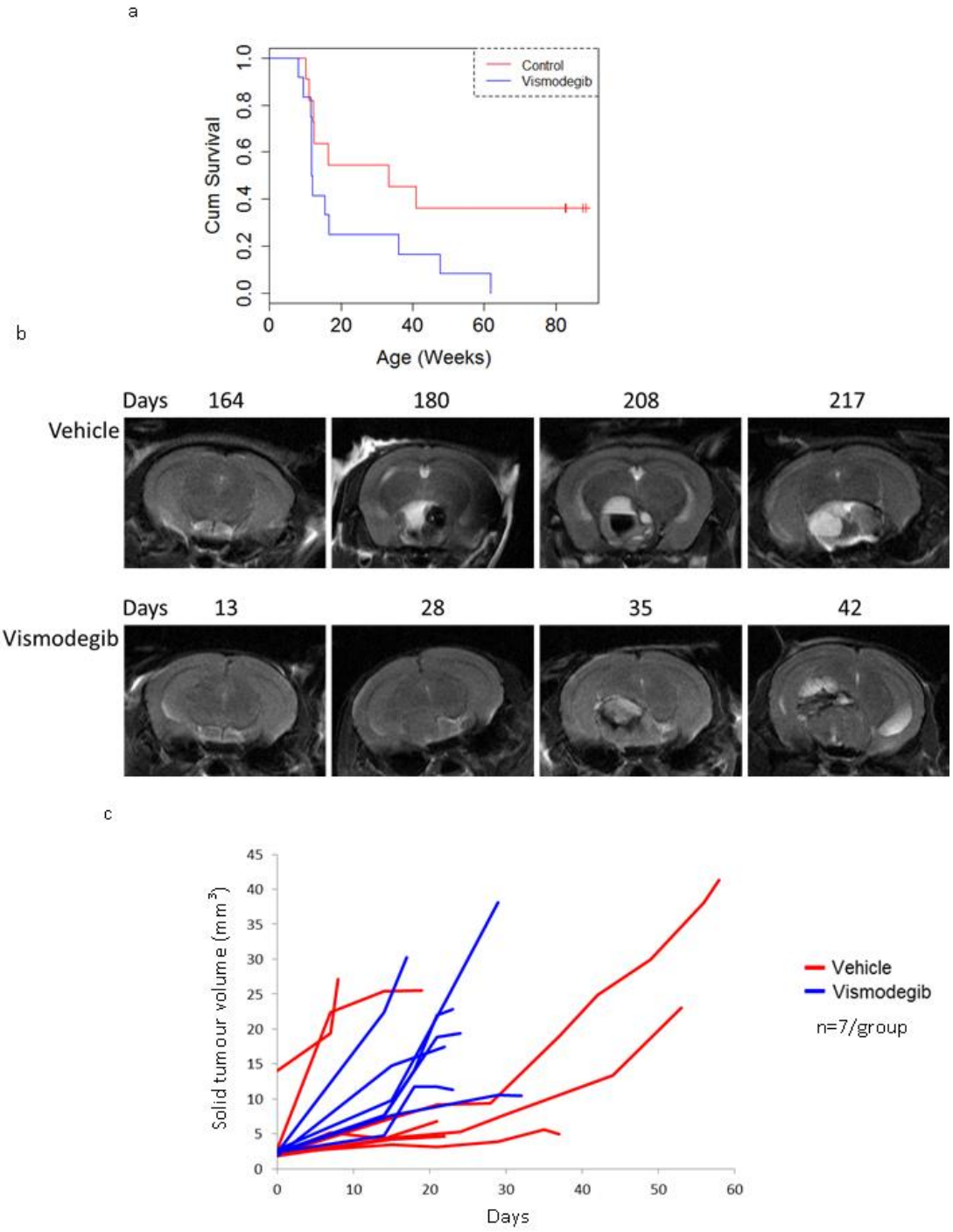

8.2.6 Discussion

Together, these results show that Vismodegib treatment promotes tumour initiation/progression in *Hesx1*$^{Cre/+;}$*Ctnnb1*$^{lox(ex3)/+}$ mice.

The SHH pathway is altered in tumours by two main mechanisms; i) mutation of pathway members, e.g. *PTCH1*. ii) paracrine activation (e.g. increased SHH expression). In the first mechanism SHH pathway inhibition has been successful (Sekulic, Migden et al. 2012). In the second mechanism, trials have largely been disappointing, yielding negative results (Amakye, Jagani et al. 2013, Ruch and Kim 2013). In some cases, adverse results, with worsened survival have been observed (Lou 2014).

Genetically engineered mouse models have revealed the underlying biological reasons for this. For instance, pancreatic adenocarcinoma studies have highlighted cross talk between the tumour (secreting Shh) and the stroma (responding and increasing GLi1 expression). Removal of SHH signalling results in promotion of angiogenesis and the emergence of aggressive epithelial lesions, increased metastasis and decreased survival (Ozdemir, Pentcheva-Hoang et al. 2014, Rhim, Oberstein et al. 2014).

Similarly, results in colorectal cancer models have shown SHH signals promoting progenitor differentiation and inhibition of proliferation. SHH pathway inhibition resulted in decreased tumour stem cell differentiation and an increase in the number of cells with tumour initiating potential, similar to that observed in the ACP model (Chia & Kuo, 2010; Gerling et al., 2016; Krausova & Korinek, 2014; Madison et al., 2005).

Together, these results suggest that targeting the SHH pathway in human ACP may be disadvantageous. However, as discussed in Chapter 6, there are clear differences between human and murine ACP, particularly with regards to which compartments in the mouse correspond to those in human ACP, and the relevance of murine late stage tumours, and non-cell autonomous tumourigenesis to human ACP is less clear.

Review of the safety data of Vismodegib submitted to Federal Drugs Authority highlights further cause for concern. This states that "Pilomatricoma (a benign cutaneous neoplasm) was observed in rats administered oral Vismodegib for 26 weeks at 100 mg/kg/day (approximately 0.8 times the systemic exposure (AUC) in patients at the recommended human dose)" (FDA 2012). Pilomatricomas, a type of hair follicle tumour, have histological similarities to ACP, being one of the few tumours to have anuclear ghost cells and so this also suggests that SHH pathway inhibition in ACP should be viewed with extreme caution (Hassanein, Glanz et al. 2003).

8.3 Chapter summary

In this chapter I present the first *in vivo* pre-clinical assessment of any potential therapy for ACP. This, and other literature, suggest that SHH pathway inhibition is unlikely to be a successful therapy for human ACP, and could indeed worsen tumour growth. Despite this apparent negative result, much can be learnt about the practicalities and feasibilities of conducting a pre-clinical study in the *Hesx1*$^{Cre/+}$*;Ctnnb1*$^{lox(ex3)/+}$ model of ACP. These lessons, along with those from the imaging, survival, transcriptomic and genomic studies will be discussed in detail in Chapter 9, suggesting appropriate future strategies to test other therapies aimed at the other pathways characterised in Chapters 5 and 6.

Chapter 9 Discussion

9.1 Introduction

The data presented in this thesis advances the understanding of the pathogenesis of human and murine ACP.

In Chapter 3, detailed phenotyping highlighted the prominent position of clusters within human ACP and the non-linear kinetics of tumour development in the emybronic mouse ACP model. In Chapter 4, targeted sequencing confirmed the clonal presence of *CTNNB1* mutations within ACP tumour epithelia. In Chapter 5, using this information and the variable tumour content of samples, the gene expression patterns relating to the complex tissue architecture of ACP was dissected *in silico*, leading to the identification of novel ACP genes and signatures of reactive glia and immune cells. This expression analysis also highlighted the molecular similarities between human ACP and odontogenesis, a theme further elaborated in Chapter 6, where the non-cell autonomous development of murine ACP could be seen to reflect epithelial-mesenchymal interactions during odontogenesis.

Similarities between human and murine ACP were observed and a number of pathways of potential therapeutic interest were characterised, both at RNA and protein level, of which pre-clinical targeting of the SHH pathway was performed in Chapter 8.

In both murine and human ACP, epithelial *CTNNB1* mutations appear to be the major driver of tumourigenesis, however in Chapter 7, we also detail for the first time, accumulation of mutations in the non-epithelial compartment (late stage non-cell autonomous tumours in mice and potentially reactive glia in humans).

In this discussion, I consider the implications for each of these findings and their significance in understanding the mechanisms of tumourigenesis and therapy. I suggest a novel model of ACP as copycat of tooth formation and ACP related inflammation as inflammasome mediated, with similarities to other more common conditions (Figures 9.1-3). In addition, I discuss the therapeutic opportunities these results present, particularly with respect to senescence, specific signalling pathways

and inflammation. I then finish by reflecting how the murine models of ACP might be used in pre-clinical testing of new ACP therapies.

9.2 Model of ACP tumourigenesis as aberrant tooth development

As discussed in the introduction, the relationship between ACP and the tooth has long been recognised by pathologists, based on morphological similarities and limited immunohistochemically studies. The results presented in Chapters 5 and 6 give novel insight into the molecular similarities and mechanisms underlying this relationship.

In Chapter 5, I identified that ACPs have a gene expression signature similar to the inner enamel epithelium and ameloblasts of the tooth and that enamel proteins are expressed in association with wet keratin. Laser capture data and immunostainings further confirmed similarities between ACP clusters and the enamel knot.

Both the enamel epithelium and the anterior pituitary are derived from oral ectoderm and mouse model results in Chapter 6 highlight how *CTNNB1* mutation alone, in either the developing pituitary, or in adult pituitary stem cells, is sufficient to activate the enamel epithelium/ameloblast transcriptional signature. In PCP, there is less activation of the ameloblast gene signature and expression of markers enamel proteins has not been observed (Sekine, Takata et al. 2004). This suggests that *BRAF* mutations may be insufficient to induce full ameloblast differentiation seen in ACP.

In the developing tooth, the enamel knots play key roles as signalling centres, controlling both local epithelial proliferation and folding and mesenchymal differentiation (Jussila and Thesleff 2012, Balic and Thesleff 2015). RNA sequencing and immunostaining results suggest analogous roles in ACP with expression of factors such as FGFs, BMPs and TGFβs in clusters, with nearby cells, both epithelial and mesenchymal, showing activation of downstream pathways. Similarly Ki67 staining showed a close relationship between clusters and epithelial proliferation. The 3D relationships of clusters, epithelia and invasion presented in Chapter 3 would also support this analogy with the enamel knot with clusters forming from

surrounding epithelia at the leading edge of teeth. Indeed, some areas (e.g. Figure 3-2) where islands of tumour appear like 'balls on a chain' are not dissimilar to the pattern of tooth development in the maxilla or mandible.

RNA sequencing of the embryonic (*Hesx1*$^{Cre/+}$*;Ctnnb1*$^{lox(ex3)/+}$) model of ACP demonstrated how at the post expansion stage there is accumulation of cells expressing dental mesenchyme/odontoblast markers, a further analogy with the developing tooth (Figure 9-2).

Whilst such an epithelial to mesenchymal interaction is not so clearly apparent in human ACP, there are notable analogies and review and immunohistochemistry of cases and the literature suggests that such processes may occur. The presence of fully formed teeth has been observed in ACP and these cases, including the presence of dentin and dentin producing cells (Seemayer, Blundell et al. 1972, Muller, Adroos et al. 2011, Beaty and Ahn 2014). Similarly, in a proportion of ACP cases, bone may be observed Osteogenesis and odontogenesis are closely related processes induced by many of the same signalling pathways (e.g. BMP signalling) (Kim, Kim et al. 2013).

Odontoblasts derive from neural crest derived mesenchymal cells. Such cells are also present within the pituitary gland, and so it is possible that the final differentiation into odontoblasts or osteoblasts may depend on the local tissue microenvironment.

A profound glial reaction is a common feature of ACP and immunostainings highlight similar paracrine signalling between tumour and glial tissue, as observed between the enamel epithelia and dental mesenchyme. This suggests similarities in the processes between activation of glia and dental mesenchyme.

In the proposed model for ACP, the final tissue phenotype reflects the local tissue micronenvironmnent; for instance, where an ACP develops in close relation with the brain (e.g. suprasellar), secreted factors e.g. FGFs, BMPs, TGFβ, result in activation of the glia, whereas when in closer relation to pituitary mesenchymal

stem cells (e.g. intrasellar), may result in odontoblast or osteoblast like differentiation (Figure 9-1).

In murine ACP, late stage tumours subsequently show evidence of less differentiation than the post expansion stage and as shown in Chapter 7 these acquire somatic mutations. Surprisingly, results of human WGS also suggest acquisition of non-clonal somatic mutations in surrounding reactive tissue (though not confirmed) suggesting analogous processes may be occurring.

Of surprise, two out of three tumours arising from mice without p53 gene expression also expressed mesenchymal markers and on clustering, group with those from *Hesx1*$^{Cre/+}$*;Ctnnb1*$^{lox(ex3)/+}$ mice with wildtype p53. Lineage tracing has demonstrated that these tumours form in a cell autonomous manner, therefore despite different cell of origin (epithelial rather than mesenchymal) the cell phenotype is similar. This suggests that the cell of origin itself is not critical for these processes to occur, rather the local tissue environment. This is supported by previous evidence showing the presence of progenitor mesenchymal cells in epithelial tumours thought to be derived from cancer stem cells by an EMT mechanism (Orciani, Davis et al. 2015, Orciani, Caffarini et al. 2017).

Figure 9-1: Model of ACP tumourigenesis as copy-cat of tooth development. The structures and molecular signatures of ACP reproduce those of tooth development, particularly at the cap stage. Blue indicates epithelial layer, representing the enamel organ of the tooth, and palisading epithelium of ACP. In green are the enamel knot and β-catenin accumulating clusters, which both have similar expression profiles. Beige represents wet keratin. Stellate reticulum is observed in both the developing tooth and ACP. In contrast to the developing tooth, which is surrounded by dental mesenchyme, ACPs often form in a supra-sellar location and induce reaction in the local glial tissue,(with thanks to Cynthia Andoniadou).

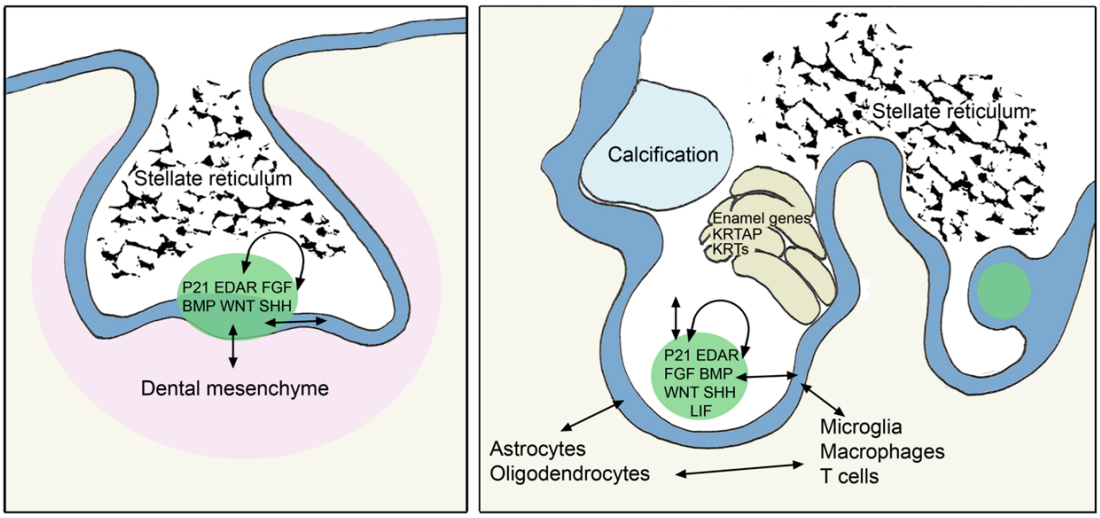

Figure 9-2: Model of murine ACP tumourigenesis. *Ctnnb1* mutation in the developing pituitary results in formation of clusters and epithelial expansion with a signature similar to the inner enamel epithelia and ameloblasts. Further paracrine signalling between the enamel knot and mesenchymal derived cells results in the expansion of a non-cell autonomous lesion/tumour. This accumulates somatic mutations, and exhibits markers of mesenchymal stem cells, brachyury and alpha fetoprotein. Further paracrine signalling occurs within the tumour.

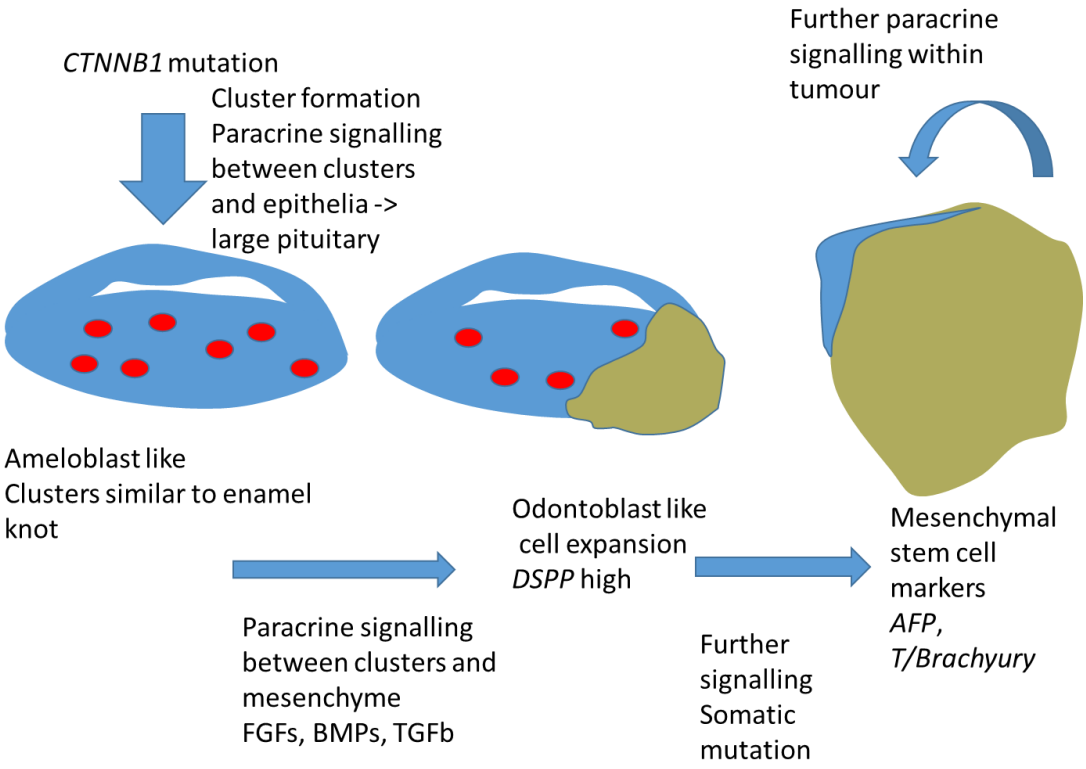

9.3 Lessons from the tooth

Understanding the relationship between ACP tumourigenesis and odontogenesis makes a large area of medical/dental research directly relevant to ACP. There is considerable interest in understanding the developmental biology of the tooth, both as means of developing tooth replacements, but also as a source of mesenchymal stem cells, of relevance to other aspects of regenerative medicine (Tucker and Sharpe 2004). There are also a large number of dental pathologies, for which there are similarities with ACP, e.g. the presence of cholesterol filled cysts.

Unlike mice, humans have a primary (milk) dentition erupting in the first two years of life, followed by secondary dentition predominantly erupting between 6-12 years. This age of secondary dentition is similar to the age distribution of childhood ACP which peaks in childhood at 5-14 years. Such an age distribution for a childhood tumour is relatively unusual, with most tumours peaking in the first few years of life or at adolescence (Bunin, Surawicz et al. 1998). This observation suggests that signals promoting secondary dentition, could also promote growth of ACP. In human ACP, the retrospective finding that patients with ACP have reduced height at one year of age suggests there may be a period of dormancy, similar to that observed in murine ACP (Muller, Emser et al. 2004). Tooth eruption requires complex changes in local physical dynamics, and the molecular signals underlying this are only partially understood (Cobourne and Sharpe 2013). Mutations of the parathyroid hormone receptor 1 (*PTH1R*), which binds parathyroid hormone, and parathyroid hormone related peptide (*PTHLH*) have been observed in patients with delayed primary eruption and of note *PTHLH* was one of the most over expressed genes in tumours compared to controls (237 fold) (Supplementary Table 2) (Cobourne and Sharpe 2013).

9.4 Specific pathways in ACP

In the next sections I discuss the individual pathways explored in this thesis. In many cases their functional significance has been explored in the developing tooth and in addition to their expression patterns, I look at how this, and data from other tumours, may help inform on the therapeutic potential of their targeting in ACP.

9.4.1 WNT pathway

In the normal developing tooth a well-orchestrated sequence of epithelial-mesenchymal interactions result in a well-structured normal tooth. In contrast, the structures of ACP are, with the rare exception of cases with compete teeth, more chaotic. ACP formation occurs in the context of mutated *CTNNB1*, and consequently persistently activated β-catenin. In animal models where the same degradation resistant form of *Ctnnb1*(*Ctnnb1*$^{lox(ex3)}$) is activated in the enamel epithelia, under the control of the *Krt14* promoter, the result is continuous tooth formation, with the presence of multiple enamel knots and with morphological similarities to ACP (Jarvinen, Salazar-Ciudad et al. 2006). Similar results are also seen when inhibiting the *Apc* gene (Wang, O'Connell et al. 2009). This suggests that, like in the developing pituitary, persistent β-catenin signalling leads to persistent epithelial proliferation in association with the presence of enamel knots/clusters.

These experiments in murine teeth are also consistent with the murine ACP models, for instance the increased pituitary size observed in *Hesx1*$^{Cre/+;}$*Ctnnb1*$^{lox(ex3)/+}$ mice from early embryological stages. They also support the findings presented in Chapter 7 that *CTNNB1* mutations are the only significant driver mutation identified in samples of high ACP tumour content.

In summary, the results of this thesis support that, like in the teeth, β-catenin mutation alone is sufficient to initiate and drive tumour growth.

In Chapter 4, the clonal presence of *CTNNB1* mutations in ACP epithelia, including non-nuclear-cytoplasmic accumulating cells, was confirmed independently by two methodologies in an overlapping dataset. As in ACP, in the developing tooth nucleo-

cytoplasmic β catenin accumulation is also limited to the enamel knot (Obara and Lesot 2004). The mechanisms of this restricted activation of the pathway are currently unknown.

Considering the origin of the enamel knot, as cells delaminating from the enamel epithelium, it is likely that ACP clusters may also delaminate from surrounding palisading epithelium. Their location, as confirmed by micro-CT in Chapter 3, at the leading edge may reflect this origin, as well as their role in epithelial proliferation and bending.

Despite decades of interest there are currently no licensed WNT inhibitors in routine clinical use. The ubiquitous and critical nature of the pathway in organ homeostasis makes developing effective drugs with safe therapeutic indexes particularly challenging (Anastas and Moon 2013).

9.4.2 Sonic Hedgehog Pathway

The SHH pathway has been suggested and discussed as a therapeutic target in ACP for several years (Andoniadou, Gaston-Massuet et al. 2012, Gomes, Jamra et al. 2015, Gump, Donson et al. 2015, Coy, Du et al. 2016). In this thesis we advance our understanding of its functional role of ACP.

The RNA sequencing results, supports previous observations that SHH is expressed in clusters, but that downstream signalling is active in both cluster and non-cluster tumour tissue. Pre-clinical testing of the SHH pathway inhibitor Vismodegib resulted in, at first surprising, significant reduction in survival. Further investigation by Dr Gabriela Carreno has identified that this may relate to accelerated tumourigenesis, as observed by the presence of tumour lesions following one week of treatment, compared to absence of lesions in controls and an increase in clonogenic potential of pituitary cells following drug treatment.

Such apparent paradoxical worsening of survival on treatment with SHH pathway inhibitors has now been observed in several other tumour types and is thought to relate to adverse effects on the tumour stroma, facilitating a more aggressive phenotype (Ozdemir, Pentcheva-Hoang et al. 2014, Rhim, Oberstein et al. 2014). In

the non-cell autonomous models of ACP tumourigenesis, the classification of tumour compartments/stroma is less clear and so the processes observed here may well be analogous to those seen in other tumours.

How these results would relate to human ACP, where SHH signalling appears predominantly intra-epithelial, is unclear. Some insight can be gained by considering the role of SHH in tooth development, where it is expressed highly by the enamel knot, as well as other epithelial structures at different stages. Manipulation of the pathway, by ectopic Shh administration or genetic manipulation of *Shh* and other pathway members has shown that, while not essential for ameloblast and odontoblast differentiation, SHH modulates both epithelial and mesenchymal derived compartments, regulates growth and determines the shape of the tooth (Dassule, Lewis et al. 2000, Cobourne and Sharpe 2005).

In addition to similarities to the odontogenesis, molecular similarities were also identified between ACP and hair follicle development, a process involving many of the same pathways. Reviewing the safety information on Vismodegib, an increased on the hair follicle tumour, Pilomatricoma, was observed following drug treatment of rats (FDA 2012). Pilomatricomas have histological similarities with ACP, including the presence of anuclear ghost cells/wet keratin. Consequently, this observation also supports caution in the use of SHH inhibitors in ACP.

Together, the results presented in this thesis suggest that SHH pathway inhibition is unlikely to be of therapeutic benefit in human ACP and that caution should be applied when considering the use of SHH pathway inhibitors in patients. As with other recent results, they highlight the need of considering the histological context and microenvironmental significance of targeting a given pathway.

In addition to informing about the functional importance of SHH signalling within ACP, the pre-clinical study also gave valuable insights into how best to test therapeutics in the murine models. These are considered further in section 9.6.

9.4.3 Fibroblast growth factors and the mitogen activate protein kinase (MAPK) pathway

The expression of FGFs by human and murine ACP clusters had been previously described. In this thesis, I comprehensively assessed expression of pathway members and activation of downstream target pERK1/2 in human and murine ACP. This highlighted expression of several FGFs (particularly 3 and 4) in both human and murine ACP. Both of these and others in human ACP clusters (e.g. 9 and 20) are known to be expressed within the enamel knot. Combined knockouts (e.g. *Fgf3-/-Fgf10-/-* or *Fgf9-/-Fgf20-/-*) effect enamel formation or the enamel knot suggests a potential functional role in ACP (Haara, Harjunmaa et al. 2012, Li, Prochazka et al. 2014, Balic and Thesleff 2015). As in the developing tooth, receptors *FGFR1* and *2* are expressed across epithelial and non-epithelial compartments in human and murine ACP.

Downstream activation, as evidenced by pERK1/2 immunostaining, highlights potential paracrine signalling, with activation both in peri-cluster tumour tissue but also at palisading epithelium and reactive glia at the leading edge of tumour invasion.

Therapeutic targeting of FGFR signalling has been achieved. This has been through FGFR inhibitors, but also through targeting of the MAPK pathway using MEK inhibitors (Touat, Ileana et al. 2015). MEK1 and 2 are dual specific kinases that activate ERK1 and ERK2 and therefore the data presented in this thesis suggests are potential therapeutic targets in ACP (Zhao and Adjei 2014). These agents are increasing being used in paediatric low grade glioma (e.g. trametinib, sulemetenib) with minimal adverse side effects, and could therefore be relatively readily used in paediatric craniopharyngioma patients (Zhao and Adjei 2014, Banerjee, Jakacki et al. 2017).

FGFR and MEK inhibitors have been predominantly successful in patients with upstream mutations activating the pathway, both alone and in combination with other agents (e.g. BRAF inhibitors). Their therapeutic role in paracrine activation of

the pathway is less clear and predominantly limited to pre-clinical studies (Touat, Ileana et al. 2015).

MEK inhibitors have not been noted to adversely affect teeth, though most studies to date have been performed in adults. Activation of the pathway in individuals with Costello syndrome, as a result of germline over-activating mutations in *HRAS,* results in defective enamel mineralisation, with increased number, proliferation and irregular orientation of ameloblasts, in some ways analogous to ACP histology (Goodwin, Tidyman et al. 2014). This phenotype has been rescued by MEK inhibition in murine models (Goodwin, Tidyman et al. 2014).

Activation of EGFR, as observed in clusters, has previously been suggested as a therapeutic target in ACP (Holsken, Gebhardt et al. 2011). Activation of the MAPK pathway is also a major downstream pathway of EGFR activation and therefore the lack of activation in clusters suggest that this is not a major mechanism in ACP. EGFR also activates AKT and JNK pathways and so these may play a more significant role it is signalling in ACP (Normanno, De Luca et al. 2006).

9.4.4 Transforming Growth Factor β family

In this thesis I build on previously described expression of TGFβ in murine ACP clusters to highlight expression of TGFβ1 by human ACP clusters and downstream activation of TGFβ signalling, as evidenced by phosphorylation of SMAD3, both within tumour epithelia, but also in reactive glia immediately surrounding the tumour.

In contrast to other family members, the role of TGFβ signalling is tooth development is less clear, though its expression has been noted in the enamel knot and at later stages in mesenchymal components (Vaahtokari, Vainio et al. 1991).

Within tumourigenesis, TGFβ signalling has been observed to have pleiotropic pro- and anti-cancer effects, depending on stage of tumour development and the local microenvironment (Massague 2008). TGFβ signalling can have profound effects on tumour stromal interactions, broadly grouped in to promoting fibrosis, angiogenesis, EMT and invasion and promoting immune tolerance (Neuzillet,

Tijeras-Raballand et al. 2015). Within the CNS it has also been implicated in the pathogenesis of reactive gliosis including activation of astrocytes and increasing GFAP expression, but also in activating neurons both within and outside the central nervous system (Hamby and Sofroniew 2010).

In contrast to TGFβ, the role of BMP signalling within the developing tooth is more established. Like with FGFs, there is reciprocal signalling between epithelial and mesenchymal components observed during different stages of development (Balic and Thesleff 2015). The results presented in this thesis are consistent with similar processes with ACP.

Modulation of BMP signalling in developing teeth, through the use of conditional knockouts of ligands, receptors, and downstream signalling molecules in both epithelial and mesenchymal compartment, as well as the use of inhibitor soaked beads, has been shown to produce a variety of abnormalities, including of both enamel and dentin (Balic and Thesleff 2015). It is likely much could be learnt from this extensive literature to generate hypotheses about the functions of individual pathway members in human and murine ACP.

The pleiotropic roles and cellular contexts of TGFβ and BMP signalling have made translation of pathway inhibitors into clinical practice particularly challenging and there are currently no licenced inhibitors of this pathway.

9.4.5 Ectodysplasin pathway

Compared with the pathways above, the Ectodysplasin pathway is relatively less characterised. The results presented in this thesis highlight for the first time the expression of pathway members within ACP.

Germline human mutations in *EDAR* results in hypohidrotic ectodermal dysplasia (HED), characterised by missing teeth as well as sparse hair and reduced sweating (Kere, Srivastava et al. 1996). Mice without functional Eda lack teeth or have abnormal tooth cusp patterning, whilst overexpression results in additional teeth, hair and mammary glands (Mikkola and Thesleff 2003, Mikkola 2009).

In the tooth, the ligand Eda is expressed by the enamel epithelium and binds and activates EDAR signalling in the enamel knot (Tucker and Sharpe 2004, Balic and Thesleff 2015). This activates Nf-kB signalling which has also recently been shown to be active in ACP clusters by other members of the laboratory (Mikkola and Thesleff 2003). It has been suggested the EDAR signalling is a critical regulator of enamel knot formation and indeed many of the genes up-regulated in clusters are downstream targets (e.g. *DKK4, SH, FGF20*) (Tucker, Headon et al. 2000, Haara, Harjunmaa et al. 2012, Jussila and Thesleff 2012). This and the more restricted physiological roles of EDAR signalling, compared to the other pathways described above, makes targeting EDAR therapeutically attractive.

There are currently no licenced EDAR antagonists, though an EDAR agonist antibody, is currently in trial for patients with HED (Kowalczyk-Quintas and Schneider 2014). A pre-clinical EDAR blocking antibody has also been developed and used *in vivo* (Kowalczyk-Quintas, Willen et al. 2014). Preliminary experiments administering the antibody to mice pregnant with $Hesx1^{Cre/+};Ctnnb1^{lox(ex3)/+}$ litters were performed by Dr Helen Fraser, though no effect on clusters was observed. However, neither was any effect on hair follicles observed and these experiments are due to be repeated.

In addition to identifying expression of the pathway in human and murine ACP, we also identified expression in normal human and murine pituitaries. The absence of a pituitary phenotype in patients with HED, or genetically manipulated mice, suggests this may not be of functional significance.

9.4.6 Other pathways

In addition to the pathways identified here, several other pathways were characterised at the RNA level in both human ACP. These have variable patterns, e.g. LIF expressed by cluster, PDGFA by glia. The functional significance of these is currently unclear, both in ACP, but also in odontogenesis.

Similarly the function many of the transcription factors identified in ACP and highlighted in this theses, e.g. *BCL11B, MSX2*, have been explored in tooth

development, with genetic manipulations resulting in varying abnormalities of odontogenesis (Golonzhka, Metzger et al. 2009, Katsuragi, Anraku et al. 2013, Babajko, de La Dure-Molla et al. 2014).

9.4.7 Summary

Collectively, the results presented in this thesis highlight a complex pattern of autocrine and paracrine signalling in both human and murine ACP. Many of the patterns recapitulate that observed in the developing tooth. Exploration of the more extensive tooth literature, where many of these pathways have been manipulated genetically and/or therapeutically, is likely to be useful in informing on their potential role in ACP.

9.5 Targeting senescence: An opportunity for tumour prevention

Cellular senescence has traditionally been considered a tumour suppressor mechanism, preventing the uncontrolled expansion of mutated cells. In recent years pro-tumourigenic roles have been elucidated through the use of co-culture experiments and co-injection of senescent cells in xenografts (Coppe, Patil et al. 2008). These effects are mediated predominantly through paracrine activities of the SASP which results in i) direct effects on growth and proliferation of tumour cells, ii) promotion of tumour angiogenesis, invasion and metastasis, iii) reprogramming into tumour cells and favouring the emergence of tumour initiating cells, iv) modulation of the local immune environment.

In this thesis, RNA sequencing results support a senescent phenotype of ACP clusters and expression of numerous secreted factors, consistent with the SASP. Work by others in the group has shown that modulation of the SASP in ACP clusters affects the formation of late stage tumours. For example, tamoxifen induced activation of *CTNNB1* in Sox2 positive adult stem cells of older adult mice, or *Apc* deletion in Rathke's pouch, results in lower levels of secreted factors and absence of tumour formation (Gonzalez-Meljem, Haston et al. 2017). These results are of significance as they highlight a critical role of the SASP in non-cell autonomous tumourigenesis.

In addition to tumourigenesis, senescent cells have a range of physiological (e.g. promoting wound repair, tumour suppression) and pathological roles (e.g. in accelerating aging) (Munoz-Espin and Serrano 2014). Consequently there is great interest in therapeutic targeting of senescent cells. The results presented in this thesis, in combination with other work in the laboratory, suggest that killing of senescent cells could be of benefit in ACP, through removing the secretion of SASP factors.

Paracrine tumourigenesis has been proposed from studies in the mouse ACP models and as shown above, it may also be relevant in human ACP, with paracrine activities of the clusters controlling cell behaviour of epithelial reactive glia. In

mouse ACP the tumour mass contains cells which do not carry mutations in *CTNNB1*, whilst in the human ACP, this is not the case, as all epithelial tumours cells carry heterozygous CTNNB1 mutations. Nonetheless, human ACP tumours often show a large component of glial reactive tissue, free of *CTNNB1* mutations too and Chapter 7's results highlight this may harbour somatic mutations, analogous to those in mouse tumours. This may reflect a local mutagenic environment relating to the activities of the SASP and thus the paracrine tumourigenesis described in mouse ACP may become of much broader interest as a model to explain the initial stages of transformation in many other tumours.

9.6 Inflammation in ACP

Targeting inflammation in ACP, particularly in ACP cysts, has been suggested by several groups (Mori, Takeshima et al. 2004, Pettorini, Inzitari et al. 2010, Donson, Apps et al. 2017, Zhou, Zhang et al. 2017) and indeed one mechanism by which IFNα may act is through modulation of the local immune response (Ferrantini, Capone et al. 2007, Pettorini, Inzitari et al. 2010).

In this thesis I have characterised the immune cell infiltrate through *in silico* dissection of mRNA expression profiles and through immuno-histochemical evaluation of cell surface markers, cytokines and their receptors. Multiplex ELISA evaluation of specific cytokines in cystic fluid was also performed and further complemented by profiling of cystic fluid by collaborators (Todd Hankinson & Benedetta Pettorini).

The results have highlighted a variable immune cell infiltrate of myeloid and lymphoid derived cells and expression of pro-inflammatory cytokines (e.g. IL1β, IL18, TNFa) and anti-inflammatory (e.g. IL10) within ACP and ACP fluid. A signature of activation of the inflammasome has been observed and similarities with other diverse diseases relating to lipid deposition and crystal induced inflammation. A suggested model of inflammation in ACP is included in Figure 9-3.

9.6.1 IL1 family and inflammasome activation

The pattern of cytokines expressed both within ACP tissue as assessed by RNA seq and by analysis of human cystic fluid is reminiscent of activation of inflammasomes. As introduced in Chapter 5, inflammasomes are an innate immune machinery that on recognition of danger associated molecular patterns (DAMPS), initiate an inflammatory response through caspase mediated activation of IL1 family members, particularly IL1β and IL18 (Guo, Callaway et al. 2015). These subsequently drive expression of further inflammatory mediators e.g. IL6, IL8 and TNF and chemokines, e.g. CCL2 (Apte and Voronov 2008). Thus inflammasome activation may be the upstream mechanism by which many of the other pro-inflammatory cytokines observed in ACP are induced (Figure 9-3). Further evidence of the potential role of

the inflammasome in ACP has been recently published. Nie *et al.*, 2017, demonstrated expression of the purine receptor P2X7R correlates with expression of IL6, IL8 and MCP1 in ACP and that knockdown in primary cell culture reduced expression of these cytokines (Nie, Huang et al. 2017). P2X7R interacts directly with the NLRP3 inflammasome, and inhibition can reduce inflammasome mediated neuro-inflammation (Franceschini, Capece et al. 2015).

Lipids and crystals can activate the inflammasome and are commonly seen in ACP, suggesting a possible relationship with ACP and the inflammation observed in other diseases, for which specific therapies targeting activation of the inflammasome are now in routine practice. Targeting of inflammasome activation in inherited disorders of inflammasome activation (e.g. cryopyrin associated periodic syndromes (CAPS), familial periodic mediterranean fever (FMF)) and crystal arthropathies (e.g. gout) through IL1 pathway inhibiting agents, (Anakinra (anti-IL1R small molecular inhibitor) and Canakinumab (anti- IL1β monoclonal antibody)) has proved remarkably effective in reducing inflammation, symptoms and reducing or normalising downstream cytokine levels (Hoffman, Rosengren et al. 2004, Church, Savic et al. 2008, Ottaviani, Molto et al. 2013, Ozen, Demirkaya et al. 2016).

These agents are in routine clinical use in both adults and children and are known to cross the blood brain barrier, as evidenced by their effect on neuro-inflammation in conditions such as neonatal-onset multisystem inflammatory disease (NOMID, a severe form of CAPS) (Goldbach-Mansky, Dailey et al. 2006, Rodriguez-Smith, Lin et al. 2017). These therefore represent potentially readily translatable therapeutics that could be used to target ACP related inflammation.

In murine ACP, *Il18* is highly expressed and *Il1a* and *Il1b* variably expressed. Lipid clefts are not observed histologically in murine tumours, and whilst the unusual MRI flair pattern observed in murine ACP suggests similarities to human ACP, though the cholesterol content is unknown. Mice do not develop atherosclerosis in the absence of high fat diets or genetic manipulation and so the lack of cholesterol clefts and differences in the inflammatory signatures may relate to species differences in lipid metabolism (Lee, Lin et al. 2017). Anakinra inhibits murine IL1R and therefore would

be a suitable agent to explore the role of IL1 activation in murine ACP, whereas Canakinumab is specific to human IL1B.

9.6.2 IL6

The high expression of IL6 identified in cystic fluid has also been shown in separate cohorts and has been suggested as a target for therapy in ACP (Mori, Takeshima et al. 2004, Donson, Apps et al. 2017, Zhou, Zhang et al. 2017). Whilst *IL6* was not significantly up-regulated in ACP, as assessed by RNA seq, others have published immunostaining showing expression within ACP (Tena-Suck, Citlaltepelt et al. 2015, Zhou, Zhang et al. 2017). A recent publication studied the effect of IL6 and IL6 blockade on primary ACP cultures finding that migration was promoted with IL-6 treatment in a concentration-dependent manner and conversely treatment with an IL6 blocking monoclonal antibody significantly decreased the migration of ACP cells. In addition, IL6 treatment increased the expression of vimentin and decreased the expression of E-cadherin in a dose-dependent manner suggesting an effect of promotion of EMT (Zhou, Zhang et al. 2017).

IL6 is a downstream target of inflammasome activation through IL1β and IL18, suggesting a possible mechanism by which its expression is induced in some tumours. IL6 is also a core member of the classical SASP. Whilst there is accumulating evidence of activation of the SASP within ACP clusters, the relevance of this in established human ACP is not yet clear.

Several IL6 blocking agents are clinically available and routinely used in children. These include tocilizumab, a humanised monoclonal antibody against IL6R and siltixumab, directed against IL6 itself. Their routine use in patients with inflammatory disorders such as rheumatoid arthritis, and in controlling cytokine release syndrome induced by immunotherapies means that these therapies could be rapidly translated to the clinic (Lee, Gardner et al. 2014, Smolen, Landewe et al. 2014). Indeed intra-cystic administration of tocilizumab to patients with ACP has already been performed (Todd Hankinson, personal communication).

Of note however, targeting of IL6 in inflammasome mediated diseases has had only limited success, both in human and mouse despite reducing IL6 expression and pathway activation (McGeough, Pena et al. 2012). This suggests that targeting alone may be insufficient.

Il6 has been previously shown to be expressed in murine ACP clusters (Gonzalez-Meljem, Haston et al. 2017). By RNA seq I also show expression in late stage murine ACP. Similarly the *Il6ra* is variably expressed in murine ACP.

Human and murine IL6 and IL6Ra vary in homology and consequently tocilizumab cannot be directly tested in murine ACP. Alternative antibodies have been used in murine and rat targeting of the pathway and these could be used as a proof-of-principle for targeting the IL6 pathway in murine experiments. How these experiments may be designed is discussed in section 9.6.

9.6.3 TNFα

TNF was also highly up-regulated in ACP and present in cystic fluid. TNF has previously been shown to be expressed in ACP and concordant with this study we confirm correlation with the inflammatory infiltrate. Like IL6, TNFα has been targeted successfully in many inflammatory conditions (e.g. rheumatoid arthritis), however its role in inflammasome mediated conditions remains unclear and incompletely evaluated (Cavagna and Taylor 2014).

9.6.4 Other inflammatory mediators

Other inflammatory mediators identified in ACP in this thesis include the chemokine CCL2, whose expression, unsurprisingly, correlated with immune cell infiltrate. Complement proteins have been identified in the cystic fluid and are implicated in lipid induced inflammasome activation (Niyonzima, Halvorsen et al. 2017). Eculizumab is a monoclonal antibody that inhibits the terminal pathway of complement activation and is used in paroxysmal nocturnal haematuria and atypical haemolytic uraemic syndrome, however a currently very high price would favour the targeting of other pathways highlighted above.

9.6.5 Anti-inflammatory mediators

In addition to pro-inflammatory mediators, upregulation of anti-inflammatory mediators (e.g. *IL10, TGFB1*) was also apparent. Whilst not up-regulated in this cohort, the anti-inflammatory enzyme IDO-1 has also been shown to be up-regulated and expressed in ACP (Donson, Apps et al. 2017).

Growth of ACP cysts is not linear and can occur in episodic manner, in some ways analogous to flares of crystal arthropathies. Whilst IL10 is not generally highly expressed in gout it, along with TGFβ, has been implicated in the resolution phase of acute arthritis (Chen, Hsieh et al. 2011).

Immune mediated control and clearance of tumours is an important anti-tumour mechanism and local immune suppression (e.g. by anti-inflammatory cytokines, IDO) as a mechanism of immune escape is an emerging hallmark of cancer (Hanahan and Weinberg 2011). The significance of these processes remains unknown in ACP, therefore some caution and careful monitoring of any immunosuppressive therapies for ACP should be employed.

Figure 9-3 Model of inflammation in ACP. Cholesterol crystals activate the Inflammasome (the most common of which is the NLRP3 Infammasome), including through actions of complement and other danger signals. This results in activation of IL1β which in turn drives increased expression of IL6, IL8, TNFα and other cytokines and chemokines activating the local immune system. Therapeutic inhibitors at different stages are shown.

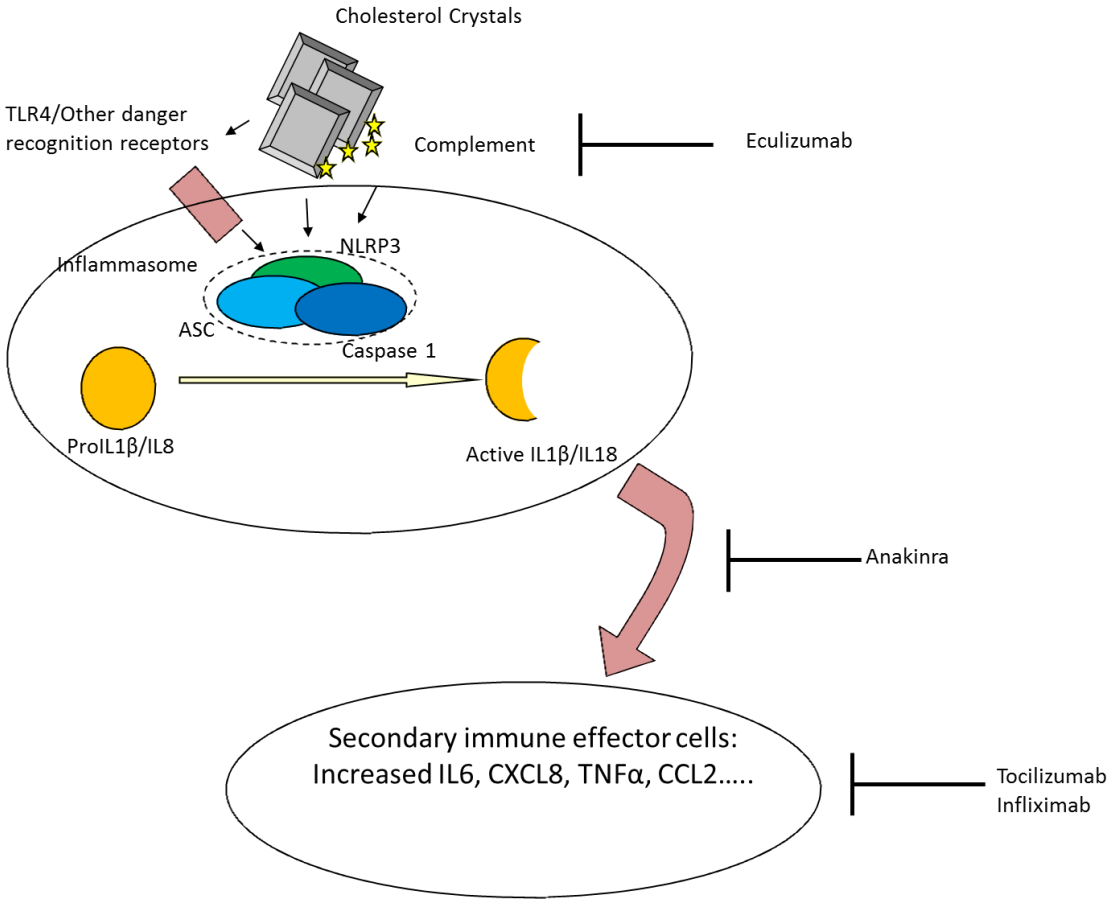

9.7 Translational strategies

This thesis has identified a number of novel therapeutic approaches in ACP, particularly targeting of the MAPK and EDAR pathways and inhibiting inflammasome mediated inflammation. In addition, improved understanding of the relationship between human and murine ACP and odontogenesis has advanced understanding of the different cellular components of human and murine ACP. Together with lessons learnt from the first pre-clinical murine ACP therapeutic trial it is now possible to develop a range of rational approaches for further pre-clinical therapeutic development for ACP.

9.7.1 Relationship of human and murine ACP

The RNA sequencing experiments have revealed many similarities between human and murine ACP, but also important differences that must be considered when testing therapeutics and interpreting results:

- Early stage murine ACP pituitaries reflect human ACP epithelia: At early stages of murine ACP development (e.g. E18.5/P1) clusters closely resemble their human counterparts; similarly GSEA shows a strong overall similarity in expression patterns with human ACP. The majority of the pituitary tissue is epithelial at this stage and signalling between clusters and epithelia/palsading epithelia, may be modelled. For instance pSMAD stainings show high expression in peri-cluster cells, though it was not explored whether these were Hesx1 or non Hesx1 lineage derived.
- Non-cell autonomous cellular accumulation represents epithelial-mesechymal interactions: The development of non-cell automonously derived lesions at mid stages reflects epithelial to mesenchymal signalling. With respect to human ACP, this likely best models features such as bony differentiation. The signalling pathways involved may also be those that result in activation of local reactive tissue (e.g. glia).
- Late stage murine ACP tumours have some similarities to human ACP at a transcriptional level, but do not so closely resemble tumour epithelia as

other stages. Similarly the relationship between late stage tumours and glial reactive tissue is unclear.

- The presence of cysts with late stage tumours suggests similarities to ACP, particularly given their similar imaging characteristics. The composition of murine ACP cysts remains to be characterised. Cholesterol clefts are not observed, despite haemorrhage, though difference in mouse and human cholesterol metabolism are known (Lee, Lin et al. 2017). There are also some similarities in the inflammatory cytokines expressed in late stage tumours (e.g. IL6, IL18), however an inflammatory infiltrate is not observed histologically and other cytokines e.g. *IL1a, IL1b, Tnf*, do not appear to be expressed.
- Death of mice is usually related to intra-cystic haemorrhage rather than solid tumour growth. Such large haemorrhage in human ACP is rare and therefore the use of this as an end point may not be the most appropriate way of assessing therapeutic efficacy.

In summary, this suggests that for testing of targeting intra-epithelial signalling within ACP, early stage mice should be used, whereas for testing inflammation and effects on cysts late stage mice should be used.

Possible methods for testing would include:

- Administration of agents in utero/early post-natal life with collection of specimens at a defined time point e.g. E18.5 or P7, followed by immune-histochemical assessment (e.g. of proliferation)
- MRI tracking of tumours, followed by administration of immune modulators once cystic growth established. Response assessed by MRI.

In addition to *in vivo* testing, other approaches include *ex vivo* culture of cells, slices, or whole pituitaries collected at stages chosen to reflect the therapeutic question. The similarities in inflammatory environment between ACP and crystal mediated diseases also suggests models of these could be adapted for ACP, for instance using ACP cystic fluid on cultured cells (e.g. macrophages), on *in vivo*, e.g. in murine air

pouches, to directly assess, monitor and potentially modulate any local inflammatory response.

As identified in the Chapters 3 and 8 there is considerable variability in the time course of tumours across different mice. This makes conducting statistically significant therapeutic trials difficult, particularly given the long latency of tumour growth. Such variability however is a characteristic of human ACP patients and thus the models may be reflecting this.

9.8 Concluding remarks

The work included in this thesis has significantly advanced the understanding of the morphological, genetic and signalling aspects of craniopharyngioma. Several pathways and processes of potential therapeutic importance have been characterised and our understanding of how to best use the pre-clinical genetically engineered mouse models of ACP significantly advanced.

References

Acosta, J. C., A. Banito, T. Wuestefeld, A. Georgilis, P. Janich, J. P. Morton, D. Athineos, T. W. Kang, F. Lasitschka, M. Andrulis, G. Pascual, K. J. Morris, S. Khan, H. Jin, G. Dharmalingam, A. P. Snijders, T. Carroll, D. Capper, C. Pritchard, G. J. Inman, T. Longerich, O. J. Sansom, S. A. Benitah, L. Zender and J. Gil (2013). "A complex secretory program orchestrated by the inflammasome controls paracrine senescence." Nat Cell Biol **15**(8): 978-990.

Agozzino, L., F. Ferraraccio, M. Accardo, S. Esposito, M. Agozzino and L. Cuccurullo (2006). "Morphological and ultrastructural findings of prognostic impact in craniopharyngiomas." Ultrastruct Pathol **30**(3): 143-150.

Ahmad, I., T. Iwata and H. Y. Leung (2012). "Mechanisms of FGFR-mediated carcinogenesis." Biochim Biophys Acta **1823**(4): 850-860.

Amakye, D., Z. Jagani and M. Dorsch (2013). "Unraveling the therapeutic potential of the Hedgehog pathway in cancer." Nat Med **19**(11): 1410-1422.

Anastas, J. N. and R. T. Moon (2013). "WNT signalling pathways as therapeutic targets in cancer." Nat Rev Cancer **13**(1): 11-26.

Andoniadou, C. L., C. Gaston-Massuet, R. Reddy, R. P. Schneider, M. A. Blasco, P. Le Tissier, T. S. Jacques, L. H. Pevny, M. T. Dattani and J. P. Martinez-Barbera (2012). "Identification of novel pathways involved in the pathogenesis of human adamantinomatous craniopharyngioma." Acta Neuropathol **124**(2): 259-271.

Andoniadou, C. L., D. Matsushima, S. N. Mousavy Gharavy, M. Signore, A. I. Mackintosh, M. Schaeffer, C. Gaston-Massuet, P. Mollard, T. S. Jacques, P. Le Tissier, M. T. Dattani, L. H. Pevny and J. P. Martinez-Barbera (2013). "Sox2(+) stem/progenitor cells in the adult mouse pituitary support organ homeostasis and have tumor-inducing potential." Cell Stem Cell **13**(4): 433-445.

Andoniadou, C. L., M. Signore, E. Sajedi, C. Gaston-Massuet, D. Kelberman, A. J. Burns, N. Itasaki, M. Dattani and J. P. Martinez-Barbera (2007). "Lack of the murine homeobox gene Hesx1 leads to a posterior transformation of the anterior forebrain." Development **134**(8): 1499-1508.

Apps, J. R., J. C. Hutchinson, O. J. Arthurs, A. Virasami, A. Joshi, B. Zeller-Plumhoff, D. Moulding, T. S. Jacques, N. J. Sebire and J. P. Martinez-Barbera (2016). "Imaging Invasion: Micro-CT imaging of adamantinomatous craniopharyngioma highlights cell type specific spatial relationships of tissue invasion." Acta Neuropathol Commun **4**(1): 57.

Apps, J. R. and J. P. Martinez-Barbera (2016). "Molecular pathology of adamantinomatous craniopharyngioma: review and opportunities for practice." Neurosurg Focus **41**(6): E4.

Apte, R. N. and E. Voronov (2008). "Is interleukin-1 a good or bad 'guy' in tumor immunobiology and immunotherapy?" Immunological Reviews **222**: 222-241.

Aylwin, S. J., I. Bodi and R. Beaney (2015). "Pronounced response of papillary craniopharyngioma to treatment with vemurafenib, a BRAF inhibitor." Pituitary.

Babajko, S., M. de La Dure-Molla, K. Jedeon and A. Berdal (2014). "MSX2 in ameloblast cell fate and activity." Front Physiol **5**: 510.

Balic, A. and I. Thesleff (2015). "Tissue Interactions Regulating Tooth Development and Renewal." Curr Top Dev Biol **115**: 157-186.

Banerjee, A., R. I. Jakacki, A. Onar-Thomas, S. Wu, T. Nicolaides, T. Young Poussaint, J. Fangusaro, J. Phillips, A. Perry, D. Turner, M. Prados, R. J. Packer, I. Qaddoumi, S. Gururangan, I. F. Pollack, S. Goldman, L. A. Doyle, C. F. Stewart, J. M. Boyett, L. E. Kun and M. Fouladi (2017). "A phase I trial of the MEK inhibitor selumetinib (AZD6244) in pediatric patients with recurrent or refractory low-grade glioma: a Pediatric Brain Tumor Consortium (PBTC) study." Neuro Oncol.

Bartels, U., N. Laperriere, E. Bouffet and J. Drake (2012). "Intracystic therapies for cystic craniopharyngioma in childhood." Front Endocrinol (Lausanne) **3**: 39.

Beaty, N. B. and E. Ahn (2014). "Images in clinical medicine. Adamantinomatous craniopharyngioma containing teeth." N Engl J Med **370**(9): 860.

Bernstein, M. L. and J. J. Buchino (1983). "The histologic similarity between craniopharyngioma and odontogenic lesions: a reappraisal." Oral Surg Oral Med Oral Pathol **56**(5): 502-511.

Bettendorf, M., M. Fehn, J. Grulich-Henn, B. Selle, K. Darge, D. K. Ludecke, U. E. Heinrich and W. Saeger (1999). "Lymphocytic hypophysitis with central diabetes insipidus and consequent panhypopituitarism preceding a multifocal, intracranial germinoma in a prepubertal girl." Eur J Pediatr **158**(4): 288-292.

Brastianos, P. K., G. M. Shankar, C. M. Gill, A. Taylor-Weiner, N. Nayyar, D. J. Panka, R. J. Sullivan, D. T. Frederick, M. Abedalthagafi, P. S. Jones, I. F. Dunn, B. V. Nahed, J. M. Romero, D. N. Louis, G. Getz, D. P. Cahill, S. Santagata, W. T. Curry, Jr. and F. G. Barker, 2nd (2016). "Dramatic Response of BRAF V600E Mutant Papillary Craniopharyngioma to Targeted Therapy." J Natl Cancer Inst **108**(2).

Brastianos, P. K., A. Taylor-Weiner, P. E. Manley, R. T. Jones, D. Dias-Santagata, A. R. Thorner, M. S. Lawrence, F. J. Rodriguez, L. A. Bernardo, L. Schubert, A. Sunkavalli, N. Shillingford, M. L. Calicchio, H. G. Lidov, H. Taha, M. Martinez-Lage, M. Santi, P. B. Storm, J. Y. Lee, J. N. Palmer, N. D. Adappa, R. M. Scott, I. F. Dunn, E. R. Laws, Jr., C. Stewart, K. L. Ligon, M. P. Hoang, P. Van Hummelen, W. C. Hahn, D. N. Louis, A. C. Resnick, M. W. Kieran, G. Getz and S. Santagata (2014). "Exome sequencing identifies BRAF mutations in papillary craniopharyngiomas." Nat Genet **46**(2): 161-165.

Bullard, D. E. and D. D. Bigner (1979). "Heterotransplantation of human craniopharyngiomas in athymic "nude" mice." Neurosurgery **4**(4): 308-314.

Bunin, G. R., T. S. Surawicz, P. A. Witman, S. Preston-Martin, F. Davis and J. M. Bruner (1998). "The descriptive epidemiology of craniopharyngioma." J Neurosurg **89**(4): 547-551.

Burghaus, S., A. Holsken, M. Buchfelder, R. Fahlbusch, B. M. Riederer, V. Hans, I. Blumcke and R. Buslei (2010). "A tumor-specific cellular environment at the brain invasion border of adamantinomatous craniopharyngiomas." Virchows Arch **456**(3): 287-300.

Buslei, R., A. Holsken, B. Hofmann, J. Kreutzer, F. Siebzehnrubl, V. Hans, F. Oppel, M. Buchfelder, R. Fahlbusch and I. Blumcke (2007). "Nuclear beta-catenin accumulation associates with epithelial morphogenesis in craniopharyngiomas." Acta Neuropathol **113**(5): 585-590.

Buslei, R., M. Nolde, B. Hofmann, S. Meissner, I. Y. Eyupoglu, F. Siebzehnrubl, E. Hahnen, J. Kreutzer and R. Fahlbusch (2005). "Common mutations of beta-catenin in adamantinomatous craniopharyngiomas but not in other tumours originating from the sellar region." Acta Neuropathol **109**(6): 589-597.

Cancer Research UK (2017).
Cao, J., J. P. Lin, L. X. Yang, K. Chen and Z. S. Huang (2010). "Expression of aberrant beta-catenin and impaired p63 in craniopharyngiomas." Br J Neurosurg **24**(3): 249-256.
Carreno, G., J. R. Apps, E. J. Lodge, L. Panousopoulos, J. M. Gonzalez-Meljem, S. Haston, H. Hahn, C. L. Andoniadou and J. P. Martinez-Barbera (2017). "Hypothalamic sonic hedgehog is required for cell specification and proliferation of LHX3/LHX4 pituitary embryonic precursors." Development **in press**.
Cavagna, L. and W. J. Taylor (2014). "The emerging role of biotechnological drugs in the treatment of gout." Biomed Res Int **2014**: 264859.
Cavalheiro, S., P. A. Dastoli, N. S. Silva, S. Toledo, H. Lederman and M. C. da Silva (2005). "Use of interferon alpha in intratumoral chemotherapy for cystic craniopharyngioma." Childs Nerv Syst **21**(8-9): 719-724.
Chen, M., S. H. Zheng, Y. Liu, J. Shi and S. T. Qi (2016). "Periostin activates pathways involved in epithelial-mesenchymal transition in adamantinomatous craniopharyngioma." J Neurol Sci **360**: 49-54.
Chen, Y. H., S. C. Hsieh, W. Y. Chen, K. J. Li, C. H. Wu, P. C. Wu, C. Y. Tsai and C. L. Yu (2011). "Spontaneous resolution of acute gouty arthritis is associated with rapid induction of the anti-inflammatory factors TGFbeta1, IL-10 and soluble TNF receptors and the intracellular cytokine negative regulators CIS and SOCS3." Ann Rheum Dis **70**(9): 1655-1663.
Chevillard, G., A. Derjuga, D. Devost, H. H. Zingg and V. Blank (2007). "Identification of interleukin-1beta regulated genes in uterine smooth muscle cells." Reproduction **134**(6): 811-822.
Choi, Y. and A. P. Chan (2015). "PROVEAN web server: a tool to predict the functional effect of amino acid substitutions and indels." Bioinformatics **31**(16): 2745-2747.
Church, L. D., S. Savic and M. F. McDermott (2008). "Long term management of patients with cryopyrin-associated periodic syndromes (CAPS): focus on rilonacept (IL-1 Trap)." Biologics **2**(4): 733-742.
Cobo, J., L. C. Hernandez, M. E. del Valle, M. Vijande and J. A. Vega (1992). "Immunohistochemical localization of epidermal growth factor and its receptor during odontogenesis in the rat." Eur J Orthod **14**(5): 333-338.
Cobourne, M. T. and P. T. Sharpe (2005). "Sonic hedgehog signaling and the developing tooth." Curr Top Dev Biol **65**: 255-287.
Cobourne, M. T. and P. T. Sharpe (2013). "Diseases of the tooth: the genetic and molecular basis of inherited anomalies affecting the dentition." Wiley Interdiscip Rev Dev Biol **2**(2): 183-212.
Cook, M. B., K. A. McGlynn, S. S. Devesa, N. D. Freedman and W. F. Anderson (2011). "Sex disparities in cancer mortality and survival." Cancer Epidemiol Biomarkers Prev **20**(8): 1629-1637.
Coppe, J. P., P. Y. Desprez, A. Krtolica and J. Campisi (2010). "The senescence-associated secretory phenotype: the dark side of tumor suppression." Annu Rev Pathol **5**: 99-118.
Coppe, J. P., C. K. Patil, F. Rodier, Y. Sun, D. P. Munoz, J. Goldstein, P. S. Nelson, P. Y. Desprez and J. Campisi (2008). "Senescence-associated secretory phenotypes reveal

cell-nonautonomous functions of oncogenic RAS and the p53 tumor suppressor." PLoS Biol **6**(12): 2853-2868.
Coy, S., Z. Du, S. H. Sheu, T. Woo, F. J. Rodriguez, M. W. Kieran and S. Santagata (2016). "Distinct patterns of primary and motile cilia in Rathke's cleft cysts and craniopharyngioma subtypes." Mod Pathol **29**(12): 1446-1459.
Crowley, R. K., O. P. Hamnvik, E. P. O'Sullivan, L. A. Behan, D. Smith, A. Agha and C. J. Thompson (2010). "Morbidity and mortality in patients with craniopharyngioma after surgery." Clin Endocrinol (Oxf) **73**(4): 516-521.
Curran, J. G. and E. O'Connor (2005). "Imaging of craniopharyngioma." Childs Nerv Syst **21**(8-9): 635-639.
Dallago, C. M., M. C. Oliveira, L. M. Barbosa-Coutinho and N. P. Ferreira (2005). "Angiogenesis in craniopharyngiomas: Microvascular density and tissue expression of the vascular endothelial growth factor (VEGF) and endostatin." Endocr Pathol **16**(4): 355-362.
Dassule, H. R., P. Lewis, M. Bei, R. Maas and A. P. McMahon (2000). "Sonic hedgehog regulates growth and morphogenesis of the tooth." Development **127**(22): 4775-4785.
Dattani, M. T., J. P. Martinez-Barbera, P. Q. Thomas, J. M. Brickman, R. Gupta, I. L. Martensson, H. Toresson, M. Fox, J. K. Wales, P. C. Hindmarsh, S. Krauss, R. S. Beddington and I. C. Robinson (1998). "Mutations in the homeobox gene HESX1/Hesx1 associated with septo-optic dysplasia in human and mouse." Nat Genet **19**(2): 125-133.
Davideau, J. L., C. Sahlberg, C. Blin, P. Papagerakis, I. Thesleff and A. Berdal (1995). "Differential expression of the full-length and secreted truncated forms of EGF receptor during formation of dental tissues." Int J Dev Biol **39**(4): 605-615.
Day, C. P., G. Merlino and T. Van Dyke (2015). "Preclinical mouse cancer models: a maze of opportunities and challenges." Cell **163**(1): 39-53.
Donson, A., J. R. Apps, A. M. Greisinger, V. Amani, D. A. Witt, R. C. Anderson, T. N. Niazi, G. Grant, M. Souweidane, J. M. Johnson, E. M. Jackson, B. K. Kleinschmidt-DeMasters, M. Handler, A. Tan, L. Gore, A. Virasami, J. M. Gonzalez-Meljem, T. S. Jacques, J. P. Martinez-Barbera, N. K. Foreman and T. C. Hankinson (2017). "Molecular Analyses Reveal Inflammatory Mediators in the Solid Component and Cyst Fluid of Human Adamantinomatous Craniopharyngioma." Journal of Neuropathology and Experimental Neurology.
Emani, M. R., E. Narva, A. Stubb, D. Chakroborty, M. Viitala, A. Rokka, N. Rahkonen, R. Moulder, K. Denessiouk, R. Trokovic, R. Lund, L. L. Elo and R. Lahesmaa (2015). "The L1TD1 protein interactome reveals the importance of post-transcriptional regulation in human pluripotency." Stem Cell Reports **4**(3): 519-528.
Esheba, G. E. and A. A. Hassan (2015). "Comparative immunohistochemical expression of beta-catenin, EGFR, ErbB2, and p63 in adamantinomatous and papillary craniopharyngiomas." J Egypt Natl Canc Inst **27**(3): 139-145.
Falcon, S. and R. Gentleman (2007). "Using GOstats to test gene lists for GO term association." Bioinformatics **23**(2): 257-258.
FDA (2012). "EveredidgeTM (vismodegib) FULL PRESCRIBING INFORMATION."
Ferrantini, M., I. Capone and F. Belardelli (2007). "Interferon-alpha and cancer: mechanisms of action and new perspectives of clinical use." Biochimie **89**(6-7): 884-893.

Forbes, S. A., D. Beare, N. Bindal, S. Bamford, S. Ward, C. G. Cole, M. Jia, C. Kok, H. Boutselakis, T. De, Z. Sondka, L. Ponting, R. Stefancsik, B. Harsha, J. Tate, E. Dawson, S. Thompson, H. Jubb and P. J. Campbell (2016). "COSMIC: High-Resolution Cancer Genetics Using the Catalogue of Somatic Mutations in Cancer." Curr Protoc Hum Genet **91**: 10 11 11-10 11 37.

Forshew, T., M. Murtaza, C. Parkinson, D. Gale, D. W. Tsui, F. Kaper, S. J. Dawson, A. M. Piskorz, M. Jimenez-Linan, D. Bentley, J. Hadfield, A. P. May, C. Caldas, J. D. Brenton and N. Rosenfeld (2012). "Noninvasive identification and monitoring of cancer mutations by targeted deep sequencing of plasma DNA." Sci Transl Med **4**(136): 136ra168.

Franceschini, A., M. Capece, P. Chiozzi, S. Falzoni, J. M. Sanz, A. C. Sarti, M. Bonora, P. Pinton and F. Di Virgilio (2015). "The P2X7 receptor directly interacts with the NLRP3 inflammasome scaffold protein." FASEB J **29**(6): 2450-2461.

Gaston-Massuet, C., C. L. Andoniadou, M. Signore, S. A. Jayakody, N. Charolidi, R. Kyeyune, B. Vernay, T. S. Jacques, M. M. Taketo, P. Le Tissier, M. T. Dattani and J. P. Martinez-Barbera (2011). "Increased Wingless (Wnt) signaling in pituitary progenitor/stem cells gives rise to pituitary tumors in mice and humans." Proc Natl Acad Sci U S A **108**(28): 11482-11487.

Gaston-Massuet, C., C. L. Andoniadou, M. Signore, E. Sajedi, S. Bird, J. M. Turner and J. P. Martinez-Barbera (2008). "Genetic interaction between the homeobox transcription factors HESX1 and SIX3 is required for normal pituitary development." Dev Biol **324**(2): 322-333.

Goldbach-Mansky, R., N. J. Dailey, S. W. Canna, A. Gelabert, J. Jones, B. I. Rubin, H. J. Kim, C. Brewer, C. Zalewski, E. Wiggs, S. Hill, M. L. Turner, B. I. Karp, I. Aksentijevich, F. Pucino, S. R. Penzak, M. H. Haverkamp, L. Stein, B. S. Adams, T. L. Moore, R. C. Fuhlbrigge, B. Shaham, J. N. Jarvis, K. O'Neil, R. K. Vehe, L. O. Beitz, G. Gardner, W. P. Hannan, R. W. Warren, W. Horn, J. L. Cole, S. M. Paul, P. N. Hawkins, T. H. Pham, C. Snyder, R. A. Wesley, S. C. Hoffmann, S. M. Holland, J. A. Butman and D. L. Kastner (2006). "Neonatal-onset multisystem inflammatory disease responsive to interleukin-1beta inhibition." N Engl J Med **355**(6): 581-592.

Goldberg, G. M. and D. E. Eshbaugh (1960). "Squamous cell nests of the pituitary gland as related to the origin of craniopharyngiomas. A study of their presence in the newborn and infants up to age four." Arch Pathol **70**: 293-299.

Golonzhka, O., D. Metzger, J. M. Bornert, B. K. Bay, M. K. Gross, C. Kioussi and M. Leid (2009). "Ctip2/Bcl11b controls ameloblast formation during mammalian odontogenesis." Proc Natl Acad Sci U S A **106**(11): 4278-4283.

Gomes, D. C., S. A. Jamra, L. F. Leal, L. M. Colli, M. L. Campanini, R. S. Oliveira, C. E. Martinelli, Jr., P. C. Elias, A. C. Moreira, H. R. Machado, F. Saggioro, L. Neder, M. Castro and S. R. Antonini (2015). "Sonic Hedgehog pathway is upregulated in adamantinomatous craniopharyngiomas." Eur J Endocrinol **172**(5): 603-608.

Gong, J., H. Zhang, S. Xing, C. Li, Z. Ma, G. Jia and W. Hu (2014). "High expression levels of CXCL12 and CXCR4 predict recurrence of adamanti-nomatous craniopharyngiomas in children." Cancer Biomark **14**(4): 241-251.

Gonzalez-Meljem, J. M., S. Haston, G. Carreno, J. R. Apps, S. Pozzi, C. Stache, G. Kaushal, A. Virasami, L. Panousopoulos, S. Neda, A. Guerro, M. Rashid, N. Jani, C. R. Goding, T. S. Jacques, D. J. Adams, J. Gil, C. L. Andoniadou and J. P. Martinez-

Barbera (2017). "Stem cell senescence drives age-attenuated induction of pituitary tumours in mouse models of paediatric craniopharyngioma." In process.
Goodwin, A. F., W. E. Tidyman, A. H. Jheon, A. Sharir, X. Zheng, C. Charles, J. A. Fagin, M. McMahon, T. G. Diekwisch, B. Ganss, K. A. Rauen and O. D. Klein (2014). "Abnormal Ras signaling in Costello syndrome (CS) negatively regulates enamel formation." Hum Mol Genet **23**(3): 682-692.
Gorlin, R. J. and A. P. Chaudhry (1959). "The ameloblastoma and the craniopharyngioma; their similarities and differences." Oral Surg Oral Med Oral Pathol **12**(2): 199-205.
Gorski, G. K., L. E. McMorrow, M. H. Donaldson and M. Freed (1992). "Multiple chromosomal abnormalities in a case of craniopharyngioma." Cancer Genet Cytogenet **60**(2): 212-213.
Goschzik, T., M. Gessi, V. Dreschmann, U. Gebhardt, L. Wang, S. Yamaguchi, D. A. Wheeler, L. Lauriola, C. C. Lau, H. L. Muller and T. Pietsch (2017). "Genomic Alterations of Adamantinomatous and Papillary Craniopharyngioma." J Neuropathol Exp Neurol **76**(2): 126-134.
Gospodarowicz, D. (1975). "Purification of a fibroblast growth factor from bovine pituitary." J Biol Chem **250**(7): 2515-2520.
Gospodarowicz, D., H. Bialecki and G. Greenburg (1978). "Purification of the fibroblast growth factor activity from bovine brain." J Biol Chem **253**(10): 3736-3743.
Gould, S. E., J. A. Low, J. C. Marsters, Jr., K. Robarge, L. L. Rubin, F. J. de Sauvage, D. P. Sutherlin, H. Wong and R. L. Yauch (2014). "Discovery and preclinical development of vismodegib." Expert Opin Drug Discov **9**(8): 969-984.
Griffin, C. A., P. P. Long, B. S. Carson and H. Brem (1992). "Chromosome abnormalities in low-grade central nervous system tumors." Cancer Genet Cytogenet **60**(1): 67-73.
Gump, J. M., A. M. Donson, D. K. Birks, V. M. Amani, K. K. Rao, A. M. Griesinger, B. K. Kleinschmidt-DeMasters, J. M. Johnston, R. C. Anderson, A. Rosenfeld, M. Handler, L. Gore, N. Foreman and T. C. Hankinson (2015). "Identification of targets for rational pharmacological therapy in childhood craniopharyngioma." Acta Neuropathol Commun **3**: 30.
Guo, H., J. B. Callaway and J. P. Ting (2015). "Inflammasomes: mechanism of action, role in disease, and therapeutics." Nat Med **21**(7): 677-687.
Haara, O., E. Harjunmaa, P. H. Lindfors, S. H. Huh, I. Fliniaux, T. Aberg, J. Jernvall, D. M. Ornitz, M. L. Mikkola and I. Thesleff (2012). "Ectodysplasin regulates activator-inhibitor balance in murine tooth development through Fgf20 signaling." Development **139**(17): 3189-3199.
Hamby, M. E. and M. V. Sofroniew (2010). "Reactive astrocytes as therapeutic targets for CNS disorders." Neurotherapeutics **7**(4): 494-506.
Hanahan, D. and R. A. Weinberg (2011). "Hallmarks of cancer: the next generation." Cell **144**(5): 646-674.
Harada, N., Y. Tamai, T. Ishikawa, B. Sauer, K. Takaku, M. Oshima and M. M. Taketo (1999). "Intestinal polyposis in mice with a dominant stable mutation of the beta-catenin gene." EMBO J **18**(21): 5931-5942.
Hassanein, A. M., S. M. Glanz, H. P. Kessler, T. A. Eskin and C. Liu (2003). "beta-Catenin is expressed aberrantly in tumors expressing shadow cells. Pilomatricoma,

craniopharyngioma, and calcifying odontogenic cyst." Am J Clin Pathol **120**(5): 732-736.
Haston, S., S. Pozzi, G. Carreno, S. Manshaei, L. Panousopoulos, J. M. Gonzalez-Meljem, J. R. Apps, A. Virasami, S. Thavaraj, A. Gutteridge, T. Forshew, R. Marais, S. Brandner, T. S. Jacques, C. L. Andoniadou and J. P. Martinez-Barbera (2017). "MAPK pathway activation in the embryonic pituitary results in stem cell compartment expansion, differentiation defects and provides insights into the pathogenesis of papillary craniopharyngioma." Development.
Helsinki, D. B. P. o. t. U. o. (1996-2007). "Gene expression in tooth."
Helsinki, D. B. P. o. U. o. (1996-2007). "Gene expression in tooth database http://bite-it.helsinki.fi Developmental Biology Programme of University of Helsinki." Retrieved 19th July, 2016.
Hill, R. M., S. Kuijper, J. C. Lindsey, K. Petrie, E. C. Schwalbe, K. Barker, J. K. Boult, D. Williamson, Z. Ahmad, A. Hallsworth, S. L. Ryan, E. Poon, S. P. Robinson, R. Ruddle, F. I. Raynaud, L. Howell, C. Kwok, A. Joshi, S. L. Nicholson, S. Crosier, D. W. Ellison, S. B. Wharton, K. Robson, A. Michalski, D. Hargrave, T. S. Jacques, B. Pizer, S. Bailey, F. J. Swartling, W. A. Weiss, L. Chesler and S. C. Clifford (2015). "Combined MYC and P53 defects emerge at medulloblastoma relapse and define rapidly progressive, therapeutically targetable disease." Cancer Cell **27**(1): 72-84.
Hindson, B. J., K. D. Ness, D. A. Masquelier, P. Belgrader, N. J. Heredia, A. J. Makarewicz, I. J. Bright, M. Y. Lucero, A. L. Hiddessen, T. C. Legler, T. K. Kitano, M. R. Hodel, J. F. Petersen, P. W. Wyatt, E. R. Steenblock, P. H. Shah, L. J. Bousse, C. B. Troup, J. C. Mellen, D. K. Wittmann, N. G. Erndt, T. H. Cauley, R. T. Koehler, A. P. So, S. Dube, K. A. Rose, L. Montesclaros, S. Wang, D. P. Stumbo, S. P. Hodges, S. Romine, F. P. Milanovich, H. E. White, J. F. Regan, G. A. Karlin-Neumann, C. M. Hindson, S. Saxonov and B. W. Colston (2011). "High-throughput droplet digital PCR system for absolute quantitation of DNA copy number." Anal Chem **83**(22): 8604-8610.
Hoffman, H. M., S. Rosengren, D. L. Boyle, J. Y. Cho, J. Nayar, J. L. Mueller, J. P. Anderson, A. A. Wanderer and G. S. Firestein (2004). "Prevention of cold-associated acute inflammation in familial cold autoinflammatory syndrome by interleukin-1 receptor antagonist." Lancet **364**(9447): 1779-1785.
Holsken, A. and R. Buslei (2017). "Models of human adamantinomatous craniopharyngioma tissue: Steps toward an effective adjuvant treatment." Brain Pathol **27**(3): 358-363.
Holsken, A., M. Gebhardt, M. Buchfelder, R. Fahlbusch, I. Blumcke and R. Buslei (2011). "EGFR signaling regulates tumor cell migration in craniopharyngiomas." Clin Cancer Res **17**(13): 4367-4377.
Holsken, A., J. Kreutzer, B. M. Hofmann, V. Hans, F. Oppel, M. Buchfelder, R. Fahlbusch, I. Blumcke and R. Buslei (2009). "Target gene activation of the Wnt signaling pathway in nuclear beta-catenin accumulating cells of adamantinomatous craniopharyngiomas." Brain Pathol **19**(3): 357-364.
Holsken, A., M. Sill, J. Merkle, L. Schweizer, M. Buchfelder, J. Flitsch, R. Fahlbusch, M. Metzler, M. Kool, S. M. Pfister, A. von Deimling, D. Capper, D. T. Jones and R. Buslei (2016). "Adamantinomatous and papillary craniopharyngiomas are characterized by distinct epigenomic as well as mutational and transcriptomic profiles." Acta Neuropathol Commun **4**(1): 20.

Holsken, A., C. Stache, S. M. Schlaffer, J. Flitsch, R. Fahlbusch, M. Buchfelder and R. Buslei (2014). "Adamantinomatous craniopharyngiomas express tumor stem cell markers in cells with activated Wnt signaling: further evidence for the existence of a tumor stem cell niche?" Pituitary **17**(6): 546-556.
Horvath, S., B. Zhang, M. Carlson, K. V. Lu, S. Zhu, R. M. Felciano, M. F. Laurance, W. Zhao, S. Qi, Z. Chen, Y. Lee, A. C. Scheck, L. M. Liau, H. Wu, D. H. Geschwind, P. G. Febbo, H. I. Kornblum, T. F. Cloughesy, S. F. Nelson and P. S. Mischel (2006). "Analysis of oncogenic signaling networks in glioblastoma identifies ASPM as a molecular target." Proc Natl Acad Sci U S A **103**(46): 17402-17407.
Huang, G. T., S. Gronthos and S. Shi (2009). "Mesenchymal stem cells derived from dental tissues vs. those from other sources: their biology and role in regenerative medicine." J Dent Res **88**(9): 792-806.
Husken, U. and M. Carl (2013). "The Wnt/beta-catenin signaling pathway establishes neuroanatomical asymmetries and their laterality." Mech Dev **130**(6-8): 330-335.
Hutchinson, J. C., M. T. Ashworth, N. J. Sebire and O. J. Arthurs (2017). "Multiple Cardiac Rhabdomyomas Visualised Using Micro-CT in a Case of Tuberous Sclerosis." Fetal Diagn Ther **41**(2): 157-160.
Hutchinson, J. C., H. Barrett, A. T. Ramsey, I. G. Haig, A. Guy, N. J. Sebire and O. J. Arthurs (2016). "Virtual pathological examination of the human fetal kidney using micro-CT." Ultrasound Obstet Gynecol **48**(5): 663-665.
Ishida, M., M. Hotta, A. Tsukamura, T. Taga, H. Kato, S. Ohta, Y. Takeuchi, S. Nakasu and H. Okabe (2010). "Malignant transformation in craniopharyngioma after radiation therapy: a case report and review of the literature." Clin Neuropathol **29**(1): 2-8.
Itoh, N. and D. M. Ornitz (2011). "Fibroblast growth factors: from molecular evolution to roles in development, metabolism and disease." J Biochem **149**(2): 121-130.
Jarvinen, E., I. Salazar-Ciudad, W. Birchmeier, M. M. Taketo, J. Jernvall and I. Thesleff (2006). "Continuous tooth generation in mouse is induced by activated epithelial Wnt/beta-catenin signaling." Proc Natl Acad Sci U S A **103**(49): 18627-18632.
Jones, D., K. M. Raine, H. Davies, P. S. Tarpey, A. P. Butler, J. W. Teague, S. Nik-Zainal and P. J. Campbell (2016). "cgpCaVEManWrapper: Simple Execution of CaVEMan in Order to Detect Somatic Single Nucleotide Variants in NGS Data." Curr Protoc Bioinformatics **56**: 15.10.11-15.10.18.
Jones, D. T., B. Hutter, N. Jager, A. Korshunov, M. Kool, H. J. Warnatz, T. Zichner, S. R. Lambert, M. Ryzhova, D. A. Quang, A. M. Fontebasso, A. M. Stutz, S. Hutter, M. Zuckermann, D. Sturm, J. Gronych, B. Lasitschka, S. Schmidt, H. Seker-Cin, H. Witt, M. Sultan, M. Ralser, P. A. Northcott, V. Hovestadt, S. Bender, E. Pfaff, S. Stark, D. Faury, J. Schwartzentruber, J. Majewski, U. D. Weber, M. Zapatka, B. Raeder, M. Schlesner, C. L. Worth, C. C. Bartholomae, C. von Kalle, C. D. Imbusch, S. Radomski, C. Lawerenz, P. van Sluis, J. Koster, R. Volckmann, R. Versteeg, H. Lehrach, C. Monoranu, B. Winkler, A. Unterberg, C. Herold-Mende, T. Milde, A. E. Kulozik, M. Ebinger, M. U. Schuhmann, Y. J. Cho, S. L. Pomeroy, A. von Deimling, O. Witt, M. D. Taylor, S. Wolf, M. A. Karajannis, C. G. Eberhart, W. Scheurlen, M. Hasselblatt, K. L. Ligon, M. W. Kieran, J. O. Korbel, M. L. Yaspo, B. Brors, J. Felsberg, G. Reifenberger,

V. P. Collins, N. Jabado, R. Eils, P. Lichter, S. M. Pfister and P. International Cancer Genome Consortium PedBrain Tumor (2013). "Recurrent somatic alterations of FGFR1 and NTRK2 in pilocytic astrocytoma." Nat Genet **45**(8): 927-932.
Jura, J., P. Wegrzyn, M. Korostynski, K. Guzik, M. Oczko-Wojciechowska, M. Jarzab, M. Kowalska, M. Piechota, R. Przewlocki and A. Koj (2008). "Identification of interleukin-1 and interleukin-6-responsive genes in human monocyte-derived macrophages using microarrays." Biochim Biophys Acta **1779**(6-7): 383-389.
Jurkiewicz, E., M. Bekiesinska-Figatowska, M. Duczkowski, W. Grajkowska, M. Roszkowski, J. Czech-Kowalska and A. Dobrzanska (2010). "Antenatal diagnosis of the congenital craniopharyngioma." Pol J Radiol **75**(1): 98-102.
Jussila, M. and I. Thesleff (2012). "Signaling networks regulating tooth organogenesis and regeneration, and the specification of dental mesenchymal and epithelial cell lineages." Cold Spring Harb Perspect Biol **4**(4): a008425.
Kalnins, V. (1971). "Calcification and amelogenesis in craniopharyngiomas." Oral Surg Oral Med Oral Pathol **31**(3): 366-379.
Karal-Yilmaz, O., A. Ozkan, E. Akgun, M. Kukut, K. Baysal, T. Avsar and T. Kilic (2013). "Controlled release of imatinib mesylate from PLGA microspheres inhibit craniopharyngioma mediated angiogenesis." J Mater Sci Mater Med **24**(1): 147-153.
Karnes, P. S., T. N. Tran, M. Y. Cui, C. Raffel, F. H. Gilles, J. A. Barranger and K. L. Ying (1992). "Cytogenetic analysis of 39 pediatric central nervous system tumors." Cancer Genet Cytogenet **59**(1): 12-19.
Kasai, H., A. Hirano, J. F. Llena and K. Kawamoto (1997). "A histopathological study of craniopharyngioma with special reference to its stroma and surrounding tissue." Brain Tumor Pathol **14**(1): 41-45.
Kato, K., Y. Nakatani, H. Kanno, Y. Inayama, R. Ijiri, N. Nagahara, T. Miyake, M. Tanaka, Y. Ito, N. Aida, K. Tachibana, K. Sekido and Y. Tanaka (2004). "Possible linkage between specific histological structures and aberrant reactivation of the Wnt pathway in adamantinomatous craniopharyngioma." J Pathol **203**(3): 814-821.
Katsuragi, Y., J. Anraku, M. Nakatomi, H. Ida-Yonemochi, M. Obata, Y. Mishima, Y. Sakuraba, Y. Gondo, Y. Kodama, A. Nishikawa, R. Takagi, H. Ohshima and R. Kominami (2013). "Bcl11b transcription factor plays a role in the maintenance of the ameloblast-progenitors in mouse adult maxillary incisors." Mech Dev **130**(9-10): 482-492.
Kawamata, T., O. Kubo and T. Hori (2005). "Histological findings at the boundary of craniopharyngiomas." Brain Tumor Pathol **22**(2): 75-78.
Keane, T. M., L. Goodstadt, P. Danecek, M. A. White, K. Wong, B. Yalcin, A. Heger, A. Agam, G. Slater, M. Goodson, N. A. Furlotte, E. Eskin, C. Nellaker, H. Whitley, J. Cleak, D. Janowitz, P. Hernandez-Pliego, A. Edwards, T. G. Belgard, P. L. Oliver, R. E. McIntyre, A. Bhomra, J. Nicod, X. Gan, W. Yuan, L. van der Weyden, C. A. Steward, S. Bala, J. Stalker, R. Mott, R. Durbin, I. J. Jackson, A. Czechanski, J. A. Guerra-Assuncao, L. R. Donahue, L. G. Reinholdt, B. A. Payseur, C. P. Ponting, E. Birney, J. Flint and D. J. Adams (2011). "Mouse genomic variation and its effect on phenotypes and gene regulation." Nature **477**(7364): 289-294.
Kelberman, D., K. Rizzoti, R. Lovell-Badge, I. C. Robinson and M. T. Dattani (2009). "Genetic regulation of pituitary gland development in human and mouse." Endocr Rev **30**(7): 790-829.

Kere, J., A. K. Srivastava, O. Montonen, J. Zonana, N. Thomas, B. Ferguson, F. Munoz, D. Morgan, A. Clarke, P. Baybayan, E. Y. Chen, S. Ezer, U. Saarialho-Kere, A. de la Chapelle and D. Schlessinger (1996). "X-linked anhidrotic (hypohidrotic) ectodermal dysplasia is caused by mutation in a novel transmembrane protein." Nat Genet **13**(4): 409-416.
Kim, J. Y., M. R. Kim and S. J. Kim (2013). "Modulation of osteoblastic/odontoblastic differentiation of adult mesenchymal stem cells through gene introduction: a brief review." J Korean Assoc Oral Maxillofac Surg **39**(2): 55-62.
Kode, A., J. S. Manavalan, I. Mosialou, G. Bhagat, C. V. Rathinam, N. Luo, H. Khiabanian, A. Lee, V. V. Murty, R. Friedman, A. Brum, D. Park, N. Galili, S. Mukherjee, J. Teruya-Feldstein, A. Raza, R. Rabadan, E. Berman and S. Kousteni (2014). "Leukaemogenesis induced by an activating beta-catenin mutation in osteoblasts." Nature **506**(7487): 240-244.
Kowalczyk-Quintas, C. and P. Schneider (2014). "Ectodysplasin A (EDA) - EDA receptor signalling and its pharmacological modulation." Cytokine Growth Factor Rev **25**(2): 195-203.
Kowalczyk-Quintas, C., L. Willen, A. T. Dang, H. Sarrasin, A. Tardivel, K. Hermes, H. Schneider, O. Gaide, O. Donze, N. Kirby, D. J. Headon and P. Schneider (2014). "Generation and characterization of function-blocking anti-ectodysplasin A (EDA) monoclonal antibodies that induce ectodermal dysplasia." J Biol Chem **289**(7): 4273-4285.
Kumar, P., S. Henikoff and P. C. Ng (2009). "Predicting the effects of coding non-synonymous variants on protein function using the SIFT algorithm." Nat Protoc **4**(7): 1073-1081.
Lammi, L., S. Arte, M. Somer, H. Jarvinen, P. Lahermo, I. Thesleff, S. Pirinen and P. Nieminen (2004). "Mutations in AXIN2 cause familial tooth agenesis and predispose to colorectal cancer." Am J Hum Genet **74**(5): 1043-1050.
Langfelder, P. and S. Horvath (2008). "WGCNA: an R package for weighted correlation network analysis." BMC Bioinformatics **9**: 559.
Langfelder, P., R. Luo, M. C. Oldham and S. Horvath (2011). "Is my network module preserved and reproducible?" PLoS Comput Biol **7**(1): e1001057.
Larkin, S. J. and O. Ansorge (2013). "Pathology and pathogenesis of craniopharyngiomas." Pituitary **16**(1): 9-17.
Larkin, S. J., V. Preda, N. Karavitaki, A. Grossman and O. Ansorge (2014). "BRAF V600E mutations are characteristic for papillary craniopharyngioma and may coexist with CTNNB1-mutated adamantinomatous craniopharyngioma." Acta Neuropathol **127**(6): 927-929.
Le Magnen, C., A. Dutta and C. Abate-Shen (2016). "Optimizing mouse models for precision cancer prevention." Nat Rev Cancer **16**(3): 187-196.
Lee, D. W., R. Gardner, D. L. Porter, C. U. Louis, N. Ahmed, M. Jensen, S. A. Grupp and C. L. Mackall (2014). "Current concepts in the diagnosis and management of cytokine release syndrome." Blood **124**(2): 188-195.
Lee, Y. T., H. Y. Lin, Y. W. Chan, K. H. Li, O. T. To, B. P. Yan, T. Liu, G. Li, W. T. Wong, W. Keung and G. Tse (2017). "Mouse models of atherosclerosis: a historical perspective and recent advances." Lipids Health Dis **16**(1): 12.
Lefranc, F., C. Chevalier, M. Vinchon, P. Dhellemmes, M. P. Schuring, H. Kaltner, J. Brotchi, M. M. Ruchoux, H. J. Gabius, I. Salmon and R. Kiss (2003). "Characterization

of the levels of expression of retinoic acid receptors, galectin-3, macrophage migration inhibiting factor, and p53 in 51 adamantinomatous craniopharyngiomas." J Neurosurg **98**(1): 145-153.
Lewis, A. M., S. Varghese, H. Xu and H. R. Alexander (2006). "Interleukin-1 and cancer progression: the emerging role of interleukin-1 receptor antagonist as a novel therapeutic agent in cancer treatment." Journal of Translational Medicine **4**.
Li, C. Y., J. Prochazka, A. F. Goodwin and O. D. Klein (2014). "Fibroblast growth factor signaling in mammalian tooth development." Odontology **102**(1): 1-13.
Li, H. (2013). "Aligning sequence reads, clone sequences and assembly contigs with BWA-MEM." arXiv.org **arXiv:1303.3997 [q-bio.GN]**.
Li, J., X. Huang, X. Xu, J. Mayo, P. Bringas, Jr., R. Jiang, S. Wang and Y. Chai (2011). "SMAD4-mediated WNT signaling controls the fate of cranial neural crest cells during tooth morphogenesis." Development **138**(10): 1977-1989.
Lou, K. (2014). "Stromal uncertainties in pancreatic cancer." SciBX **7**(23).
Louis, D. N., H. Ohgaki, O. D. Wiestler and W. K. Cavenee (2016). "World Health Organisation Histological Classification of Tumours of the Central Nervous System. ." International Agency for Research on Cancer, France.
Louis, D. N., A. Perry, G. Reifenberger, A. von Deimling, D. Figarella-Branger, W. K. Cavenee, H. Ohgaki, O. D. Wiestler, P. Kleihues and D. W. Ellison (2016). "The 2016 World Health Organization Classification of Tumors of the Central Nervous System: a summary." Acta Neuropathol **131**(6): 803-820.
Love, M. I., W. Huber and S. Anders (2014). "Moderated estimation of fold change and dispersion for RNA-seq data with DESeq2." Genome Biol **15**(12): 550.
Lujambio, A., L. Akkari, J. Simon, D. Grace, D. F. Tschaharganeh, J. E. Bolden, Z. Zhao, V. Thapar, J. A. Joyce, V. Krizhanovsky and S. W. Lowe (2013). "Non-cell-autonomous tumor suppression by p53." Cell **153**(2): 449-460.
Malgulwar, P. B., A. Nambirajan, P. Pathak, M. Faruq, V. Suri, C. Sarkar, A. Jagdevan, B. S. Sharma and M. C. Sharma (2017). "Study of beta-catenin and BRAF alterations in adamantinomatous and papillary craniopharyngiomas: mutation analysis with immunohistochemical correlation in 54 cases." J Neurooncol.
Mallucci, C., B. Pizer, J. Blair, M. Didi, A. Doss, S. Upadrasta, W. Newman, S. Avula and B. Pettorini (2012). "Management of craniopharyngioma: the Liverpool experience following the introduction of the CCLG guidelines. Introducing a new risk assessment grading system." Childs Nerv Syst **28**(8): 1181-1192.
Martelli, C., F. Iavarone, F. Vincenzoni, D. V. Rossetti, L. D'Angelo, G. Tamburrini, M. Caldarelli, C. Di Rocco, I. Messana, M. Castagnola and C. Desiderio (2014). "Proteomic characterization of pediatric craniopharyngioma intracystic fluid by LC-MS top-down/bottom-up integrated approaches." Electrophoresis **35**(15): 2172-2183.
Martinez-Barbera, J. P. (2015). "60 YEARS OF NEUROENDOCRINOLOGY: Biology of human craniopharyngioma: lessons from mouse models." J Endocrinol **226**(2): T161-172.
Martinez-Barbera, J. P. and R. Buslei (2015). "Adamantinomatous craniopharyngioma: pathology, molecular genetics and mouse models." J Pediatr Endocrinol Metab **28**(1-2): 7-17.
Massague, J. (2008). "TGFbeta in Cancer." Cell **134**(2): 215-230.

Massague, J. (2012). "TGFbeta signalling in context." Nat Rev Mol Cell Biol **13**(10): 616-630.
McGeough, M. D., C. A. Pena, J. L. Mueller, D. A. Pociask, L. Broderick, H. M. Hoffman and S. D. Brydges (2012). "Cutting edge: IL-6 is a marker of inflammation with no direct role in inflammasome-mediated mouse models." J Immunol **189**(6): 2707-2711.
Memarzadeh, S., L. Xin, D. J. Mulholland, A. Mansukhani, H. Wu, M. A. Teitell and O. N. Witte (2007). "Enhanced paracrine FGF10 expression promotes formation of multifocal prostate adenocarcinoma and an increase in epithelial androgen receptor." Cancer Cell **12**(6): 572-585.
Metscher, B. D. (2009). "MicroCT for comparative morphology: simple staining methods allow high-contrast 3D imaging of diverse non-mineralized animal tissues." BMC Physiol **9**: 11.
Mikkola, M. L. (2009). "Molecular aspects of hypohidrotic ectodermal dysplasia." Am J Med Genet A **149A**(9): 2031-2036.
Mikkola, M. L. and I. Thesleff (2003). "Ectodysplasin signaling in development." Cytokine Growth Factor Rev **14**(3-4): 211-224.
Momota, H., S. Ichimiya, T. Ikeda, T. Yamaki, T. Kikuchi, K. Houkin and N. Sato (2003). "Immunohistochemical analysis of the p53 family members in human craniopharyngiomas." Brain Tumor Pathol **20**(2): 73-77.
Monti, S., P. Tamayo, J. Mesirov and T. Golub (2003). "Consensus clustering: A resampling-based method for class discovery and visualization of gene expression microarray data." Machine Learning **52**(1-2): 91-118.
Mori, M., H. Takeshima and J. Kuratsu (2004). "Expression of interleukin-6 in human craniopharyngiomas: a possible inducer of tumor-associated inflammation." Int J Mol Med **14**(4): 505-509.
Moschovi, M., G. A. Alexiou, A. Dastamani, K. Stefanaki, N. Prodromou, H. Hatzigiorgi, K. Karamolegou and F. Tzortzatou-Stathopoulou (2010). "Alpha-fetoprotein secretion in a craniopharyngioma. Are craniopharyngiomas part of the germ cell tumor family?" Acta Neurol Belg **110**(3): 272-275.
Muller, C., N. Adroos, Z. Lockhat, T. Slavik and H. Kruger (2011). "Toothy craniopharyngioma: a literature review and case report of craniopharyngioma with extensive odontogenic differentiation and tooth formation." Childs Nerv Syst **27**(2): 323-326.
Muller, H. L. (2010). "Childhood craniopharyngioma--current concepts in diagnosis, therapy and follow-up." Nat Rev Endocrinol **6**(11): 609-618.
Muller, H. L., A. Emser, A. Faldum, G. Bruhnken, N. Etavard-Gorris, U. Gebhardt, R. Oeverink, R. Kolb and N. Sorensen (2004). "Longitudinal study on growth and body mass index before and after diagnosis of childhood craniopharyngioma." J Clin Endocrinol Metab **89**(7): 3298-3305.
Muller, H. L., T. E. Merchant, S. Puget and J. P. Martinez-Barbera (2017). "New outlook on the diagnosis, treatment and follow-up of childhood-onset craniopharyngioma." Nat Rev Endocrinol.
Munoz-Espin, D. and M. Serrano (2014). "Cellular senescence: from physiology to pathology." Nat Rev Mol Cell Biol **15**(7): 482-496.

Musani, V., P. Gorry, A. Basta-Juzbasic, T. Stipic, P. Miklic and S. Levanat (2006). "Mutation in exon 7 of PTCH deregulates SHH/PTCH/SMO signaling: possible linkage to WNT." Int J Mol Med **17**(5): 755-759.
Neuzillet, C., A. Tijeras-Raballand, R. Cohen, J. Cros, S. Faivre, E. Raymond and A. de Gramont (2015). "Targeting the TGFbeta pathway for cancer therapy." Pharmacol Ther **147**: 22-31.
Nicholes, K., S. Guillet, E. Tomlinson, K. Hillan, B. Wright, G. D. Frantz, T. A. Pham, L. Dillard-Telm, S. P. Tsai, J. P. Stephan, J. Stinson, T. Stewart and D. M. French (2002). "A mouse model of hepatocellular carcinoma: ectopic expression of fibroblast growth factor 19 in skeletal muscle of transgenic mice." Am J Pathol **160**(6): 2295-2307.
Nie, J., G. L. Huang, S. Z. Deng, Y. Bao, Y. W. Liu, Z. P. Feng, C. H. Wang, M. Chen, S. T. Qi and J. Pan (2017). "The purine receptor P2X7R regulates the release of pro-inflammatory cytokines in human craniopharyngioma." Endocr Relat Cancer **24**(6): 287-296.
Nik-Zainal, S., H. Davies, J. Staaf, M. Ramakrishna, D. Glodzik, X. Zou, I. Martincorena, L. B. Alexandrov, S. Martin, D. C. Wedge, P. Van Loo, Y. S. Ju, M. Smid, A. B. Brinkman, S. Morganella, M. R. Aure, O. C. Lingjaerde, A. Langerod, M. Ringner, S. M. Ahn, S. Boyault, J. E. Brock, A. Broeks, A. Butler, C. Desmedt, L. Dirix, S. Dronov, A. Fatima, J. A. Foekens, M. Gerstung, G. K. Hooijer, S. J. Jang, D. R. Jones, H. Y. Kim, T. A. King, S. Krishnamurthy, H. J. Lee, J. Y. Lee, Y. Li, S. McLaren, A. Menzies, V. Mustonen, S. O'Meara, I. Pauporte, X. Pivot, C. A. Purdie, K. Raine, K. Ramakrishnan, F. G. Rodriguez-Gonzalez, G. Romieu, A. M. Sieuwerts, P. T. Simpson, R. Shepherd, L. Stebbings, O. A. Stefansson, J. Teague, S. Tommasi, I. Treilleux, G. G. Van den Eynden, P. Vermeulen, A. Vincent-Salomon, L. Yates, C. Caldas, L. van't Veer, A. Tutt, S. Knappskog, B. K. Tan, J. Jonkers, A. Borg, N. T. Ueno, C. Sotiriou, A. Viari, P. A. Futreal, P. J. Campbell, P. N. Span, S. Van Laere, S. R. Lakhani, J. E. Eyfjord, A. M. Thompson, E. Birney, H. G. Stunnenberg, M. J. van de Vijver, J. W. Martens, A. L. Borresen-Dale, A. L. Richardson, G. Kong, G. Thomas and M. R. Stratton (2016). "Landscape of somatic mutations in 560 breast cancer whole-genome sequences." Nature **534**(7605): 47-54.
Niyonzima, N., B. Halvorsen, B. Sporsheim, P. Garred, P. Aukrust, T. E. Mollnes and T. Espevik (2017). "Complement activation by cholesterol crystals triggers a subsequent cytokine response." Mol Immunol **84**: 43-50.
Normanno, N., A. De Luca, C. Bianco, L. Strizzi, M. Mancino, M. R. Maiello, A. Carotenuto, G. De Feo, F. Caponigro and D. S. Salomon (2006). "Epidermal growth factor receptor (EGFR) signaling in cancer." Gene **366**(1): 2-16.
Obara, N. and H. Lesot (2004). "Subcellular localization of beta-catenin and cadherin expression in the cap-stage enamel organ of the mouse molar." Histochem Cell Biol **121**(4): 351-358.
Oikonomou, E., D. C. Barreto, B. Soares, L. De Marco, M. Buchfelder and E. F. Adams (2005). "Beta-catenin mutations in craniopharyngiomas and pituitary adenomas." J Neurooncol **73**(3): 205-209.
Orciani, M., M. Caffarini, G. Sorgentoni, R. A. Ricciuti, G. Arnaldi and R. Di Primio (2017). "Effects of somatostatin and its analogues on progenitor mesenchymal cells isolated from human pituitary adenomas." Pituitary **20**(2): 251-260.

Orciani, M., S. Davis, G. Appolloni, R. Lazzarini, M. Mattioli-Belmonte, R. A. Ricciuti, M. Boscaro, R. Di Primio and G. Arnaldi (2015). "Isolation and characterization of progenitor mesenchymal cells in human pituitary tumors." Cancer Gene Ther **22**(1): 9-16.
Ottaviani, S., A. Molto, H. K. Ea, S. Neveu, G. Gill, L. Brunier, E. Palazzo, O. Meyer, P. Richette, T. Bardin, Y. Allanore, F. Liote, M. Dougados and P. Dieude (2013). "Efficacy of anakinra in gouty arthritis: a retrospective study of 40 cases." Arthritis Res Ther **15**(5): R123.
Ozdemir, B. C., T. Pentcheva-Hoang, J. L. Carstens, X. Zheng, C. C. Wu, T. R. Simpson, H. Laklai, H. Sugimoto, C. Kahlert, S. V. Novitskiy, A. De Jesus-Acosta, P. Sharma, P. Heidari, U. Mahmood, L. Chin, H. L. Moses, V. M. Weaver, A. Maitra, J. P. Allison, V. S. LeBleu and R. Kalluri (2014). "Depletion of carcinoma-associated fibroblasts and fibrosis induces immunosuppression and accelerates pancreas cancer with reduced survival." Cancer Cell **25**(6): 719-734.
Ozen, S., E. Demirkaya, B. Erer, A. Livneh, E. Ben-Chetrit, G. Giancane, H. Ozdogan, I. Abu, M. Gattorno, P. N. Hawkins, S. Yuce, T. Kallinich, Y. Bilginer, D. Kastner and L. Carmona (2016). "EULAR recommendations for the management of familial Mediterranean fever." Ann Rheum Dis **75**(4): 644-651.
Paulus, W., C. Stockel, J. Krauss, N. Sorensen and W. Roggendorf (1997). "Odontogenic classification of craniopharyngiomas: a clinicopathological study of 54 cases." Histopathology **30**(2): 172-176.
Pettorini, B. L., R. Inzitari, L. Massimi, G. Tamburrini, M. Caldarelli, C. Fanali, T. Cabras, I. Messana, M. Castagnola and C. Di Rocco (2010). "The role of inflammation in the genesis of the cystic component of craniopharyngiomas." Childs Nerv Syst **26**(12): 1779-1784.
Plowman, P. N., G. M. Besser, J. Shipley, B. Summersgill, J. Geddes and F. Afshar (2004). "Dramatic response of malignant craniopharyngioma to cis-platin-based chemotherapy. Should craniopharyngioma be considered as a suprasellar 'germ cell' tumour?" Br J Neurosurg **18**(5): 500-505.
Preda, V., S. J. Larkin, N. Karavitaki, O. Ansorge and A. B. Grossman (2015). "The Wnt signalling cascade and the adherens junction complex in craniopharyngioma tumorigenesis." Endocr Pathol **26**(1): 1-8.
Prieto, R., J. M. Pascual, I. Subhi-Issa, M. Jorquera, M. Yus and R. Martinez (2013). "Predictive factors for craniopharyngioma recurrence: a systematic review and illustrative case report of a rapid recurrence." World Neurosurg **79**(5-6): 733-749.
Puget, S., M. Garnett, A. Wray, J. Grill, J. L. Habrand, N. Bodaert, M. Zerah, M. Bezerra, D. Renier, A. Pierre-Kahn and C. Sainte-Rose (2007). "Pediatric craniopharyngiomas: classification and treatment according to the degree of hypothalamic involvement." J Neurosurg **106**(1 Suppl): 3-12.
Raghavan, R., W. T. Dickey, Jr., L. R. Margraf, C. L. White, 3rd, C. Coimbra, L. S. Hynan and E. J. Rushing (2000). "Proliferative activity in craniopharyngiomas: clinicopathological correlations in adults and children." Surg Neurol **54**(3): 241-247; discussion 248.
Reimand, J., T. Arak, P. Adler, L. Kolberg, S. Reisberg, H. Peterson and J. Vilo (2016). "g:Profiler-a web server for functional interpretation of gene lists (2016 update)." Nucleic Acids Res **44**(W1): W83-89.

Rhim, A. D., P. E. Oberstein, D. H. Thomas, E. T. Mirek, C. F. Palermo, S. A. Sastra, E. N. Dekleva, T. Saunders, C. P. Becerra, I. W. Tattersall, C. B. Westphalen, J. Kitajewski, M. G. Fernandez-Barrena, M. E. Fernandez-Zapico, C. Iacobuzio-Donahue, K. P. Olive and B. Z. Stanger (2014). "Stromal elements act to restrain, rather than support, pancreatic ductal adenocarcinoma." Cancer Cell **25**(6): 735-747.

Rickert, C. H. and W. Paulus (2003). "Lack of chromosomal imbalances in adamantinomatous and papillary craniopharyngiomas." J Neurol Neurosurg Psychiatry **74**(2): 260-261.

Rienstein, S., E. F. Adams, D. Pilzer, A. A. Goldring, B. Goldman and E. Friedman (2003). "Comparative genomic hybridization analysis of craniopharyngiomas." J Neurosurg **98**(1): 162-164.

Ritchie, M. E., B. Phipson, D. Wu, Y. Hu, C. W. Law, W. Shi and G. K. Smyth (2015). "limma powers differential expression analyses for RNA-sequencing and microarray studies." Nucleic Acids Res **43**(7): e47.

Rodriguez-Smith, J., Y. C. Lin, W. L. Tsai, H. Kim, G. Montealegre-Sanchez, D. Chapelle, Y. Huang, C. H. Sibley, M. Gadina, R. Wesley, B. Bielekova and R. Goldbach-Mansky (2017). "Cerebrospinal Fluid Cytokines Correlate With Aseptic Meningitis and Blood-Brain Barrier Function in Neonatal-Onset Multisystem Inflammatory Disease: Central Nervous System Biomarkers in Neonatal-Onset Multisystem Inflammatory Disease Correlate With Central Nervous System Inflammation." Arthritis Rheumatol **69**(6): 1325-1336.

Roson-Burgo, B., F. Sanchez-Guijo, C. Del Canizo and J. De Las Rivas (2016). "Insights into the human mesenchymal stromal/stem cell identity through integrative transcriptomic profiling." BMC Genomics **17**(1): 944.

Ruch, J. M. and E. J. Kim (2013). "Hedgehog signaling pathway and cancer therapeutics: progress to date." Drugs **73**(7): 613-623.

Rueckel, J., M. Stockmar, F. Pfeiffer and J. Herzen (2014). "Spatial resolution characterization of a X-ray microCT system." Appl Radiat Isot **94**: 230-234.

Rumayor, A., R. Carlos, H. M. Kirsch, B. A. de Andrade, M. J. Romanach and O. P. de Almeida (2015). "Ghost cells in pilomatrixoma, craniopharyngioma, and calcifying cystic odontogenic tumor: histological, immunohistochemical, and ultrastructural study." J Oral Pathol Med **44**(4): 284-290.

Santos, M. C., P. B. Silva, C. O. Rodini, G. Furukawa, D. S. Marco Antonio, A. Zanotto-Filho, J. C. Moreira and O. K. Okamoto (2015). "Embryonic Stem Cell-Related Protein L1TD1 Is Required for Cell Viability, Neurosphere Formation, and Chemoresistance in Medulloblastoma." Stem Cells Dev **24**(22): 2700-2708.

Scales, S. J. and F. J. de Sauvage (2009). "Mechanisms of Hedgehog pathway activation in cancer and implications for therapy." Trends Pharmacol Sci **30**(6): 303-312.

Schwalbe, E. C., J. T. Hayden, H. A. Rogers, S. Miller, J. C. Lindsey, R. M. Hill, S. L. Nicholson, J. P. Kilday, M. Adamowicz-Brice, L. Storer, T. S. Jacques, K. Robson, J. Lowe, D. Williamson, R. G. Grundy, S. Bailey and S. C. Clifford (2013). "Histologically defined central nervous system primitive neuro-ectodermal tumours (CNS-PNETs) display heterogeneous DNA methylation profiles and show relationships to other paediatric brain tumour types." Acta Neuropathol **126**(6): 943-946.

Scott, A. E., D. M. Vasilescu, K. A. Seal, S. D. Keyes, M. N. Mavrogordato, J. C. Hogg, I. Sinclair, J. A. Warner, T. L. Hackett and P. M. Lackie (2015). "Three dimensional imaging of paraffin embedded human lung tissue samples by micro-computed tomography." PLoS One **10**(6): e0126230.
Scotting, P. J., D. A. Walker and G. Perilongo (2005). "Opinion - Childhood solid tumours: a developmental disorder." Nature Reviews Cancer **5**(6): 481-488.
Seemayer, T. A., J. S. Blundell and F. W. Wiglesworth (1972). "Pituitary craniopharyngioma with tooth formation." Cancer **29**(2): 423-430.
Sekine, S., S. Sato, T. Takata, Y. Fukuda, T. Ishida, M. Kishino, T. Shibata, Y. Kanai and S. Hirohashi (2003). "Beta-catenin mutations are frequent in calcifying odontogenic cysts, but rare in ameloblastomas." Am J Pathol **163**(5): 1707-1712.
Sekine, S., T. Shibata, A. Kokubu, Y. Morishita, M. Noguchi, Y. Nakanishi, M. Sakamoto and S. Hirohashi (2002). "Craniopharyngiomas of adamantinomatous type harbor beta-catenin gene mutations." Am J Pathol **161**(6): 1997-2001.
Sekine, S., T. Takata, T. Shibata, M. Mori, Y. Morishita, M. Noguchi, T. Uchida, Y. Kanai and S. Hirohashi (2004). "Expression of enamel proteins and LEF1 in adamantinomatous craniopharyngioma: evidence for its odontogenic epithelial differentiation." Histopathology **45**(6): 573-579.
Sekulic, A., M. R. Migden, A. E. Oro, L. Dirix, K. D. Lewis, J. D. Hainsworth, J. A. Solomon, S. Yoo, S. T. Arron, P. A. Friedlander, E. Marmur, C. M. Rudin, A. L. Chang, J. A. Low, H. M. Mackey, R. L. Yauch, R. A. Graham, J. C. Reddy and A. Hauschild (2012). "Efficacy and safety of vismodegib in advanced basal-cell carcinoma." N Engl J Med **366**(23): 2171-2179.
Senbabaoglu, Y., G. Michailidis and J. Z. Li (2014). "Critical limitations of consensus clustering in class discovery." Sci Rep **4**: 6207.
Sharma, J., C. M. Bonfield, A. Singhal, J. Hukin and P. Steinbok (2015). "Intracystic interferon-alpha treatment leads to neurotoxicity in craniopharyngioma: case report." J Neurosurg Pediatr **16**(3): 301-304.
Sharpe, P. T. (2016). "Dental mesenchymal stem cells." Development **143**(13): 2273-2280.
Shida, N., N. Nakasato, K. Mizoi, M. Kanaki and T. Yoshimoto (1998). "Symptomatic vessel narrowing caused by spontaneous rupture of craniopharyngioma cyst--case report." Neurol Med Chir (Tokyo) **38**(10): 666-668.
Shroff, B., J. E. Kashner, J. D. Keyser, C. Hebert and K. Norris (1996). "Epidermal growth factor and epidermal growth factor-receptor expression in the mouse dental follicle during tooth eruption." Arch Oral Biol **41**(6): 613-617.
Smolen, J. S., R. Landewe, F. C. Breedveld, M. Buch, G. Burmester, M. Dougados, P. Emery, C. Gaujoux-Viala, L. Gossec, J. Nam, S. Ramiro, K. Winthrop, M. de Wit, D. Aletaha, N. Betteridge, J. W. Bijlsma, M. Boers, F. Buttgereit, B. Combe, M. Cutolo, N. Damjanov, J. M. Hazes, M. Kouloumas, T. K. Kvien, X. Mariette, K. Pavelka, P. L. van Riel, A. Rubbert-Roth, M. Scholte-Voshaar, D. L. Scott, T. Sokka-Isler, J. B. Wong and D. van der Heijde (2014). "EULAR recommendations for the management of rheumatoid arthritis with synthetic and biological disease-modifying antirheumatic drugs: 2013 update." Ann Rheum Dis **73**(3): 492-509.
Sosa-Olavarria, A., L. Diaz-Guerrero, A. Reigoza, A. Bermudez and M. Murillo (2001). "Fetal craniopharyngioma: early prenatal diagnosis." J Ultrasound Med **20**(7): 803-806.

Spencer, D. H., M. Tyagi, F. Vallania, A. J. Bredemeyer, J. D. Pfeifer, R. D. Mitra and E. J. Duncavage (2014). "Performance of common analysis methods for detecting low-frequency single nucleotide variants in targeted next-generation sequence data." J Mol Diagn **16**(1): 75-88.
Stache, C., A. Holsken, S. M. Schlaffer, A. Hess, M. Metzler, B. Frey, R. Fahlbusch, J. Flitsch, M. Buchfelder and R. Buslei (2015). "Insights into the infiltrative behavior of adamantinomatous craniopharyngioma in a new xenotransplant mouse model." Brain Pathol **25**(1): 1-10.
Steinbok, P. (2015). "Craniopharyngioma in Children: Long-term Outcomes." Neurol Med Chir (Tokyo) **55**(9): 722-726.
Sterkenburg, A. S., A. Hoffmann, U. Gebhardt, M. Warmuth-Metz, A. M. Daubenbuchel and H. L. Muller (2015). "Survival, hypothalamic obesity, and neuropsychological/psychosocial status after childhood-onset craniopharyngioma: newly reported long-term outcomes." Neuro Oncol **17**(7): 1029-1038.
Subramanian, A., P. Tamayo, V. K. Mootha, S. Mukherjee, B. L. Ebert, M. A. Gillette, A. Paulovich, S. L. Pomeroy, T. R. Golub, E. S. Lander and J. P. Mesirov (2005). "Gene set enrichment analysis: a knowledge-based approach for interpreting genome-wide expression profiles." Proc Natl Acad Sci U S A **102**(43): 15545-15550.
Sulkava, M., E. Raitoharju, M. Levula, I. Seppala, L. P. Lyytikainen, A. Mennander, O. Jarvinen, R. Zeitlin, J. P. Salenius, T. Illig, N. Klopp, N. Mononen, R. Laaksonen, M. Kahonen, N. Oksala and T. Lehtimaki (2017). "Differentially expressed genes and canonical pathway expression in human atherosclerotic plaques - Tampere Vascular Study." Sci Rep **7**: 41483.
Sun, H. I., E. Akgun, A. Bicer, A. Ozkan, S. U. Bozkurt, O. Kurtkaya, D. Y. Koc, M. N. Pamir and T. Kilic (2010). "Expression of angiogenic factors in craniopharyngiomas: implications for tumor recurrence." Neurosurgery **66**(4): 744-750; discussion 750.
Tan, T. S., L. Patel, J. S. Gopal-Kothandapani, S. Ehtisham, E. C. Ikazoboh, R. Hayward, K. Aquilina, M. Skae, N. Thorp, B. Pizer, M. Didi, C. Mallucci, J. C. Blair, M. N. Gaze, I. Kamaly-Asl, H. Spoudeas and P. E. Clayton (2017). "The neuroendocrine sequelae of paediatric craniopharyngioma: a 40-year meta-data analysis of 185 cases from three UK centres." Eur J Endocrinol **176**(3): 359-369.
Tang, R., J. M. Buckley, L. Fernandez, S. Coopey, O. Aftreth, J. Michaelson, M. Saksena, L. Lei, M. Specht, M. Gadd, Y. Yagi, E. Rafferty, E. Brachtel and B. L. Smith (2013). "Micro-computed tomography (Micro-CT): a novel approach for intraoperative breast cancer specimen imaging." Breast Cancer Res Treat **139**(2): 311-316.
Taylor, M. D., P. A. Northcott, A. Korshunov, M. Remke, Y. J. Cho, S. C. Clifford, C. G. Eberhart, D. W. Parsons, S. Rutkowski, A. Gajjar, D. W. Ellison, P. Lichter, R. J. Gilbertson, S. L. Pomeroy, M. Kool and S. M. Pfister (2012). "Molecular subgroups of medulloblastoma: the current consensus." Acta Neuropathol **123**(4): 465-472.
Tena-Suck, M. L., S. Citlaltepelt, M. E. HC, C. SG and M. CL (2015). "Running Head: Craniopharyngioma and Immune Response." Journal of Neurology and Neuroscience **6**(3): 10.
Tena-Suck, M. L., M. E. Hernandez-Campos, A. Ortiz-Plata, C. Salinas-Lara, A. L. Colin-Gonzalez and A. Santamaria (2014). "Intracerebral injection of oil cyst content of human craniopharyngioma (oil machinery fluid) as a toxic model in the rat brain." Acta Histochem **116**(3): 448-456.

Tena-Suck, M. L., A. Y. Morales-Del Angel, M. E. Hernandez-Campos, F. Fernandez-Valverde, A. Ortiz-Plata, A. D. Hernandez and A. Santamaria (2015). "Ultrastructural characterization of craniopharyngioma at the tumor boundary: A structural comparison with an experimental toxic model using "oil machinery" fluid, with emphasis on Rosenthal fibers." Acta Histochem **117**(8): 696-704.
Thesleff, I. (2003). "Epithelial-mesenchymal signalling regulating tooth morphogenesis." J Cell Sci **116**(Pt 9): 1647-1648.
Tischler, G. and S. Leonard (2014). "biobambam: tools for read pair collation based algorithms on BAM file." Tischler and Leonard Source Code for Biology and Medicine 2014, 9:13
Topalian, S. L., J. M. Taube, R. A. Anders and D. M. Pardoll (2016). "Mechanism-driven biomarkers to guide immune checkpoint blockade in cancer therapy." Nat Rev Cancer **16**(5): 275-287.
Touat, M., E. Ileana, S. Postel-Vinay, F. Andre and J. C. Soria (2015). "Targeting FGFR Signaling in Cancer." Clin Cancer Res **21**(12): 2684-2694.
Tsoukalas, N., M. Tolia, I. D. Kostakis, N. Pistamaltzian, D. Tryfonopoulos, G. Lypas, G. Koumakis, V. Barbounis, N. Goutas and A. Efremidis (2013). "Coexistence of intracranial germ cell tumor and craniopharyngioma in an adolescent: case report and review of the literature." Int J Clin Exp Med **6**(3): 211-218.
Tucker, A. and P. Sharpe (2004). "The cutting-edge of mammalian development; how the embryo makes teeth." Nat Rev Genet **5**(7): 499-508.
Tucker, A. S., D. J. Headon, P. Schneider, B. M. Ferguson, P. Overbeek, J. Tschopp and P. T. Sharpe (2000). "Edar/Eda interactions regulate enamel knot formation in tooth morphogenesis." Development **127**(21): 4691-4700.
Vaahtokari, A., S. Vainio and I. Thesleff (1991). "Associations between transforming growth factor beta 1 RNA expression and epithelial-mesenchymal interactions during tooth morphogenesis." Development **113**(3): 985-994.
Vaquero, J., M. Zurita, S. de Oya, S. Coca, C. Morales and C. Salas (1999). "Expression of vascular permeability factor in craniopharyngioma." J Neurosurg **91**(5): 831-834.
Vidal, S., K. Kovacs, R. V. Lloyd, F. B. Meyer and B. W. Scheithauer (2002). "Angiogenesis in patients with craniopharyngiomas: correlation with treatment and outcome." Cancer **94**(3): 738-745.
Vincenti, M. P. and C. E. Brinckerhoff (2001). "Early response genes induced in chondrocytes stimulated with the inflammatory cytokine interleukin-1beta." Arthritis Res **3**(6): 381-388.
Visser, J., J. Hukin, M. Sargent, P. Steinbok, K. Goddard and C. Fryer (2010). "Late mortality in pediatric patients with craniopharyngioma." J Neurooncol **100**(1): 105-111.
Wang, H. W., Y. H. Wu, J. Y. Hsieh, M. L. Liang, M. E. Chao, D. J. Liu, M. T. Hsu and T. T. Wong (2010). "Pediatric primary central nervous system germ cell tumors of different prognosis groups show characteristic miRNome traits and chromosome copy number variations." BMC Genomics **11**: 132.
Wang, R. N., J. Green, Z. Wang, Y. Deng, M. Qiao, M. Peabody, Q. Zhang, J. Ye, Z. Yan, S. Denduluri, O. Idowu, M. Li, C. Shen, A. Hu, R. C. Haydon, R. Kang, J. Mok, M. J. Lee, H. L. Luu and L. L. Shi (2014). "Bone Morphogenetic Protein (BMP) signaling in development and human diseases." Genes Dis **1**(1): 87-105.

Wang, X. P., D. J. O'Connell, J. J. Lund, I. Saadi, M. Kuraguchi, A. Turbe-Doan, R. Cavallesco, H. Kim, P. J. Park, H. Harada, R. Kucherlapati and R. L. Maas (2009). "Apc inhibition of Wnt signaling regulates supernumerary tooth formation during embryogenesis and throughout adulthood." Development **136**(11): 1939-1949.
Weaver, J. M., C. S. Ross-Innes, N. Shannon, A. G. Lynch, T. Forshew, M. Barbera, M. Murtaza, C. A. Ong, P. Lao-Sirieix, M. J. Dunning, L. Smith, M. L. Smith, C. L. Anderson, B. Carvalho, M. O'Donovan, T. J. Underwood, A. P. May, N. Grehan, R. Hardwick, J. Davies, A. Oloumi, S. Aparicio, C. Caldas, M. D. Eldridge, P. A. Edwards, N. Rosenfeld, S. Tavare, R. C. Fitzgerald and O. Consortium (2014). "Ordering of mutations in preinvasive disease stages of esophageal carcinogenesis." Nat Genet **46**(8): 837-843.
Wilkerson, M. D. and D. N. Hayes (2010). "ConsensusClusterPlus: a class discovery tool with confidence assessments and item tracking." Bioinformatics **26**(12): 1572-1573.
Wong, H., B. Alicke, K. A. West, P. Pacheco, H. La, T. Januario, R. L. Yauch, F. J. de Sauvage and S. E. Gould (2011). "Pharmacokinetic-pharmacodynamic analysis of vismodegib in preclinical models of mutational and ligand-dependent Hedgehog pathway activation." Clin Cancer Res **17**(14): 4682-4692.
Wong, H., J. Z. Chen, B. Chou, J. S. Halladay, J. R. Kenny, H. La, J. C. Marsters, Jr., E. Plise, P. J. Rudewicz, K. Robarge, Y. Shin, S. Wong, C. Zhang and S. C. Khojasteh (2009). "Preclinical assessment of the absorption, distribution, metabolism and excretion of GDC-0449 (2-chloro-N-(4-chloro-3-(pyridin-2-yl)phenyl)-4-(methylsulfonyl)benzamide), an orally bioavailable systemic Hedgehog signalling pathway inhibitor." Xenobiotica **39**(11): 850-861.
Xavier, G. M., A. L. Patist, C. Healy, A. Pagrut, G. Carreno, P. T. Sharpe, J. P. Martinez-Barbera, S. Thavaraj, M. T. Cobourne and C. L. Andoniadou (2015). "Activated WNT signaling in postnatal SOX2-positive dental stem cells can drive odontoma formation." Sci Rep **5**: 14479.
Xu, J., C. You, S. Zhang, S. Huang, B. Cai, Z. Wu and H. Li (2006). "Angiogenesis and cell proliferation in human craniopharyngioma xenografts in nude mice." J Neurosurg **105**(4 Suppl): 306-310.
Xu, J., S. Zhang, C. You, X. Wang and Q. Zhou (2006). "Microvascular density and vascular endothelial growth factor have little correlation with prognosis of craniopharyngioma." Surg Neurol **66 Suppl 1**: S30-34.
Yokozeki, M., E. Afanador, M. Nishi, K. Kaneko, H. Shimokawa, K. Yokote, C. Deng, K. Tsuchida, H. Sugino and K. Moriyama (2003). "Smad3 is required for enamel biomineralization." Biochem Biophys Res Commun **305**(3): 684-690.
Yoshimoto, M., S. R. de Toledo, N. S. da Silva, J. Bayani, A. P. Bertozzi, J. N. Stavale, S. Cavalheiro, J. A. Andrade, M. Zielenska and J. A. Squire (2004). "Comparative genomic hybridization analysis of pediatric adamantinomatous craniopharyngiomas and a review of the literature." J Neurosurg **101**(1 Suppl): 85-90.
Young, M. D., M. J. Wakefield, G. K. Smyth and A. Oshlack (2010). "Gene ontology analysis for RNA-seq: accounting for selection bias." Genome Biol **11**(2): R14.
Zada, G., N. Lin, E. Ojerholm, S. Ramkissoon and E. R. Laws (2010). "Craniopharyngioma and other cystic epithelial lesions of the sellar region: a review of clinical, imaging, and histopathological relationships." Neurosurg Focus **28**(4): E4.

Zhang, B. and S. Horvath (2005). "A general framework for weighted gene co-expression network analysis." Stat Appl Genet Mol Biol **4**: Article17.
Zhang, Y., K. Chen, S. A. Sloan, M. L. Bennett, A. R. Scholze, S. O'Keeffe, H. P. Phatnani, P. Guarnieri, C. Caneda, N. Ruderisch, S. Deng, S. A. Liddelow, C. Zhang, R. Daneman, T. Maniatis, B. A. Barres and J. Q. Wu (2014). "An RNA-sequencing transcriptome and splicing database of glia, neurons, and vascular cells of the cerebral cortex." J Neurosci **34**(36): 11929-11947.
Zhao, Y. and A. A. Adjei (2014). "The clinical development of MEK inhibitors." Nat Rev Clin Oncol **11**(7): 385-400.
Zhou, J., C. Zhang, J. Pan, L. Chen and S. T. Qi (2017). "Interleukin6 induces an epithelialmesenchymal transition phenotype in human adamantinomatous craniopharyngioma cells and promotes tumor cell migration." Mol Med Rep **15**(6): 4123-4131.